Structural study of quantum dot: polymer nanocomposite films

By
Fahad Alshammari

Supervisors: Richard A.L. Jones & Dr Andrew Parnell

A thesis submitted in partial fulfilment for the degree of Doctor of Philosophy in Physics

Department of Physics and Astronomy
The University of Sheffield

2023

Declaration

The work described in this thesis was undertaken at The University of Sheffield Between October 2019 and September 2023 under the supervision of Professor Richard Jones and Dr Andrew Parnell. Unless stated it is the work of the author and has not been submitted in whole or in part for any other degree at this or any other institution.

Fahad Alshammari
2023

Acknowledgements

I deeply need to thank God for giving me the strength and blessings to finish this stage of my life. Next, I would like to express my great gratitude to all those who have supported and accompanied me during my PhD work. First of all, It has been a great honour and privilege for me to have worked under the supervision of **Prof. Richard Jones**, Professor of soft Condensed Matter Physics, Vice-President for Regional Innovation and Civic Engagement and professor of Materials Physics and Innovation Policy at the University of Manchester; and to **Dr Andrew Parnell** Dr of polymer physics at University of Sheffield, I thank them for their constant supervision, recommendations and suggestions during all years involved in my research work. I could not have imagined having a better advisor and mentor for my Ph. D., and without their excellent guidance and continuous support, knowledge and perceptiveness, I would never have finished. I would like to thank them for providing me with many opportunities and independence by giving me the freedom to develop myself as a genuinely independent researcher with creativity by developing my ideas. Their professional and personal attitude has made my stay at the University a very rewarding and memorable experience. It is my great pleasure and honour to be their student.

With great pleasure, I would like to express my deep sense of obligation and gratitude to all the polymer physics members at Sheffield University for their constant support and encouragement during my research work. Also, my heartfelt thanks and appreciation to Dr. Rachel C. Kilbride, Dr. Michael P. Weire and Dr. Daniel T. Toolan for their support, encouragement and ideas during this journey. I would like to acknowledge my earnest thanks to the other research and support staff at the university and the administrative staff, without whom this thesis could not have been completed. I am very much thankful to the head of the department and all teaching staff of The University of Sheffield for giving me space, encouragement and all possible help to complete my research.

My unbound gratitude goes to my family, in particular, my beloved mother for her prayers and moral support and my family, my wife Bushra for her patience and prayers, and my kids Reema, Hatim and the new arrival Sarah, who are a source of unending joy, happiness and smiles; also, my gratitude goes to my Brothers for their support and encouragement.

Finally, I would like to thank my sponsor, the Saudi Government, the University of Hail, the Royal Embassy, the Saudi Cultural Bureau and the Ministry of Higher Education for my scholarship and for supporting my studies.

Dedication

To The Glory of God To my late father, who unfortunately didn't stay in this world long enough to see his son in what he aspires to.

Abstract

Nanocomposite films consisting of quantum dots (QDs) embedded in a host polymer matrix have attracted immense research attention over the last few decades due to the tunable properties and potential of these films. Such hybrid composite films can combine the unique properties of polymers, which include flexibility, low cost, being lightweight and easily processible, with the quantum size confinement effects of QDs. QDs have rational design rules that enable tailored and highly controlled optical properties. In terms of potential applications, these films have potential in photonic devices; this includes laser diodes, light-emitting diodes, solar and photovoltaic cells, photodetectors, photon-upconversion and photon-multipliers. However, these films suffer from structural/ morphological issues; the QDs tend to aggregate when incorporated into the polymer matrix, due to the presence of cohesive forces, which hinder the optical properties of these nanocomposite films, leading to loss of the nanocomposite films' optical, electronic and mechanical properties. This thesis aims to develop and discover processing routes that could optimise the performance of optoelectronic devices by controlling the morphology and dispersion of QDs in nanocomposite films.

The experiments used device relevant Lead Sulphide quantum dots (PbS QDs) dispersed into three host polymers (PS, PMMA and F8BT); the nanocomposite films were characterised via ellipsometry, Atomic Force Microscopy (AFM) and Grazing Incident Small angle X-ray scattering (GISAXS). It was found that the QDs are well dispersed in the initial nanocomposite casting solution in the presence of a solvent, with a measured quantum dot core diameter of 4.8nm, and that aggregation occurs during the casting process; this casting was done via spin coating. The thickness of the spin-coated films, the QDs distribution at the film surface and the QD aggregation size were partially controlled by the host polymer M_w, which all increased with increasing polymer M_w and decreased with it. Exchanging the native stabilising ligands (OA) with shorter length carbon ligands Hexanoic and Decanoic acid ligands (HA and DA) reduced the film thickness, it also gave QD-poor domain in the film's surface morphology, aggregation size and interparticle separation compared to films with native OA ligands. This indicates the increased miscibility of the QDs with the polymer matrix. Lastly, the effect of QDs particle volume fractions and polymers matrix was investigated; it was found that increasing the QD volume fraction and decreasing the volume

fraction of polymer results in better miscibility and also with a notable reduction in aggregation sizes than when reducing the QDs volume fraction and increasing the volume fraction of polymer. Two films in this experiment show well-dispersed QDs in the polymer matrix, PMMA (2600 M_w): PbS QDs-DA (PbS QDs volume fraction ~ 0.024) and PS (1800 M_w): PbS QDs-DA (PbS QDs volume fraction ~ 0.024), where the crystal grain size is around 5nm and nearly reaches the QDs core diameter (4.8nm). Overall, these results enable us to understand some of the fundamental factors influencing the self-assembly of the QDs: polymer nanocomposite films and provide strategies for producing well-dispersed QDs in a polymer matrix.

Table of contents

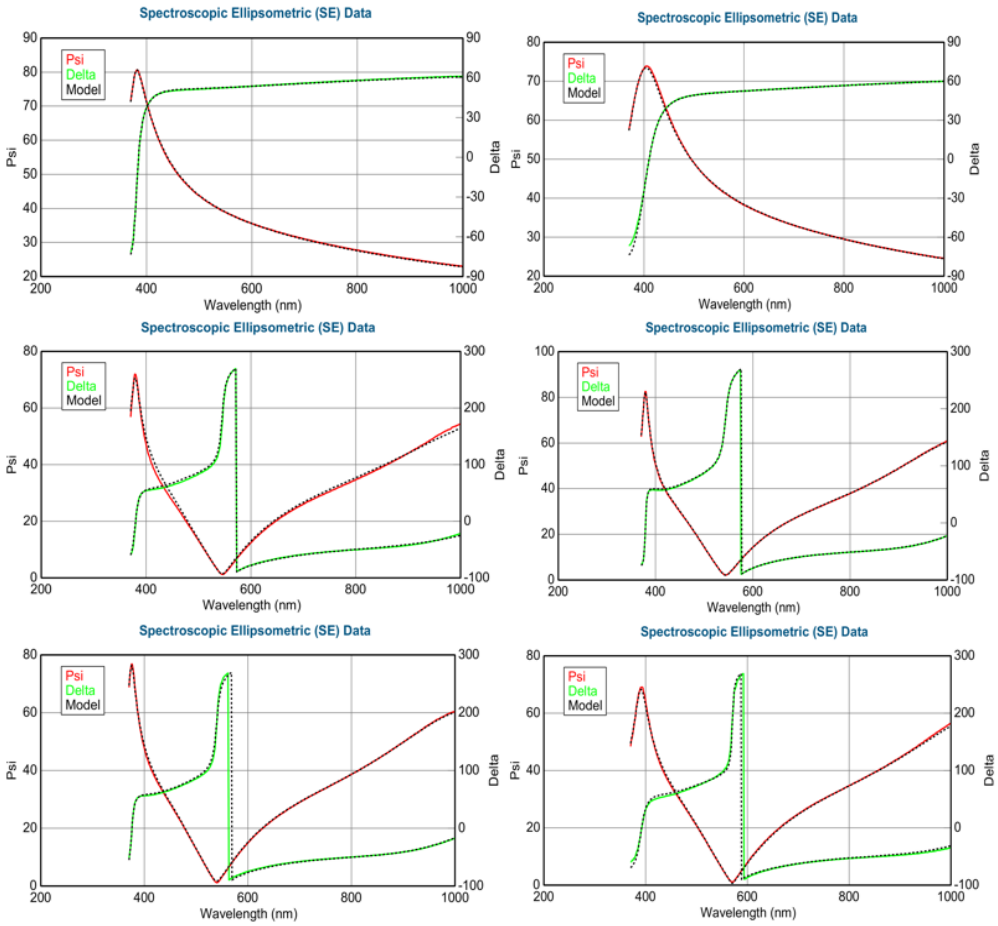

List of tables

List of figures

Symbols and Abbreviations

QDs:	Quantum Dots
PbS QDs:	Lead sulphide Quantum Dots
PMMA:	Poly Methyl Methacrylate
PS:	Polystyrene
F8BT:	Poly (9,9-dioctylfluorene-alt-benzothiadiazole)
OA:	Oleic acid
HA:	Hexanoic Acid
DA:	Decanoic Acid
M_w:	Molecular weight of the polymer
SF:	Singlet fission
CB:	Conduction band
VB:	Valence band
Eg:	Band gap
MEG:	Multiple exciton generation
T_g:	Glass transition temperature
R_g:	Polymer Radius of gyration
AFM:	Atomic Force Microscopy
SAXS:	Small-Angle X-Ray Scattering
GISAXS:	Grazing-Incident Small Angle Scattering
DLS:	Dynamic Light Scattering
DSC:	Differential Scanning Calorimetry
FNCFs:	Functional Nano-Composite Films
InNP:	Indium nitride nanoparticles
MA:	Methylammonium
MWCNT:	Multi-Walled Carbon Nanotubes
NMR:	Nuclear Magnetic Resonance

PDBF: (poly(2-(6-fluoro-7-methyl-benzo[c][1,2,5]thiadiazol-4-yl)-4-(heptadecane-9-yl)-6-methyl-4H- dithieno[3,2-b:20,30-d]pyrrole))

PDBT: poly(2,6-(N-(1-octylnonyl)dithieno[3,2-b:20,30-d]pyrrole)-alt-4,7-(2,1,3-benzothiadiazole))

PDFT: (poly(4-(hep-tadecan-9-yl)-2-methyl-6-(5-(7-(5-methylthiophen-2-yl)benzo[c]-[1,2,5]thiadiazol-4-yl)thiophen-2-yl)-4H-dithieno[3,2-b:20,30-d]-pyrrole))

PDTD: (poly(2,5-bis(2-ethyl-hexyl)-3-(5-(4-(heptadecan-9-yl)-6-methyl-4H-dithieno[3,2-b:20,30-d]pyrrol-2-yl)thiophen-2-yl)-6-(5-methylthiophen-2-yl)-2,5-dihydropyrrolo[3,4-c]pyrrole-1,4-dione)),

PDTT: (poly(4-(heptadecan-9-yl)-2-methyl-6-(5-(7-(5-methylfuran-2-yl)benzo[c]-[1,2,5]thiadiazol-4-yl)furan-2-yl)-4H-dithieno[3,2-b:20,30-d]pyrrole))

PEVA: Poly (Ethylene-co-Vinyl Acetate)

PINC: Polymer- Inorganic Nanocomposite

PSPD: Position-Sensitive Photodiode

PVDs: Photovoltage Devices

PVs: Photovoltaics

rGO: reduced Graphene Oxide

SA: Stearic Acid

SANS: Small-Angle Neutron Scattering

SE-HPLC: Size Exclusion High-Performance Chromatography

TEM: Transmission Electron Microscopy

TGA–MS: Thermogravimetric Analysis–Mass Spectrometry

TIPS: Tetracene: 5,12-Bis ((triisopropylsilyl)ethynyl)tetracene

TOPO: Trioctylphosphine oxide

UV: Ultraviolet

XPS: X-Ray Photoelectron Spectroscopy

XRD: X-Ray Diffraction

FWHM: Full Width of the half maximum

Chapter 1 Introduction and Objectives of the Project

1.1. Introduction

Nanocomposite Films consisting of semiconducting nanocrystals or quantum dots (QDs) embedded within polymer matrices can make functional materials with potential applications such as solar cells [1-4], light-emitting diodes [5, 6], photodetectors photon-upconversion [7], and photon-multipliers [8]. These materials can combine the attractive properties of the polymer host, such as being lightweight, low cost, and flexibility, with the strong quantum size confinement effects of the QDs, also having well-controlled optical properties [9].

There has been growing research interest in these materials in the last three decades. The reason for this is informed by the unique properties of these nanocomposite films, principally in renewable energy conversion and storage [2, 9]. The key benefits of these nanocomposite films are their lightweight, and simple manufacturing methods. In addition, nanocomposite materials have attracted attention because of their combined properties, such as barriers to gases and moisture, efficient thermal and electrical conductivity, stiffness, toughness, and mechanical strength. As a result of all these properties, nanocomposite materials have been widely used in different applications such as sensors, energy devices, medicine, and advanced goods and materials [10].

Regarding the structure of the polymers, preparation methods, and the nanoparticles, there are three structural types of composites based on how the nanoparticles are dispersed in the polymer. Composites can either be exfoliated nanocomposites, intercalated, or phase-separated micro-composites, as illustrated in Figure 1.1 [11].

The nanoparticles can be classified into three categories based on their structure; firstly spherical nanoparticles, which have a spherical shape with a diameter typically ranging from 1 to 100nm, secondly rod shaped nanoparticles, nanoparticles with a cylindrical shape; and finally, sheet or platelet-shaped nanoparticles that have a flat form, (Figure 1.2).

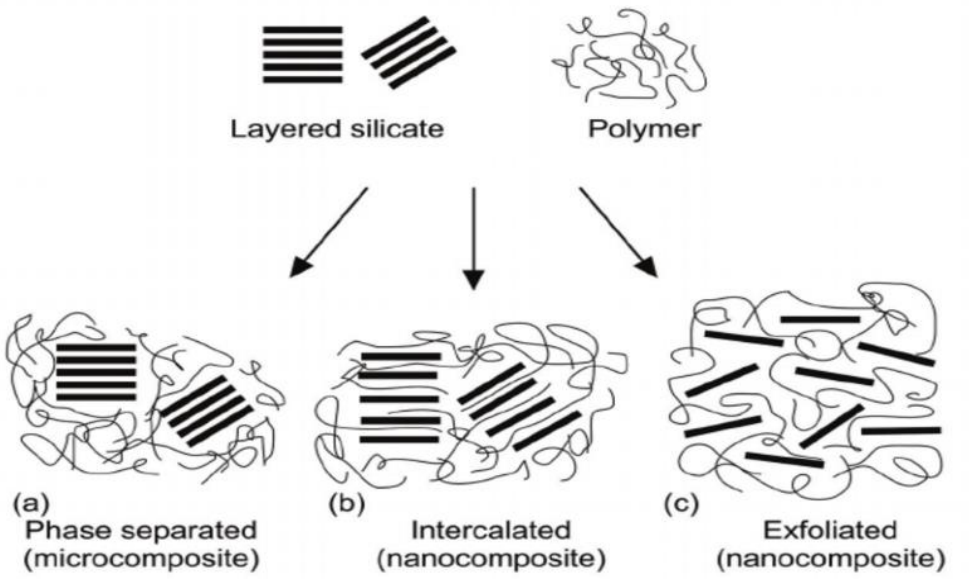

Figure 1.1/ Different nanocomposites generated from polymer-clay interactions [11].

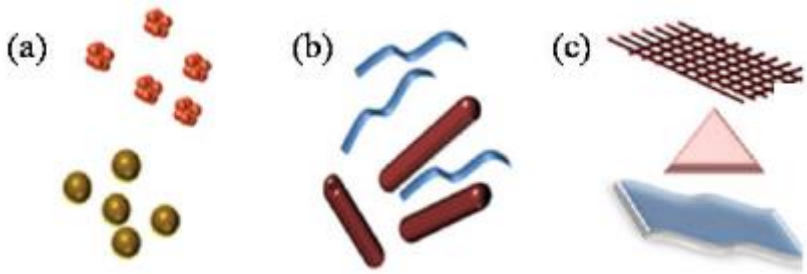

Figure 1.2/ classifications of the nanoparticles; (a) 0D sphere and cluster, (b) 1D nanorods and nanowires, (c) 2D sheets, nanofilms and network.

Despite the increased use of nanocomposite films in various fields, as mentioned above, the structural issues still need to be addressed so that improvement in the properties of these films is still a critical concern that hinders the wide-scale industrial use of these films [5, 12, 13]. The QDs tend to be phase segregated when incorporated into the polymer matrix due to cohesive forces, leading them to be aggregated. This, for example, lowers the photoluminescence quantum efficiency and reduces the triplet harvesting efficiency, which results in a loss of optical properties of the nanocomposites in optoelectronic devices [14, 15]. Moreover, the nanoparticle aggregation that follows insufficient dispersal into the polymer matrices causes an interfacial area restriction, degrading the mechanical and optical properties in the nanocomposite and reducing the potential enhancement of the mechanical and optical properties [16-18].

QD aggregation can form large agglomerates within the nanocomposite film, which may create weak points or defects, reducing overall film mechanical strength. As QD aggregates may decrease the flexibility of the nanocomposite film, by disrupting the regular packing or alignment of the polymer matrix, hindering the mobility of the polymer chains, and reducing the flexibility and elasticity of the nanocomposite film.

In addition, the QD aggregation can affect the optical properties of the nanocomposite films in many ways, such as altering the absorption and emission spectra, where the electronic states can interact, resulting in a shift in the energy levels and broadening of the absorption and emission peaks. These spectral changes can affect the colour and intensity of the light absorption and emission, potentially leading to a redshift or a blueshift in the optical response of the film. Also, QD aggregation can affect the bandgap; when the QDs aggregate, the electronic structure and energy levels of the QDs can change, affecting the bandgap and optical properties of the film. These changes may result in shifts in the absorption edge or changes in the energy required for electronic transitions, influencing the perceived colour and optical response of the film[19, 20].

Thus, there is a need to modify the physical interaction of the polymers and surface chemistry of the QDs to improve the chemical and physical interactions of QDs within the polymer chains to overcome the cohesive forces between QDs and the polymer chains that contribute to agglomeration or aggregation of the QD to achieve the desired nanocomposite film properties (Figure 1.3) [21, 22].

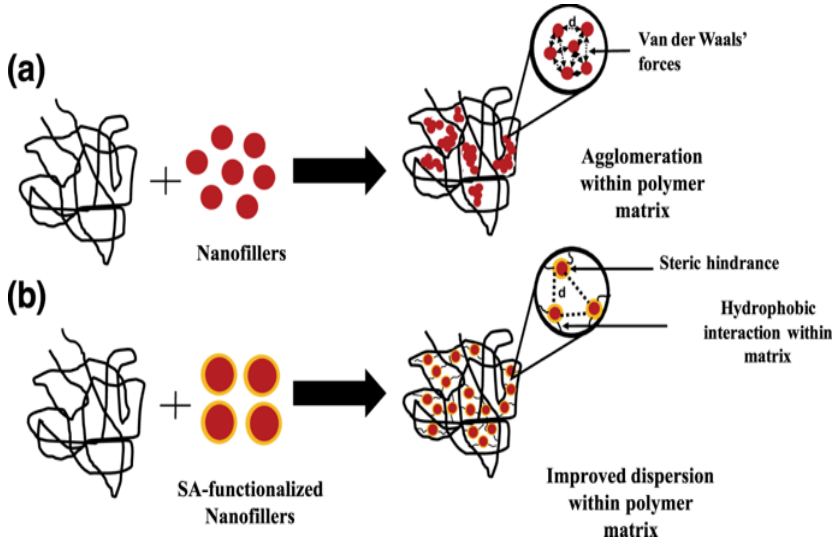

Figure 1.3/ a) The nanofillers aggregate when incorporated into the polymer matrix. b) Stearic acid (SA) capping the nanofillers for better dispersion within the polymer matrices. This is an example of modifying the nanoparticles surface, which results in a better nanoparticle dispersion within the polymer matrix.

1.1.1. Renewable energy

Over the years, the world has experienced a massive increase in oil and gas consumption for energy generation, resulting in adverse environmental impacts, including climate change. Overcoming potential environmental hazards from hydrocarbon exploitation and their depletion requires advanced investment in renewable energies. Wind power and photovoltaics (PVs) have seen an uplift in their use, with substantial progress made in this field over the last two decades. The research on storage and conversion of green energy has reached commercial viability with lithium batteries powering vehicles instead of conventional fossil fuels [23, 24]. As the most plentiful, cleaner, and long-lasting renewable energies, wind and solar continue attracting significant interest; nanocomposites play an important role in these technologies.

However, one of the research concerns is how to harness and efficiently store renewable energy for further applications. For example, thermal thin films have been noted to be less effective in solar energy collection due to their low thermal storage and low conductivity, limiting their commercial or practical use. In wind generation, there are growing concerns about the inefficiencies of conventional metal materials used for turbine blades due to metal corrosion, weight, and costs, which hinder their use. In lithium-ion batteries, the main

concern has been the short lifespan of these batteries due to the high corrosion levels of conventional cathode materials. These shortcomings raise the need for additional research to achieve higher efficiency in the renewable energy field.

Considering the above, well-designed nanocomposite films have been reported as potential solutions to improve renewable energy exploitation. Shang et al. proposed a di-functional nanocomposite material based on gold nanoparticles to achieve fast solar-to-heat conversion[9]. In thermal applications, thin nanocomposite films have been used for protection and as excellent materials to regulate heat or solar transfer[25]. QDs in solar photoconversion are reported to increase the efficiency and speed of photon energy conversion through photoinduced electron-hole pairs[26, 27].

The following sections further detail the application of QDs in renewable energy, specifically focusing on Photovoltaic Devices (PVDs).

1.1.1.1. Photovoltaic devices

As the demand for PVDs increases amid the uptake of renewable energy sources, there is a need to address the shortcomings of traditional solar panels. Some of the potential shortcomings include limited storage and use of space. Functional nanocomposite materials are attractive in addressing these shortcomings and making PVDs more efficient. The use of transparent plastics or polymers such as poly(ethylene-co-vinyl acetate) (PEVA) in solar panels can be used both in commercial greenhouses and in PV modules[28].

Nonetheless, the main concern in PVD modules is how to reach a proper structure via achieving a high level of dispersion of the contents without compromising the thermal and optical properties of the materials.

Over the last two decades, advances in material science have revealed that QDs or nanocrystalline semiconductors have the potential to improve PV modules in terms of absorbing ultraviolet light and selectively emitting visible light, thereby increasing the overall energy conversion efficiency[29]. However, the main challenge is stabilising QDs to ensure a longer PV lifetime and easier incorporation into polymer systems[29, 30]. So, more work is

needed to modify the physical and chemical properties of the QDs and polymer matrices to improve the miscibility between them.

1.2. Outlines of the project

This thesis addresses the structural issue in nanocomposite films consisting of QDs embedded into a polymer matrix, these kinds of films often suffer from the QDs being aggregated when incorporated into the polymer matrix. These can be used in various applications, in particular, these nanocomposite films have potential applications in the area of optoelectronics - for example, as efficient downconverters for use as sensitising solar cells to increase the efficiency and trying to break the well-known Shockley-Queisser limit, whereby the maximum solar conversion efficiency is at around 33.7% for a single p-n junction photovoltaic cell. In this application, the nanocomposite films contain QDs incorporated into a polymer matrix and are to be used as a front converter combined with a Singlet fission (SF) material. The SF material nanocomposite films; will absorb the high-energy photon to form two triplet excitons; then, these two triplet excitons will transfer to the QDs, leading to the emission of two low-energy photons for each high-energy photon absorbed; this happens via radiative electron-hole recombination. Finally, the emitted photons are absorbed in a conventional solar cell, minimising the thermalisation losses in this device (Figure 1.4).

However, the QDs tend to phase segregate when incorporated into the polymer matrix from solution, due to cohesive forces, leading them to aggregate (Figure 1.5 a), lowering their photoluminescence quantum efficiency and reducing the triplet harvesting efficiency. The QDs suffer from surface trap states when aggregated; these trap states act as non-radiative recombination centres, and the competition between the radiative and non-radiative routes minimises the photoluminescence quantum yield of the QD. So, to get the best from this device, the QDs need to be spread throughout the nanocomposite film to obtain the desired morphology (Figure 1.5 b).

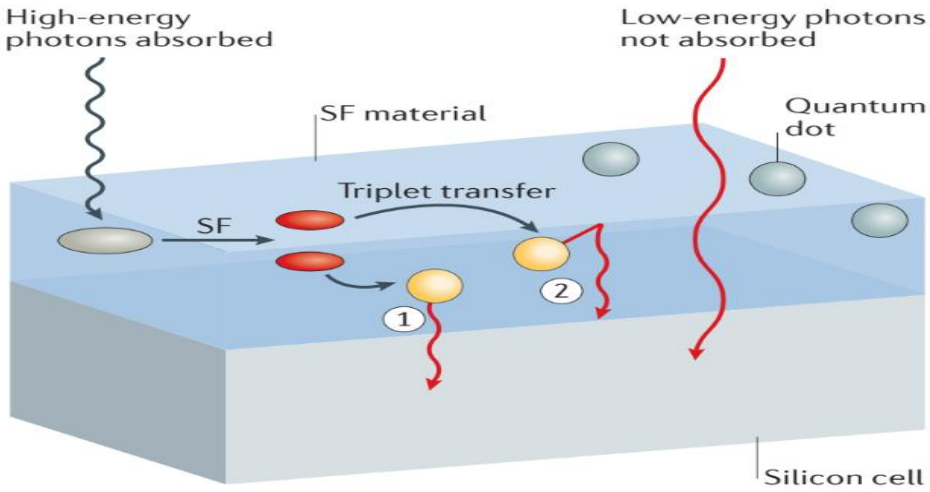

Figure 1.4/ A schematic of a singlet fission device that contains QDs within a Polymer matrix[31].

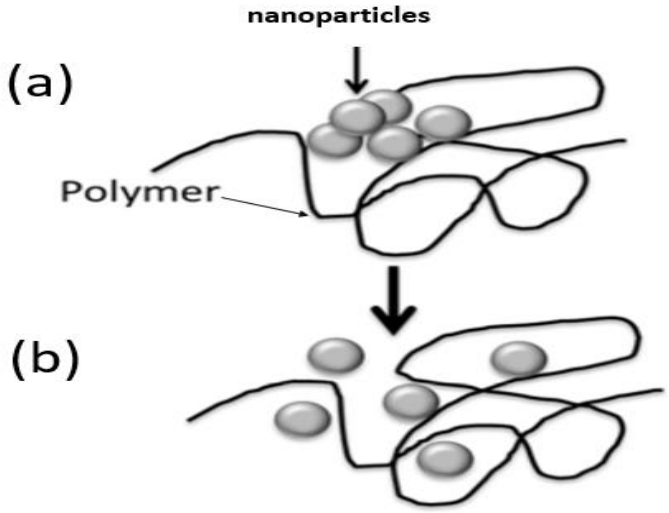

Figure 1.5/ (a) aggregation of nanoparticles in a polymer matrix; (b) well dispersed (isolated) nanoparticles in a polymer matrix.

The structure of the thesis follows the chronological order of work conducted to achieve the stated aims and objectives. As such, the thesis content is organised into seven chapters, including this introductory chapter.

Chapter 2 provides a brief literature review of QDs, polymers and previous research on nanocomposite films consisting of them. It outlines an introduction to QDs and polymers and establishes the background knowledge to understand them.

Chapter 3 discusses the characterisation and Experimental Techniques that will be used in this project and the principles of them.

Chapter 4 focuses on the effect of host polymer molecular weight on the nanocomposite film morphology of Lead Sulphide quantum dots and polymer matrix.

Chapter 5 explores the Impact of ligand exchange on the nanocomposite film morphology of Lead Sulphide quantum dots and polymer matrix.
Chapter 6 presents the results of the impact of changing the volume fraction of both polymers and QDs on the dispersibility of the quantum dots into the polymer matrix.
Chapter 7 summarizes all of the key results of this QDs/polymer nanocomposite structural study and provides suggestions for future research.
Finally, the references to all published works utilized in creating this thesis are listed at the end of the study.

1.3. Objectives of the project

This project will study the processing routes and nanoscale morphology of lead Sulphide quantum dots (PbS QDs) incorporated into a polymer matrix (PS, PMMA and F8BT), aiming to develop or discover processing routes that could optimise the performance of optoelectronic devices via controlling the morphology of these nanocomposite films.

To achieve the primary goal of the project, the following processing aspects need to be explored and understood:

- Discover the effect of the Polymer molecular weight (M_w) on depletion forces and the final morphology of the nanocomposite films.
- The effect of ligands on the stability of the colloidal QDs incorporated into the polymer matrix.
- Controlling and determining the effect of QDs volume fraction on the morphology of the nanocomposite films.
- Characterizing the process routes of the films and their final film morphology.

Finally, it is worth noting that this project is focused on studying the structural issue for the simple case of polymers: PbS QDs and does not include the singlet fission materials, which I leave for future work. I keep it simpler to achieve a mechanistic understanding to underpin subsequent work on complex systems.

Chapter 2 Literature Review

2.1. Colloidal quantum dots

Nanocrystals made of semiconductor materials with 1-10 nm diameters are named Quantum Dots (QDs). The most numerous elements used to make the QDs in the literature are from the II, VI, and IV groups in the periodic table, such as (CdS, PbSe, PbS, and ZnO) and, less commonly, from the V and III groups, such as (InSb, InAs, and GaAs) [32]. Colloidal QDs provide a remarkable and direct visual illustration of quantum mechanics. The sizes and atomic structures of quantum dot nanocrystals can be visualised using electron microscopy. When illuminated using UV (ultraviolet) light, solutions of the nanocrystals glow in distinct and vibrant colours. Figure 2.1 shows the direct connection between the colours, ranging from blue to red, with the increase in size of the nanoparticles. In summary, the electrical and photophysics properties of the QDs (due to the quantum confinement size effect) can be tuned by controlling the physical dimensions (shape, size), unlike bulk semiconductors.

The QDs form a set of nanoparticles with a wide range of applications, including fluorescent biological labels, solar cells, and composites, and show the remarkable diversity and evolution of nanotechnology over the past few decades [33-35].

Fundamentally, colloidal QD are composites that consist of QDs and an organic ligand shell. The organic shell provides stability in solvents[36, 37], prevents the QDs from merging [36, 38], passivates undercoordinated atoms in QDs that would lead to exciton traps[39, 40], works as a soft matter in the gathering of artificial solids[41-43] and enable the process of the QDs modification [44, 45]. Besides the contribution of the ligands to the properties of the QDs, they are vital in their synthesis.

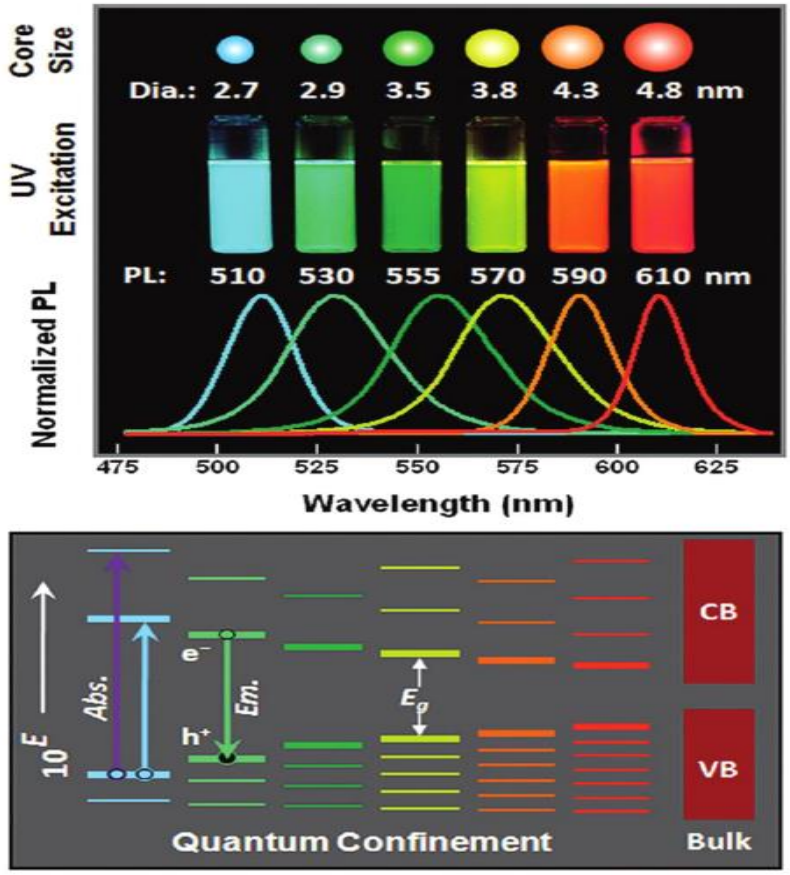

Figure 2.1/ illustration of the change colour and the energy levels of CdSe/ZnS with changes in QDs size, as an example of QD behaviour [32].

Nanotechnology has evolved from a concept in the 1960s into a multidisciplinary applied science and technology subject. In particular, public agencies, including universities, the military, and private companies, have rolled out numerous research programs focusing on nanotechnology in the past three decades. Researchers indicate that nanotechnology is an exciting field that allows creativity in developing new materials with meticulously designed Nano-sized architectures. Reed et al. were the first to mention 'Quantum Dots' in the literature. Their paper describes the epitaxial growth of multilayer islands of AlxGa1−xAs and GaAs with x−y dimensions of ~255 nm as being a ‘system of spatially quantised’ within which carriers have “zero degrees of freedom” [46].

Brus and Steigerwald applied this zero-dimensional (0D) materials concept to 'colloidal Quantum Dots' using wet chemical synthesis instead of growing them epitaxially by the Stranski-Krastanov process. The terms “colloidal semiconductor nanocrystal” and “colloidal quantum dot” are used interchangeably throughout the literature [47].

Developing colloidal quantum dots, which have various properties, is one of the milestones achieved through researchers' creativity in nanotechnology-oriented research. Because of the tremendous effort and resources focused on nanotechnology, researchers consistently identify new techniques for modifying nanoparticles, including colloidal QDs. Thus, nanotechnology is continuously yielding new and innovative functions and features that can be used to enhance technology and, in turn, society.

2.1.1. Physical properties of the colloidal QDs

The physical properties of QDs can be illustrated using the analogy of an electron incarcerated in a potential energy well, which is one of the most rudimentary quantum mechanics problems. While the size of the box is reducing, the kinetic energy of the electron is increasing because of the uncertainty relation (change in x (Δx)*change in p (Δp); $\frac{h}{2}$), which is one of the overarching quantum mechanics principles. In this regard, when the box's length:

$$L = \Delta X \qquad 2.1$$

The momentum:

$$p = mv \qquad 2.2$$

Where m is the mass and v is the velocity, the electron's kinetic energy is a finite value greater than zero. Specifically, the minimum kinetic energy is given by:

$$E = \frac{h^2}{2meL^2} \qquad 2.3$$

Where h is the Plank's constant, and me is the mass of the electron. The minimum kinetic energy expression is a fundamental principle that explains the impact of size on the semiconductor quantum dots' colour.

The kinetic energy of electrons in a quantum box arises from their motion within the box. In the context of a particle in a box, the kinetic energy is a result of the quantization of energy levels due to the confinement of the particle. The kinetic energy is related to the size of the box and is a fundamental concept in quantum mechanics. The energy of the particle in the

box is partly potential energy, which is not yet "realized" as motion, and partly kinetic energy, which is the energy of its actual motion. The kinetic energy of the electron is actually the total energy of the electron when it is confined to move in one dimension within the box. The energy of a particle in a box is quantized, and the kinetic energy is a significant feature of the particle-in-a-box quantum states. This concept is relevant to quantum dots, as they also involve the confinement of particles, leading to quantized energy levels and a relationship between kinetic and potential energy.

Furthermore, as shown in Figure 2.2, the defining feature of semiconductors is that they have an energy gap, referred to as the band gap (E_g), between an empty continuum of states, known as the conduction band (CB), and the packed continuum of energy states, referred to as the valence band (VB) [48]. Because a nanocrystal is similar to a small semiconductor, the bandgap between the empty and the valence state enlarges as the size of the crystal gets smaller. In this regard, the kinetic energy expression of the free electron indicates a considerably small impact on the box at the nanometre scale [49]. Nevertheless, while in solid crystalline states, electrons behave as if they have an effective mass, which may be even ten times less than that of a free electron, the expression of the box analogy utilises the mass m of the free electron. Thus, the uncertainty equation must be adjusted for quantum dots by replacing the free electron mass m with an 'effective mass m*' of an electron in a crystalline state or an assembly in the nanoparticle.

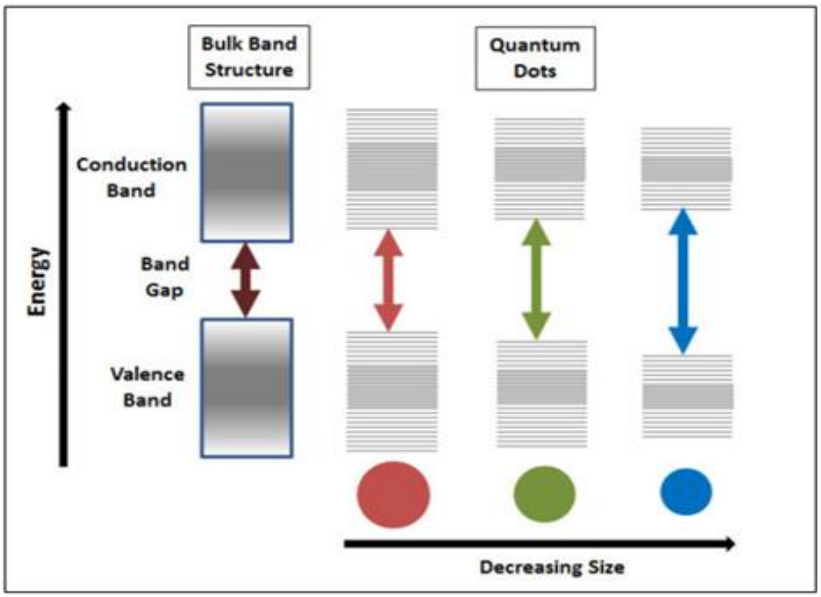

Figure 2.2/Effect of decreasing the box size on the energy gap of a semiconductor QD [48].

Moreover, when the QD get excited with energy higher than the band gap (E_g), the electrons will move to the conduction band, leaving holes in the semiconductor's valence band. The hole and electron pair are called an exciton, often called the Bohr radius $\alpha_\circ$, which is often used to describe the size of an exciton, which is a fundamental particle in the study of semiconductor materials. This different from the original Bohr radius, where it is a fundamental constant in quantum mechanics that represents the most probable distance between the nucleus and the electron in a hydrogen atom in its ground state.
The Bohr radius depends on the properties of the materials, and it is given by:

$$\alpha_\circ = \frac{h^2 \varepsilon}{e^2}\left(\frac{1}{m_e * } + \frac{1}{m_h * }\right) \qquad 2.4$$

Where ε is the bulk dielectric constant, e is the elementary charge, and m_e* and m_h* are the effective masses of the electrons and holes, respectively. The three-dimensional confinement size effect of holes and electrons arises when the size of the QDs decreases below the Bohr radius. This has pioneered the development of studies that relate bandgap energy to the size of semiconductor quantum dots. Below is presented a model with approximation to empirical measurements:

$$Eg\ (QD)\ = Eg\ (b) = \frac{h^2}{8R^2}\left(\frac{1}{m_e * } + \frac{1}{m_h * }\right) - \left(\frac{1.8e^2}{4\pi\varepsilon_\circ \varepsilon R}\right) \qquad 2.5$$

Where $E_{g,}$ QDs and $E_{g,}$ b are the bandgap energies of the quantum dot and bulk solid, respectively, R is the QDs radius.

As a result, The QDs present unique optical and electronic properties compared to bulk materials [50, 51].

2.1.2. Electronic properties of the colloidal QDs

The electronic properties of colloidal Quantum Dots (QDs) are determined by their size and chemical composition. For instance, as the size of a QD diminishes, the confinement experienced by the semiconductor's charge carriers increases, and the energy disparity between conduction bands and valence also referred to as the energy bandgap, increases. This affects the absorption and photoluminescence; the QDs can undergo radiative recombination, where an electron in the conduction band recombines with a hole in the valence band, resulting in photoluminescence (emission) with a wavelength longer than the absorbed light, and the emission wavelength can be tuned by controlling the QD size.

Moreover, the colloidal QDs exhibit a phenomenon known as multiple exciton generation (MEG). When a high-energy photon is absorbed, it can generate multiple electron-hole pairs (excitons) due to the strong Coulomb interaction within the confined volume (Figure 2.3). MEG allows for generating multiple charge carriers from a single adsorbed photon, offering potential advantages in photovoltaic applications, as it finds a solution for the energy loss that occurs from the excess energy of the photon [52-55].

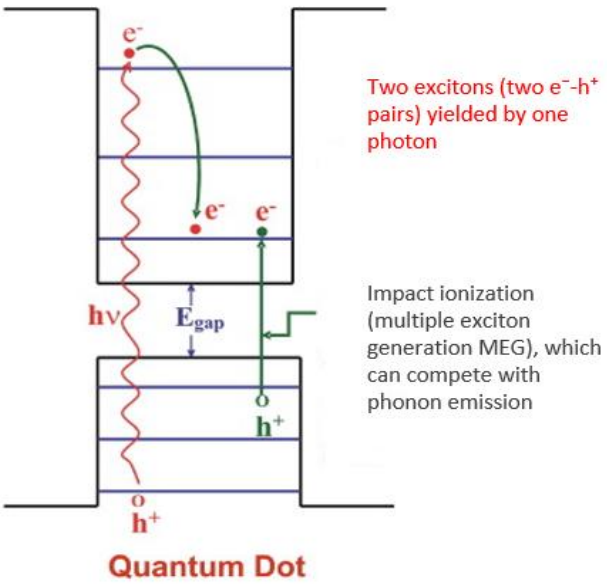

Figure 2.3/ Sketch illustrating the multiple exciton generation (MEG) processes in a QD.

2.1.3. Lead Sulphide quantum dots (PbS QDs)

During the last few decades, a concerted focus has been on nanocrystalline semiconductors that offer enhanced magnetic, electronic, optical, photochemical, and photophysical properties. These Nano QDs differ from the bulk samples of the same material compositions, and these effects are due to quantum size effects [56]. One of the most important materials is Lead sulphide (PbS); a unique semiconductor, Lead Sulphide (PbS), has been studied intensively in the last two decades or more. It is a unique material due to the large Bohr radius exciton that gives the electrons and holes strong quantum confinement; PbS belongs to the semiconductor group of IV-VI materials with a small bandgap (0.41 ev) at 300k and a large excitation Bohr radius (18 nm) compared to other semiconductors [57]. PbS quantum dots (QDs) are toxic to human cells, inducing changes in molecular markers for carcinogenesis and DNA damage[58]. The toxicity of PbS QDs can be attributed to various sources, such as the leakage of toxic metal ions, imbalance in the systemic manifestation of reactive oxygen species (ROS), and their high atomic number, which can lead to unwanted leakage of lead ions in biological environments[59]. The use of PbS-QDs due to its lower amount and higher efficiency shows promise for potential applications. However, the high toxicity of PbS QDs remains a concern, particularly in biomedical applications, and their potential impact should be carefully considered.

Several methods are used to produce PbS QDs, such as gas phase, solution phase, solid-state synthesis, glass host fabrication, and polymer films in solution. As in this work, we use PbS QDs made in solution following the Hines and Scholes (wet chemical synthesis method [60]), which will be detailed in Chapter 4. Colloidal QDs are synthesised with a residual coating of stabilising organic surfactant ligands. This ligand layer coats the outer surface of the QDs core, providing dielectric contrast with the QDs core and acting to solubilise the QDs in a range of organic solvents, depending on the exact ligand chemistry. Controlling the initial particle growth and nucleation event using suitable ligands and solvents is crucial because they are essential in creating a monodisperse species and assisting in nanocrystal growth. In this regard, Oleic acid (OA) is reported to be the most appropriate ligand to stabilise PbS QDs, by controlling the size and shape of the particles in the organic solution and insulating them from surrounding QDs [61, 62].

Colloidal quantum dots have huge potential for various applications due to their stability and the ability to adjust their light absorption and emission via QD particle size. During their synthesis, they have a layer of organic surfactant ligands that stabilise them, affect their solubility and interaction with other QD, and subsequently incorporate them into a host polymer matrix. The solubility of the colloidal QD and their interactions are influenced by the chemistry of the ligands on their surface. Moreover, it is possible to change the surface chemistry of the QD by exchanging the ligand layer with different molecules of choice. For specific applications, it is helpful to add more complex ligands to the QD, such as in photocatalysis [63, 64], photon upconversion [65], singlet fission[66], other optical applications [67], and in electronic device fabrication [68].

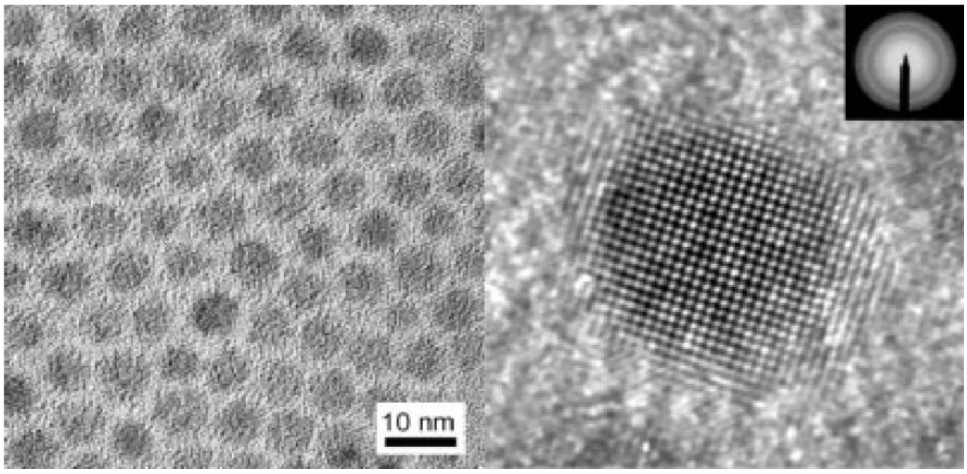

Figure 2.4/ High-Resolution Transmission Electron Microscopy (HRTEM) images of colloidal PbS QDs with exciton absorption at 1440nm[62].

2.2. Polymer

2.2.1. Structural and polydispersity of the polymers

Polymers are large molecules formed from a chain of small building block repeat units connected by covalent bonds, and these molecules are known as monomers [69]. The polymerisation degree, n, is the number of monomer links in the chain, and the polymer distinguishing feature is that it is long. DNA molecules, with an n of around 100 million, are some of the longest-known polymers. A polymer molecule size is defined via the molar mass M (g mol^{-1}), which, for commercially available polymers, perhaps passes several hundred thousand and is limited via polymer synthesis constraints [70]. In Figure 2.5, the structure of the polymer poly (ethylene), $(C_2H_4)_n$ is shown as an example of a typical polymer structure.

Polydispersity measures the size heterogeneity of molecules or particles in a mixture. Moreover, polydispersity is typical in any batch of synthetic polymers, meaning it has a distribution in the length of molecule synthesis by polymerisation. The molar mass average number M_N calculates the molar mass average of the distribution, this is weighted according to the chain number n_N with a given polymerisation degree,

$$MN = \sum_{N} nN\ MN \qquad 2.6$$

While the molar mass average weight (molecular mass) M_w calculates the molar mass average of the weighted distribution, according to the weight of the chains w_N with a given polymerisation degree,

$$Mw = \sum_{N} wN\ Mn \qquad 2.7$$

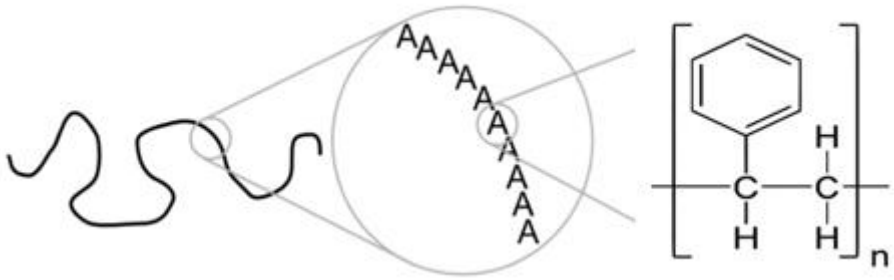

Figure 2.5/ The chemical structure of poly (styrene), $(C_8H_8)_n$, an example of a simple polymer structure.

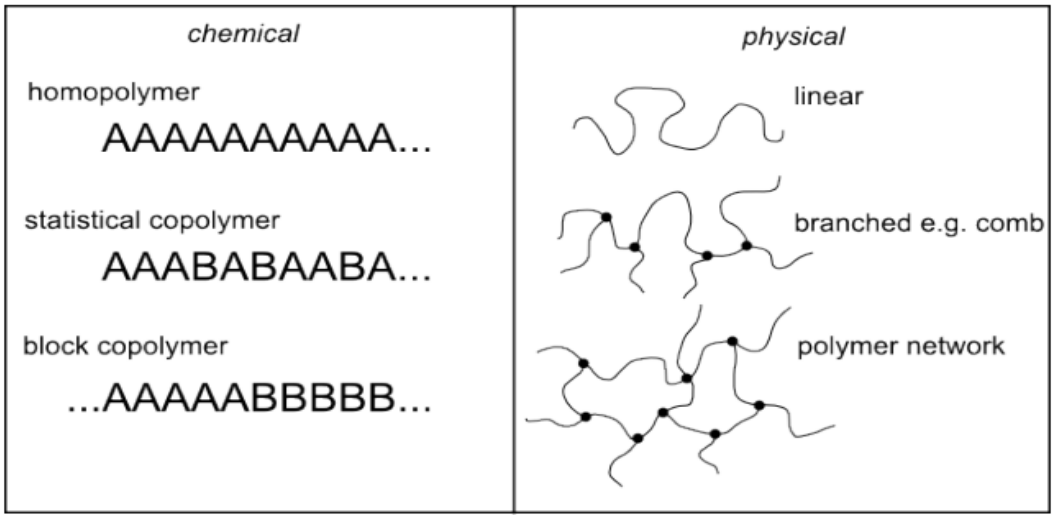

Figure 2.6/ Basic polymer structure illustration on the lift, homopolymers, statistical copolymers, and block copolymers. On the right, linear, branched and network polymers.

The polydispersity index (PI) M_W/M_N is a broadness measure of the molar mass distribution and is equal to 1 for the samples that a completely monodisperse, i.e., where the length of all the chains is precisely the same.

The simplest polymers are polymers with identical repeat units, using different combinations of monomers is possible, put together in any chemically possible configuration. As a result, there are many types of polymer families with other chemical and physical structures, the most basic of which are summarised in Figure 2.6. Homopolymers have an identical monomer sequence, while polymers with two or more distinct monomer types are called heteropolymers. A block copolymer is a heteropolymer with two different chains of homopolymer connected via a covalent bond.

Flexibility is a key feature of polymer molecules. For many synthetic polymers such as poly (ethylene), the flexibility is due to bond angle flexibility between contiguous monomers along the backbone. As an example of a biopolymer, the DNA is stiffer than most synthetic polymers and can form randomly coiled conformations despite its large size and intrinsic stiffness [71].

Because polymers are not always miscible, phase separation often occurs with nanoparticles, resulting in the development of a nanostructured object with a particular structure, meaning that each defined polymeric phase has a defined arrangement. Despite this understanding, deciphering the structure of polymer phases is considerably difficult [51]. Nevertheless, it can be achieved through several approaches, which implement Transmission Electron Microscopy (TEM) and Atomic Force Microscopy (AFM) combined with selective phase staining or through Differential Scanning Calorimetry (DSC) or Nuclear Magnetic Resonance (NMR) or via small angle X-ray scattering (SAXS) and small angle neutron scattering (SANS)[72].

2.2.2. Miscibility of the polymers

2.2.2.1. Miscibility of two polymers

For a blend of two non-compatible polymers, it is clear that it can achieve varying structures, including hemispherical particles such as half-moons, core-shell particles, and particles with several inclusions [73]. The properties of two blends of polymers usually depend on the degree of miscibility between components, solvent, composition and the morphology of the blends. Generally, polymer blends show immiscibility or partial miscibility due to the large size of the polymer chains, the interfacial tension between the segregated phases, or the lack of adhesion between the two polymers [74]. After blending, it is possible to check the

miscibility of two polymers by examining the glass transition temperature (T_g). If there is a single T_g, the blend is miscible, and when the blends exhibit more than one T_g, this means they are immiscible or partially miscible [75].

2.2.2.2. Miscibility of particles mixed with one polymer

The miscibility of one polymer mixed with nanoparticles often exists in three scenarios; first, a miscible blend; happens when a polymer and nanoparticles can be uniformly dispersed and mixed at the molecular level; this occurs when there is a strong interaction between the polymer and the nanoparticles. The second is an immiscible blend; in many cases, polymer and nanoparticles do not mix well at the molecular level due to physical forces, primarily the depletion force (The depletion force is an effective attractive force that occurs between large colloidal particles suspended in a solution of non-adsorbing, smaller species, such as polymers or fine colloidal particles. It arises due to the exclusion of these smaller particles from the vicinity of the larger particles, leading to an entropic attraction), different polarity and chemical structures between the components. When an immiscible blend forms, phase separation occurs, forming distinct phases of polymer-rich and nanoparticle-rich regions. Thirdly, partial miscibility occurs when favourable interactions are not strong enough to achieve complete miscibility between the polymer and nanoparticle.

Kinetically trapped structures should be separated from thermodynamic structures among these morphologies. In particular, because the chains' mobility is sufficiently high to achieve the lowest energy conformation, thermodynamic structures are achieved, especially when particles are subjected to temperatures in excess of the glass transition temperature.

2.2.3. Polymer-colloid interactions

2.2.3.1. Colloid-limit

To characterise interactions between bare colloidal particles, the famous DLVO theory is must be used. This states that the only interactions between colloidal particles are van der Waals and electrostatic[76, 77]. Other forces will be at work when colloids are present with smaller particles or solutes. To account for this condition in the CL, Asakura and Oosawa proposed the Asakura-Oosawa (AO) model [78, 79].

Colloidal particles are classified as hard spheres (HS) with diameter s, whereas polymers are identified as smaller spheres (referred to as 'penetrable' or 'phantom' hard spheres (PHS) with diameter 2d. These PHS have an HS contact with the colloidal particles, but they do not interact with one another and can pass through other PHS. The depletion layer surrounds each colloidal particle with zero polymer segment concentration, while the bulk concentration outside the layer remains constant. This produces an isotropic osmotic pressure gradient in a single sphere. In the case of two spheres separated by a distance of 2d, the depletion layers overlap and the possibility of chains entering the space between the particles is zero, implying that the dispersion medium between the particles is pure solvent. The osmotic pressure gradient is now anisotropic due to the absence of polymer chains in the overlap zone, resulting in a net osmotic force pushing particles together[80]. The size of the depletion interaction is proportional to the solution osmotic pressure, with a range of the order of the macromolecular diameter, implying that the depletion layer thickness is about R_g. The polymer molecule size thus determines the sets of attraction; the strength can be adjusted using the polymer concentration[81].

2.2.3.2. Protein-limit

Significant advancements in this research have enabled the quantification of depletion interactions in the protein limit. Joanny and colleagues proposed mean-field treatment for the semi-dilute regime[82]. De Gennes expanded this mean-field argument to the situation of $\sigma << \zeta$, demonstrating that scaling principles imply a weak attractive potential between colloidal particles. This means that it is significantly more difficult to initiate phase separation in the PL[83]. The CL layer thickness is of the same order as the polymer R_g. When the size ratio of the CP mixture approaches or exceeds unity, the depletion layer thickness deviates significantly from R_g.

Odijk presented a study on the interaction of proteins, which are termed hard spheres, with macromolecules whose characteristic length scale (R_g for low concentration or ζ for high concentration) is substantially bigger than s, the diameter of the protein sphere. The profile of polymer segment concentration in a semi-dilute polymer solution was shaped around a very small sphere, as was the second virial coefficient between the colloid and polymer for $R_g >> \sigma$. According to this concept, mixing very small spheres with very massive chains should result in no phase separation[84].

2.2.4. Coils, globules, and the radius of gyration

A flexible polymer chain explores space in the conformation of a random walk known as a coil when placed in a solvent to magnify its configurational entropy (Figure 2.7). For example, stretched states, where the chain is laid out end-to-end, are highly unfavourable entropically, since they require long-range chain ordering. This gives rise to the entropic elasticity effect; this effect happens when a force restores the coil configuration to a disordered one when a stretching force is applied [69].

A polymer chain of N monomers with characteristic size a vectors series a_i and assuming that the neighbouring links orientations are uncorrelated (*the freely jointed chain model[71, 85]*) gives a mean-squared end-to-end distance for the polymer chain of

$$r^2 = Na^2 \qquad 2.8$$

Which is the characteristic of random walk displacement. The bonds between monomers in a polymer chain are restricted to certain bond angles[86]. To account for correlations, we can use an *equivalent freely jointed chain*; the chain is split into subunit lengths b that are selected to be greater than the correlations range, where b is the *statistical length of the segment* or *Kuhn length*. The Flory ratio of characteristic C_∞ (in the extended chain limit) relates the sizes of a and b

$$C\infty = \frac{b^2}{a^2} \qquad 2.9$$

And the relation

$$r^2 = N_b\, b^2 \qquad 2.10$$

Describes the end-to-end mean-squared distance of rescaled polymer chain with N_b Kuhn monomers of size b. A real polymer chain with correlations between the vectors a_i of monomer still acts as a random walk but with an increase in the size of step b. The chain can be considered stiff on the length scales of the Kuhn length or less.

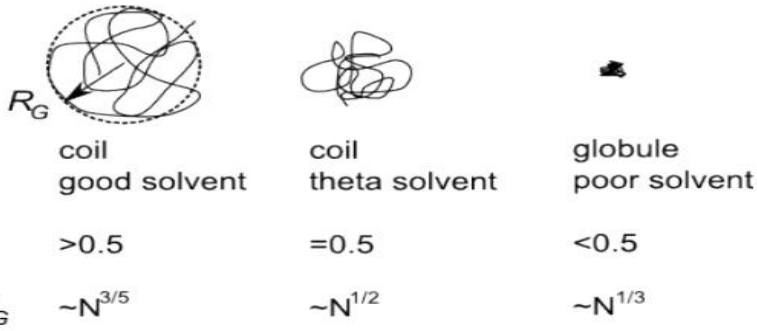

Figure 2.7/ Illustration of a polymer coil in solution, and the coil-globule transition from good solvent, theta solvent to poor solvent.

Moreover, an ideal polymer chain cannot form an ideal random walk because two monomers cannot be in the same position in space. This causes the volume v surrounding a given monomer to be excluded, into which another monomer may not penetrate. For simplicity, assuming b = a, the excluded volume parameter v is known as

$$v = a^3(1 - 2\chi) \qquad 2.11$$

Where χ is the Flory interaction parameter [70], which takes into account interactions of the polymer-solvent, polymer-polymer and solvent-solvent, as shown in the equation below

$$\chi = \frac{1}{2kBT} z\,(2\epsilon_{ps} - \epsilon_{pp} - \epsilon_{ss}) \qquad 2.12$$

Where ϵ_{ps}, ϵ_{pp} and ϵ_{ss} are the interaction energies of the polymer-solvent, polymer-polymer and solvent-solvent, respectively, while z is the neighbour number for each segment chain or solvent molecule. Good solvent conditions are represented when $\chi < \frac{1}{2}$ where the coil of the polymer is expanded and the size of the coil scales as $R_g \sim N^{3/5}$. The state of theta $\chi = \frac{1}{2}$ means that polymer repulsive / interactions of solvent cancel the effect of excluded volume, and thus the chain acts as an ideal random walk with $R_g \sim N^{1/2}$. In the case of $\chi > \frac{1}{2}$ the coil collapses into a compact globule, changing the excluded volume parameter sign signifying the monomer-monomer attractive interaction (the effective monomer volume is given by |v| where v < 0 [71]), Figure 2.7.

In polymer solutions, the three main regimes are dilute, semi-dilute, and concentrated. The crossover between these regimes leads to changes in the internal structures of the polymer solution. The semi-dilute regime can be further divided into entangled and non-entangled subregimes. The entangled semi dilute regime of neutral polymer chains exists above the chain's overlap concentration, denoted as c*. This is the concentration at which the polymer chains begin to overlap. The entanglement concentration, c**, is the concentration at which the polymer chains become significantly entangled.

The dynamic behaviour of semi-dilute polymer solutions is governed by an interplay between solvent quality, concentration, and molecular weight. In the dilute regime, the individual polymer coils are far apart and do not interact, while in the semi-dilute entangled regime, the behaviour is more complex due to the presence of entanglements.

The parameter c* represents the transition from the dilute to the semi-dilute regime, where polymer chains begin to interact, while c** signifies the onset of significant entanglement within the semi-dilute regime.

The crossover concentrations c* and c** are important in understanding the behaviour of polymer solutions and are used to define the boundaries between different concentration regimes, each with its own distinct structural and rheological properties[87, 88].

2.2.5. M_w-viscosity relation

The relationship between the molecular weight (M_w) and viscosity of polymer solutions is complex and varies depending on the concentration and the internal structure of the solution. In general, the viscosity of polymer solutions is influenced by the size of the polymer chains, which is related to the M_w. The Mark-Houwink equation, given by

$$[\eta] = KM^{\alpha} \qquad 2.13$$

, describes the dependence of intrinsic viscosity on the M_w of the polymer, where $[\eta]$ is the intrinsic viscosity, M is the molecular weight, and K and α are constants for a particular polymer.

In concentrated polymer solutions, the viscosity is shown to be a power law function of the radius, and it decreases with decreasing radius under conditions where the chains are entangled. The effective viscosity in polymer solutions also depends on their size, and it is a well-defined function of the concentration. The crossover between the dilute, semi-dilute, and

concentrated regimes leads to changes in the internal structures of the polymer solution, impacting the Mw-viscosity relationship. The concentration of the solution is a crucial factor in assessing viscosity, as a higher concentration leads to a higher viscosity measurement [89, 90].

2.2.6. M_w- Tg relation

The relationship between the glass transition temperature (T_g) and the molecular weight (M_w) of polymers is often described by the Fox equation, which states that Tg is inversely proportional to M_w. For linear polymers, the dependence of T_g on molar mass can be expressed by the equation

$$Tg = [\frac{1}{Tg} + \frac{K}{Mw}]^{-1} 2.14$$

Where K is a polymer-dependent constant and M_w is the weight average molecular weight. This equation suggests that as M_w increases, T_g decreases. However, it's important to note that this relationship is more applicable to low Mw polymers and may not hold at high M_w.
The effect of M_w on T_g is influenced by various factors such as the molecular structure, the presence of bulky side groups, and polymer architecture. In some cases, the presence of bulky, inflexible side groups can increase the T_g of the material due to decreased mobility, counteracting the expected decrease in T_g with increasing M_w.

While the Fox equation provides a general understanding of the Mw-Tg relationship, it may not accurately predict the behaviour of high M_w polymers. The relationship between T_g and Mw is complex and can be influenced by multiple factors including polymer structure, chain flexibility, and intermolecular interactions. Therefore, it should not be expected that T_g will always decrease at high M_w, and the specific impact of Mw on T_g should be evaluated in the context of the polymer's unique characteristics

2.3. Colloid crystallisation (aggregation)

Colloidal crystallisation is the process by which small particles suspended in a liquid come together to form larger particles that eventually settle into a regular crystalline structure. This process is driven by the attractive forces between the particles, typically due to van der Waals forces or electrostatic interactions, and also can happen solely due to entropy.

Colloidal aggregation can occur through mechanisms such as Brownian motion, depletion, or electrostatics. In the Brownian motion mechanism, particles undergo random thermal movements, and when two particles come close enough, they can stick together due to attractive forces. In the depletion mechanism, large particles (such as polymers) are added to the system, creating a depletion region around them, where smaller particles can aggregate. In the electrostatic mechanism, charged particles can attract each other due to opposite charges.

Once aggregation begins, the resulting clusters can continue to grow by incorporating more particles. As the clusters grow larger, they become more stable due to the reduction in surface area per particle, which lowers the overall energy of the system. Eventually, the clusters can become large enough to settle out of the solution and form a crystalline aggregate. The close-packed lattices are the preferred packing symmetry for spherical particles (hard-sphere) and are widely reported in the literature[70, 91].

The close-packed structure is often divided into two crystal structures in the literature: hexagonal close-packed (HCP) and face-centred cubic (FCC), and both have the maximum packing fraction (0.74) when packed [92-94]. The literature states that the HCP structure is more stable than the FCC structure for spherical particles like QDs[95, 96]. Figure 2.8. Illustrates the difference between the packing types; once a close-packed layer is placed, two methods exist for identifying subsequent layers. In the FCC structure, the sequence of the layers alternates as ABCABC…. While it is ABABA in the HCP structure with stacking along the sequence (111) and (001), respectively [70, 97].

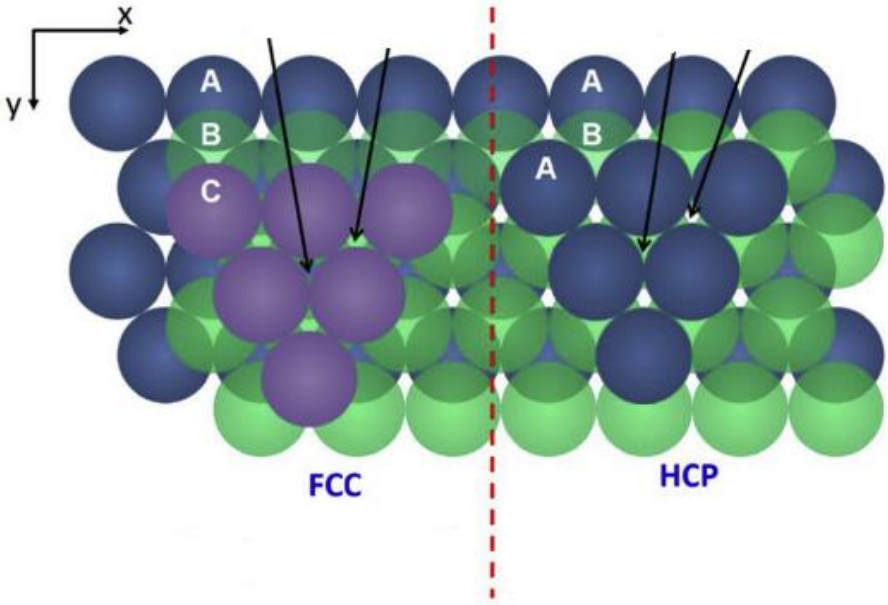

Figure 2.8/ Sketch illustrating the differences between (HCP) and (FCC) close-packed structures. The arrows refer to the difference in the arrangement of the layers.

2.3.1. Depletion interaction

In the past decade, there has been renewed interest in the depletion effect due to its significant role in various industrial and biological projects. This phenomenon causes colloidal dispersions to undergo phase separation, leads to the clustering of red blood cells, facilitates protein crystallisation, and contributes to the helical structure of long molecular chains[98, 99].

The depletion interaction is the most important interaction affecting colloidal aggregation in a colloidal system containing, for example, inorganic particles embedded in a polymer matrix; therefore, it must be understood. The interactions between the PbS QDs and the polymer solution will be considered in my work. In this context, the depletion interaction is vitally important.

The depletion interaction is an attractive interaction that arises whenever the solution contains something else besides the suspended particles, intermediate-size particles between the solution size and the suspended particles. The most common example is when a suspension includes a polymer dissolved in a solution that does not adsorb to the surface of particles[70].

Figure 2.9. Illustrates this situation; the polymer molecules are excluded from the region between the surfaces of the particles (depletion zone). The depletion regions overlap when they come close together; this results in a volume of solution between the particles in which the polymer molecule concentration is less than in the bulk solution. As a result, a difference in osmotic pressure arises outside and inside the depletion zones, inducing a depletion force or effect that works to push the particles together[70, 100]. The depletion effect embodies the alteration of both translational and conformational entropy in polymers and the solvent. Also, it is a crucial factor in controlling the stability of colloidal dispersions. It is possible for phase separation to occur, which is affected by various factors, such as the concentration and molecular weight (M_w) of the polymer, the length of the chain, the quality of the solvent, and the size of the particles. To fully comprehend the phase behaviour of colloid dispersions, it is crucial to have accurate knowledge of the depletion potential[100].

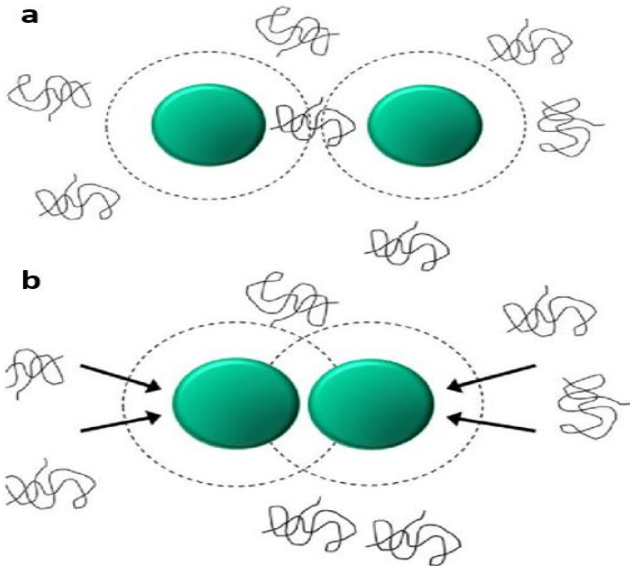

Figure 2.9/ Sketch illustrating the effect of depletion interaction, a) well-dispersed QDs; b) polymer coils (black squiggly lines) are excluded from the depletion zones near the QDs surface due to an imbalance in the osmotic pressures, resulting in an attractive force between the QDs.

2.4. Nanocomposites

Nanocomposite materials include multiphase solid compounds with two or more phase materials with a length scale on the order of >100 nm. The nano-scale structures within composite materials have defined distances between the alternating phases that constitute the

material [31]. Recently, a focus has been on improving nanocomposite properties by doping photo-selective materials to enhance solar energy conversion efficiency. QDs such as InNP, CdSSe, CdZnS, and CdTe have been reported to enhance the properties of nanocomposite materials considering their low bandgap energy. A new class of nanocomposites based on graphene (GQDs) or carbon (CQDs) has emerged with superior solubility, facile passivation, biocompatibility, and chemical inertness. Lower band gap QDs such as PbS, CdS and CdSe have high conduction bands that can be enhanced to achieve higher efficiency in electronic conversion [101, 102].

Thus, solar cells that include organic polymers and semiconductor QDs can provide a flexible, cost-effective, lightweight, and efficient alternative to bulk conventional solar cells with less than 20% power conversion efficiency if the structural issues are resolved, as we will see in the following sections.

2.4.1. Polymer-QDs nanocomposite

Quantum Dots (QDs) are synthetic semiconductor particles measuring a few nanometres in size, with unique optical and electronic properties from those of larger particles. Thus, they are also called semiconductor nanocrystals or colloidal nanoparticles [23, 24, 103]. QDs typically measure 2–10 nm in diameter and are considered nanoscale semiconductor crystals because their nanosize-dependent properties are due to the confinement of electrons and electron holes (h^+, the conceptual opposite of an electron)[24]. The ability to adjust the optoelectronic features of QDs by selecting their size, shape, and ligands is a significant breakthrough afforded by the nanoscale nature of QDs [104].

Due to their unique quantum mechanics (quantum confinement effects), QDs exhibit a narrow emission spectrum, high fluorescence emission, photostability, broad excitation wavelength and biocompatibility [23, 24, 105]. They can transmit electrons in size-tuneable emission spectra ranging from visible to near-infrared (NIR) spectral regions; hence they can emit different coloured light when exposed to ultraviolet (UV) light [25]. Due to these unique optoelectronic properties, QDs attract a wide range of applications, including nanocomposite

materials, solar cells, lighting, fluorescent biomolecular tagging or labelling in biological systems, fluorometric sensors, displays, and radiological medical imaging [24, 103, 106].

QDs-based nanocomposite materials produced by incorporating QDs into a polymer matrix have promising potential for applications in photonic devices, including laser and light-emitting diodes, solar and photovoltaic cells, displays and optical amplifiers [105]. Polymer-QDs nanocomposite combines the unique optoelectronic properties of QDs with the technological amenability of polymers [24, 105]. From the polymer literature, the first paper that mentioned the word "nanocomposite" appeared in 1990. This paper describes cars equipped with clay-polymer hybrid parts driven through fields and towns. Commercially, the nylon-clay six nanocomposites were used to make the covers of timing belts for Toyota cars. This was the first example of a commercial polymer nanocomposite [26].

Polymers are amenable to incorporating semiconductor nanocrystals because they are relatively inexpensive, flexible, easily synthesised into films by simple spin-coating technique and readily patternable by UV photolithography or electron-beam (e-beam). Notably, the highly transparent characteristics of most polymers at wavelengths > 400 nm makes them suitable optical material for waveguiding in integrated optical devices Polymer-QDs based nanocomposites, especially polymethyl methacrylate (PMMA) and polystyrene (PS)-QDs, and have already been fabricated into a microcavity laser and double-colour waveguiding in integrated optical devices [105].

Metal chalcogenides (MC), including metal sulphide, selenide and telluride, are widely studied QDs. MCs have attracted immense interest for use in MCQDs due to their unique and excellent quantum confinement that produces MCQDs with size-dependent photoemission characteristics [25, 27]. MCs are suitable for synthesising functional MCQDs materials for photo-electrocatalysis and photovoltaic cell application, and they are also amenable to biomolecular modifications [28]. Examples include cadmium chalcogenides (cadmium sulphide-CdS, cadmium selenide-CdSe and cadmium telluride CdTe), lead chalcogenides (lead sulphide-PbS and lead selenide PbSe) and antimony chalcogenides (antimony sulphide-

Sb2S3 and antimony selenide Sb2Se3). These MCs produce QDs with varying degrees of desirable characteristics and, therefore, require careful selection depending on the intended material application [107]. For example, lead chalcogenides QDs are suitable for strongly quantum-confined systems such as size-tunable electron transitions at NIR spectral regions. This property makes lead chalcogenides QDs ideal for device applications in telecommunications, biomedical electronics, and optoelectronics [108].

The present study aims to develop well-dispersed QDs in a polymer matrix to form nanocomposite films suitable for use in various applications, including optimising the performance of optoelectronic devices via controlling the morphology of these nanocomposite films. This project focuses on dispersibility issues that occur with incorporating the QD into polymer matrices. In particular, the synthesis of Lead sulphide quantum dots (PbS QDs) nanocomposite films by embedding PbS QDs into PMMA, polystyrene (PS) or poly(9,9-dioctylfluorene-alt-benzothiadiazole) (F8BT) polymer matrix. I first review the history, application, significance, and structural limitations of PbS QDs nanocomposite films and possible solutions.

2.4.2. Polymer-PbS QDs nanocomposite films

Organic-inorganic nanocomposites consisting of PbS QDs implanted into polymer matrix have attracted immense attention due to the quantum-size effect that PbS QDs exhibit. This was discovered before 1987 [109]. Organic colloidal semiconductor PbS QDs consists of core nanocrystals composed of 100-1000 PbS atoms (group IV semiconductors) and surface organic ligands. The crystallites' diameter is in the nanometer range, with their surface covered with organic molecules and metal complexes. For example, as shown in Figure 2.10, an octahedral PbS quantum dot has central metal ions (Pb cations) covered with chalcogenide anions (sulphides) and organic ligands (oleate or oleic acid)[110, 111]

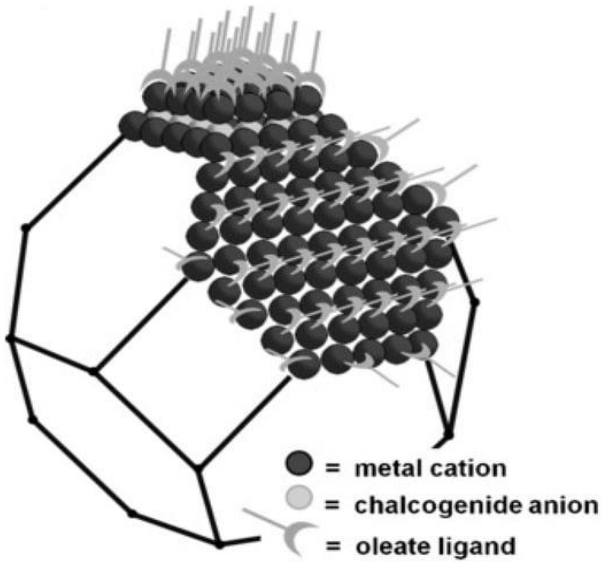

Figure 2.10/ Pb-terminated octahedral truncated PbS quantum dot with Pb cations, S anions, and organic ligands. [110].

The chemical preparation of colloidal semiconductor particles has a long history, dating back at least 114 years ago when it was discovered that the colour of the colloids changed with the growth of colloidal particles[112]. The first three-dimensional quantum size effect of small PbS in PbS QDs was observed and correctly explained by Wang, Suna, Mahler and Kasowski[109]. They observed that PbS QDs exhibited well-defined clusters in zeolites, with a possibility of forming unique three-dimensional highly stable superlattice structures. Polymer-PbS QDs nanocomposite films were first synthesised by Wang, Suna, Mahler and Kasowski using ethylene-15% methacrylic acid copolymer (E- MAA)[109]. PbS QDs photovoltaic devices have undergone significant research since they were first introduced in 2008, resulting in a massively improved power conversion efficiency of about 12%[104].

Later, more suitable polymer hosts for PbS QDs nanocomposite films were discovered in several studies. Patel et al. summarise that semiconducting conjugated or insulating polymers are the most suitable hosts for nanocomposites consisting of PbS QDs. Many of these semiconducting polymers were discovered or described between 1994 and 2016[113]. More insulating polymer hosts than conjugated polymer hosts have been found, as listed in Table 2.1. However, each polymer has unique structural limitations. For example, PbS/polyvinylpyrrolidone (PVP) nanocomposite films exhibited strong interaction between PbS and PVP, which limits nanoparticle aggregation [113].

Semiconducting conjugated polymer hosts	Semiconducting, insulating polymer hosts
Poly[2-methoxy-5-(2′-ethylhexyloxy-p-Phenylenevinylene)] (MEH-PPV)	Polyacryl amide (PAM),
Poly(2-(6-cyano-6′-methyl heptyloxy)-1,4-Phenylene) (CN-PPP),	Poly-p-xylylene (PPX)
Poly(3-hexylthiophene-2,5-diyl) (P3HT)	Polyacrylonitrile (PAN),
Polypyrrole (PPy),	Poly(methyl methacrylate) (PMMA)
Poly[2-methoxy-5-(3′,7′-dimethyloctyloxy)-1,4-phenylenevinylene] (MDMO-PPV)	Polystyrene (PS)
	Poly thiourethane (PTU)
	Polyvinyl alcohol (PVA)
	Poly(vinyl acetate) (PVAc)
	Poly(vinyl pyrrolidone) (PVP)
	Polyvinylidene fluoride (PVDF)
	Poly(ethylene oxide) (PEO)

Table 2.1/ Semiconducting conjugated and insulating polymer hosts for PbS QDs /polymer nanocomposites.

2.4.2.1. Importance and applications

This section briefly summarises some applications of the PbS QDs-polymer nanocomposite films in optoelectronic applications and spectroscopic techniques, including multi-colour photoluminescence optical waveguiding photodiodes and solar cells.

2.4.2.1.1. ***Photoluminescent optical waveguiding***

A recent study synthesised light-emitting UV-curable active PbS QDs-polymer nanocomposite using a vacuum-assisted microfluidic technique[114]. The produced PbS QDs-polymer nanocomposite that exhibited size-tunable light emission at NIR wavelengths. Their brightness was about 30-fold that of PbS-Epoxy (SU-8) polymer composites suitable for optical waveguide applications. This supported the idea that polymers other than SU-8 are

also suitable for synthesising PbS QDs-polymer nanocomposite for optical waveguides applications [105, 114].

2.4.2.1.2. ***Infrared detection devices***

Infrared (IR) detection is critical for technologies, including night vision, thermal medical imaging diagnosis, and proximity detection [115]. Conventional IR detectors use vacuum-processed materials such as indium gallium arsenide (InGaAs) and Cadmium mercury telluride (CdHgTe), which are relatively expensive. Recent discoveries of solution-synthesised colloidal QDs as excellent IR light-detecting materials have made producing low-cost IR detection devices possible. PbS QDs have emerged as superior IR light harvesting materials for use in Polymer-PbS QDs nanocomposite films for photodiodes[111, 115].

2.4.2.1.3. ***Photovoltaic cell applications***

There is a growing demand for highly efficient photovoltaic (solar) devices for renewable solar energy harvesting. Hybrid nanocomposites (HCs) synthesised from combining conjugated polymers and colloidal semiconductor nanocrystals have emerged as promising materials for photovoltaic applications [111, 116]. In 2012, a patent was published, 'photovoltaic nanocomposite comprising solution-processed inorganic bulk nano-heterojunctions, solar cell and photodiode devices consisting of the nanocomposite' [117]. Since then, several studies have evaluated the photovoltaic application of various quantum dots optimising them by carefully selecting group IV semiconductors and appropriate surface ligands (anions and polymers). Unlike other types of solution-processed photovoltaic devices, especially organic or organic-inorganic perovskite, QD solar cells have greater efficiency performance.

For example, PbS QDs-polymer nanocomposites possess photovoltaic properties that make them potentially efficient for applications in solar cells. PbS QDs have gained remarkable research attention as potentially superior solution-based nanomaterials for third-generation photovoltaic (PV) devices. This strong interest is attributed to their size-tuneable band gap,

environmental stability (especially air exposure), and relatively low-cost solution synthesis and processing [118]. Indeed, PbS QD photovoltaic devices have received considerable focus in research since they were first introduced in 2008, resulting in remarkably improved power conversion efficiency of about 12% [104, 118].

PbS QDs-polymer nanocomposites possess optimised morphology if wide-bandgap polymers are used. It was recently demonstrated that the unique electro-optical properties of PbS-QDs and spectroscopic (wide-bandgap) properties of polymers resulted in photovoltaic cells with remarkably larger photocurrent densities. This was attributed to efficient charge/exciton processes afforded by the wide-bandgap polymer, which also hinders the population of mid-gap states on PbS QDs [116]. In general, surface molecules of PbS QDs-polymer HCs (sulphide anion and polymer ligand) prevent aggregation of PbS QDs, with the interface between QDs and surface ligands influencing the electronic structure, conferring a wide-bandgap for superior optoelectronic properties [111].

2.4.2.2. Structural shortcomings

Despite many studies that report the importance of QDs-polymer nanocomposite films in many applications, as mentioned above, the morphological issue of these materials continues to be of considerable importance [5, 19, 119]. For instance, in earlier studies by S. Coe-Sullivan et al. and B. Torriss et al. and F. Teng et al., the QDs aggregation was shown to occur during the spinning process. They observed that the QDs aggregation caused a photoluminescence (PL) concentration quench and subsequently, an energy transfer reduction in the nanocomposite films [5, 19, 20].

PbS QDs-polymer nanocomposites have several structural limitations that must be overcome to obtain their maximum optoelectronic properties for applications in IR detection, photodiodes, and photovoltaic devices. Although PbS QDs-polymer HCs have reduced the aggregation of the central QDs, this is only partial, and therefore, a definitive strategy is required to solve this problem. The aggregation of central PbS QDs occurs through cation-polymer bridges, limiting their optoelectronic properties in a concentration-dependent manner. For example, aggregation of QDs in PbS QDs-polymer HCs leads to a concentration

dependence of the photophysical properties of the complexes. Aggregation of QDs affects their mobility in liquid and solid states. Although QDs tend to aggregate into larger colloidal-size particles, nano-aggregates exhibit infinitely complex patterns, resulting in fractal structures that impact surface interaction processes [120]. The main problem with QD aggregation is that it affects the photophysics properties of the solid nanocomposites [120].

The tendency of the particles to aggregate, which results in diminished or distorted optical characteristics, is one of the main difficulties researchers studying PbS QDs must overcome. Due to factors like the size, surface chemistry, and passivation level of the nanocrystals, PbS QDs can merge. The level of aggregation has a considerable impact on both the optical properties and application possibilities of PbS QDs. Optimising these attributes requires understanding how the particles agglomerate (the colloidal crystallisation or aggregations and the most important forces that cause it have been explained previously in this literature.

2.4.2.3. Efforts to solve the structural issue

To solve QDs aggregation when QDs are incorporated into polymer matrices, we must consider all elements of the nanocomposite films, such as the properties of host polymers and QDs. Possible ways to achieve PbS QDs with improved photophysics properties include changing the molecular weight of the host polymer, ligand exchange and adjusting the PbS QDs volume fraction.

2.4.2.3.1. M_w of the host polymer

In host–guest systems of the synthesised nanocomposite, the molecular weight (M_w) of the host polymer determines the aggregation, stability, dispersibility, and mobility properties of the guest QDs [121, 122]. One of the benefits of a host polymer with relatively lower M_w is reducing the QDs aggregation is the efficient encapsulation of QDs. According to Jia, Listak, Witherspoon, Kalu, Yang and Bockstaller [121], the higher the M_w of the host polymer matrix, the faster the nanoparticle coarsening or aggregation rate due to the cluster polymer viscosity. This is explained by the network characteristics of high-M_w polymers that increase nano viscosity in the context of nanoparticle diffusion (mobility) within host polymers. This means that a high-polymer M_w is not an ideal host polymer host choice for producing

nanomaterials with excellent optoelectrical properties because these applications require well-dispersed QDs within the polymer matrices.

For instance, a previous study evaluated the influence of polyvinylpyrrolidone (PVP) molecular weight on the stability and spectral luminescence properties of PbS nanocrystals in composite sols. The stability of spectral properties of PbS sols increased with decreasing M_w of PVP. Thus, the formation of large particle aggregates in PbS composite sols was associated with unstable spectral properties, including a high level of light scattering. High molecular weight polymer was thus related to aggregates tendencies of nanocomposite [122]. A similar observation was noted where QD aggregation in luminescent solar concentrators (LSCs) resulted in light scattering, which was the major cause of low efficiencies of the solar collection capacity[123].

Ramkumar and Ju [124] visualised six polymer-QDs nanocomposites through the field emission scanning electron microscopy (FE-SEM) technique. The study generally noted that the polymer host forms a smooth and plain morphology due to its repeating units and high molecular weight. However, polymer M_w can be beneficial to a certain degree, above which it limits the dispersibility of QDs in the polymer.

So, the host polymer M_w in the nanocomposite system consisting of QDs incorporated into a polymer matrix is essential due to its effect on the morphological and optoelectrical properties. Ideally, as seen in the literature, the polymer host M_w should not be too high, where the high M_w results in an increase in the nanocomposite's phase segregation components. Also, Polymer hosts with the ideal M_w can enhance the dispersibility and mobility of PbS QDs and potentially increase the charge-carrier transport ability of polymer-PbS QDs nanocomposite films, hence their optoelectronic properties. Despite this, the effect of the host polymer M_w on the final morphology of the blend films has yet to be discussed deeply in the literature, particularly its impact on the depletion force that causes the QDs aggregation in QDs: polymer systems.

2.4.2.3.2. ***Ligands exchange***

The organic ligands shell structure is essential in the synthesis of QDs self-assemblies besides enabling QDs stability[38]; in this matter, the OA ligands mentioned to be the most proper in controlling the shape and size of the QDs and protecting the QDs from the aggregation in the organic solvents[61]. However, for some applications, when the QDs are incorporated into a polymer matrix, the OA is a steric hindrance for the interaction, leading to phase segregations of the components and hence, loss of the nanocomposite properties. So, using ligand-exchanged PbS QDs is essential for enhancing the structural and photophysical properties of PbS QDs in some media, such as polymers.

It was recently demonstrated that swapping OA ligands in Oleate-PbS QDs for inorganic-organic hybrid material, methylammonium lead triiodide (CH3NH3PbI3, MAPI) resulted in a core PbS with a shell of lead triiodide (PbI3-), which effectively hinders PbS QDs aggregation tendency as shown in Figure 2.11 [125]. The core-shell structure of PbS QDs was further enhanced by adding toluene, which resulted in PbS-CH3NH3PbI3. This nanomaterial exhibited enhanced light absorption and photoelectric properties[125]. The ligands shell structure affects the colloidal QDs properties; for instance, the photoluminescence can be influenced by order or disorder in the shell [126-128].

MAPI-PbS QDs exhibited characteristics of Schottky barrier solar cells, which had almost 5-fold higher photoconversion efficiency than Oleate-PbS QDs lacking a ligand exchange. The observed photoconversion gain was attributed to a larger barrier height of the core-shell structure of PbS-CH3NH3PbI3, which hinders their aggregation and MAPI shell, which conferred a trap state passivation on the PbS QDs surface. Improved fill factor and photocurrent were attributed to reduced aggregation, which improved PbS QDs mobility, shortened inter-QDs distance, and enhanced charge transport velocity [125, 129]. The steric bulkiness of the native ligands (aliphatic chains) can complicate the passivation of the QDs surface, leading to atoms being undercoordinated and potentially trapping[40, 130].

The benefit of the ligand exchange strategy was later tested by Fukuda, Takahashi, Takahira, Wang, Kubo and Segawa [131], where ligand-exchanged PbS QDs were synthesised by swapping oleate in Oleate-PbS QDs for 1,2-ethanedithiol (EDT). EDT-exchanged PbS layers improved photovoltaic performance, especially doubling the photoconversion efficiency

initially observed with Oleate-PbS QDs. PbS QDs with EDT ligands are widely used as a hole extraction layer in PbS quantum dot solar cells, especially in those with remarkable efficiency, where lead iodide (PbI2) ligands are utilised in the active layer of photovoltaic devices.

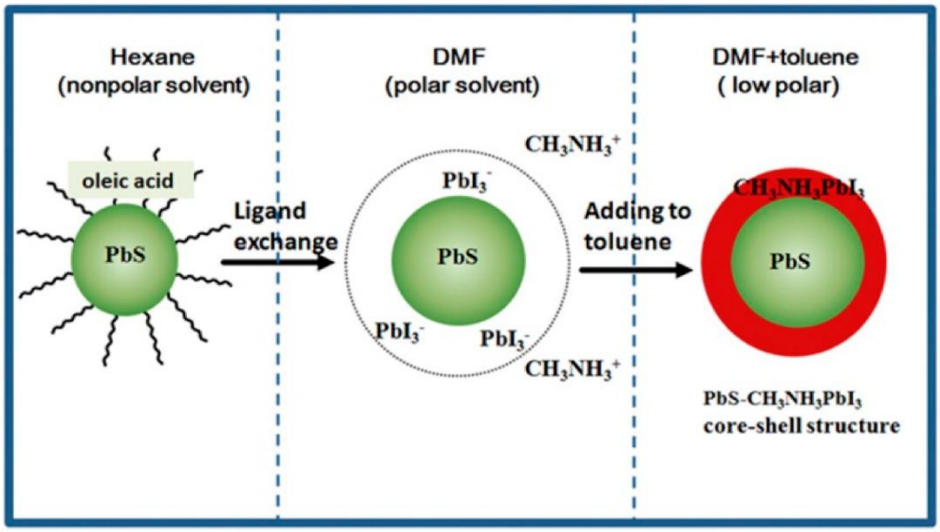

Figure 2.11/ Example of the ligand-exchanged PbS QDs[125].

Interestingly, ligand-exchanged PbS QDs from Oleate-PbS QDs (Oleic Acid - OA) to Hexanoate-PbS QDs (Hexanoic Acid - HA), and Decanoate-PbS QDs (Decanoic Acid -DA) have been proposed using other similar chalcogenide anions [29, 132]. Through thermogravimetric analysis, Park, Kim and Kim demonstrated that Hexanoate- and Decanoate- Indium Phosphide (InP) QDs had higher mass (87.3 and 84 wt %) than Oleate-PbS QDs (82.1 wt %). This means that HA and DA enhance the packing density of QDs and increase the miscibility, which helps reduce QDs aggregation and improve the mobility or dispersibility of QDs in polymer matrices. Therefore, this strategy is like to improve the photophysics properties of HA- and DA-PbS QDs making them even better for photovoltaic applications.

To summarise this section, the OA ligands are the most suitable for PbS QDs that stabilise and isolate them from aggregation in organic solvents. However, for specific applications, the OA ligands need to be replaced with layers with different molecules of choice by a process called exchange ligands; this is because the OA ligands work as a steric hindrance for the interaction in some media, such as polymers; which leads to phase segregations of the

components or QDs aggregation, hence lose structural and photophysical properties of the QDs.

2.4.2.4. Some other strategies to disperse the QDs into polymers host

2.4.2.4.1. ***Surface modification of the QDs***

In a landmark work, researchers modified particle surfaces with silane coupling agents to enh ance compatibility between the polymer and QDs surfaces to enhance the composite material properties[133, 134]. A nanoparticle was modified with a 3-methacryloxypropyl trimethoxysilane coupling agent. Unmodified nanoparticles have only -OH groups on their surface, but silane-modified nanoparticles have 3-methacryloxypropyl trimethoxysilane molecules.
Modified nanoparticles behave differently in organic solvents and polymer matrices than unm odified nanoparticles, with improved dispersion in both media[135].

Grafting synthetic polymers to the substrate surface improves chemical functionality and cha nges the surface topology of inorganic and organic materials. The polymer-grafted inorganic nanoparticles are classified as organic-inorganic nanocomposite particles. Monomers' low molecular weight allows them to penetrate nanoparticles and interact with act ivated areas on their surfaces.The interstitial volume inside nanoparticle aggregates is partiall y filled with grafted macromolecular chains, causing the aggregated nanoparticles to split furt her. Furthermore, the hydrophobic surface of the nanoparticles increases filler-matrix miscibility, which increases the dispersion behaviour of bare and polymer-grafted nanoparticles in a polymer matrix[136].

Other strategies for surface modification of inorganic nanoparticles include adsorption with polymeric dispersants and in situ surface modification. Adsorption of polymeric dispersants is a straightforward way for improving nanoparticle dispersion in aqueous systems. Hydrophilic nanoparticles can be dispersed in highly polar organic solvents with anionic or cationic polymer dispersants. These dispersants improve nanoparticle dispersibility by increasing surface charge and generating steric repulsive interactions between polymer chains.
Anionic surfactants, including polycarboxylic acids and salts, have been employed to disperse oxide nanoparticles like TiO_2, $Al2O_3$, and Fe_2O[137, 138]. In situ surface

modification approaches, conducted during nanoparticle production, have also been reported in the literature. Some of these approaches include the reverse micelle method, thermal decomposition of organometallic compounds, and polyol procedures.
To prevent nanoparticle aggregation, capping agents or surfactants (e.g.TOPO, oleic acid, and amines) are added to the synthesis solution. Surfactant-
capped nanoparticles synthesised during in situ surface modification can be modified for cert ain surface properties[139].

2.5. Summary

Despite substantial research on the structural issues that show with incorporating the QD into the polymer matrix, the QD aggregation, which is the main issue, still exists. This means there is a need for more understanding of the mechanism interaction of QDs and the polymer matrix, aiming to solve this issue and produce PbS QD: polymer nanocomposite films that can be used in various applications.

So, to have a comprehensive view of this issue, the thesis examines and understands the physical forces that cause the QD aggregation, such as depletion forces, and examines the chemistry between the QDs and polymer matrix. To do so, the effect of the host polymer M_w and the QDs volume fraction on the morphology of the QD: Polymer nanocomposite will be examined; this is expected to determine the interparticle interaction role in mediating through the physical force (depletion force).

Studying chemistry between the QDs and polymer matrix will be done via exchange ligands where the native ligands will be replaced with different ligands (probably shorter-length ligands). The approach of the exchange ligands is expected to control the QDs surface chemistry via changing the length of the native ligand to shorter ligands, hence controlling the QDs: polymer self-assembly and increasing the interactions of QD-QD and QD-polymer matrix, which is expected to improve the miscibility between the QD and polymer matrix. Moreover, engineered quantum dots with shortened ligands can improve the dispersion of quantum dots in nanocomposite films, leading to enhanced optical properties and potential applications in areas such as photocatalysis Additionally, the volume fraction of the QDs and polymer must be considered, where it is a key parameter in optimising the nanocomposite

film structure, for example, the arrangement and distribution of the QDs within the polymer matrix.

Chapter 3 Characterisation and Experimental Techniques

The characterisation of nanocomposites entails measuring, evaluating, and assessing nanomaterials' chemical and physical properties. Nanocomposites that measure less than 100 nm are often engineered because of their unique properties [140]. Unlike conventional materials, nanocomposites' chemical concentration or composition must be improved for their complete characterisation. Nanocomposites differ in dispersion, crystallinity, surface properties, shape, and size, so good characterisation techniques must be used [141]. Many types of equipment and instruments are used to characterise nanomaterials, including spectroscopy and microscopy methods. As applied to the current project, the main characterisation techniques comprise Small angle X-ray scattering (SAXS), ellipsometry, and Atomic Force Microscopy (AFM). The principles of these characterisation techniques and some examples from previous studies are further discussed in subsequent subsections.

3.1. Small-angle X-ray scattering (SAXS)

Small-angle X-ray scattering (SAXS) is a widely used characterisation technique on a range of particles, peptides, and macromolecular samples between 1 and 100 nm. SAXS is used to identify the shape and size of particles, in addition to the internal structure of partially ordered and disordered nanomaterials. Figure 3.1 shows the principle of SAXS, where a monochromatic X-ray beam with a scattering angle of 0.1–1° and wavelength of between 0.7 nm and 0.2 nm is projected on a sample under study. Most of the X-rays pass through the material sample without interaction. A small percentage of emitted X-ray photons strike electrons from the sample atoms, resulting in inelastic scattering of the photons. Elastically scattered photons maintain their wavelength and kinetic energy and slightly change their vector. An X-ray sensitise detector situated on the opposite side of the sample from the X-ray emitter obtains the scattered X-ray pattern and is used to identify information about the sample under investigation. However, since most X-ray photons pass through samples without interaction, detecting weak signals with low scattering angles may be difficult. Therefore, an X-ray beam of non-scattered photons is blocked before it can reach an X-ray detector using either line or point collimation.[142].

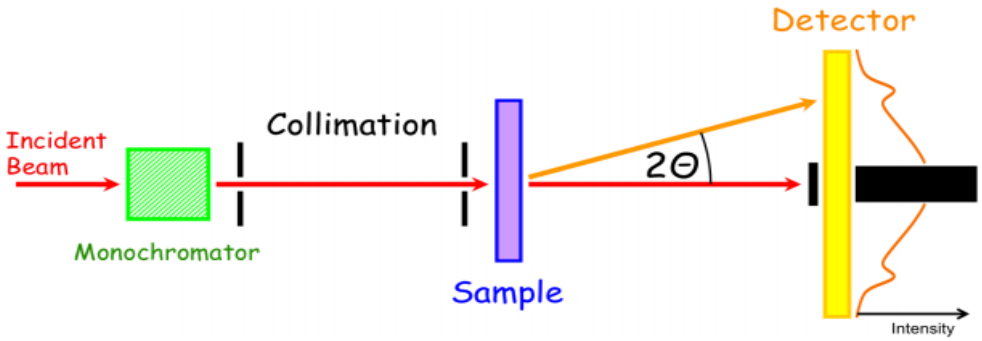

Figure 3.1/ A schematic illustration of small-angle X-ray scattering

Structural information from a nanoparticle can be obtained using SAXS based on the principle that when X-rays are scattered, their orientation direction depends on the relative position of their atoms. As shown in Figure 3.2, the wave vector (K_o), wavelength (λ), and magnitude ($\frac{2\pi}{\lambda}$) interact with a nanocomposite sample. The interaction results in a scattered wave (k_f) with a scattering angle of 2θ. The resulting transfer of momentum (q^) is illustrated as

$$q\hat{} = k\hat{}f \; - \; k\hat{}_{\circ} \qquad 3.1$$

Whereas its magnitude (q^) aligns with the following:

$$q = (\frac{4\pi \; sin \; \theta}{\lambda}) \qquad 3.2$$

Using Bragg's law, a length scale *d* can probe the equation as ($\frac{2\pi}{\lambda}$). A 2D detector is used to measure scattered intensity I (q). Further, the 2D intensity can be averaged for samples with randomly oriented molecules to obtain their 1D profile in terms of I (q) as a function of q [143].

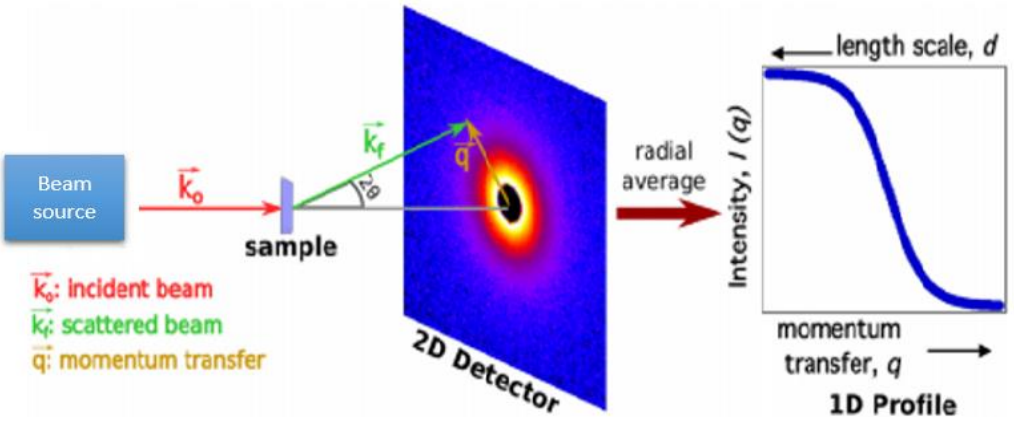

Figure 3.2/The interaction process of the X-ray beam with nanocomposite samples [143].

SAXS has been used to determine the size of nanoparticles based on quasi-spherical PbS. The researchers noted that SAXS was adequate in characterising the diameter of nanoparticles, dispersion of particles, and their size distribution. The researchers provided SAXS calibrated sizing from 2.5nm to 7 nm on PbS material. Figure 3.3 shows the results obtained for the diameter characterisation of the spherical PbS QDs and the clear link with peak absorption wavelength [144].

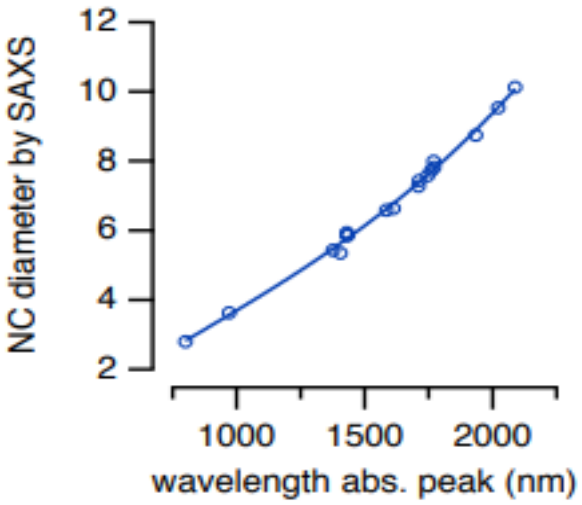

Figure 3.3/ Relation between the QD diameter and peak wavelength absorption for PbS spherical nanocrystals [144].

Also, SAXS has been used to characterise PbS QDs with an OA ligand layer. The SAXS data obtained enabled accurate measurement of PbS volume fractions in the nanomaterials,

making it possible calculating the relative mass fractions of PbS–OA in a QD solution (Figure 3.4)[145].

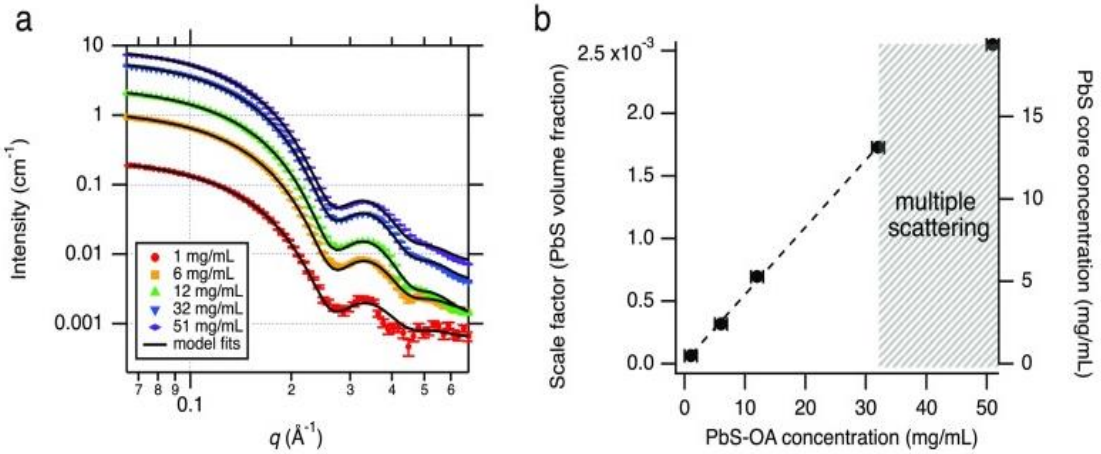

Figure 3.4/ Small-angle X-ray scattering (SAXS) data :(a) the concentration of PbS-OA at different concentrations, (b) the volume fraction of PbS cores against their effective concentration, as a function of concentration in PbS-OA solution[145].

This project used the Xeuss 2.0 instrument to carry out the SAXS measurement with an Excillium Metal Jet liquid gallium X-ray source. Collimating slits of 0.5 x 0.6 mm ("high flux" mode) were used to collect the scattering data for 900s for each sample. A vertically-offset Pilatus 1M detector was used to record the scattering pattern with a detector to sample distance of 1226mm, calibrated using standard silver behenate to achieve a q-range of 0.001-1 Å^{-1}.

Solution capillaries. For the solution scattering the specimens were measured in borosilicate glass capillaries 2mm diameter of external with a 0.01 mm wall thickness. Data were adjusted for background (solvent and glass capillary), transmission, acquisition and sample thickness time before placing the data on an absolute scale (cm^{-1}) using scattering from a glassy carbon as a standard sample [146]. The data were fitted via Sas view ("core−shell sphere") with a hard-sphere form factor whose radius is bound to be the sum of the shell thickness and core radius. The high electron density of the PbS quantum dot (QD) cores (length density of the X-ray scattering, xSLD, of PbS for a Ga source, = 50.7 × 10−6 Å−2) translates to an excellent contrast of X-ray with organic materials and solvents (e.g., xSLD toluene = 8.03 × 10−6 Å−2).

The data reduction was performed using the GIXSGUI MATLAB toolbox that provides script-based access and a graphical user interface to visualise scatter grazing incidence X-ray

data from nanostructures in thin films and on surfaces [147]. The GIXSGUI MATLAB offers routine surface scattering data reduction methods such as two-dimensional intensity reshaping and one- dimensional intensity line cut.

The graphing package **origin software** was used to draw the 1D graphs and to fit the peaks using the Gaussian fitting [148, 149]. From the *peaks analyser tool*, it was possible to select the peaks that needed to be fit. In this experiment, I fitted one peak in each sample to have the peak position and the full width of the half maximum (FWHM).

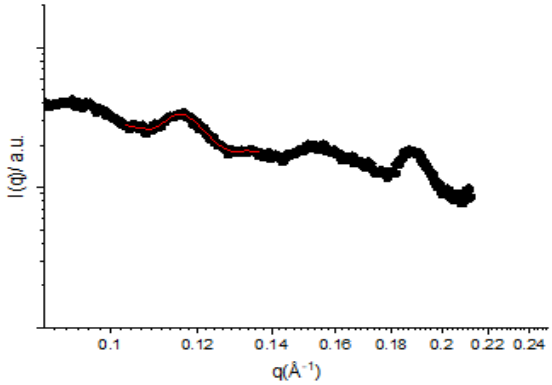

Figure 3.5/The peaks around 0.11Å selected to fit (using Gaussian fitting) in origin software to gain some data such as peak position and the FWHM.

3.1.1. GISAXS

GISAXS is a member of the SAXS approach family and the small-angle complement to GIWAXS. It is a surface method used to characterise nanoscale surfaces and thin films. The main difference between Grazing-Incidence Small Angle X-ray Scattering (GISAXS) and Small-Angle X-ray Scattering (SAXS) lies in the angle at which the X-rays interact with the sample surface. SAXS is used for nanomaterials in liquid or powder form, GISAXS is applied to surface layers on flat substrates and provides information about the size, shape, and alignment of nanoscale features on the sample surface. The limited penetration depth of the X-rays into the sample in GISAXS, especially for thin films, results in low background scattering from the bulk of the material, enhancing the sensitivity to surface structures. Figure 3.6 provides some basic information that can be obtained from the GISAXS in this experiment, such as the direct reflection beam which originates from the X-ray beam that strikes the sample surface at a very shallow angle. This beam is reflected and detected,

providing information about the surface structure and morphology of the sample. Also, the rings observed in GISAXS patterns are a result of the scattering of X-rays from the nanostructured surface of the sample. These rings correspond to the distribution of electron densities on the surface, reflecting the size, shape, and arrangement of PbS QDs. For instance, ordered normal and lateral density fluctuations in the sample can lead to the formation of these characteristic rings in the GISAXS pattern.

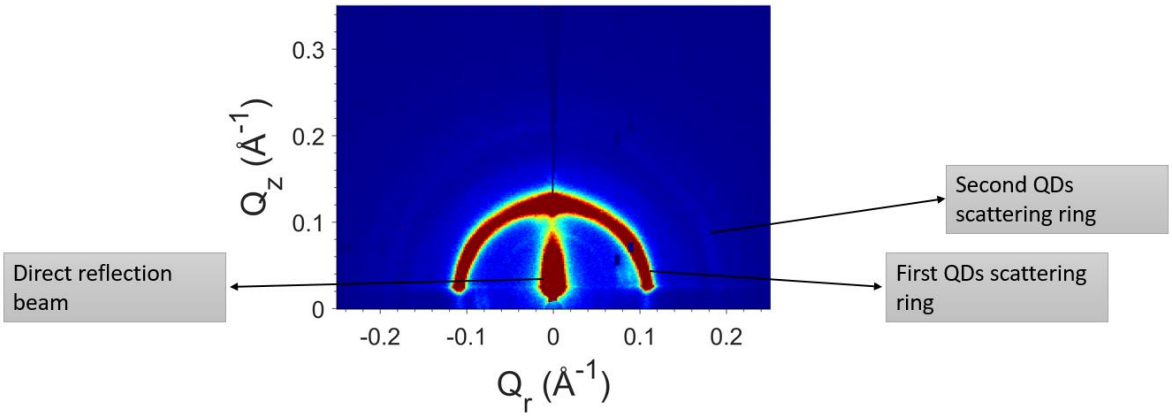

Figure 3.6/ a 2D reshaped GISAXS image showing some basic features that can be obtained from the GISAXS.

3.2. Atomic force microscopy (AFM)

The surface morphology of polymer quantum dots in the nanocomposite films was studied via atomic force microscopy (AFM). AFM is one of the most effective tools for imaging surfaces in a non-destructive manner on numerous length scales, ranging from nanometres to tens or even hundreds of microns with ~ 5 Å resolution. Also, the AFM is expected to be able to give some details about the shape, texture and topography of nanocomposite films with minimum sample preparation, as will be detailed in this chapter.

Atomic Force Microscopy (AFM) measures particles' surface characteristics and morphology. The AFM can generate information about samples on the Angstrom scale with minimum sample preparation; Figure 3.7 shows the basic principle of AFM. The AFM principle is based on the use of a cantilever that has a sharp tip used to scan the surface of a sample. As the tip approaches the surface, the attractive force between the tip and the sample surface causes the cantilever to deflect towards the surface. In contrast, when the cantilever comes close and touches the sample surface, there are increasing repulsive forces causing the cantilever to deflect from the surface (Figure 3.8). The attractions and deflections are

measured using a laser beam. An incident beam from the top of a cantilever is used to track the changes and recorded on a Position-Sensitive Photodiode (PSPD). A sample with lowered and raised surfaces causes the cantilever to deflect, revealing the accurate topographic map or morphology of the sample surface [150].

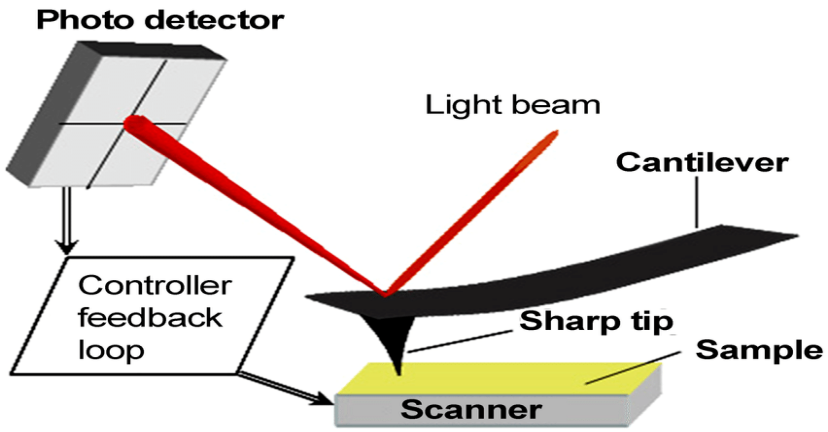

Figure 3.7/ Schematic illustration of the atomic force microscopy setup.

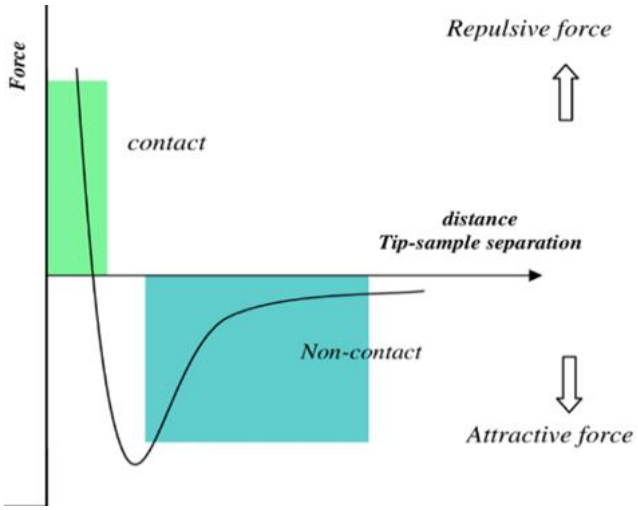

Figure 3.8/ Schematic showing the attractive and repulsive forces that affect the cantilever in the AFM.

This is an example of using AFM to characterise the nanocomposite films' surface morphology. AFM has been used to examine the shape and thickness of reduced Graphene Oxide (rGO)- PbS thin films. AFM images and their associated line profile cross-sections are

shown in Figure 3.9. The smooth morphology of the thin PbS films showed a uniform distribution of QDs on the surface of graphene. The thickness of the PbS film was between 12-22 nm showing the formation of monolayers of PbS on quantum dots attached to rGOs from all sides. The surface roughness of the rGO-PbS was estimated to reduce from a particle size of 2.9 nm to 1.7 nm [151].

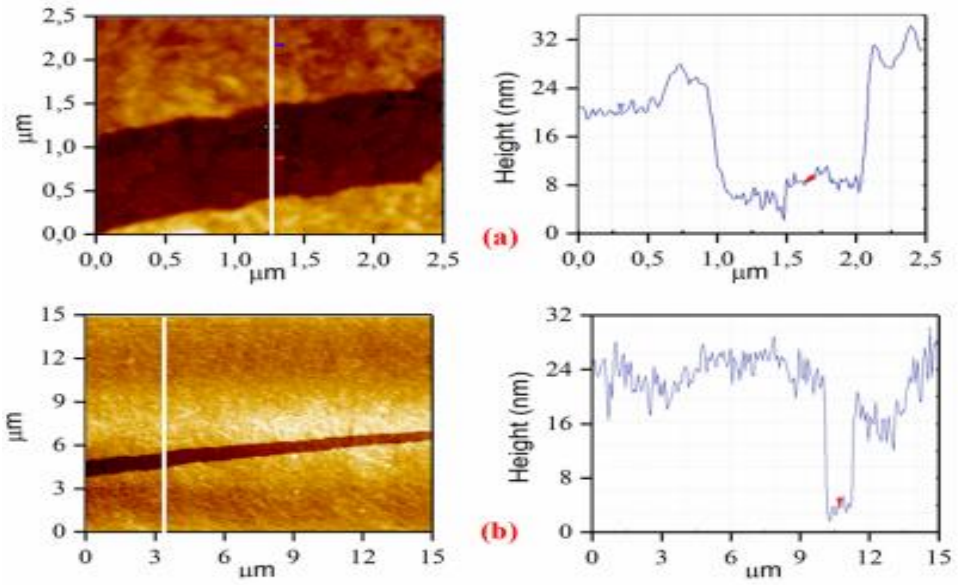

Figure 3.9/ AFM images and their respective cross-sections (a, b) of the rGO–PbS thin films[151].

In addition, AFM is used to examine hybrid polymer–PbS cells consisting of PbS nanocrystals and conjugated polymers. Figure 3.10 reveals that blending PbS QDs with polymer for hybrid solar cells can produce different morphologies. The morphology of the PbS/PDBT polymer shows particles with relatively smooth and uniform surfaces. By comparison, the PbS/P3HT combination shows an extremely coarse surface morphology with the formation of large polymer or large QD domains. For other polymers that included PDTT, PDFT, PDTD, and PDBF, the surface roughness after adding PbS increased gradually. The phase segregation differs by the type of polymer used with PbS due to differences in miscibility between the polymers and the QDs. Thus, these AFM results show that the technique is suitable for characterising thin-film PbS QDs polymer composites to characterise the surface morphology, shape, and texture[152].

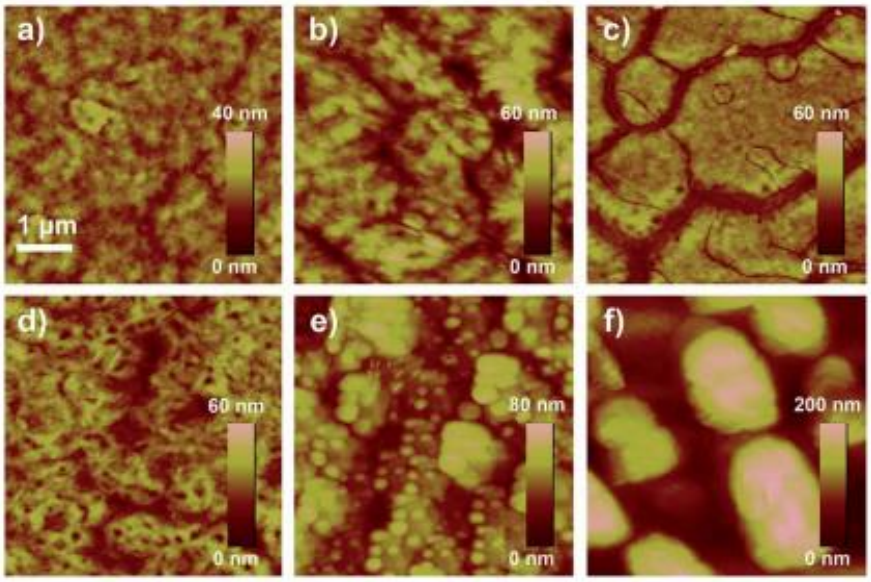

Figure 3.10/ AFM images of the PbS-polymer blend layers for PDBT (a); PDBF (b); PDTD (c); PDTT (d); PDFT (e); and P3HT (f) [152].

In this project, tapping mode was conducted in the air using a Digital Instruments Dimension AFM and a Nanoscope 4 /3A controller and software. The software's auto-tune function was used to determine the cantilever's resonant frequency. The tip was manually lowered to within a few hundred microns of the surface of the sample before using the sample engage function on the Nanoscope software to reliably approach the tip to the surface of the sample and engage the surface. The cantilever is driven to oscillate at the selected resonant frequency as the tip is lowered to the surface in this process. The tip engaged with the surface, and scanning begins when the tip-surface interactions decrease the amplitude from the accessible amplitude to below a chosen level (the amplitude set point), with the piezo height being adjusted during scanning via the feedback loop to maintain a constant oscillation amplitude of the cantilever. The amplitude, piezo stage and, phase of the cantilever oscillation were captured as 2-dimensional images. The exact imaging parameters differ from image to image, but the initial parameters were used: scan size 10µm, scan rate 1 Hz, samples/line 512, line 512, proportional gain (~0.3) and integral gain (~0.6).

The Gwydion software was used for imaging filtration, Gwyddion is a modular program for SPM (scanning probe microscopy) data visualisation and analysis [153]. Gwyddion provides many data processing functions, including all the standard statistical characterisation, filtering or grain marking functions levelling and data correction. In this experiment (*measure distance and directions between points tool*) has been used to measure the diameter of the

domains or the zones in the surface morphology of the nanocomposite films in this project, as shown in Figure 3.11.

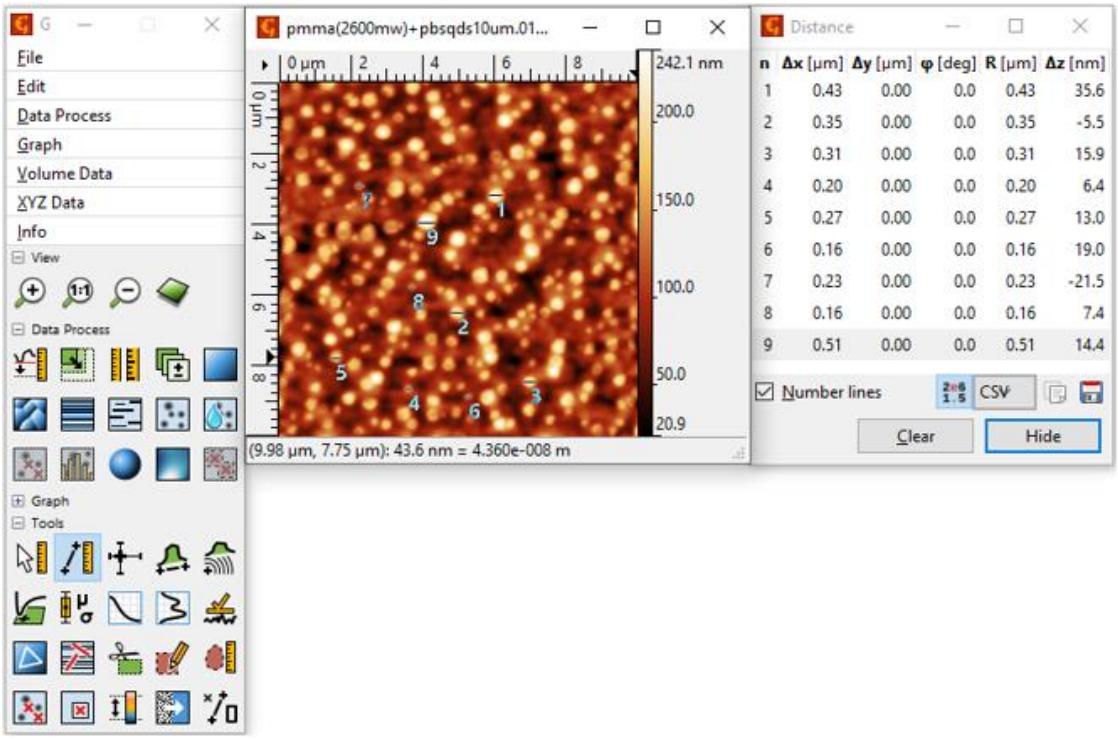

Figure 3.11/ Example of calculating the average diameter of QD-poor domain using Gwyddion (measure distance and directions between points tool, highlighted in blue in the tools panel on the left). The sample is PMMA (2600M_w): PbS QDs-OA.

3.3. Ellipsometry

Ellipsometry is an optical technique used to examine the dielectric properties of thin films. This method characterises the polarisation changes of thin films upon transmission or reflection. The ellipsometer is used to make optical measurements based on five principle steps. As shown in Figure 3.12, a source of light with a known polarisation state is manipulated using compensators and polarisers. Then, an oblique reflection of the beam is projected on the sample, resulting in an emergent beam with an altered polarisation state. The new polarisation state of the beam is analysed. The step is followed by parameter determination to characterise information relating to the two polarisation states, Rp and Rs. Finally, sample parameters are deduced via modelling parameters, including film thickness and optical properties of the sample [154].

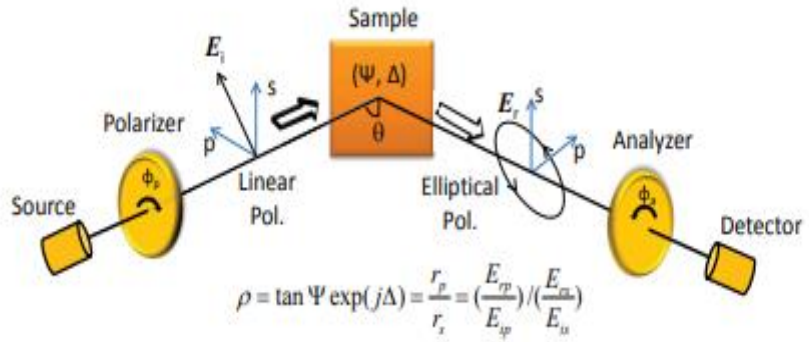

Figure 3.12/The basic principles of the ellipsometer.

Ellipsometry was previously used to model the dielectric function of PbS QDs as a function of the average particle diameter. The researchers achieved this by modifying central energies in the E-k diagram's critical point. The results revealed the suitability of this technique for determining the electrical and optical properties of PbS QDs in a nanocomposite material. Figure 3.13 and Figure 3.14 show the electric and optical properties of PbS QDs obtained using ellipsometry[155].

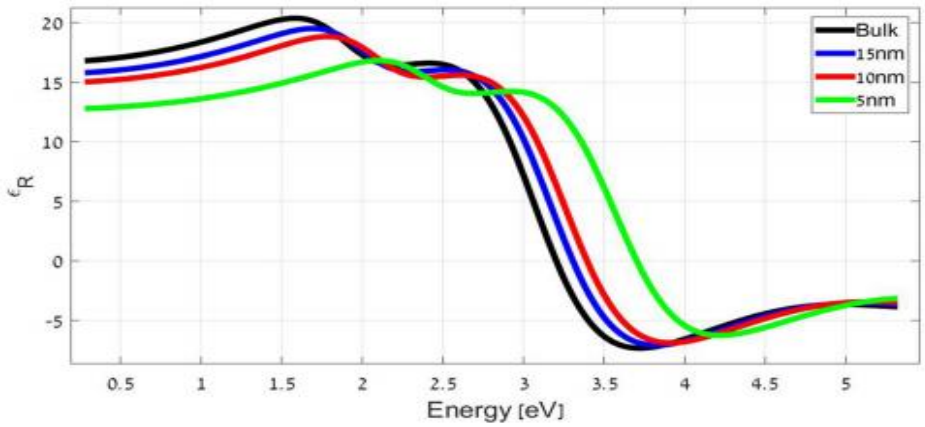

Figure 3.13/ Obtained dielectric results of PbS QDs for particles of different average diameters.

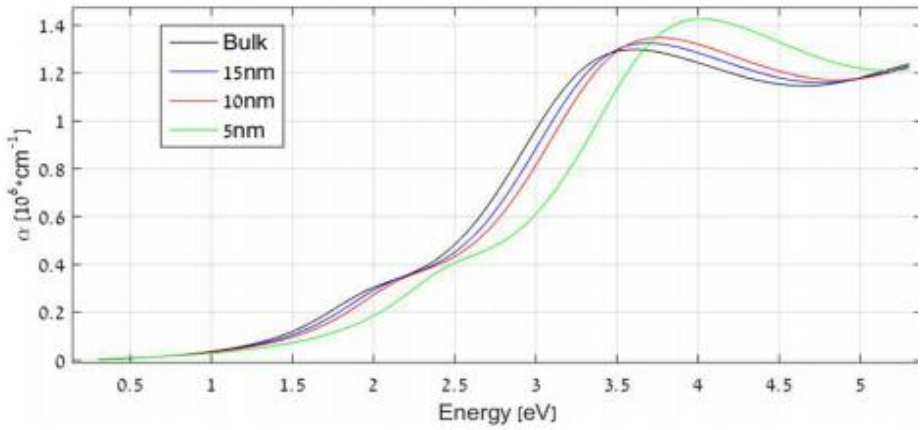

Figure 3.14/ Optical spectra for bulk PbS and PbS QDs of average diameters ranging from 5 nm, 10 nm, and 15 nm.

In this project, I mainly focused on the thickness of the films and I used Ellipsometry for this purpose. As showing in Figure 3.15, building the model is starting with the substrate which silicon, then NTVE JAW and finally Cauchy film. The Cauchy model is a valuable tool in ellipsometry for studying the thickness of materials, offering simplicity, accuracy, and improved reliability in the characterization of thin films and substrates. Also, the Cauchy model includes roughness as a fitting parameter in this model.

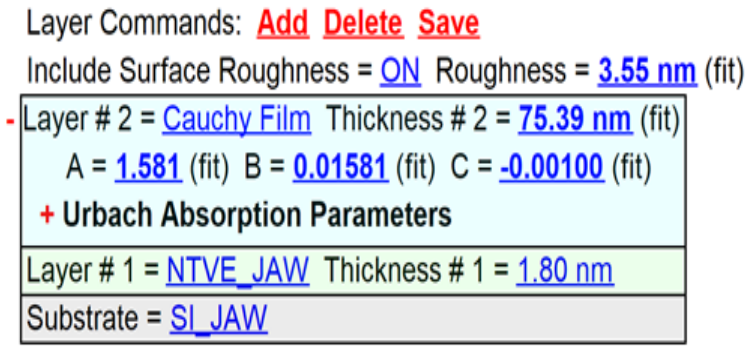

Figure 3.15/ Data obtained from a film in this project showing that the model used.

Chapter 4

Understanding the effect of host polymer molecular weight on the nanocomposite film morphology of Lead Sulphide quantum dots and polymer matrix

4.1. Introduction

The main object of the project is to understand the force that controls the dispersion of Quantum Dots (QDs) into a polymer matrix to form Nanocomposite films with potential uses in technological applications such as optoelectronic devices. The key parameters controlling the interaction between the polymers and the QD, such as the effect of Polymer molecular weight (M_w) and viscosity on the depletion force, are examined in this chapter. The polymer molecular weight (M_w) is a critical aspect which the study must examine. This would be expected to determine how the interparticle interaction is mediated through the depletion force (for polymers that do not interact with the nanoparticle surface) or the bridging interaction (for polymers that interact with the nanoparticle surfaces).

Three different kinds of blend films are discussed, including PS: PbS QDs-OA, PMMA: PbS QDs-OA and F8BT: PbS QDs-OA; these experiments were carried out by varying the host polymers M_w and seeing how this affects the structure of the nanocomposite films. The reason for employing three different polymers is that each has different features: PS is easily monodisperse and hydrophobic, PMMA is more hydrophilic and also monodisperse, and F8BT is a conjugated polymer and more complicated being a semicrystalline polymer.

The blend films were characterised via Ellipsometry and Atomic Force Microscopy (AFM) for thickness and surface morphology, respectively, while the nanostructure and ordering were characterised via Grazing-Incident Small Angle Scattering (GISAXS).

4.2. Experimental methods

In these experiments, three different polymers, each with a range of different molecular weights (M_w), were used as host polymers: Polystyrene (PS), Poly (methyl methacrylate) (PMMA) and Poly (9,9-dioctylfluorene-alt-benzothiadiazole) (F8BT). The polymers were purchased from different suppliers with high purity (≥ 99%), and the suppliers characterisation data is shown in

Table 4.1.

Lead Sulphide Quantum Dots capped by Oleic Acid ligands (PbS QDs-OA), 1000nm emission peak with a concentration of 8.7 mg/ml toluene, were purchased from Quantum solution. All materials were used as received without any further purification.

Polymer	supplier	M_w (g/mol)	M_n (g/mol)	PDI (M_w/ M_n)
PS	Polymer source	1,800	1600	1.13
PS	Polymer source	7,500	7000	1.07
PS	Sigma-Aldrich	40,000	39,000	1.02
PS	Polymer source	50,000	49,000	1.02
PS	Polymer source	90,000	86,538	1.04
PS	Polymer source	350,000	339,805	1.03
PS	Polymer source	850,000	790,000	1.08
PS	Polymer source	1,600,000	1,500,000	1.10
PMMA	Polymer source	2,600	2,500	1.09
PMMA	Polymer source	8,400	7,000	1.19
PMMA	Polymer source	40,000	36,363	1.10
PMMA	PSS	50.000	48,543	1.03
PMMA	Polymer source	350,000	336,538	1.04
PMMA	Polymer source	1,000,000	666,666	1.5
PMMA	Polymer source	1,500,000	1,271,186	1.18
F8BT	Sigma-Aldrich	75,000	72,815	1.03
F8BT	Sigma-Aldrich	200,000	192,307	1.04

Table 4.1/ The polymers used in this experiment and the suppliers, values for M_w, M_n and PDI taken from the suppliers datasheets.

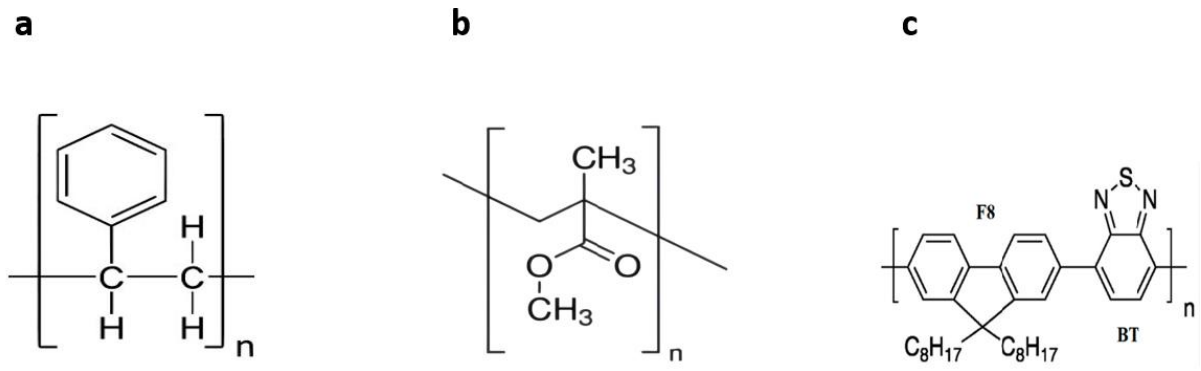

Figure 4.1/ Schematic structure of; a) polystyrene, b) Poly methyl methacrylate, c) Poly (9,9-dioctylfluorene-alt-benzothiadiazole) polymers.

substance	**empirical formula**	**Density (g/cm^{-3})**	**Melting temperature (^oC)**	**Boiling temperature (^oC)**
Lead Sulphide	PbS	7.6	1,118	1,281
Oleic Acid	$C_{18}H_{34}O_2$	0.895	14	360
Polystyrene	$(C_8H_8)_n$	0.96-1.05	240	430
Poly methyl methacrylate	$(C_5O_2H_8)_n$	1.18	-48	101
Poly (9,9-dioctylfluorene-alt-benzothiadiazole)	$(C_{35}H_{42}N_2S)_n$	1	215	240
Toluene	C7H8	0.87	-95	110

Table 4.2/ Some properties of the materials and solvent used in this experiment.

4.2.1. Synthesis of Lead Sulphide Colloidal Quantum Dots Capped via Oleic Acid (PbS QDs-OA).

The methods of synthesis used by the **Quantum solution** were as follows; a master batch of PbS nanocrystals capped via Oleic Acid was synthesised via the Hines and Scholes method [60]. Oleic Acid (OA, 90%, 12.6 mmol, 4 ml), Lead Oxide (1,25g, 5.6 mmol), and 1-Octadecene (ODE, 90%, 78mmol, 25mL) were placed in a 3-flask necked round bottomed and degassed in the vacuum (<10-2 mbar) for 2 hours at 110 C° with stirring to form a colourless solution. A syringe containing hexamethyldisilathiane (TMS2S, 95%, 592 µL, 2.8 mmol) and ODE (13.9 mL, 43 mmol) were prepared in a nitrogen glovebox. Under nitrogen flow, the flask was injected rapidly via the syringe contents at 110 C° and allowed to cool.

The reaction mixture was transferred to an argon glovebox upon cooling to 60 C°. Then, the nanocrystals were precipitated in butanol/ethanol, and for 30 minutes, they were centrifuged. Then, the nanocrystals were suspended in hexane and precipitated with ethanol again. For storage, the purified nanocrystals were suspended in toluene.

4.2.2. Samples preparations

The preparation of the nanocomposite films started by making the polymer solutions, which were prepared according to weight percentage. The whole polymer solutions (PS, PMMA and F8BT) with different M_w are made 5% by weight in toluene and left to dissolve for 48 hours at room temperature. After that, a 450nm filter was used to filter the polymer solutions from any large impurities.

Then, 200µL from the polymer solution was mixed with another 200µL from the PbS QDs-OA in a small glass tube to make the nanocomposite solutions with a quantum dots volume fraction around 0.0024 (PbS QDs $\phi \simeq 0.0024$) and polymer volume fraction around 0.021,0.018 and 0.021 for PS, PMMA and F8BT (Table 4.3), respectively. The polymer and PbS QDs-OA solution were left at room temperature for 48-72 hours to ensure the nanocomposite solution mixed well without any precipitates. Finally, for each sample, 30 µL from the nanocomposite solutions were deposited on clean silicon substrates and spun using a spin coater for 30 s at 2000 rpm (Figure 4.2).

substance	**Volume fraction(ϕ)**	**Volume percentage (%)**
PbS-OA	0.0024	0.24
PS	0.021	2.1
PMMA	0.018	1.8
F8BT	0.021	2.1

Table 4.3/ The volume percentage and volume fraction of the nanocomposites. The initial weight fraction of PS: PbS QD-OA nanocomposite is (0.24% QDs, 2.1% PS and 97.66% toluene), the initial weight fraction of PMMA: PbS –OA nanocomposite (0.24% QDs, 2.04% PMMA and 97.96 % toluene) and the initial weight fraction of F8BT: PbS –OA nanocomposite (0.24% QDs, 2.1% F8BT and 97.66% toluene).

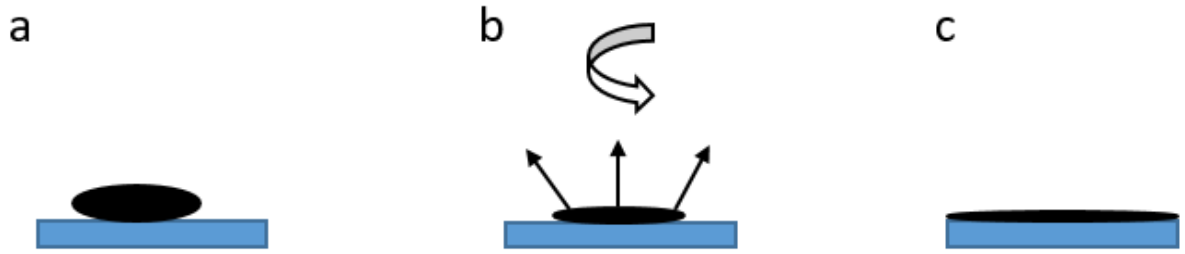

Figure 4.2/The process of nanocomposite film formation during spin coating: a) the solution on the silicon substrate before spinning; b) during spinning (2000 rpm), the solvent is being lost in this step, and the film becomes very viscous. C) Finally, the film becomes glassy after the majority of the solvent is removed.

4.3. Results and Discussion

4.3.1. Ellipsometry

Ellipsometry was used to measure the nanocomposite film thickness; Spectroscopic ellipsometry is an optical technique used for analysis and metrology. An elliptically polarised light beam is shone on the sample of interest; then, the reflected light beam is analysed to see the effect of the sample on the light beam polarization.

In this experiment, the ellipsometry data shows that the nanocomposite films thickness increased as the M_w of the host polymers increased, as seen in Table 3, Table 4, Table 5 and Figure 3. In the PS system, the sample with lower polymer M_w (PS 1800 M_w: PbS QDs-OA) has a lower thickness (101nm) than the other samples with the same host polymer but higher M_w such as PS(7.5k M_w), PS(40k M_w), PS(50K M_w), PS (89K M_w), PS(350K M_w), PS(850K M_w) and PS(1.6M M_w) where have thicknesses of 196nm, 211nm, 231nm, 237nm, 258nm, 291nm, and 321nm respectively.

Similar behaviour is shown in PMMA and F8BT systems, as illustrated in Table 4.5, Table 4.6 and Figure 4.3. The thickness of a PMMA (2600 M_w): PbS QDs-OA nanocomposite film is 136nm; this keeps increasing as the PMMA M_w increases until it reaches the greatest thickness (389nm) in the highest PMMA M_w 1.5M M_w.

The increase in the thickness of the nanocomposite films when the M_w of the host polymers increases is due to the rise in the viscosity of the nanocomposite solutions. Further, it was noticed that the viscosity of the solutions increases with the M_w of the polymers, which agrees with previous studies [156]. Rising M_w means an increase in the initial viscosity of the solutions, leading to increases in the thickness of the blend films due to the change in the rheology of the films when spin-coated. In simple terms, the ability to reduce the thickness of a polymer solution becomes harder as the viscosity of the solution increases.
So, the thickness is set solely by the initial solution viscosity. This confirms why the thickness of the films increased with an increase in the polymer M_w, which is consistent with the power-law exponent relationship (Figure 4.3)[156, 157].

Films	Thickness (nm)	Error bar (nm)
PS(1800 M_w): PbS QDs-OA	101	± 2.87
PS(7.5k M_w): PbS QDs-OA	196	± 2.34
PS(40kM_w): PbS QDs-OA	211	± 0.98
PS(50K M_w): PbS QDs-OA	231	± 3.06
PS (89K M_w): PbS QDs-OA	237	± 2.65
PS(350K M_w): PbS QDs-OA	258	± 1.47
PS(850K M_w): PbS QDs-OA	291	± 1.29
PS(1.6M M_w): PbS QDs-OA	321	± 2.98

Table 4.4/ thicknesses of the PS: PbS QD-OA nanocomposite films,

Films	Thickness (nm)	Error bar (nm)
PMMA(2600 M_w): PbS QDs-OA	136	± 1.09
PMMA(8.4K M_w): PbS QDs-OA	186	± 2.04
PMMA(40K M_w): PbS QDs-OA	194	± 0.45
PMMA(50K M_w): PbS QDs-OA	199	± 1.34
PMMA(350K M_w): PbS QDs-OA	224	± 2.76

PMMA(1M M_w): PbS QDs-OA	340	± 3.09
PMMA(1.5M M_w): PbS QDs-OA	389	± 1.56

Table 4.5/ PMMA: PbS –OA nanocomposite films thicknesses,

Films	Thickness (nm)	Error bar (nm)
F8BT(75K M_w): PbS QDs-OA	205	± 1.15
F8BT(200K M_w): PbS QDs-OA	249	± 2.016

Table 4.6/ F8BT: PbS –OA nanocomposite films thicknesses,

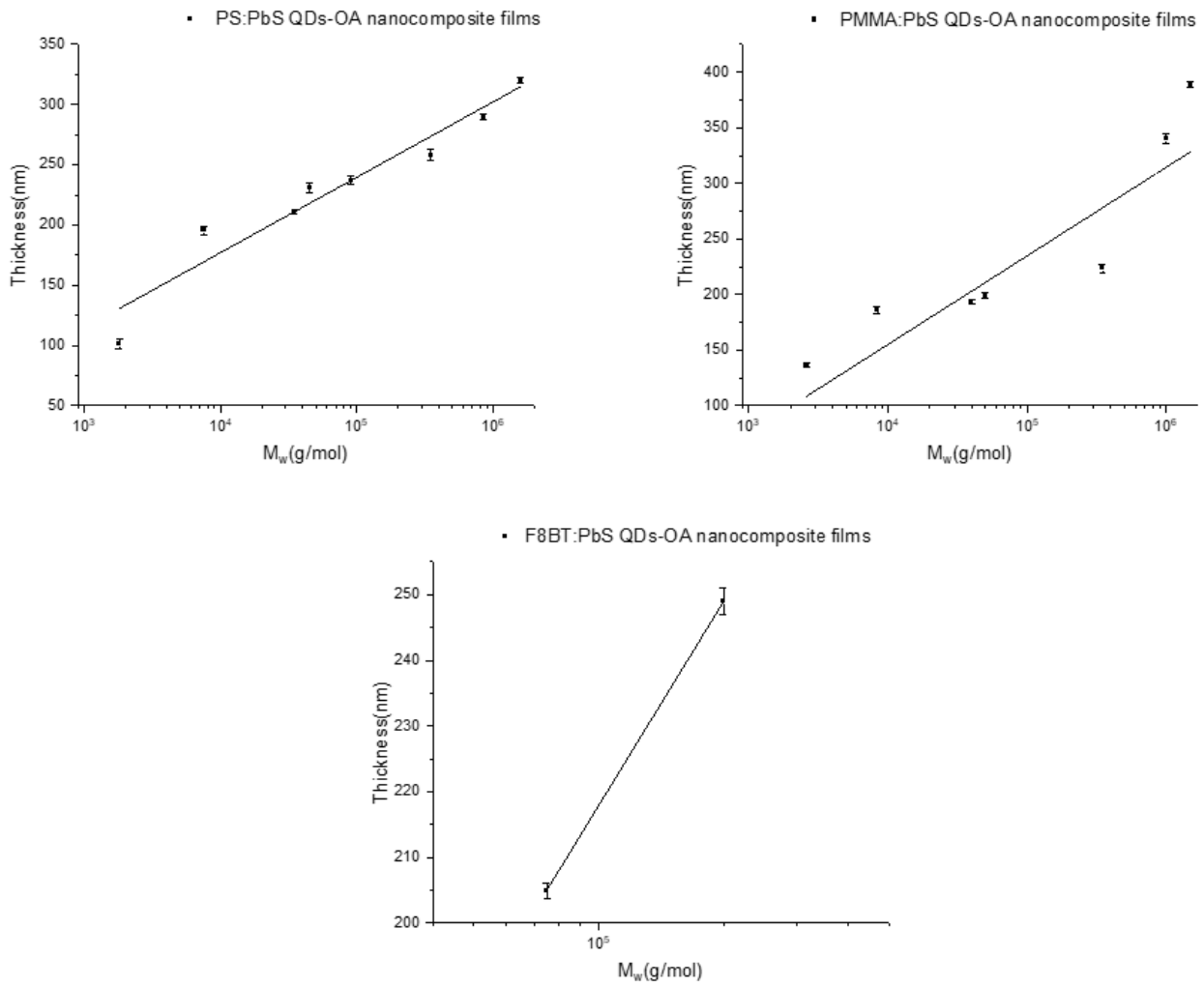

Figure 4.3/nanocomposite films thicknesses vs host polymers M_w in all the three systems, (a) PS: PbS QD-OA; (b) PMMA: PbS –OA,; (c) F8BT: PbS –OA.

4.3.2. AFM

The surface morphology of a series of polymer quantum dot (QD) blend films has been investigated via atomic force microscopy (AFM). AFM is one of the most powerful tools for imaging surfaces in a non-destructive manner on numerous lengthscales, ranging from nanometres to tens or even hundreds of microns with ~ 5 Å resolution. Also, the AFM is expected to be able to give some details about the shape, texture and topography of nanocomposite films with minimum sample preparation, as will be detailed in this section.

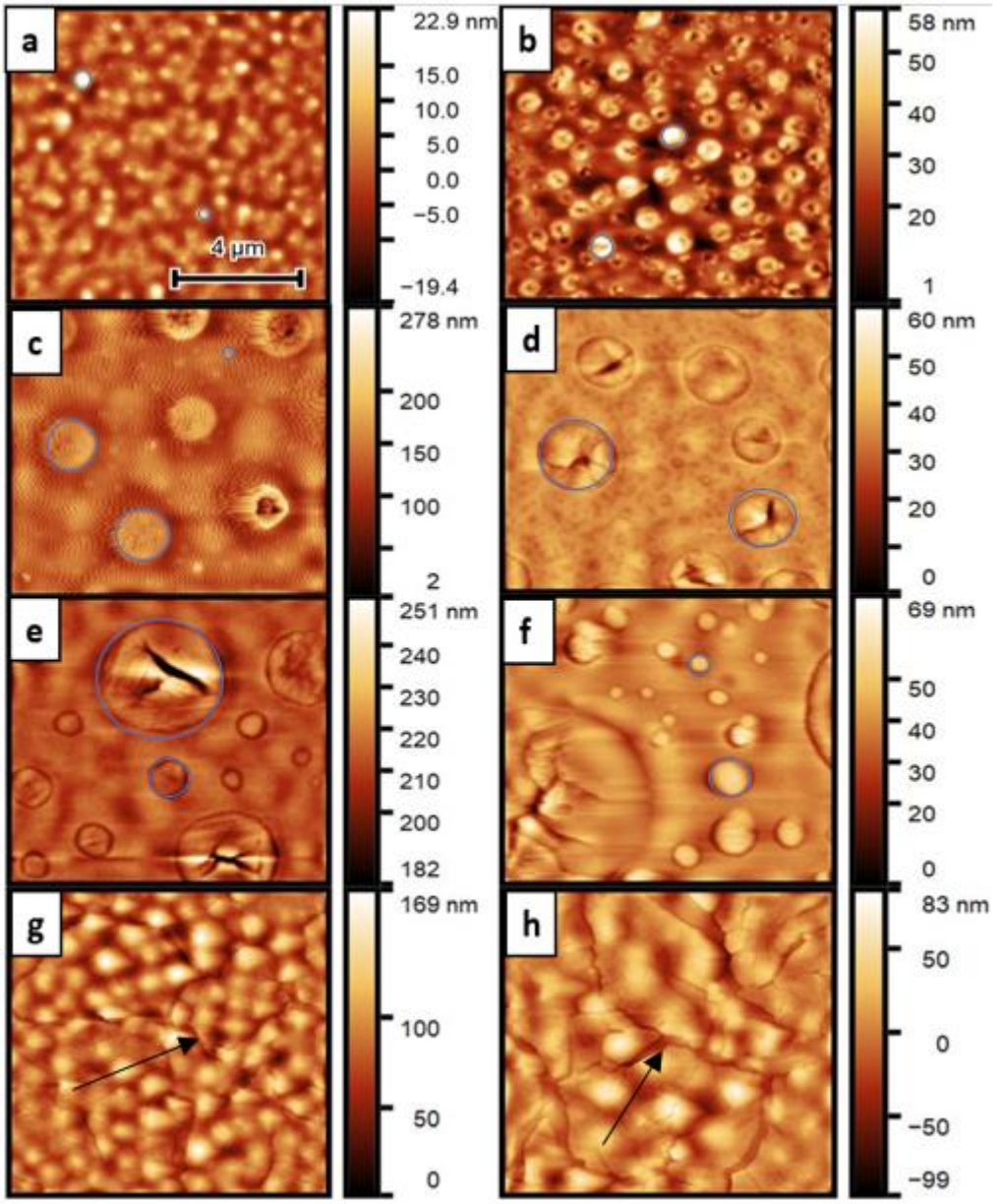

Figure 4.4/ AFM images of the PS: PbS QDs-OA nanocomposite films. All samples were spun cast from this solution of PS: PbS QDs nanocomposite; each sample differed from others in Mw of the PS. (a); PS 1800 Mw (b);PS 7.5k Mw (c); PS 40k Mw; (d); PS 50k Mw (e); PS 89k Mw (f); PS 350k Mw (g); PS 850k Mw (h); PS 1.5M Mw. The blue circle refer to the QD-rich domains, while the black arrows refer to cracks. All the samples have the same scan size (10µm).

Figure 4.4. Shows substantial surface morphology differences measured from samples of the PS: PbS QD nanocomposite films with different PS molecular weights (M_w). The nanocomposite films showed some domains and cracks in the surface morphology; these

domains have different sizes and could be QD aggregations (QD-rich domains). For instance, the film PS: PbS QD with 1800 M_w PS (Figure 4.4 a) shows QD-rich domains that have an average diameter (240nm), and this is small compared to other samples, such as the films of PS: PbS QDs with PS M_w 7.5k, 40k, 50k and 89k where they have an average diameter 500nm, 660nm, 700nm and 935nm respectively.
The QD-rich domains have a spherical shape and increased in size and became fewer in number as the molecular weight (M_w) of the PS increased, when imaged using the same scan size of 10μm. This can be seen in Figure 4.4 a, b, c, d and f with PS M_w of 7.5k, 40k, 50k, 89k, and 350k, respectively. The samples of Figure 4.4 c, d, e and f showed a distribution in the size of the QDs-rich domains over the surface of the specimen beside the large and prominent domains (Figure 4.7).

In contrast, the PS: PbS QDs films with much higher PS M_w (850k and 1.5m M_w) look relatively smooth (Figure 4.4 g and h). These films do not shown any QD-rich domains in their surface morphology as was seen for the films with lower M_w of. Instead, they showed flat planar structures with cracks in the surface morphology breaking up the QD-rich domains. The cracks in the PS (1.5M M_w): PbS QDs sample are broader and fewer than those in the PS (850k M_w): PbS QDs.

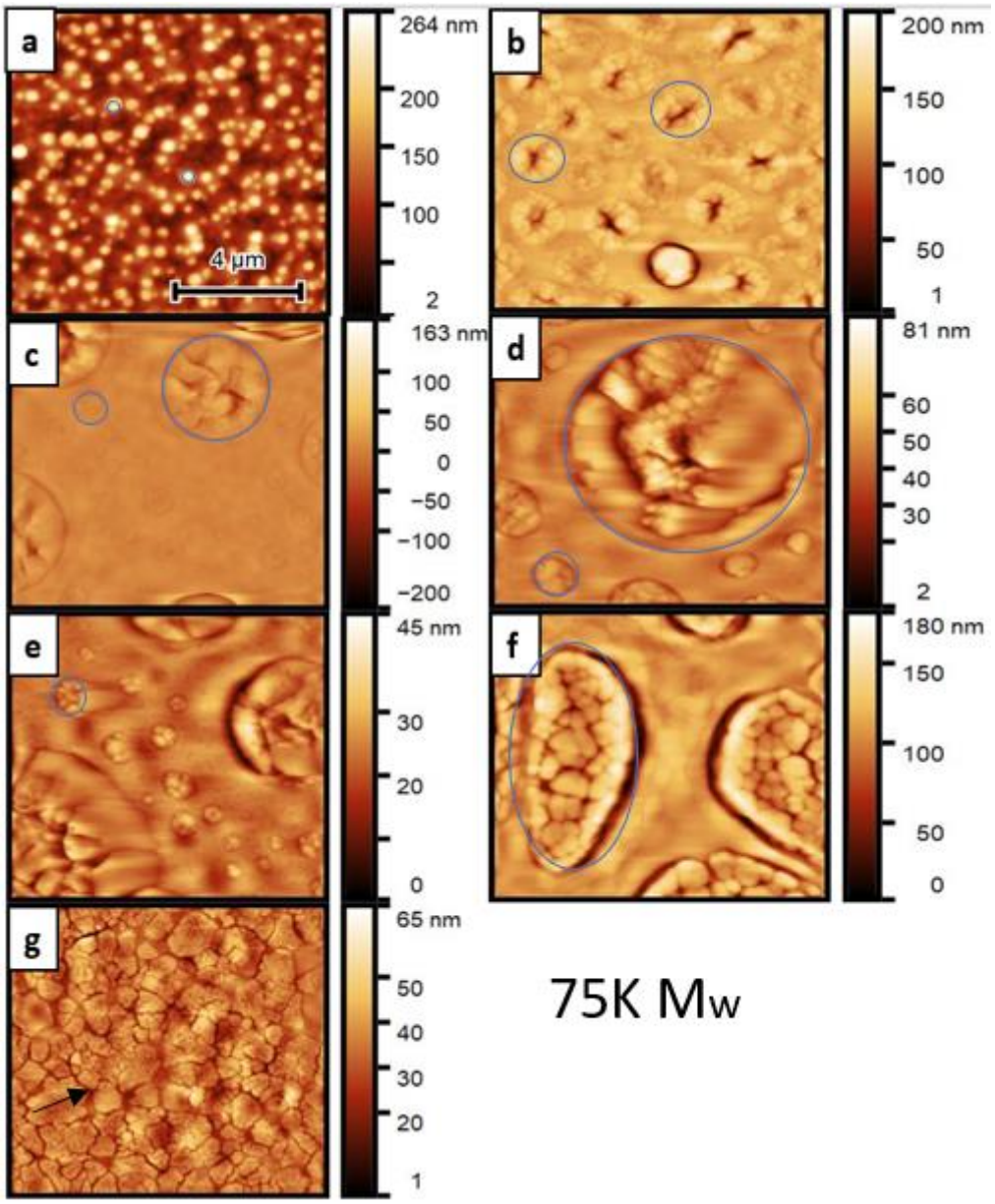

Figure 4.5/ AFM images of the PMMA: PbS QDs-OA nanocomposite films. Again, all samples were spun cast from the solution of PMMA: PbS QDs-OA nanocomposite and each specimen differed from the others in the M_w of the PMMA used. (a); PMMA 2600 M_w; (b); PMMA 8.4k M_w; (c); PMMA 40K M_w; (d); PMMA 50K M_w; (e); PMMA 350K M_w; (f); PMMA 1M M_w; (g); PMMA 1.5M M_w. The blue circle refer to the QD-rich domains, while the black arrows refer to cracks. The scan size of all samples is (10µm).

Figure 4.5 shows the surface morphology of the PMMA: PbS QDs with different M_w of PMMA. Several morphology changes are seen with changing the M_w of the PMMA. They generally show similar morphology changes to the behaviour seen for PS: PbS QDs (Figure 4.4), albeit with some differences. In (Figure 4.5 a), an image of the surface morphology of PMMA (2600 M_w): PbS QDs nanocomposite film is shown. In this film, it can be seen that

many QD-rich domains vary in size and have an average diameter of around 400 nm. This is small compared to other samples, such as the films of PMMA: PbS QDs with PMMA M_w 8400, 40k, 50k and 350k with an average diameter of 810nm, 1300nm, 1520nm and 2100nm, respectively. The QD-rich domains turned out to be oval on a sample with PMMA M_w 350k with a diameter of 2600nm (Figure 4.5 f).

As the M_w of the PMMA increased, the QD-rich domains became bigger and fewer when imaged using the same scan size of 10µm; this can be seen in (Figure 4.5 b, c, d, e and f) with M_w of the PMMA 8.4k M_w, 40k M_w, 50k M_w, 350k M_w and 1m M_w respectively. Also, the samples of Figure 4.5 c, d and e showed a distribution in the size of the QD-rich domains over the surface of the samples beside the large QD-rich domains, similar to the behaviour of the PS: PbS QD nanocomposite films in Figure 4.4, as seen the size distribution in Figure 4.7 .

However, the nanocomposite film with much higher M_w of PMMA 1.5M M_w (Figure 4.5 g) showed some small cracks in the surface morphology instead of spherical QD-rich domains presented in the films with lower PMMA M_w.

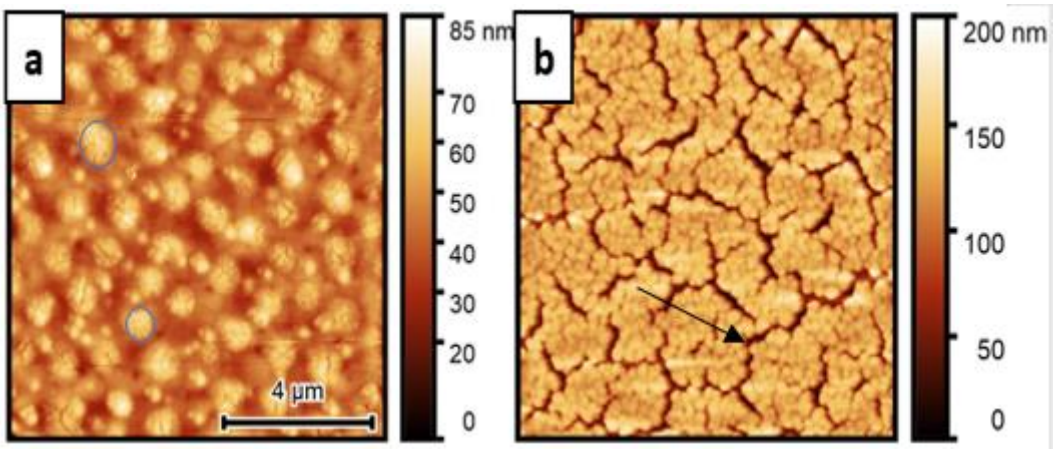

Figure 4.6/ AFM images of the F8BT: PbS QD-OA nanocomposite films, similar to the previous two figures, the samples were spun cast from the solution of F8BT: PbS QD-OA nanocomposite and the difference between the samples is the F8BT M_w used. (a); 75k; (b)200k. The blue circle refer to the QD-rich domains, while the black arrows refer to cracks. The scan size of all samples is (10µm).

The surface morphology of the F8BT: PbS QD-OA nanocomposite films with two different M_w of F8BT is shown in Figure 4.6. The specimen with lower F8BT M_w (F8BT 75k M_w: PbS

QD-OA Figure 4.6 a) shows some spherical QD-rich domains that vary in size in the surface morphology with an average diameter of 750nm. On the other hand, the sample with a higher M_w of the host polymer (F8BT 200k M_w: PbS QD-OA Figure 4.6 b) shows no QD-rich domains in the surface morphology; instead, it shows some cracks all over the sample surface.

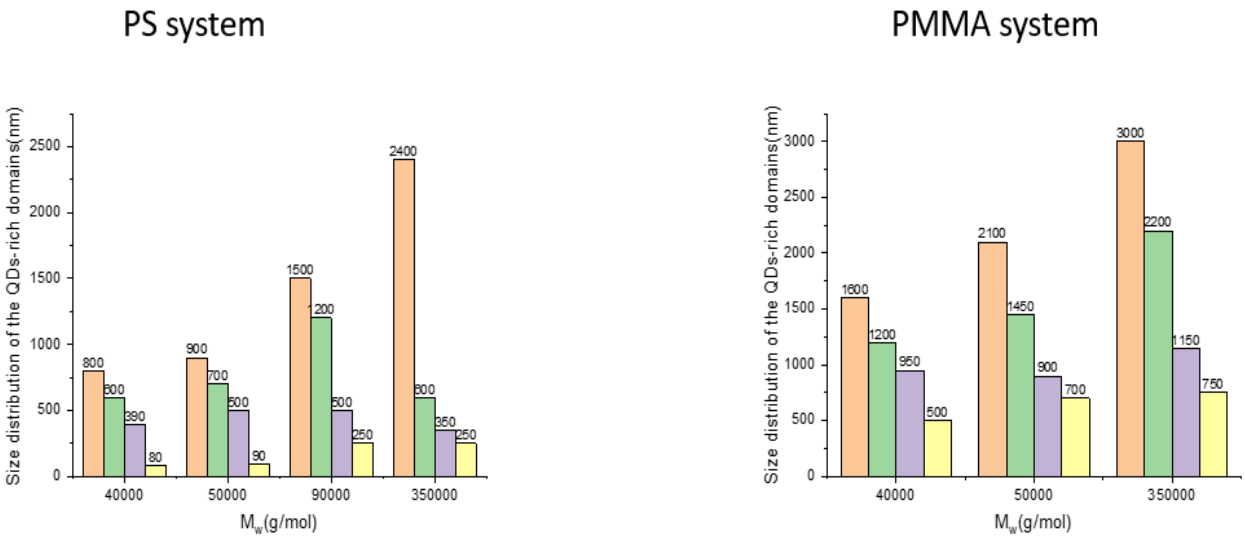

Figure 4.7/ size distribution of some samples from PS system and PMMA system, this to show the distinct QDs-rich domains size distribution in these samples.

Generally speaking, in this experiment, substantial morphology differences have been observed for each polymer blend film, such as different QD-rich domain sizes and cracks. The QD-rich domains and cracks in the surface morphology of the blend films result from phase segregation, which can be largely affected by the miscibility between the polymer and the QD.

Varying the molecular weight (M_w) of the host polymers (PS, PMMA and F8BT) affects the surface morphology of the blend films, as seen in Figure 4.4, Figure 4.5 and Figure 4.6. The different sizes of these zones and the cracks are most likely due to differences in the amount of depletion forces or depletion interaction in these films. The depletion interactions are attractive interactions caused by osmotic pressure[158]. In this experiment, the polymer coils are probably pushed aside and excluded from the depletion zones between the colloidal QDs

when the solvent leaves during drying. This means that the variation in the osmotic pressure leads to a force that pushes the QDs together [70]. As a result, the colloidal QDs continue to attract each other to make the QD-rich domains (Figure 4.8).

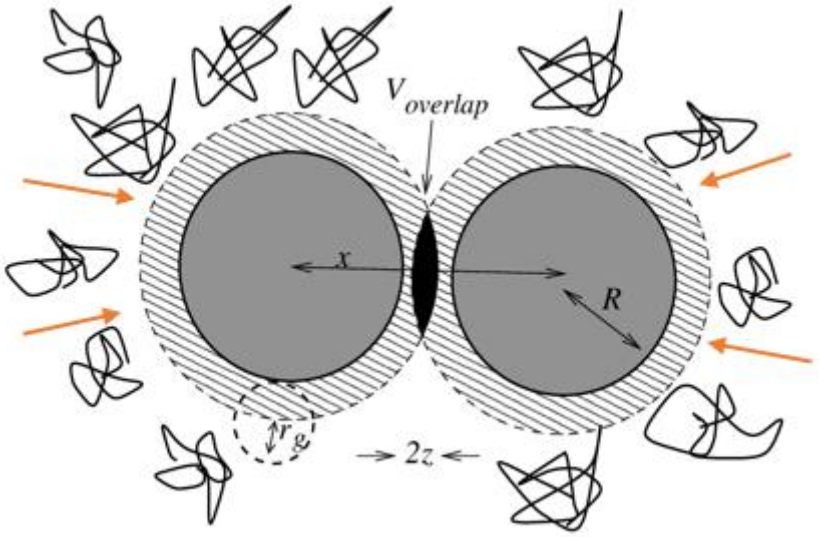

Figure 4.8/ Sketch illustrating the effect of depletion interaction, the polymer coils are excluded from the depletion zones near the QDs surface due to unbalanced osmotic pressures resulting in an attractive force between the QDs(the orange arrows represent the attractive force that pushes the QDs to each other).

The differences in the sizes of the QD-rich domains in the surface morphology of the blend films result from the changes in the magnitude of the depletion force. These changes could be due to many reasons, but what is apparent is that these changes happened because the depletion interaction or depletion force is increased with increasing polymer M_w, as has been seen before in the literature in some studies [71, 122, 159]. The size of the depletion interaction correlates to the solution osmotic pressure, with an amount of the order of the macromolecular size indicating that the depletion layer thickness is about R_g. The sets of attraction thus get determined by the size of the polymer molecules; this is why the size of aggregations zones in the surface morphology of films decreased with decreasing the polymer M_w [81]. The presence of the polymer causes some interaction between the colloidal QDs because of the depletion interaction, which depends on the size of the M_w of the polymer. So, as the M_w of the polymers increases, the depletion force also increases, which is why the average size of the QD-rich domains became larger with increasing the M_w of the polymers.

However, the films with higher M_w of the polymers such as PS (850k M_w): PbS QDs, PS (1.5M M_w): PbS QDs-OA, PMMA (1.5M M_w): PbS QDs-OA and F8BT (200k M_w): PbS Q – OA (Figure 4.4 g and h), (Figure 4.5 g) and (Figure 4.6 b) respectively, do not show any QD-rich domains in their surface morphology. This could be due to the high viscosity of the solutions used to make these films, which makes the movements of the components slower, so the zones cannot form the surface morphology at the short timescales of spin coating (~ 30s). Instead, they make surface cracks, which could be due to the region of the QDs, and these become weaker spots than the surrounding material, resulting in cracks. So, the effect of the viscosity increase via increasing the M_w of the host polymers is that is reaches a point when it prevents the zone formation in the surface morphology.

The QD-rich domains diameters were measured; before taking the average diameter for each sample because they vary in size, as shown in Table 4.7. Then, the average diameters were plotted against the M_w of the host polymer, as illustrated in Figure 4.9.

PS		**PMMA**	
Mw (g/mol)	The average diameter of the zones (nm)	Mw (g/mol)	The average diameter of the zones (nm)
1800	240	2600	400
7500	500	8400	810
40k	660	40k	1300
50k	700	50k	1520
89k	935	350k	2100
350k	1280	1M	2600
850k	---	1.5M	---
1.6M	---		

Table 4.7/ the average sizes of the QDs aggregations in both systems (PS and PMMA), showing the differences in the size of the QDs-rich domains as the M_w changed.

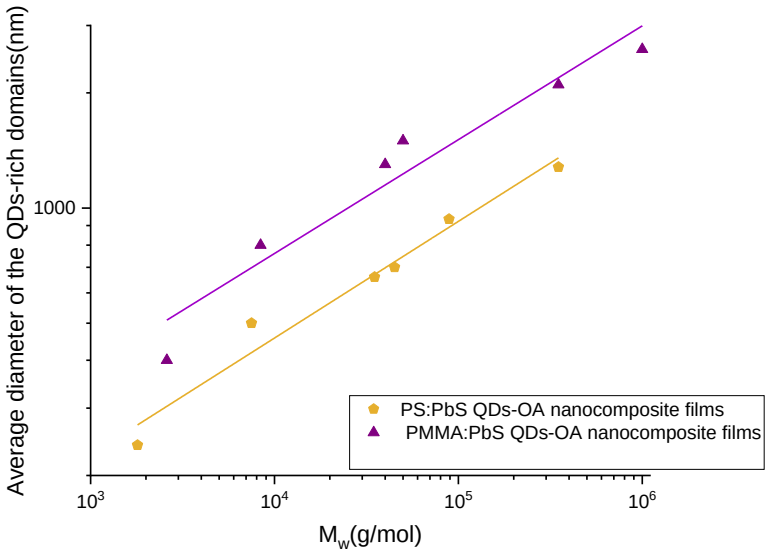

Figure 4.9/ Average diameter of the QD-rich domains vs M_w of the polymers (PS and PMMA) in the PS: PbS QDs and PMMA: PbS QDs nanocomposite films samples.

So, from Table 4.7 and Figure 4.9, the size of the QD-rich domains increased with increasing M_w of the host polymer. As previously explained, this is probably due to an increase in the depletion interaction force in solution as the M_w increased.

The average size of the QD-rich domains in the PMMA: PbS blend films is larger than that of the QD-rich domains in the PS: PbS QDs blend films. This could be because of differing polymer chemistries, for instance, PS being nonpolar and PMMA being more polar, or it could be related to the bridging interaction, which could influence the surface morphologies of the nanocomposite films.

In addition, the radius of gyration (Rg) has a power-law exponent relationship with the M_w [160], and it was calculated for both polymers (PS and PMMA) from this equation:

$$(R^2) \backsimeq C\infty\, N\, I^2 \qquad 4.1$$

Where $C\infty$ is the characteristic ratio of the polymers, N is M_w/molecular weight per repeat unit, which is for PS $(\frac{Mw}{104})$ and PMMA $\left(\frac{Mw}{337.4}\right)$, and I^2 is the length of a single bond, the $R_g \alpha N^{3/5}$ because the polymers are dissolved in a good solvent (toluene), and the R_g values and the average sizes of the QDs-poor domains are presented in

Table 4.8 before they are plotted against each other, as displayed in Figure 4.11.

PS		PMMA	
The average diameter of the zones (nm)	R_g (nm)	The average diameter of the zones (nm)	R_g (nm)
240	2.37	400	1.26
500	5.59	810	2.55
660	14	1300	6.52
700	16.38	1520	7.45
935	24.66	2100	23.97
1280	56	2600	45
---	95.53	---	57.39
---	139.63		

Table 4.8/ illustrates the radius of gyration of both polymers (PS and PMMA) vs the average diameter of QD-rich domains.

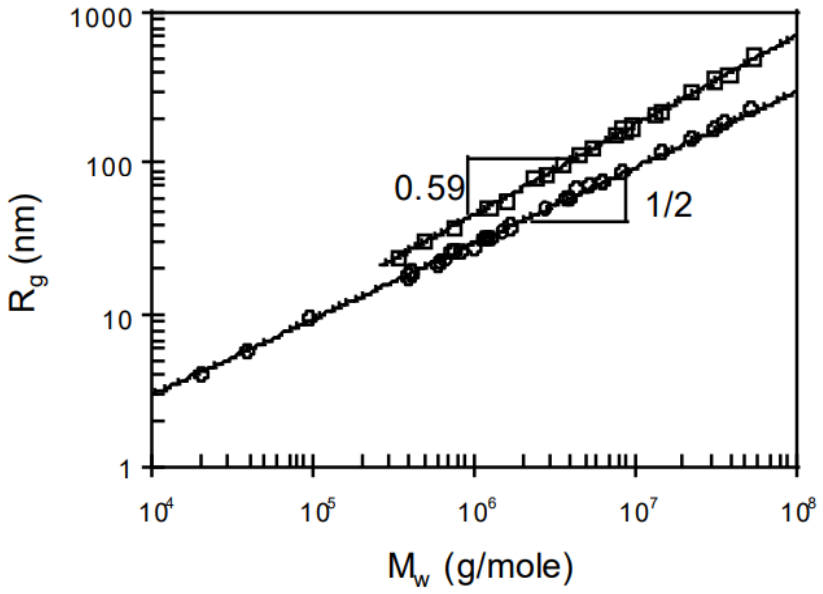

Figure 4.10/The relationship between the radius of gyration (R_g) and the molecular weight (M_w) of the polymer in a good solvent (taken from [160]).

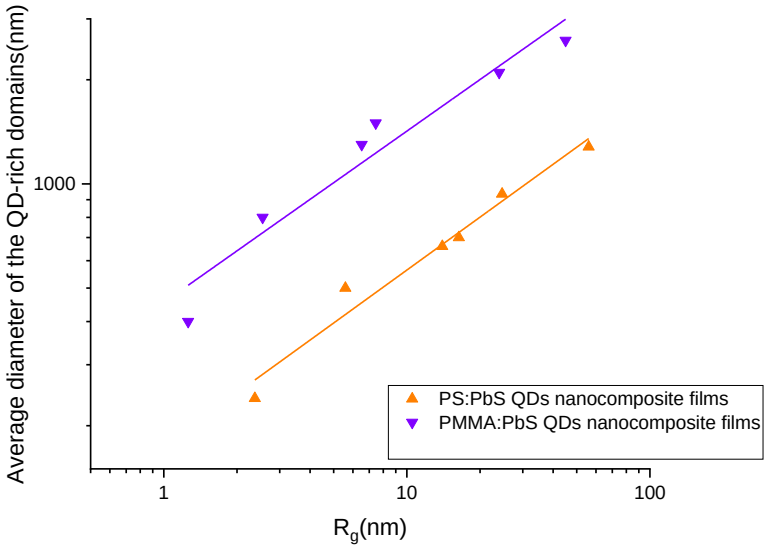

Figure 4.11/ Average size of the QDs-poor domains vs radius of gyration (R_g) of the polymers (PS and PMMA) in the PS: PbS QDs and PMMA: PbS QDs nanocomposite films samples.

Increasing the M_w of the polymers means increasing the Rg of polymers, resulting in a higher degree of interpenetration between the polymer chains and the QDs. This increases the depletion force between the polymer chains and the QDs because, with higher polymer R_g, the mobility of the QDs is reduced, effectively blocking the diffusion of QDs [7, 9 and 10]. It can be seen that the average size of the QDs aggregates increases with increasing R_g of the polymer; this is evidence of the effect of the M_w on depletion force interaction[161].

To sum up, the depletion force that causes the QD-poor domains in the surface morphology of the blend films could be partially controlled by changing the M_w of the host polymers. The specimens with a low polymer M_w showed smaller QD-poor domains than those with a higher M_w, indicating more miscibility. This means that reducing the M_w of the host polymers reduces the strength of the depletion force, resulting in smaller QD aggregations and better dispersion of QDs into the polymer matrices. The high viscosity of the blended films in the specimens that have a high polymer M_w prevents the making of spherical depletion zones because the viscosity makes the movements of the blend films slower, and this results in the QD-poor domains, which cannot be made in the short timescales take for spin coating (~ 30s).

4.3.3. GISAXS

GISAXS is a relatively new technique which provides insights into thin film nanostructure for samples, compared to conventional scattering methods such as light, neutron scattering and X-ray diffraction. GISAXS is an essential tool that offers representative information about the inner morphology of nanocomposite films and ideally complements high-resolution surface techniques such as AFM. In this experiment, this section is separated into solution scattering and thin film scattering. The solution scattering will show the dispersion state of the QDs in the nanocomposite solution as well as the QD core diameter. Thin film scattering will reveal the QDs dispersion state once the solvent is removed and the films solidify, in addition to interparticle separation and grain size.

4.3.3.1. Solution scattering

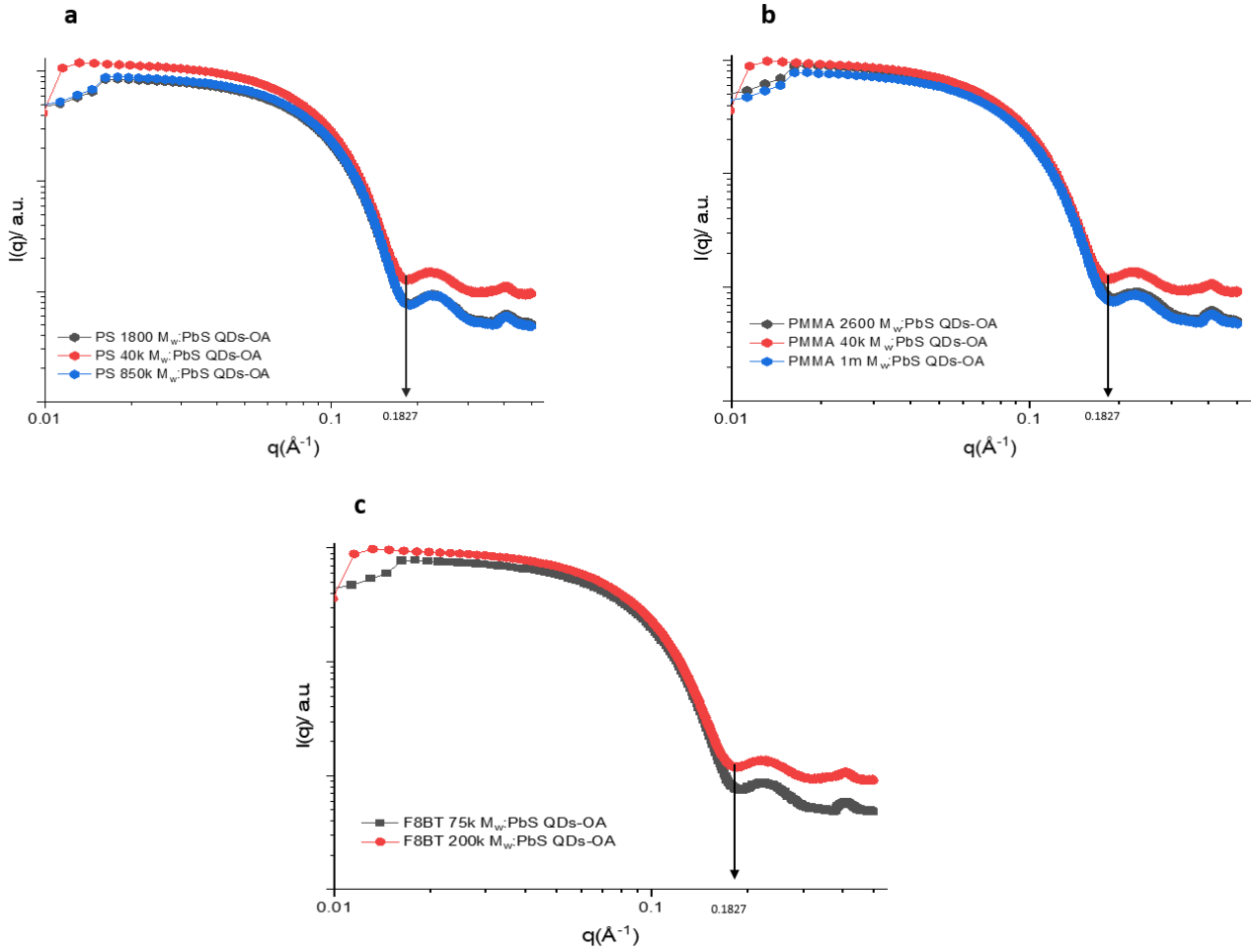

Figure 4.12/ Solutions scattering of the three systems with different host polymers M_w, (a) PS: PbS QDs-OA; (b) PMMA: PbS QDs-OA; (c) F8BT: PbS QDs-OA.

Figure 1.10 presents the solution scattering data of the three systems (PS, PMMA and F8BT). For each system, three different M_w of the host polymer were chosen (low-medium-high) except the F8BT system since only two other M_w are available. The solution scattering was used to measure PbS QDs-OA core size and examine the dispersion state of the QDs in the nanocomposite precursor solutions.

To predict the PbS QD-OA core radius, the q positions of the integrated data were used (as illustrated by arrows in Figure 4.12), and use the equation $\frac{4.49}{q}$ (. The q values in the samples are 0.1827 $Å^{-1}$ giving a core radius of the PbS QDs-OA about 24 Å. For further confirmation,

the data were fitted via Sas view ("core−shell sphere") with a hard-sphere form factor whose radius is bound to be the sum of the shell thickness and core radius. The high electron density of the PbS quantum dot (QD) cores (length density of the X-ray scattering, xSLD, of PbS for a Ga source, = 50.7 × 10−6 $Å^{-2}$) translates to an excellent contrast of X-ray with organic materials and solvents (e.g., xSLD toluene = 8.03 × 10−6 $Å^{-2}$) [144] [145]. This showed the same result of the QDs radius 24 Å (≃ 4.8nm) and polydispersity of 0.1, Figure 4.13.

The solution scattering results have shown that the PbS QDs-OA are well dispersed within the polymer matrices in the solution state with the presence of the solvent (Toluene); the absence of a peak of the structure factor-aggregation ≃ 0.1 $Å^{-1}$ demonstrates this. In the next section, the thin film blends will be examined after the solvent is evaporated and the films reach the glassy dry state.

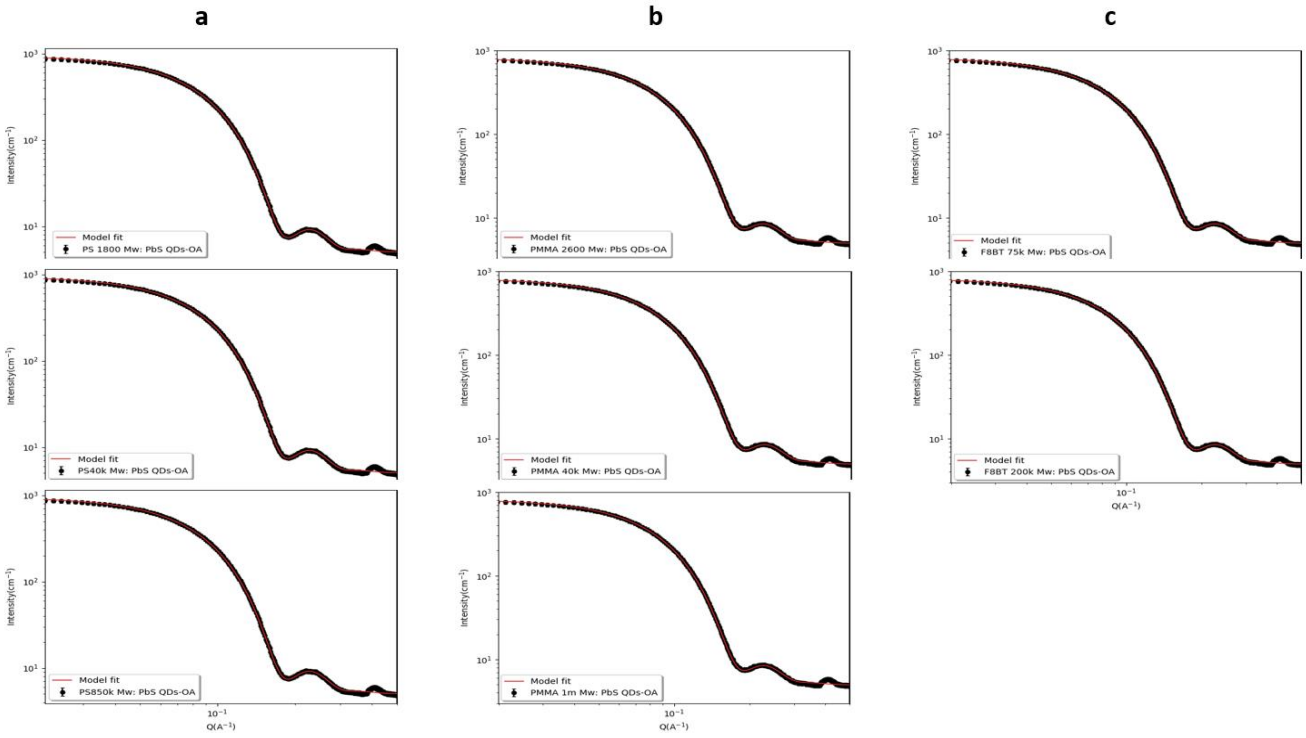

Figure 4.13/The SAS view fitting (core−shell sphere) of the solution scattering of the PS (a), PMMA (b) and F8BT (c): PbS QDs-OA nanocomposite films with a hard-sphere model represented by red lines.

4.3.3.2. Thin film scattering

The 2D reshaped GISAXS images of the blend films are shown in Figure 4.14, Figure 4.15 and Figure 4.16. The inner structure of the blend films is mixed randomly between the ordered surface layer and a disordered surface layer in the PS and PMMA systems, while the two samples in the F8BT system look similar. The specimens in the PS system, such as PS (50k M_w): PbS QDs-OA, PS (350k M_w): PbS QDs-OA, PS (1.5M M_w): PbS QDs-OA (Figure 4.14d, f and h respectively) display disordered structure or random orientation, while the other samples showed an ordered structure. The specimen of PMMA (1M M_w): PbS QDs-OA (Figure 4.15 f) is the only sample that showed a disordered structure in the PMMA system. The presence of disorder in the QD monolayer may explain the differences in intensity between the samples; qualitatively, the rod-type feature scattering was recognised as mainly a well-ordered monolayer with a degree of disorder.

The superlattice structure and orientations affect the ordered and disordered structures. Generally, the q spacing is consistent with the oriented pattern in the isotopically oriented samples, which suggests that all samples formed the same unit cell, the orientation of the unit cell has the closed packed (111) superlattice plane parallel to the substrate, still, the samples may vary in grain sizes, which could disrupt the unit cell orientation relative to the substrate [162, 163].

The films in the three systems show two continuous rings, one around q ~ 0.1 $Å^{-1}$ another faint ring around q ~ 0.2 $Å^{-1}$. From the two peaks positions, it is possible to identify the QDs aggregation morphology from the consecutive ratios of reciprocal Bragg spacing for the observed structure. Further, the morphology type could be estimated from GISAXS by comparing the observed reflection positions (d-spacing) with a given lattice characteristic [164-167]. The reflection positions show ratio $q_i/q_1 = 1, \sqrt{3}, \sqrt{4}, \sqrt{7}$ where q_i is the position of the reflection; these ratios are consistent with hexagonal closed-packed (HCP) packing compared with the reflection reference positions. So, the QDs aggregation in the blend films formed a (HCP) structure in all samples in this experiment (Figure 4.17).

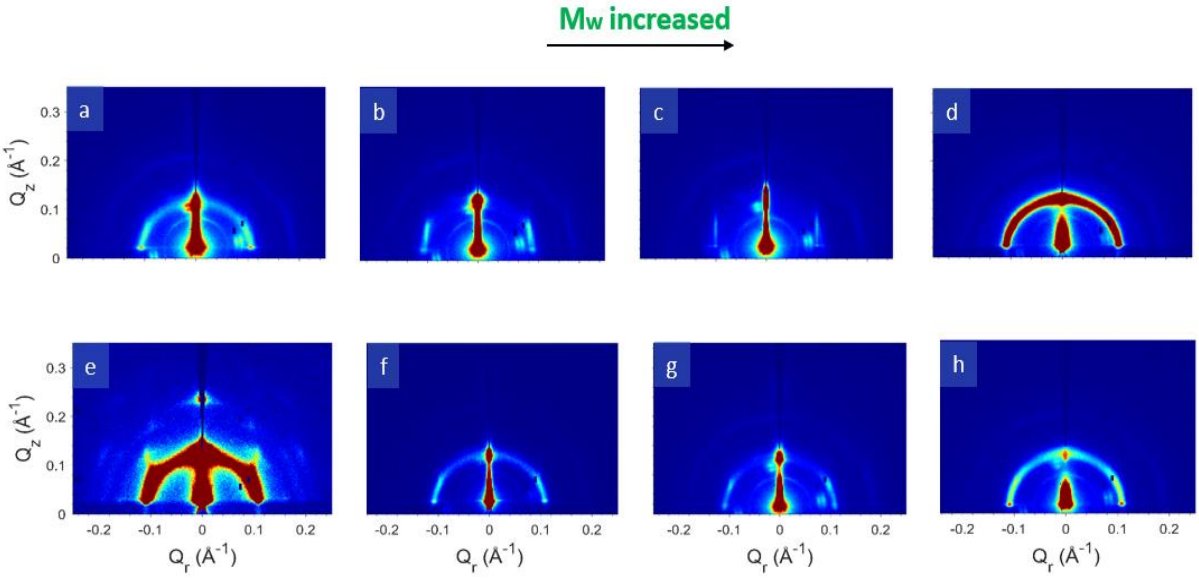

Figure 4.14/ 2D reshaped GISAXS images of the PS: PbS QDs-OA blend films. The samples have a range in PS M_W as follows: a)1800 b)7.5k c)40k d)50k e)89k f)350k g)850k h)1.5M.

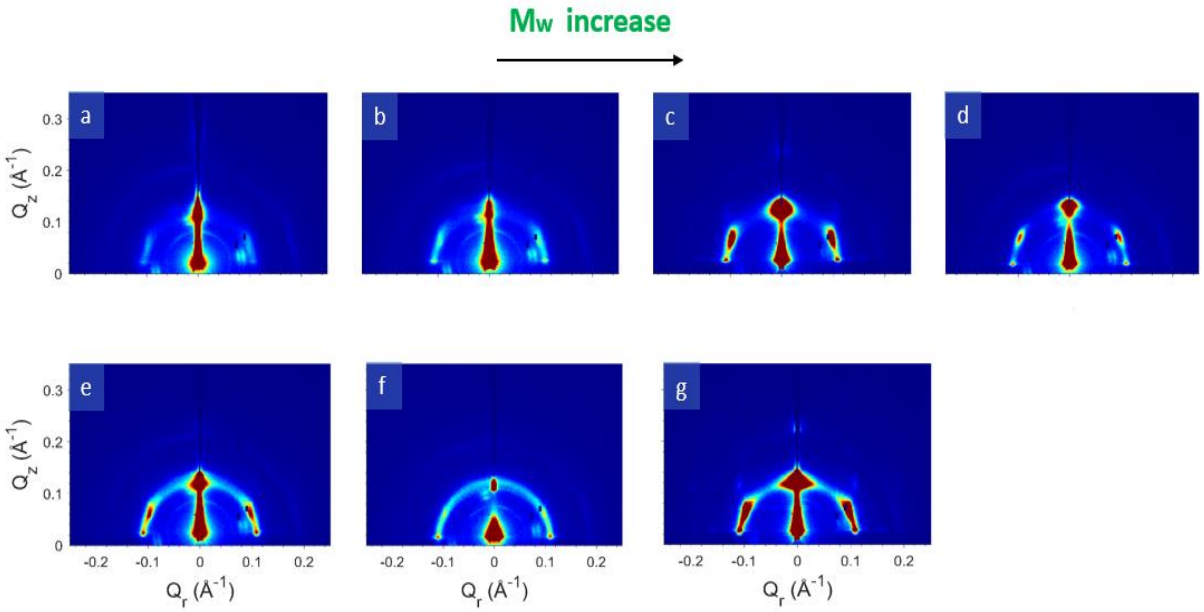

Figure 4.15/ 2D reshaped GISAXS images of the PMMA: PbS QDs-OA blend films. The samples have a range in PMMA M_W as follows: a)2600 b)8.4k c)40k d)50k e)350k f)1M g) 1.5M.

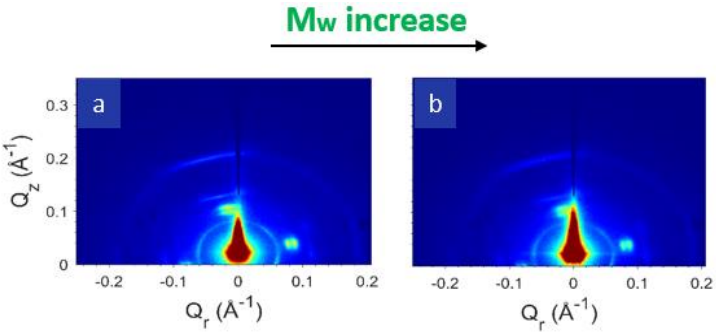

Figure 4.16/ 2D reshaped GISAXS images of the F8BT: PbS QDs-OA blend films. The difference between the samples is the F8BT M_w; a) 75k b) 200k.

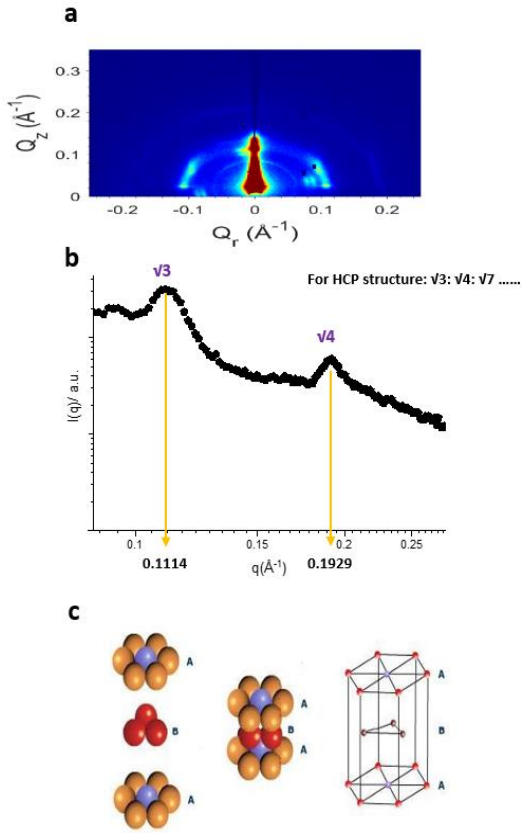

Figure 4.17/ PMMA 8.4k M_w: PbS QDs-OA film, (a) 2D reshaped GISAXS image of the film, (b)1D radially integrated GISAXS, (c) illustration of the HCP structure. The graph shows how to get the observed structure's aggregate structure from the consecutive reciprocal Bragg spacing ratio.

The data was radially integrated to gain further insight into the inner morphology and learn more about the dispersion state of the QDs in the nanocomposite films. The apparent peaks around 0.1 Å^{-1} were fitted in all the specimens to estimate the crystal grain size from the full-

width half maximum (FWHM) of the diffraction peaks using the Scherrer equation [168-172] (Figure 4.18).

$$D = \frac{2\pi K}{\Delta q} \qquad 4.2$$

Where D is the crystal grain size, K is the Scherrer constant, and Δq is the FWHM, the Scherrer constant for the spherical crystals is 0.94 [173]. This equation helps determine general trends and make internal comparisons. For a rough size estimation, it is sufficient to analyse just one peak. However, one must be cautious when interpreting data from samples with low diffraction quality because the physical parameters may differ significantly from the obtained values[174].

Looking into the QDs aggregations, the inter-particle separation refers to the distance between particles in a given system, the inter-particle separation for the PS: PbS QDs-OA, PMMA: PbS QDs-OA and F8BT: PbS QDs-OA aggregates were calculated, first obtaining the centre-to-centre distance of the QDs from the q values at the peak centre and applying d = 2π/q, then, subtracting the core diameter of the QDs (48Å) from the obtained centre-to-centre distance (Figure 4.20), and this data including grains size are presented in Table 8.1, Table 8.2 and Table 8.3 in the Appendix.

The grains size that form from (PS: PbS QDs-OA), (PMMA: PbS QDs-OA) and (F8BT: PbS QDs-OA) blend films range between 37-56nm, 35-59nm and 52-62 nm, respectively, around 7 to 13 times bigger than the core diameter of the PbS QDs-OA (~ 4.8nm), and this is indicating to that the PbS QDs-OA become aggregated during the drying process as the solvent is evaporated.

The M_w of the host polymer affects the inner morphology of the blend films; changing the polymer M_w affects the grain size and the interparticle separation, as seen in Table 8.1, Table 8.2, Table 8.3 (in the Appendix) and in Figure 4.21. The aggregation grain size increased with increasing the host polymer M_w in all three systems; for instance, the grain size in the specimen of PS (1800 M_w): PbS QDs-OA is 37nm, and this increased to 56nm in a specimen of PS (1.5M M_w): PbS QDs-OA which has the highest polymer M_w in PS system. Similarly, the grain size in the lowest M_w polymer (2600 M_w) in the PMMA system is 35nm; this keeps

increasing to reach 59nm at the highest M_w of the PMMA polymer (1.5M M_w), which is illustrated in Figure 4.21.

To look into the aggregation, the interparticle separation has slight changes in (PS: PbS QDs-OA) and (F8BT: PbS QDs-OA) systems, where it ranges between 8-9 Å, while it is 8 Å in all samples of PMMA: PbS QDs-OA system.

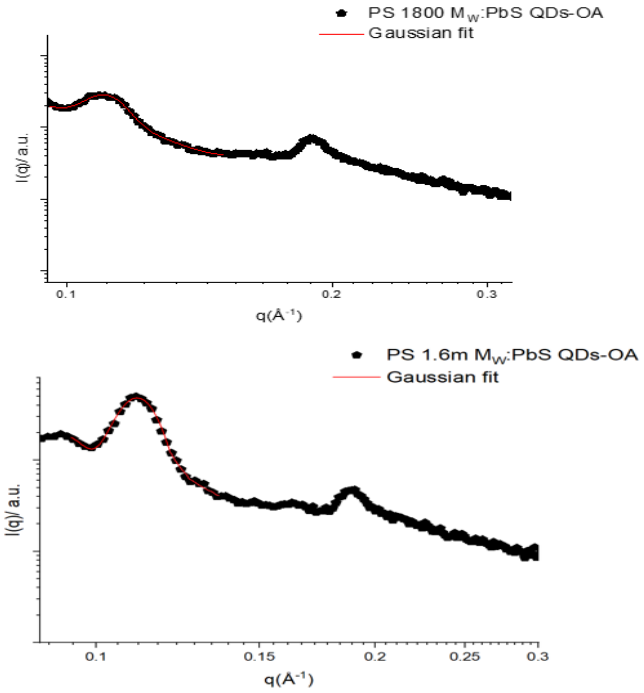

Figure 4.18/ radially integrated GISAXS data of PS 1800 M_w: PbS QDs-OA and PS 1.6m M_w: PbS QDs-OA, an example of the PS system integrated data. This shows the difference in the aggregation's peaks when the PS M_w was altered.

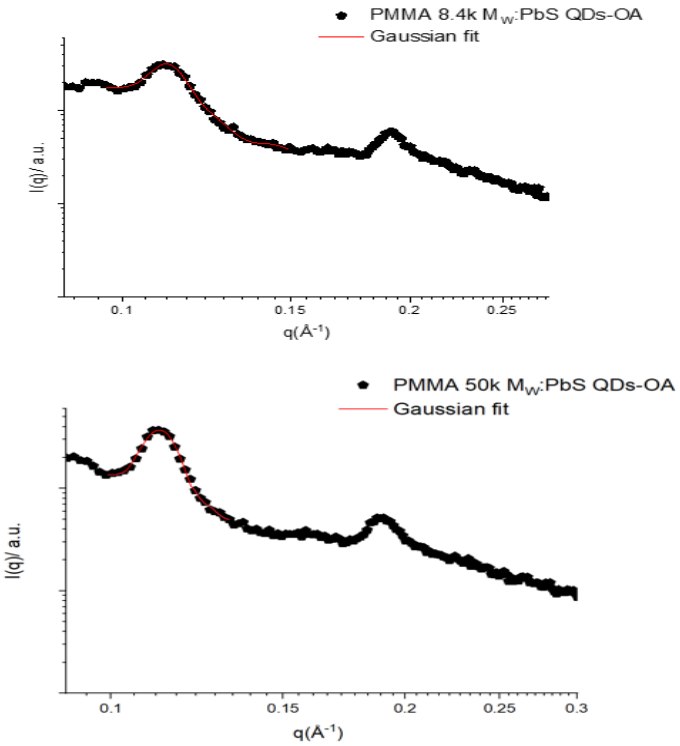

Figure 4.19/ radially integrated GISAXS data of PMMA 8.4k M_w: PbS QDs-OA and PMMA 350k M_w: PbS QDs-OA, an example of the PMMA system integrated data. Also, this shows the difference in the aggregation's peaks when the PMMA M_w increased.

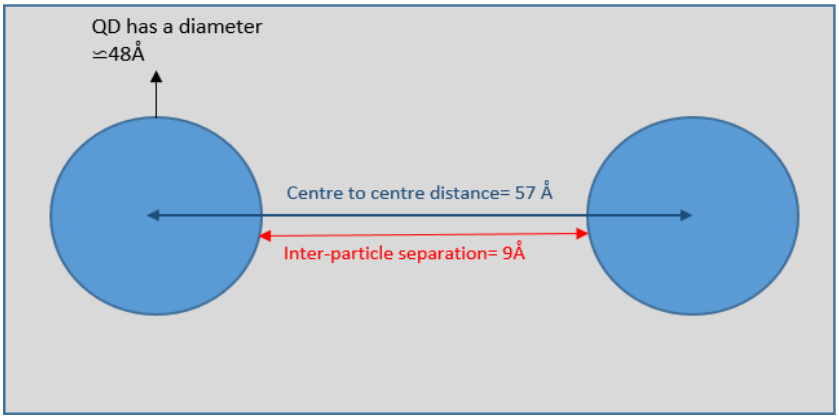

Figure 4.20/ schematic drawing illustrating the parameters from GISAXS that provide the interparticle separation.

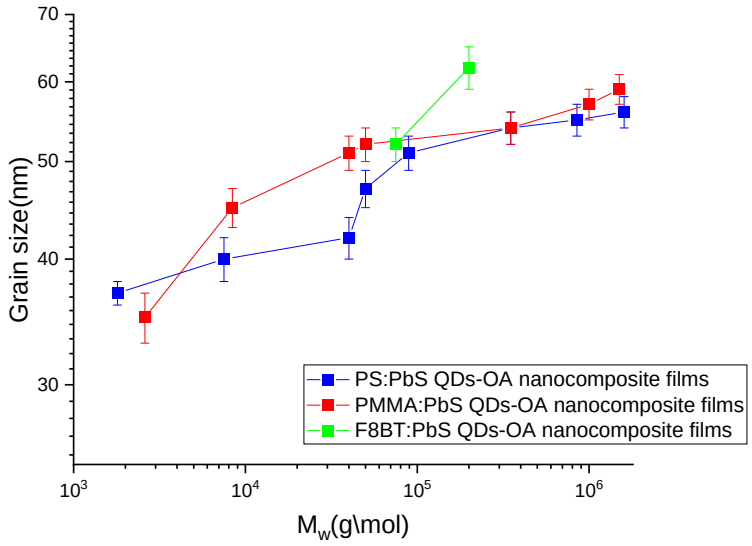

Figure 4.21/Effect of polymer M_w on the grain size in blends films in PS: PbS QDs-OA, PMMA: PbS QDs-OA and F8BT: PbS QDs-OA systems. A relationship appeared between the polymer M_w and the PbS QDs-OA aggregations; the grain size increased as the host polymer M_w increased.

So, increasing the Polymer M_w increases the size of the PbS QDs-OA aggregates and changes the interparticle separation; the relationship between QDs aggregation in polymer matrices and host polymer M_w is complex and depends on several factors, such as the nature of the polymer and QDs as well as the processing conditions used. In this experiment, the increase in the PbS QD-OA aggregation with polymer M_w (Figure 4.21) is believed to be due to increasing the depletion interaction as the polymer M_w increased, as mentioned in the AFM section.

So, changing the host polymer M_w affects the surface morphology of the blend films and the inner morphology. Varying the polymer M_w affects the depletion force that causes the QDs aggregations; increasing polymer M_w increases the depletion amount, which leads to larger grain sizes (QDs aggregation). Raising the M_w of polymers means bigger polymer R_g, as seen in Figure 4.10. The size of the depletion interaction correlates to the solution osmotic pressure, with an amount of the order of the macromolecular size indicating that the depletion layer

thickness is about R_g. The sets of attraction thus get determined by the size of the polymer molecules (colloidal and protein limited)[81]. Also, increasing polymer R_g reduces the space for the QDs to fit in. This has a greater ability to increase the range and scale of the depletion force, leading to a stronger depletion interaction between the QDs.

The QD-poor domains seen in the AFM and the grain size found by GISAXS showed similar behaviour, both increased with increasing polymer M_w. However, the sizes are different; the depletion zones in the AFM are much bigger, perhaps because of the differences in the surface morphology from the bulk, resulting in these size differences (Figure 4.22). Moreover, the QDs aggregation could be influenced not only by the intermolecular interactions between the polymer chains and QDs explained above but also via the growing polymer crystal front to either QDs drive expulsion "impurities" or distort in the case of occlusion QDs [175]. The polymer crystal could be bigger in the polymer with higher M_w and then bigger R_g, resulting in a bigger aggregation of the QDs [8].

Some factors determine the interparticle separation, including the interaction type between QDs and the polymer chains, solvent nature, and the QDs size. The slight changes in the interparticle separation in the (PS: PbS QDs-OA) and (F8BT: PbS QDs-OA) systems and the 8 Å in (PMMA: PbS QDs-OA) system in this experiment are probably due to either the ligands being tilted or partially interdigitated in neighbouring QDs because it is lower than the extended length of the ligands[176]. The extended length of the ligands is represented by the number of carbons in the ligands, which is 18 carbons in the Oleic Acid (OA). So, from to have no ligands interdigitating between the QDs, it needs to have an interparticle separation around 36 Å (3.6nm); in other words, two full ligands length between two QDs (one from each), which is not the situation in this experiment (Figure 4.23)[163].

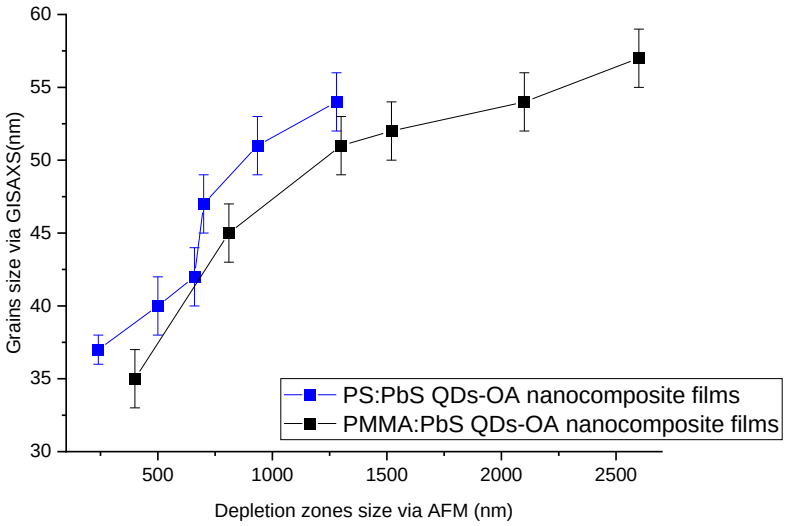

Figure 4.22/ Grain size found via GISAXS vs average depletion diameter found via AFM for PS and PMMA systems, same behaviour but a different size. (The F8BT system is not included in this graph because only one sample from the two studies showed a depletion zone).

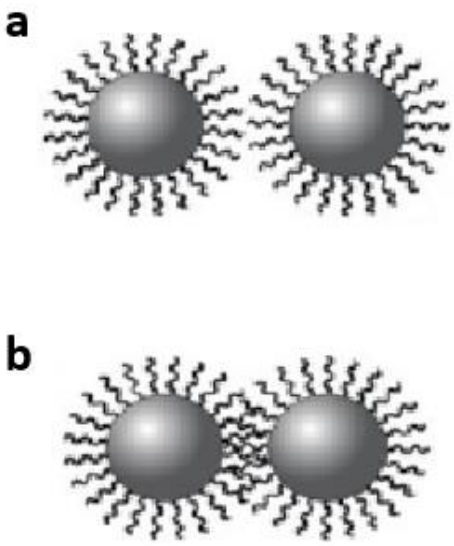

Figure 4.23/ Sketch illustrates the difference in the interparticle separation due to the state of the ligands: (a) complete interparticle separation between the neighbouring QDs (two full ligands length), (b) the interparticle separation decreased because the ligands interdigitating between the neighbouring QDs, which I believe this is the case in this experiment.

4.4. Conclusion

The effect of polymer M_w on the final morphology of the nanocomposite films of PS, PMMA and F8BT when blended with PbS QDs-OA was investigated in this experiment. The results indicated that the film thickness, which was measured via ellipsometry, increased with the M_w of the host polymer. This is due to the viscosity increase as the polymer M_w increases viscosity, determining the slower thinning during spin coating.

AFM was used to probe the surface topography of the blended films; the results showed some domains on the surface of the films, which are believed to be QDs-poor domains. The average diameter of the QDs-rich domains size increased as the polymer M_w increased; for example, it is around 240 nm in PS (1800 M_w): PbS QDs-OA, which grew to 1280 nm in PS (350k M_w): PbS QDs-OA. Another example is the average diameter of the QDs-rich domains in a specimen of PMMA (2600 M_w): PbS QDs-OA is around 280 nm, which grows to 2600 nm in PMMA (1m Mw): PbS QDs-OA. Interestingly, the specimen that has high polymer M_w, such as PS (850k and 1.6m M_w), PMMA (1.5m Mw) and F8BT (200k M_w): PbS QDs-OA showed no QDs-rich domains, which is probably because of the high viscosity that makes the movements of the components slower and cannot form in the short timescale of spin coating (30s).

The inner structure was investigated via GISAXS by fitting the peaks around 0.1 $Å^{-1}$. It was found that the PbS QDs-OA aggregated where the grain size is 7-13 times the core diameter of the PbS QDs-OA (4.8 nm) in all three systems. The grain size increases with polymer M_w for all the specimens in this experiment. This could be due to many factors, but in this experiment, I think this may be due to increasing the depletion interaction with M_w of the host polymer. The aggregation crystal structure was estimated from the observed reflection positions (d-spacing); the reflection positions of the peaks show a ratio $q_i/q_1 = 1, \sqrt{3}, \sqrt{4}, \sqrt{7}$, consistent with a hexagonal closed-packed (HCP) structure.

Finally, the depletion force that causes the QDs Aggregations could be partially controlled by changing the M_w of the polymer host. This means that reducing the M_w of the host polymers reduces the depletion force, resulting in smaller QD aggregates and better dispersion of QDs into the polymer matrices. The specimens with a low M_w showed better miscibility between

the polymer chains and the QDs, as they have smaller QDs-poor domains and smaller grain sizes than those with a higher M_w. Even though, the main aim of the project which is to disperse the QDs to the polymer matrix is not fully reached in this chapter. This means that more effort is needed to solve this issue.

Chapter 5

Impact of ligand exchange on the nanocomposite film morphology of Lead Sulphide quantum dots and polymer matrix

5.1. Introduction

The last chapter showed that the cohesive forces that cause the QDs aggregation, which happens when QDs are incorporated into polymer matrices, can be partially controlled by varying the host polymer M_w. However, this did not reach the dispersed within the polymer matrix, which is the project's main objective.

Even though OA ligands have been mentioned as being the optimum ligands for the synthesis process, where they stabilise the QDs by controlling the shape and size of the QDs, preventing the QDs from aggregation in organic solvents [57, 61], it has also been mentioned that in the case of QD/QD and QD/polymer interactions could be modified with different ligands for better QDs dispersion and interaction with the surroundings, where the OA ligands often prevent this from happening due to the insulating nature of them, which end with structural issues, such as aggregation or phase separation of the components.

So, in this chapter, the strategy has changed from trying to control the cohesive forces to changing the chemistry between QDs and the polymer chains by adjusting the QDs ligands besides trying to control the cohesive force. So, instead of the native ligands (OA), Hexanoic acid (HA) and Decanoic acid (DA), which are both shorter-length chains than the native ligands (OA) and also belong to the carboxylic acid group, will be used in this experiment. The ligands exchange approach is employed to control the QDs surface chemistry by adjusting the length of the ligand and hence the polymer: QDs self-assembly, switching the nature of the QDs from the OA (native ligands) to (HA and DA) (Figure 5.1).

Successfully modifying the QDs surface chemistry approach by utilising ligands chemically similar to the host polymer could help achieve good QDs dispersibility into the polymer matrices, which was demonstrated before [177, 178].

5.2. Experimental methods

This experiment used three different M_w of the PS and PMMA (low-medium-high) and the two M_w of F8BT that were available, as presented in Table 5.1. The Hexanoic Acid (HA) and Decanoic Acid (DA) were purchased from (Sigma- Aldrich) and have been used as received without any further purification.

Samples preparations and the use of the instruments (Ellipsometry, AFM, and GISAXS) have been explained in detail previously in this thesis.

Polymer	supplier	M_w (g/mol)	M_n (g/mol)	PDI (M_w/ M_n)
PS	Polymer source	1,800	1600	1.13
PS	Sigma-Aldrich	40,000	39,000	1.02
PS	Polymer source	850,000	790,000	1.08
PMMA	Polymer source	2,600	2,500	1.09
PMMA	Polymer source	40,000	36,363	1.10
PMMA	Polymer source	1,000,000	666,666	1.5
F8BT	Sigma-Aldrich	75,000	72,815	1.03
F8BT	Sigma-Aldrich	200,000	192,307	1.04

Table 5.1/ The host polymers that were chosen in this experiment.

substance	**empirical formula**	**Density (g/cm^3)**	**Melting temperature (^oC)**	**Boiling temperature (^oC)**
Hexanoic Acid	$C_6H_{12}O_2$	0.93	-3.4	205
Decanoic Acid	$C_{10}H_{20}O_2$	0.89	31.6	269

Table 5.2/ some important properties of the ligands used in this experiment.

substance	Volume fraction(ϕ)	Volume percentage (%)
PbS-(HA-DA)	0.0024	0.24
PS	0.021	2.1
PMMA	0.018	1.8
F8BT	0.021	2.1

Table 5.3/ the volume percentage and volume fraction of the nanocomposites. The initial weight fraction of PS: PbS QD-OA nanocomposite is (0.24% QDs, 2.1% PS and 97.66% toluene), the initial weight fraction of PMMA: PbS –OA nanocomposite (0.24% QDs, 2.04% PMMA and 97.72 % toluene) and the initial weight fraction of F8BT: PbS –OA nanocomposite (0.24% QDs, 2.1% F8BT and 97.66% toluene).

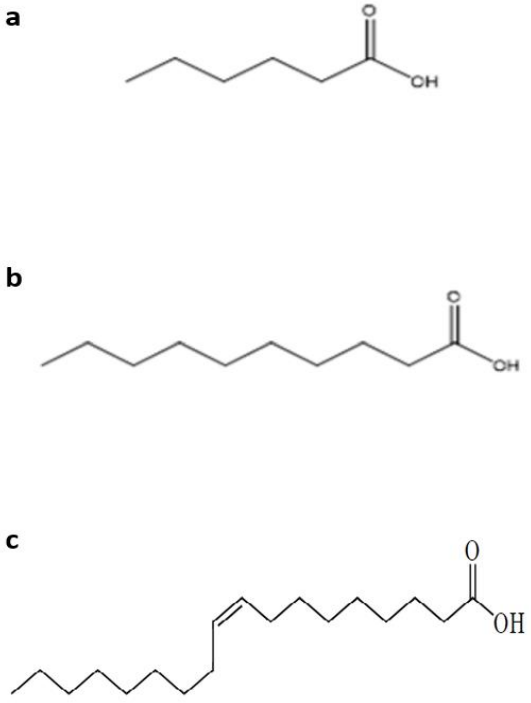

Figure 5.1/ Schematic structure of the (a) Hexanoic Acid (HA), (b) Decanoic Acid (DA), and (c) Oleic Acid (OA) all have a similar structure, but they differ in chains length, where HA has six carbon, DA has ten carbon and OA has 18 carbons.

5.2.1. Ligands exchange from OA to HA and DA

A 2 molar excess of Hexanoic Acid (HA) and Decanoic Acid (DA) was added to the PbS QDs-OA (10 mg ml^{-1} in toluene) based on an estimated PbS: OA mass balance of 1:1:21 and left for 48 h. Then acetone (20 ml) was added to precipitate the nanocrystals of PbS (HA and DA); the mixtures were centrifuged for 20 min at 12,000 rpm and 20 C°, after that the supernatant was removed, and the QDs residue re-dispersed in toluene (1 mL). The

purification process cycles (dispersion/ precipitation/ centrifugation) were repeated three times, and the QDs were re-dispersed in toluene for final dispersion and storage.

This method has been used before by Daniel T. W. Toolan and Michael P. Weir [176]; in this work, they demonstrated how modified QD self-assemble with TIPS-Tc to produce hybridised QD/TIPS-Tc nanocomposite materials, where the QD dispersion is controlled using the QD ligand. It is possible to direct self-assembly at length scales ranging from nanometres to microns by controlling QD ligand chemistry, resulting in materials with potential applications in solar energy conversion materials where well-dispersed QD nanostructures are desired, but also in thermoelectric and QD semiconducting devices where linked QD nanomorphologies are helpful.

5.3. Results and Discussion

5.3.1. Ellipsometry

Like the last chapter, the film thicknesses of the PS, PMMA, and F8BT blend systems were measured via ellipsometry. The blend film thickness ranged between 69-216nm, 86-142nm, and 91-156nm for PS, PMMA, and F8BT systems, as presented in Tables 1.3, 1.4, 1.5, and Figure 5.2. Also, similar behaviour of the samples, as seen in the last chapter, was noticed here; the thickness of the nanocomposite films increased as the polymer M_w increased. Nevertheless, the blend film thicknesses are lower with the (HA and DA) ligands compared to the film thickness with the native ligands (OA), where they ranged between 101-321nm, 136-389nm, and 205-249nm for PS, PMMA, and F8BT systems, respectively, as seen in the last chapter.

Changing the PbS QDs Ligands from the native ligands (OA) to the ligands of (HA and DA) affects their chemical properties and interactions with the polymer matrices. It was noticed that the viscosity of the nanocomposite solutions decreased with HA and DA ligands compared to the solution with OA ligands. The HA and DA ligands have shorter chain lengths than the OA ligands, as seen in Figure 5.1; this leads to a decrease in the QDs size (core + shell), which changed the volume fractions of the QDs, resulting in lower viscosity of

the solution with HA and DA ligands compared the solution with OA ligands, as seen from this equation.

$$\eta = \eta o(1 + 2.5\phi) \qquad 5.1$$

Where η is the viscosity, ηo is the viscosity of the dispersing liquid and ϕ is the volume fraction of QD [70]. This affects the thickness of the films by decreasing them compared to the films with long-length ligands (OA), as seen in Table 5.4, Table 5.5, Table 5.6 and Figure 5.2. Also, the thickness of the nanocomposite films increased with increases in the polymers M_w, as shown in Figure 5.2. The influence of the host polymer M_w has been explained previously in this thesis.

Films	Thickness (nm)	Error bar (nm)
PS(1800 Mw)+PbS QDs-HA	69	± 3
PS(1800 Mw)+PbS QDs-DA	75	± 3
PS(1800 Mw)+PbS QDs-OA	101	± 3
PS(40k Mw)+PbS QDs-HA	201	± 4
PS(40k Mw)+PbS QDs-DA	203	± 5
PS(40k Mw)+PbS QDs-OA	211	±2
PS(850k Mw)+PbS QDs-HA	209	± 5
PS(850kMw)+PbS QDs-DA	216	± 5
PS(850kMw)+PbS QDs-OA	291	±2

Table 5.4/ thicknesses of the PS system samples. The data of films with OA ligands are taken from Chapter 4 for comparison.

Films	Thickness (nm)	Error bar (nm)
PMMA(2600 Mw)+PbS QDs-HA	86	± 4
PMMA(2600 Mw)+PbS QDs-DA	93	± 4
PMMA(2600 Mw)+PbS QDs-OA	136	± 1
PMMA(40k Mw)+PbS QDs-HA	113	± 4
PMMA(40k Mw)+PbS QDs-DA	103	± 5
PMMA(40k Mw)+PbS QDs-OA	194	± 3
PMMA(1M Mw)+PbS QDs-HA	122	± 5

PMMA(1M Mw)+PbS QDs-DA	142	± 4
PMMA(1M Mw)+PbS QDs-OA	340	± 3

Table 5.5/ thicknesses of the PMMA system samples. The data of films with OA ligands are taken from Chapter 4 for comparison.

Films	Thickness (nm)	Error bar (nm)
F8BT(75k Mw)+PbS QDs-HA	91	± 4
F8BT(75k Mw)+PbS QDs-DA	80	± 3
F8BT(75k Mw)+PbS QDs-OA	205	± 3
F8BT(200k Mw)+PbS QDs-HA	145	± 6
F8BT(200k Mw)+PbS QDs-DA	156	± 5
F8BT(200k Mw)+PbS QDs-OA	249	± 2

Table 5.6/ thicknesses of the F8BT system samples. The data of films with OA ligands are taken from Chapter 4 for comparison.

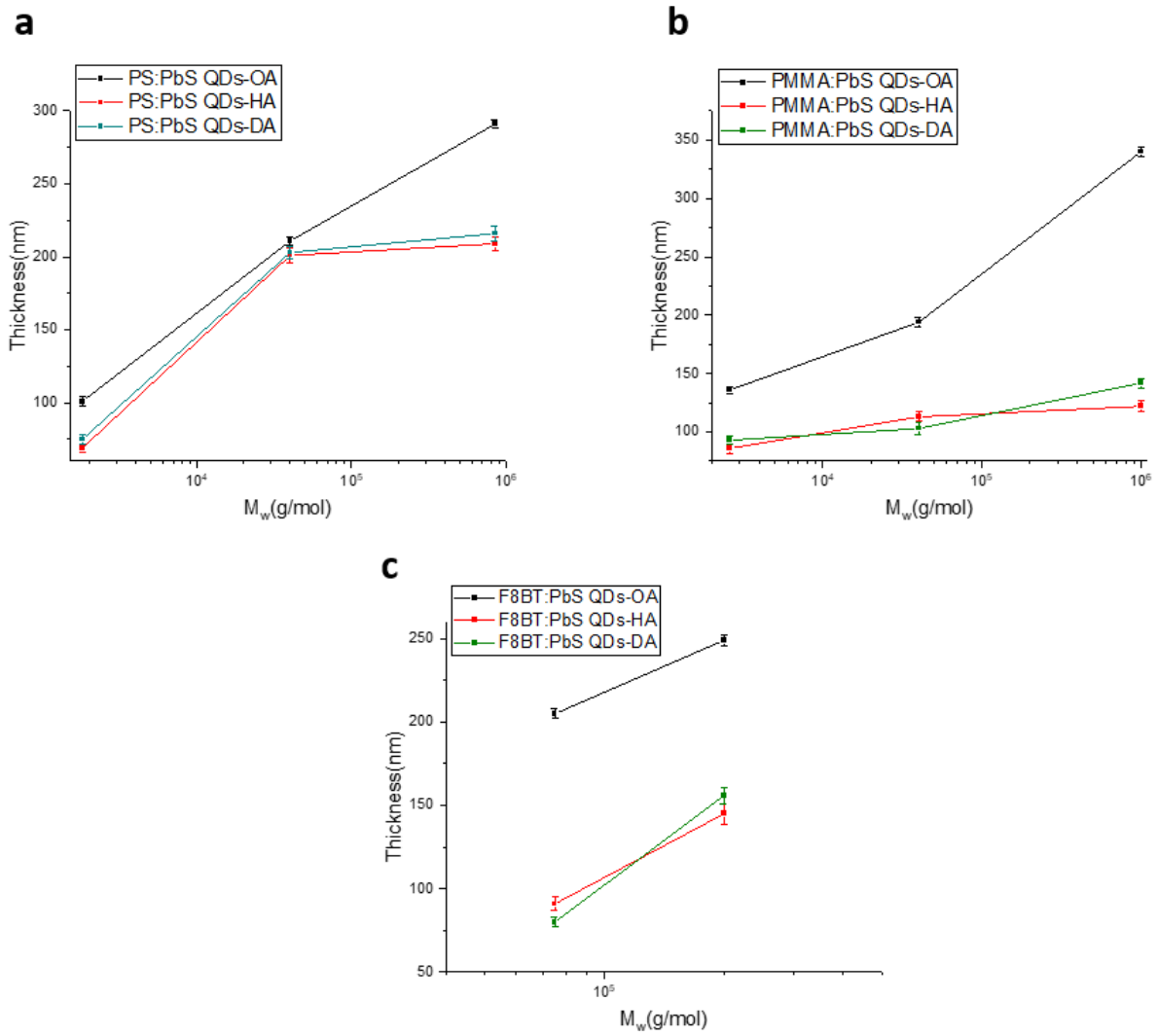

Figure 5.2/The effect of the host polymer M_w and the ligands changed on the blend film thicknesses; (a) PS system, (b) PMMA system, (c) F8BT system (The data of films with OA ligands are taken from Chapter 4 for comparison).

5.3.2. AFM

The surface morphology images of PS: PbS QDs-(HA-DA), PMMA: PbS QDs-(HA-DA), and F8BT: PbS QDs-(HA-DA) blends films are shown in Figure 5.3, Figure 5.4 and Figure 5.5, respectively. Several surface morphological changes were noted between the blend films, such as the size and shape of the QD-poor domains. The average QDs-rich domains diameter was calculated similarly to the last chapter, and the values are presented in Table 5.7, Table 5.8 and Table 5.9.

It has been seen in Chapter 4 that a QD-poor domain and cracks formed in the surface morphology of the nanocomposite films that consist of polymer (PS-PMMA-F8BT) mixed with PbS QDs-OA. The QDs-rich domains increase in size with an increase in the host polymer M_w due to a rise in the depletion force that causes the formation of QDs-rich domains in the surface morphology. The films with high M_w of the host polymer, such as PS (850k M_w): PbS QDs-OA, PS (1.5M M_w): PbS QDs-OA, PMMA (1.5M M_w): PbS QDs-OA and F8BT (200k M_w): PbS QDs-OA form cracks and this related to the higher viscosity of these solutions which slow down the components movement upon drying

In this experiment, similar behaviour was shown by the PS system where the QDs-rich domains form in the surface morphology of the blend films. These domains are increased with the increase in the M_w of the PS, as seen in Figure 5.3. Compared to nanocomposite films with OA ligands seen in Chapter 4, QDs-rich domains are smaller in size in the films with HA and DA (Figure 5.7). Also, the film of PS (850k M_w): PbS QDs-OA showed cracks on surface morphology; this changed when the ligands changed to HA and DA to form QDs-rich domains.

The average QDs-rich domains diameter is 120nm in the sample of PS (1800 M_w): PbS QDs-HA (Figure 5.3 a); this increased to 250nm and 550nm in the PS (40k M_w): PbS QDs-HA and PS (850kM_w): PbS QDs-HA (Figure 5.3 c, d) respectively. Similar behaviour was noted in the same samples with different QDs ligands (DA); the average QDs-rich domains diameter in the sample of PS (1800 M_w): PbS QDs-DA (Figure 5.3 b) is 130nm, and this extended to 230nm and 520nm in samples of PS (40K M_w): PbS QDs-DA and PS (850K M_w): PbS QDs-DA (Figure 5.3 d, f).

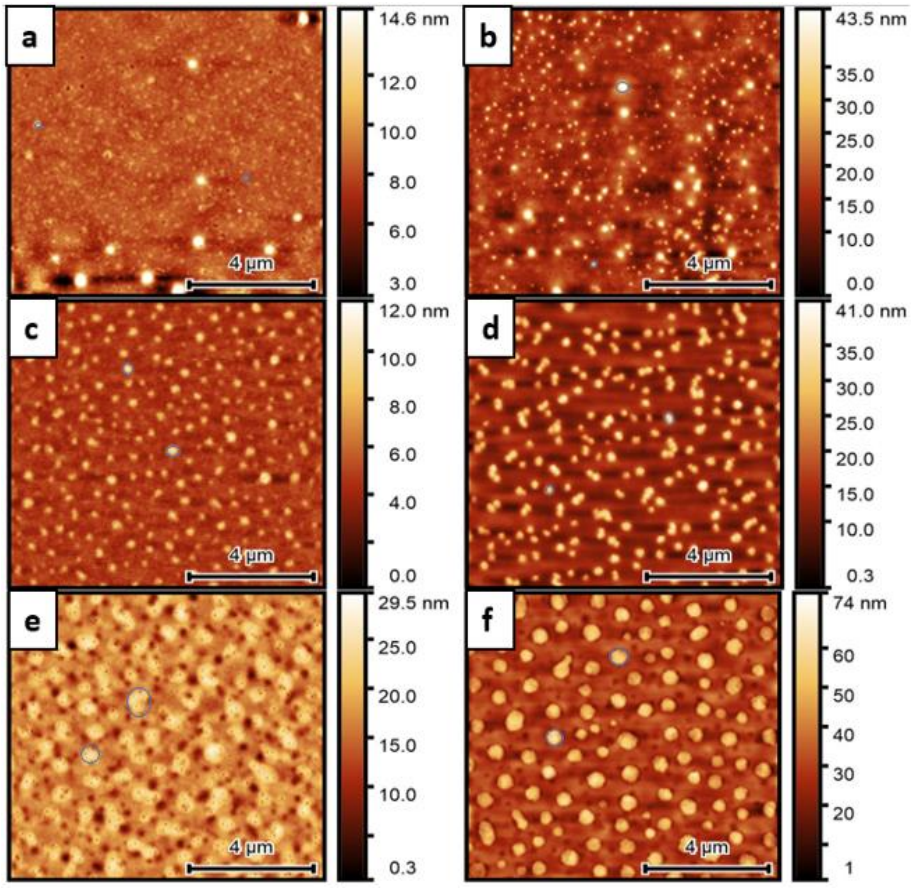

Figure 5.3/ *AFM images of the PS: PbS QDs nanocomposite films, the samples differ in QDs ligands and Polymer Mw as follows: a) PS(1800 Mw): PbS QDs-HA; b) PS(1800 Mw): PbS QDs-DA; c) PS(40k Mw): PbS QDs-HA; d) PS (40k Mw): PbS QDs-DA; e) PS(850k Mw): PbS QDs-HA; f) PS(850k Mw):PbS QDs-DA.(scan size is 10µm for all samples).*

The films in the PMMA system show QDs-rich domains that increase with the M_w of PMMA except films of PMMA (1M M_w): PbS QDs-HA and PMMA (1M M_w): PbS QDs-DA, where they do not form spherical QDs-rich domains, as seen in Figure 5.4 e and f. The QDs-rich domains are smaller in size in the films with HA and DA ligands than in those with OA ligands seen in Chapter 4, as seen in Figure 5.7.

The PMMA: PbS QDs films show similar morphological changes to the behaviour seen in the PS: PbS QDs films, albeit with some differences; the blend films show some QDs-rich domains in the surface morphology, which increased with the PMMA M_w. However, the QDs-rich domains in PMMA (1M M_w): PbS QDs-HA and PMMA (1M M_w): PbS QDs-DA (Figure 5.4 e, f) do not form a spherical shape, so their diameter could not be calculated, instead, the films show two different distinct layers, which indicate a phase segregated

occurred in their surface morphology. The average QDs-rich domains diameter in the PMMA (2600 M_w): PbS QDs-HA (Figure 5.4 a) film is 180nm, while it is 830nm in the film of PMMA (40K M_w): PbS QDs-HA (Figure 5.4 c). This was also noted with the same samples with (DA) ligands: PMMA (2600 M_w): PbS QDs-DA and PMMA (40K M_w): PbS QDs-DA (Figure 5.4b, d), where the QDs-rich domains are 185nm and 678nm, respectively.

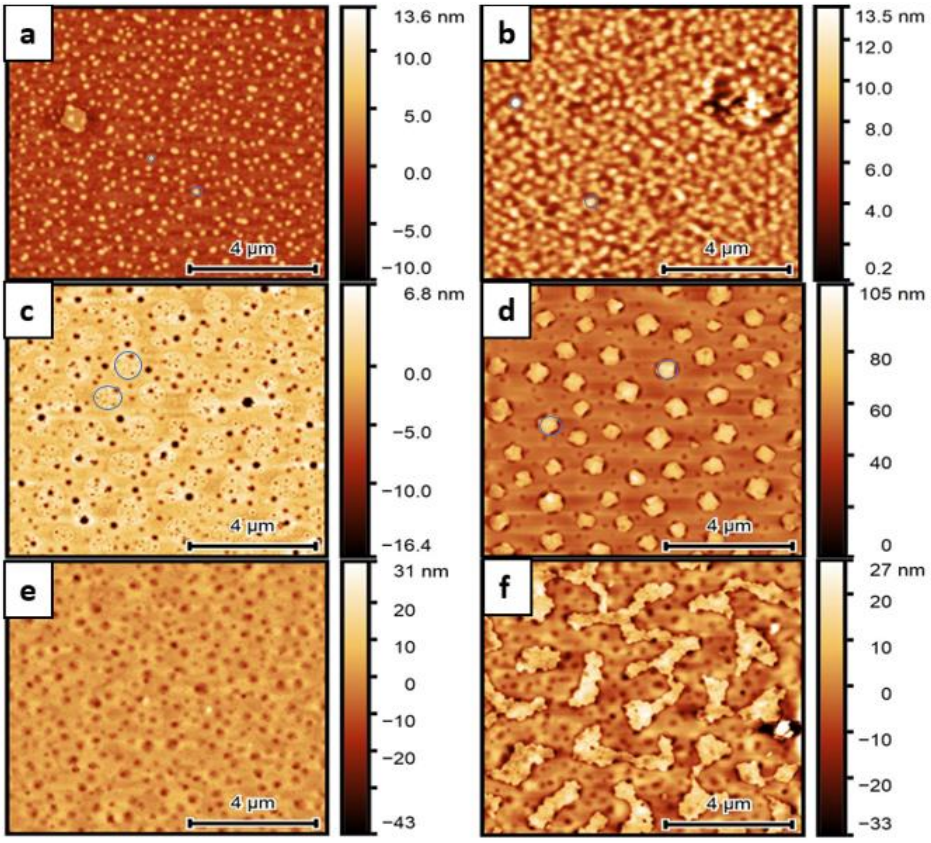

Figure 5.4/ AFM images of the PMMA: PbS QDs nanocomposite films; also, the films differ in the QDs ligands and polymer Mw as follows: a) PMMA(2600 Mw): PbS QDs-HA; b)PMMA(2600 Mw): PbS QDs-DA; c)PMMA(40k Mw): PbS QDs-HA ; d)PMMA(40k Mw): PbS QDs-DA; e)PMMA (1M Mw): PbS QDs-HA; f)PMMA(1M Mw): PbS QDs-DA. (Scan size is 10µm for all samples).

Figure 5.5 shows the surface structure of the blend films in the F8BT system. There are some holes in the surface of F8BT (75k M_w): PbS QDs-HA and F8BT (75k M_w): PbS QDs-DA films, while the films of F8BT (200k M_w): PbS QDs-HA and F8BT (200k M_w): PbS QDs-DA show flat planar surface. This is different compared to films with OA ligands where the surface F8BT (75k M_w): PbS QDs-OA show QDs-rich domains and the film of F8BT (200k M_w): PbS QDs-OA show cracks.

So, the F8BT system exhibits dark holes or spots in the surface films that have an average diameter reaching 175nm for F8BT (75k M_w): PbS QDs-HA film (Figure 5.5 a), while it is 180nm in F8BT (75k M_w): PbS QDs-DA film (Figure 5.5 b). The blend films of F8BT (200k M_w): PbS QDs-HA and F8BT (200k M_w): PbS QDs-DA show no QDs-rich domains or cracks. Instead, they show flat planar structures without any further details.

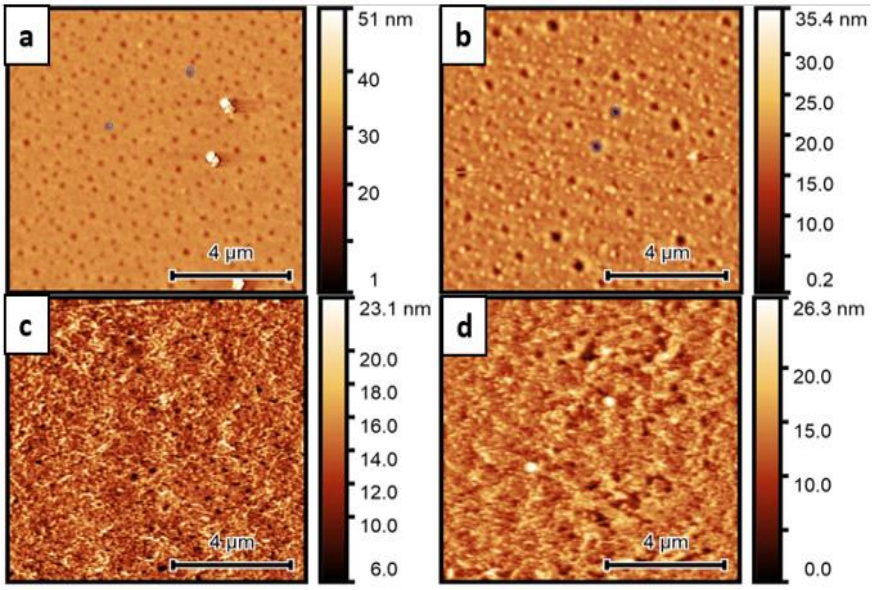

Figure 5.5/ AFM images of F8BT: PbS QDs nanocomposite films, a)F8BT(75k M_w): PbS QDs-HA ; b)F8BT(75k M_w): PbS QDs-DA ; c)F8BT(200k M_w): PbS QDs-HA ; d)F8BT(200k M_w): PbS QDs-DA.

Samples	The average diameter of **QD-rich domains** (nm)
PS(1800 Mw): PbS QDs-HA	120
PS(1800 Mw): PbS QDs-DA	130
PS(40K Mw): PbS QDs-HA	250
PS(40K Mw): PbS QDs-DA	230
PS(850K Mw): PbS QDs-HA	550
PS(850K Mw): PbS QDs-DA	520

Table 5.7/The average diameter of the QDs-rich domains in PS: PbS QDs nanocomposite films with different ligands and polymer M_w.

Samples	The average diameter of the **QD-rich domains** (nm)
PMMA(2600 Mw): PbS QDs-HA	180
PMMA(2600 Mw): PbS QDs-DA	185

PMMA(40K Mw): PbS QDs-HA	830
PMMA(40K Mw): PbS QDs-DA	678
PMMA(1M Mw): PbS QDs-HA	----
PMMA(1M Mw): PbS QDs-DA	----

Table 5.8/The average diameter of the QD-rich domains in PMMA: PbS QDs nanocomposite films with different ligands and polymer M_w.

Samples	The average diameter of the **QD-rich domains** (nm)
F8BT(75k Mw): PbS QDs-HA	175
F8BT(75k Mw): PbS QDs-DA	180
F8BT(200k Mw): PbS QDs-HA	----
F8BT(200k Mw): PbS QDs-DA	----

Table 5.9/The average diameter of the QD-rich domains in F8BT: PbS QDs nanocomposite films with different ligands and polymer M_w.

Varying the Polymers M_w and exchanging QDs ligands from the native ligands (OA) to HA and DA both affect the surface morphology of the blend films. The effect of the changing polymers M_w is represented by an increase in the QDs-rich domains size when the polymer M_w increased, as shown in Table 5.7Table 5.8Table 5.9 and *Figure 5.6*. This could result from the change in the amount of the depletion force or depletion interaction as the M_w of the polymers changed (the effect of the polymer M_w has been detailed in the last chapter).

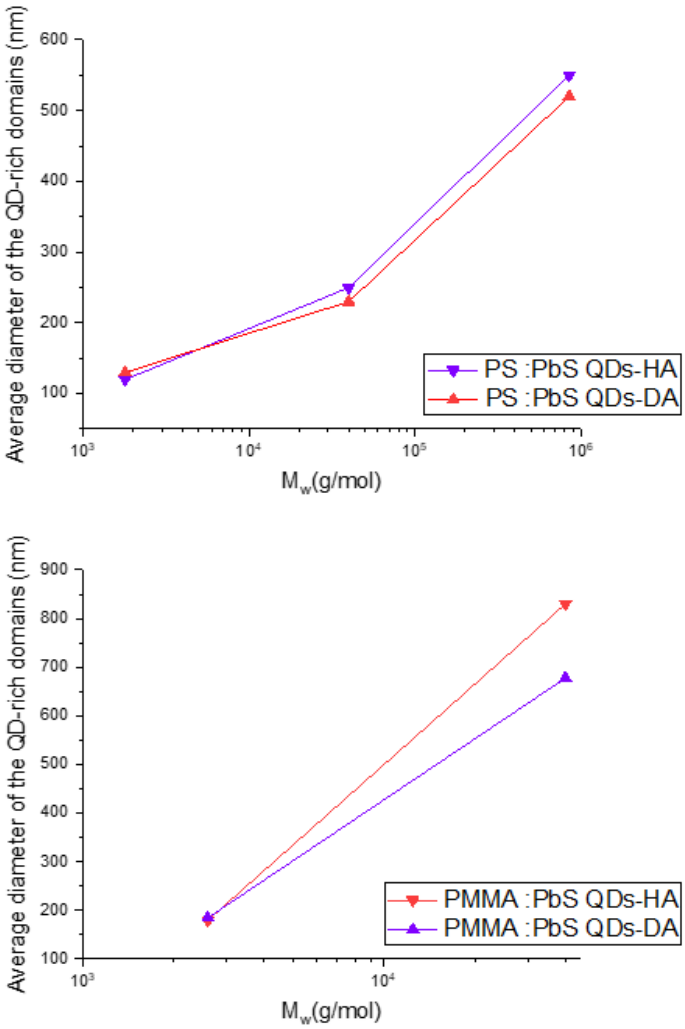

Figure 5.6/ the effect of the polymers M_w on the QD-rich domain size; (a) PS system, (b) PMMA system, and F8BT systems are not included because the QD-poor domain in the samples with 200k M_w are not spherical in shape, so it cannot be calculated.

Figure 5.7 compares the effects of the ligand exchange on the QDs-rich domains size in the PS and PMMA systems. The average QDs-rich domains size in the samples with OA ligands is bigger than in the samples with HA and DA ligands. The average diameter of the QDs-rich domains in PS (1800 M_w): PbS QDs-OA and PS (40k M_w): PbS QDs-OA films are 240nm and 660nm; this reduced to 120nm, 130 nm, 250 nm, and 230 nm in PS (1800 M_w): PbS QDs-HA, PS (1800 M_w): PbS QDs-DA, PS (40K M_w): PbS QDs-HA, and PS(40K M_w): PbS QDs-HA, respectively.

Similar behaviour was noted in PMMA and F8BT systems; the average diameter of the QDs-rich domains in PMMA (2600 M_w): PbS QDs-OA and PMMA (40k M_w): PbS QDs-OA are

280 nm and 1250 nm; this decreased to 180 nm, 185 nm, 830 nm and 678 nm in the PMMA (2600 M_w): PbS QDs-HA, PMMA (2600 M_w): PbS QDs-DA, PMMA (40k M_w): PbS QDs-HA and PMMA (40k M_w): PbS QDs-DA. Also, the film of F8BT (75k M_w): PbS QDs-OA has an average QDs-rich domains diameter of 750 nm; this changed to become holes with the HA and DA ligands with a diameter of 175 nm and 185 nm, respectively.

So, adjusting the surface chemistry of the PbS QDs by changing the ligands from the native ligands (OA) to the shorter chain length ligands (HA and DA) has reduced the QDs-rich domain sizes seen in the surface morphology of the blend films. This indicates a change in the relative interaction between the PbS QDs and the polymer chains, which decreases the QDs-rich domain size with HA and DA ligands compared to OA. HA and DA are shorter chains; this means different interaction parameters, such as more favourably for the interactions with the polymer chains than the native ligands, the long chains ligands of the OA have unfavourable interactions with the polymer chain, leading to a bigger driving force for aggregations of QDs. This results in smaller QDs-rich domains compared to the films with OA ligands on the surface of the blend films. The more hydrophilic ligand means more favourability of interaction, resulting in more compatibility between the QDs and the polymer chains. These properties could modify the surface chemistry of the PbS QDs and increase the miscibility between the polymers chains and QDs, which results in better miscibility and dispersibility of the QDs into the polymer matrix. The phase segregations in the surface morphology of PMMA (1M M_w): PbS QDs-HA and PMMA (1M M_w): PbS QDs-DA could be due to the high viscosity of the solution and this is because the high polymer M_w, which makes the movements of the components slower and do not have time to form the QDs-rich domains.

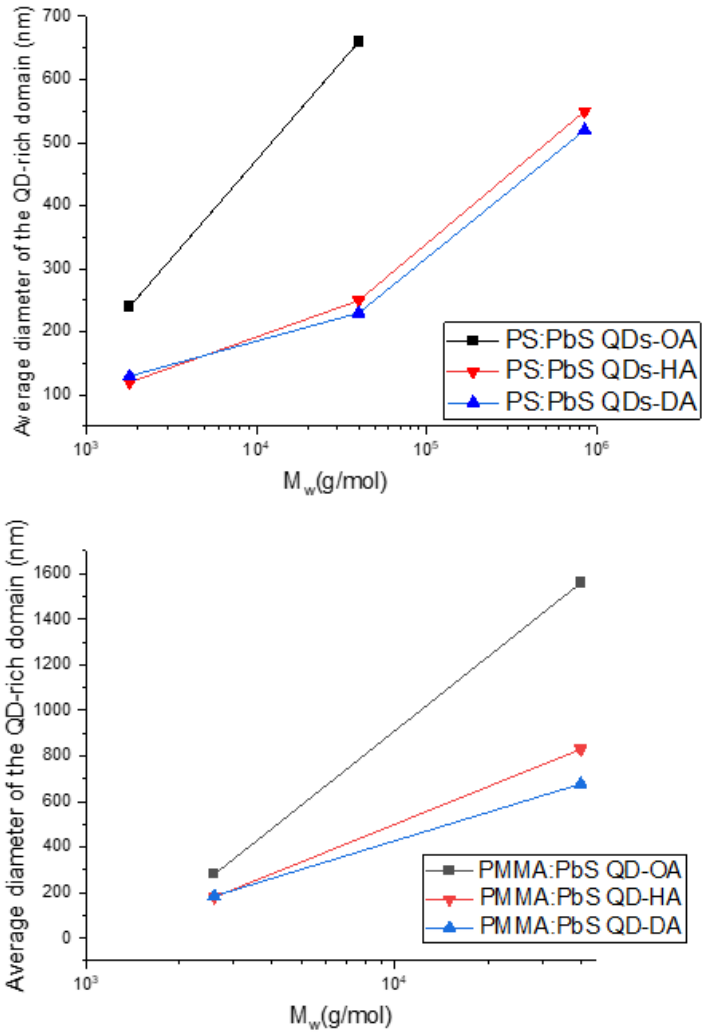

Figure 5.7/the ligands (OA, HA, and DA) and the polymers M_w affect the QD-rich domain size. The data for films with OA ligands is taken from Chapter 4.

5.3.3. GISAXS

The internal morphology of the blend of QD–HA and DA: polymer films was investigated via GISAXS. GISAXS is an excellent tool for analysing the nanostructure and ordering nanocomposite films. It gives valuable information about the internal morphology, such as the dispersion state of the QDs in both nanocomposite solution and nanocomposite films, morphology, grain size and interparticle separation.

5.3.3.1. Solution scattering

The integrated solution scattering data of the PS, PMMA and F8BT systems are presented in Figure 5.8. Similar to what has been seen in the last chapter, the samples show no aggregations of the PbS QDs with HA and DA ligands in the solution state with the presence of the solvent; this is demonstrated by the absence of the structure factor peak, which would signify aggregation ≃0.11 $Å^{-1}$; and this indicates that the aggregation happens during the drying and when the solvent evaporates.

As seen in the last chapter, the core radius of the QDs is predicted from the q positions in the integrated data (as illustrated by arrows in Figure 5.8). The QDs core radius in the samples with HA and DA ligands ≃ 24Å and polydispersity of 0.1, which is similar to those with OA ligands in the last chapter. This means the QD diameter is unchanged with the HA and DA ligands, where it is ≃ 4.8nm. Fitted data also confirm this via Sas view ("core−shell sphere") with a hard-sphere structure factor whose radius is constrained to be the sum of the shell thickness and core radius (Figure 5.9, Figure 5.10 and Figure 5.11). In the solution scattering whole the samples show the same result, where the QDs are well dispersed and they have the same core radius ≃ 24Å.

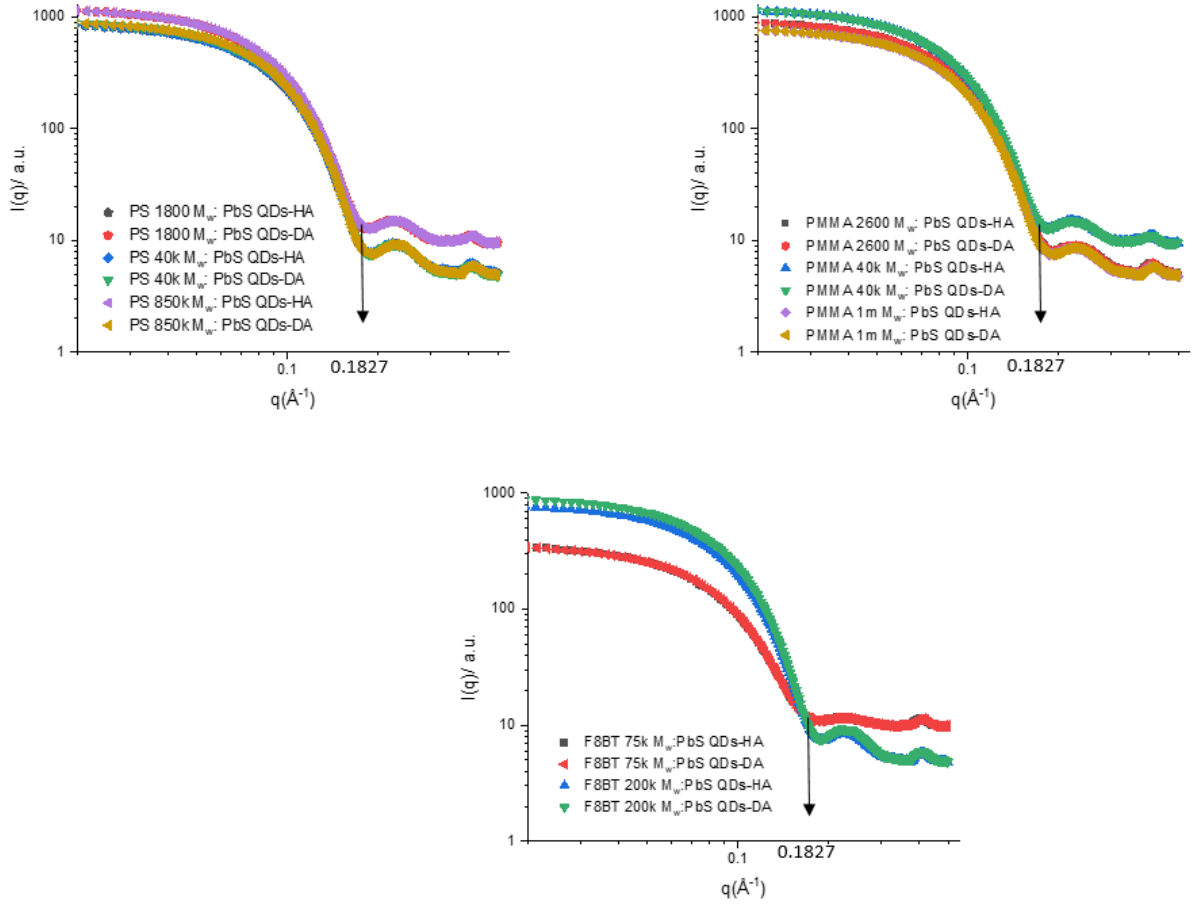

Figure 5.8/Solution scattering data of the PS, PMMA, and F8BT systems with HA and DA ligands and different polymer M_w.

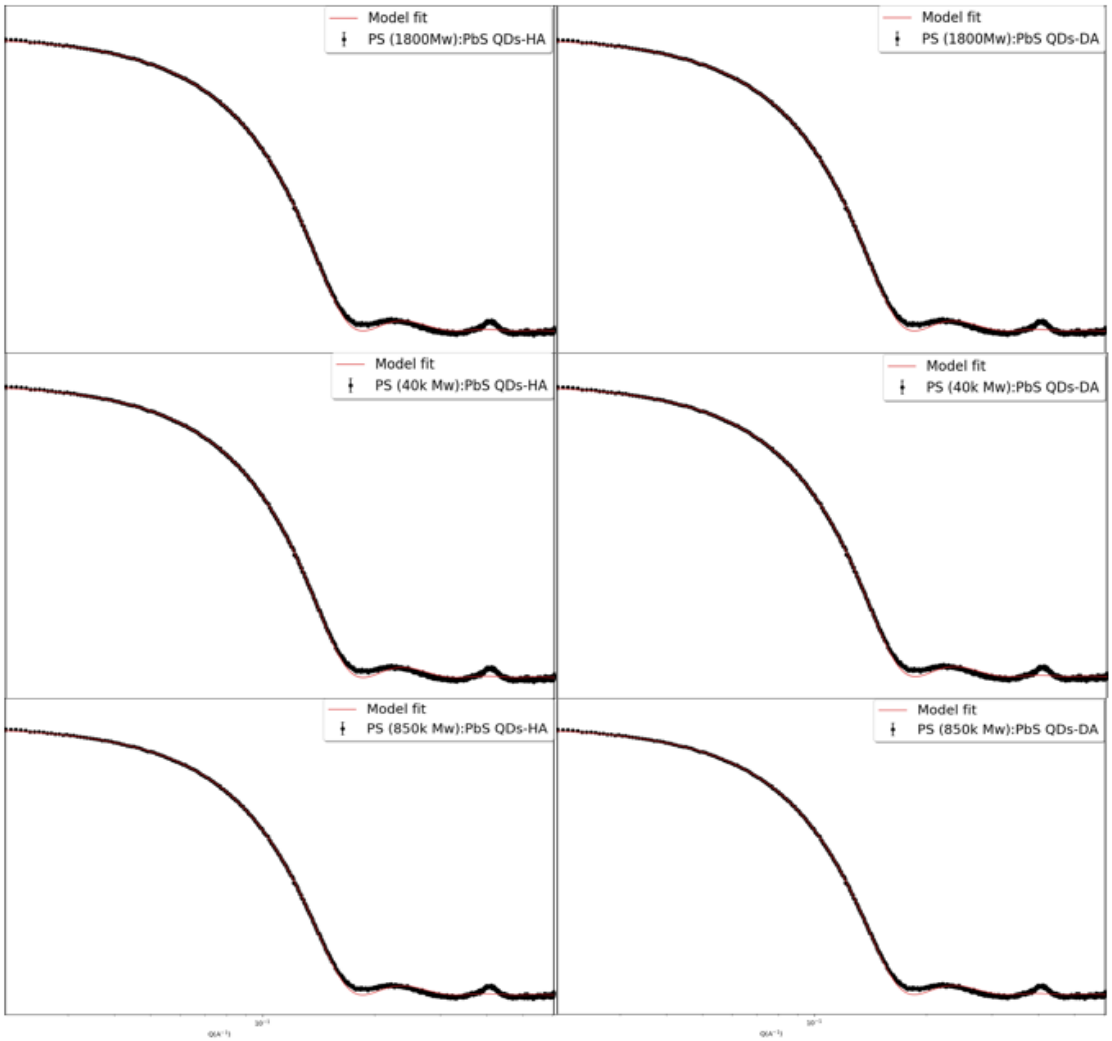

Figure 5.9/ Solution scattering of the PS: PbS QDs-HA and DA system, the SAS view fitting (core−shell sphere) with a hard-sphere model represented by red lines.

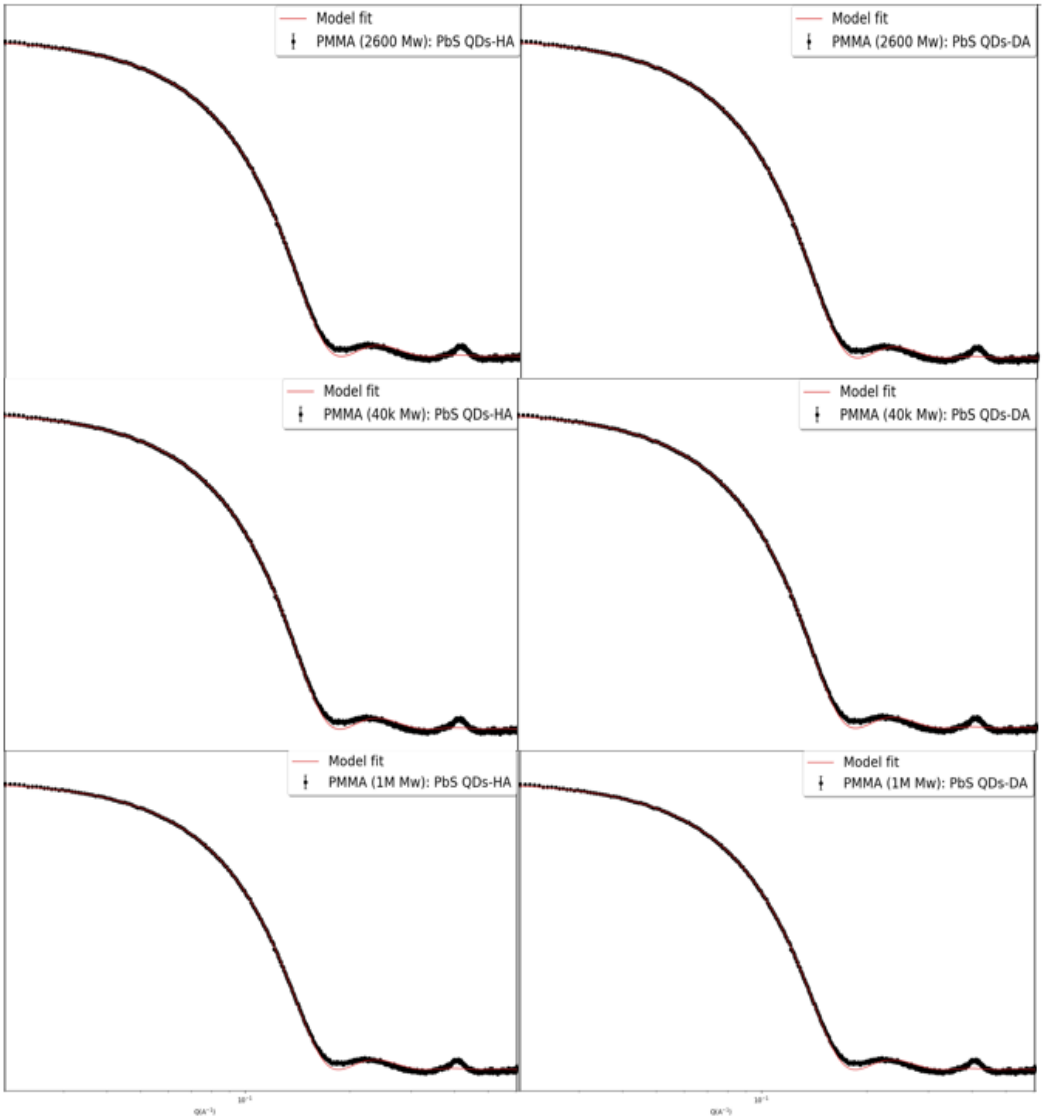

Figure 5.10/ Solution scattering of the PMMA: PbS QDs-HA and DA system, the SAS view fitting (core−shell sphere) with a hard-sphere model represented by red lines.

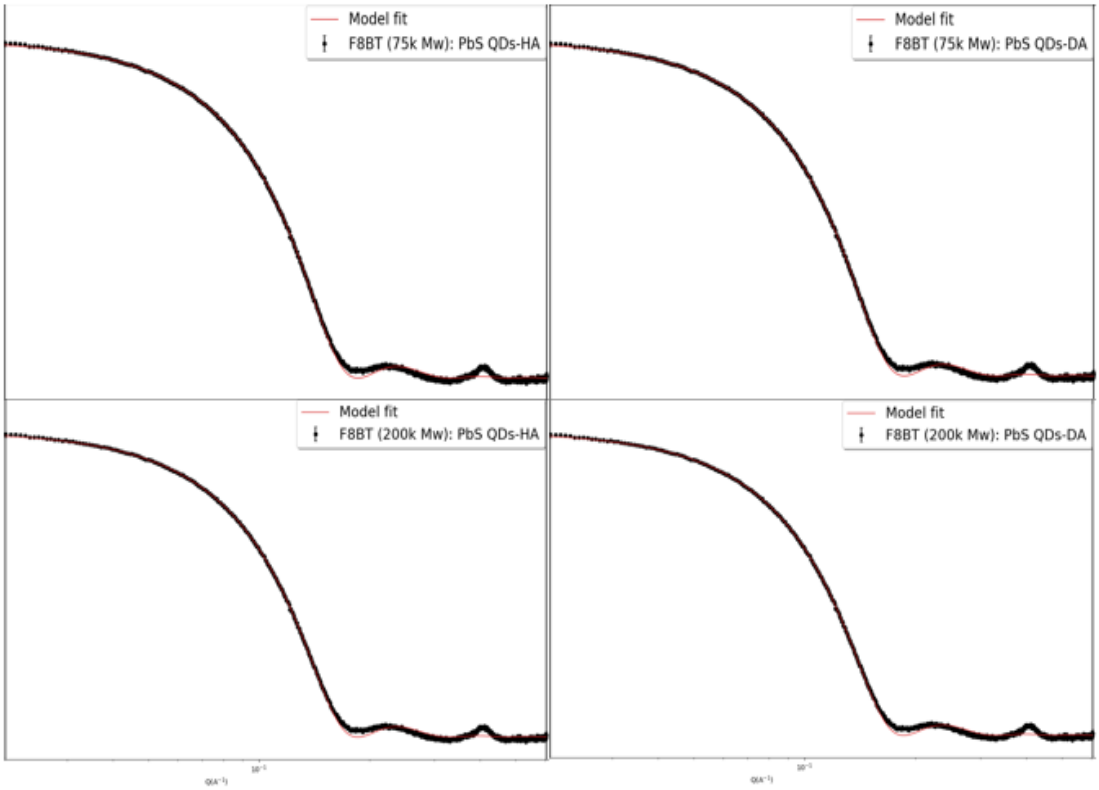

Figure 5.11/ Solution scattering of the F8BT: PbS QDs-HA and DA system, the SAS view fitting (core−shell sphere) with a hard-sphere model represented by red lines.

5.3.3.2. Thin films scattering

This section studies the internal morphology of the blend films of the three systems (PS-PMMA-F8BT). The 2D reshaped GISAXS images of the blend films are shown in Figure 5.12, Figure 5.13 and Figure 5.14. The inner structure of the nanocomposite films has some changes with the carboxylic acid active group (-COOH) ligands (HA-DA), such as the QDs aggregation peak positions and morphology. Generally, the films show an aggregation of the PbS QDs when incorporated into the host polymer matrices and during the drying process (solvent evaporation) in all three systems; this is demonstrated by the apparent peak of the structure factor aggregation, which is not visible in the solution scattering, as seen in Figure 5.16.

Most of the blend films show HCP aggregation structure where the position of the reflections show ratios $q_i/q_1 = 1, \sqrt{3}, \sqrt{4}, \sqrt{7}$, and these are consistent with HCP packing compared with the reflection reference positions, similar to what was seen in the last chapter[167]. However, the specimens of PS (40k M_w): PbS QDs-HA and PS (40k M_w): PbS QDs-DA (Figure 5.12 c and d) and PMMA 2600 M_w: PbS QDs-DA and PMMA 40k M_w: PbS QDs-DA (Figure 5.13 b

and d) in the PMMA system have an extra peak around ~0.15 $Å^{-1}$ in common with the other peaks of ~ 0.11 $Å^{-1}$ and ~ 0.18 $Å^{-1}$, which showed different QDs aggregations morphology where the positions of the reflections display ratios $q_i/q_1 = 1, \sqrt{4/3}, \sqrt{8/3}, \sqrt{11/3}$; these ratios are consistent with FCC packing compared with the reference reflection positions[166, 167]. This means these blend films have shown a change in the crystal aggregation morphology from HCP to form a face-centred cubic closed-packed (FCC-CP) morphology. The QDs are described as being ordered on a face-centred cubic (FCC) lattice with paracrystalline distortion. The distortion factor of the paracrystalline is a convenient metric for quantifying the film QDs ordering [179]. HCP and FCC-CP morphologies differ simply by the stacking sequence of layers, as shown in Figure 5.15 [96]. Moreover, the unit cell orientation in these films changed relative to the substrate to be (100) plane parallel to the substrate[39, 163].

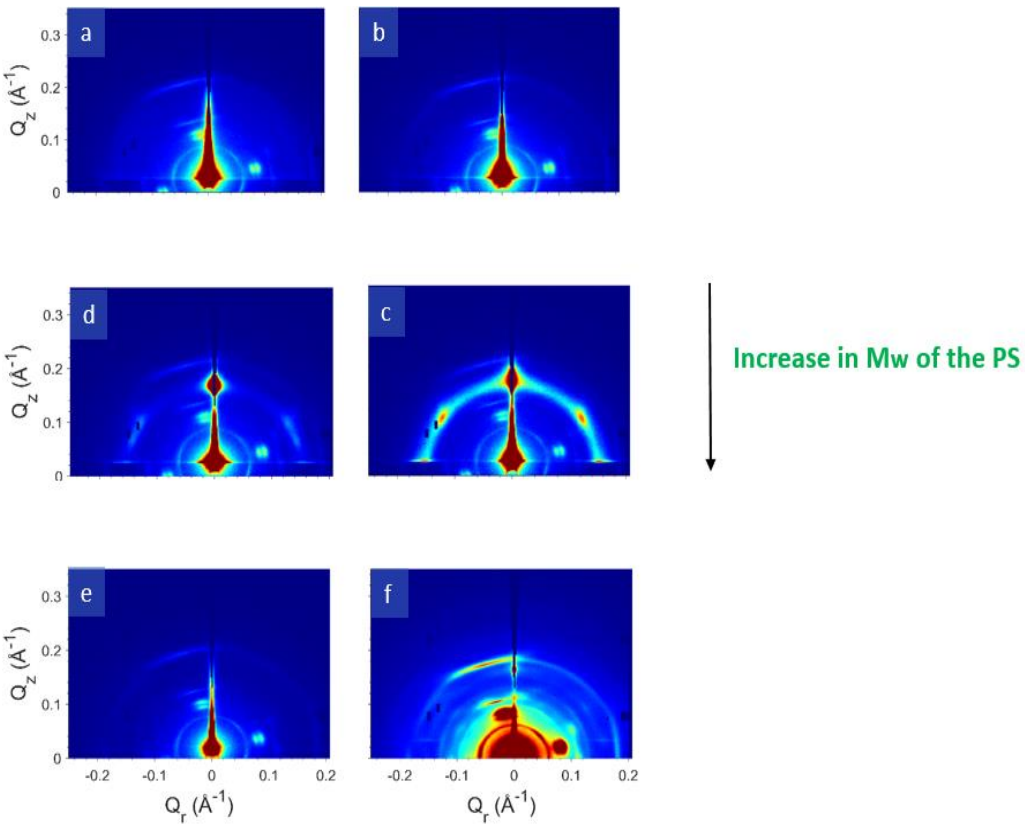

Figure 5.12/ 2D reshape GISAXS images of samples of PS system, (a) PS 1800 M_w: PbS QDs-HA; (b) PS 1800 M_w: PbS QDs-DA; (c) PS 40k M_w: PbS QDs-HA; (d) PS 40k M_w: PbS QDs-DA; (e) PS 850k M_w: PbS QDs-HA; (f) PS 850k M_w: PbS QDs-DA.

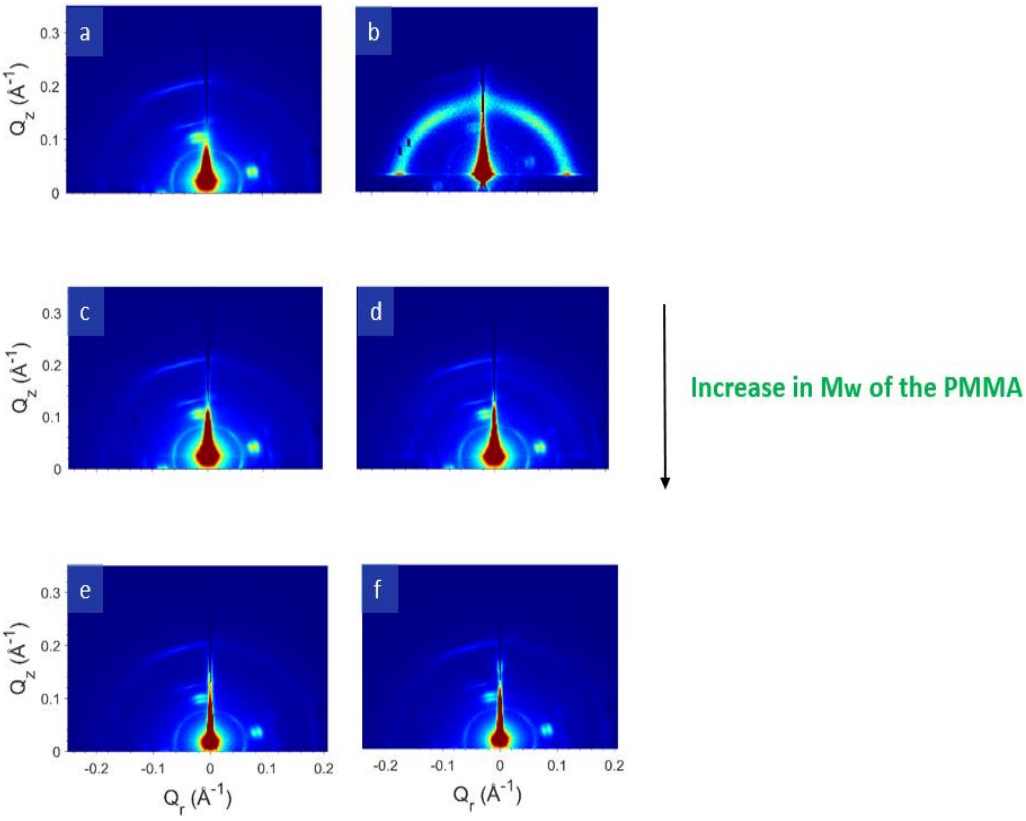

Figure 5.13/ 2D reshape GISAXS images of samples of PMMA system, (a) PMMA 2600 M_w: PbS QDs-HA; (b) PMMA 2600 M_w: PbS QDs-DA; (c) PMMA 40k M_w: PbS QDs-HA; (d) PMMA 40k M_w: PbS QDs-DA; (e) PMMA 1M M_w: PbS QDs-HA; (f) PMMA 1M M_w: PbS QDs-DA.

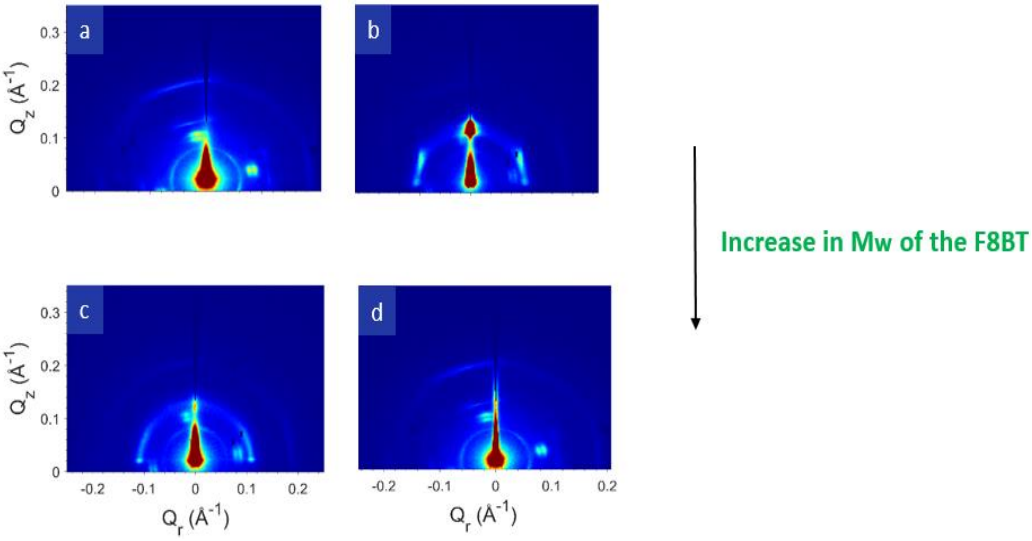

Figure 5.14/ 2D reshape GISAXS images of the samples of F8BT system, (a) F8BT 75k M_w: PbS QDs-HA; (b) F8BT 75k M_w: PbS QDs-DA; (c) F8BT 200k M_w: PbS QDs-HA; (d) F8BT 200k M_w: PbS QDs-DA

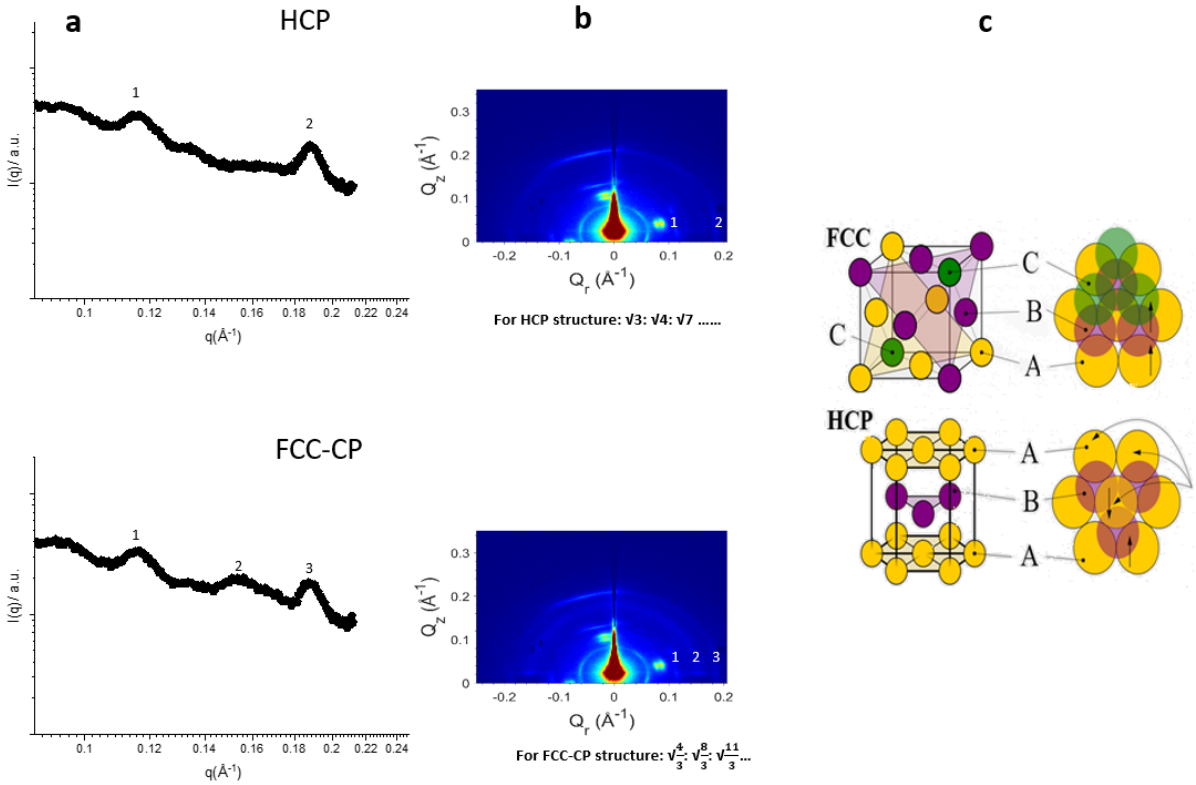

Figure 5.15/ PMMA (40k M_w): PbS QDs-HA and PMMA (40k M_w): PbS QDs-DA nanocomposite films. (a) 1D radially integrated GISAXS, (b) 2D reshaped GISAXS image of the blend films, (c) Sketch shows the difference between the HCP and FCC-CP structures. The graph illustrates how to get the different aggregate structures from the consecutive reciprocal Bragg spacing ratio for the observed structure.

To gain further insight into the inner morphology of the nanocomposite films, the data was radially integrated, and the peak of the structure factor-aggregation (~ 0.11 $Å^{-1}$) was fitted to estimate the crystal grains size from the full-width half maximum (FWHM) of the diffraction peaks by the Scherrer equation similar to what have seen in the last chapter [168, 172]. Figure 5.16 presents an example of the radially integrated data, and the results are illustrated in Table 8.4, Table 8.5 and Table 8.6 for PS, PMMA and F8BT systems, respectively.

The grain size that forms from the blend films of (PS: PbS QDs-HA and DA, PMMA: PbS QDs-HA and DA and F8BT: PbS QDs-HA and DA) range between 25-41nm, 23-51nm and 37-49nm, respectively. This indicates aggregations of the PbS QDs where the grain size is 5-11 times bigger than the core diameter of the PbS QDs (~ 4.8nm).

The behaviour of the QDs aggregation is still affected by the polymer M_w as seen in the last chapter, despite the change in the QDs surface chemistry. From Table 8.4, Table 8.5, Table 8.6

(in the Appendix) and Figure 5.17, it can be seen that the grain size increased with the polymer M_w; for example, the PS (1800 M_w): PbS QDs-HA and PS (1800 M_w): PbS QDs-DA films have grains size 25nm and 26nm, respectively. This increased to 28nm, 30nm, 36nm and 41nm in PS (40k M_w): PbS QDs-HA, PS (40k M_w): PbS QDs-DA, PS (850k M_w): PbS QDs-HA and PS (40k M_w): PbS QDs-DA films, respectively. This behaviour was also noted in the PMMA and F8BT systems, where the grains sizes in the PMMA 2600 M_w: PbS QDs-HA and PMMA 2600 M_w: PbS QDs-DA films are 23nm and 24nm; this increased to 31nm, 34nm, 50nm and 51nm in films of PMMA 40k M_w: PbS QDs-HA, PMMA 40k M_w: PbS QDs-DA, PMMA 1M M_w: PbS QDs-HA and PMMA 1M M_w: PbS QDs-DA, respectively.

However, the size of the QDs aggregations in the films with HA and DA ligands are smaller than the same films with the native ligands (OA) seen in the last chapter (Figure 5.17). This behaviour is attributed to two reasons: the shorter chain length of (HA and DA) ligands compared to the native ligand (OA), which makes the QDs closer, as seen from the interparticle separation and significantly changes the interaction parameters. This leads to increasing interaction between the QD-QD and QD-polymer and reduces the driving force of aggregation; this results in reduced size of the crystal grains or aggregations of QDs. Secondly, this is probably due to the unfavourable or non-interacting nature of the oleate ligand for interaction with the polymer chains [145]; this minimises the interaction resulting in a significant driving force for QDs aggregations. On the other hand, this is not the situation with the HA and DA ligands, which are chemically more suitable (similar) to the polymer chains than the oleate ligands. This reduces the unfavourable interactions and enhances the miscibility between the QDs and the polymer chains, which results in smaller QDs aggregations and better dispersion of the QDs in the polymer matrix [180].

Looking at the aggregations, the inter-particle separation has been found in the same way as in the last chapter. The inter-particle separation in the blend films ranges between 4-6 Å, 4-6 Å and 5-6 Å in the PS: PbS QDs-(HA and DA), PMMA: PbS QDs-(HA and DA) and F8BT: PbS QDs-(HA and DA) systems, respectively.

The slight change in the inter-particle separation between the films could be because of the same reasons explained in the last chapter (the ligands being tilted or partially interdigitated

in neighbouring QDs, where they are less than the extended length of the ligands [176]). The blend films with (HA) have slightly shorter interparticle separation than the films with (DA) ligands; this is expected because (HA) is a shorter length chain that contains six carbons rather than (DA), which has ten carbons [163]. Figure 5.19 shows estimations of the ligand length compared to the interparticle separation; the blue and red lines represent the extremes that might be observed in the interparticle separation; the blue is one ligand length, and the red is two ligands length[163]. To have a complete interparticle separation in films with no ligands interdigitating or folding back on the QDs, the interparticle separation in the blend films with HA ligands needs to be around 14 Å and in the films with DA ligands, around 22 Å according to Weidman et al.[163], this is not the case in this experiment, which indicates that the ligands either interdigitate between the surrounding QDs or fold back on the QDs.

Compared to the films with the (OA) native ligands that were seen in the last chapter, it can be seen that the inter-particle separation is slightly smaller in the films with ligands (HA and DA). This is probably because the HA and DA are shorter-length chains than OA ligands with different chemistry, making the distance between the QDs smaller; this also indicates that the ligands were exchanged successfully. Also, the slight change in the interparticle separation with HA and DA ligands could be ascribed to a difference in the interaction parameters between PbS QDs-OA and PbS QDs-DA and HA [179].

Figure 5.18 compares the domains or the depletion zones in the surface morphology of the nanocomposite films and the grain sizes found via GISAXS. Both have similar behaviour where they are increased with the host polymer M_w. However, they have different sizes, where the domains in the surface morphology are bigger. This could be because the AFM only probes the surface morphology, which may differ from the bulk.

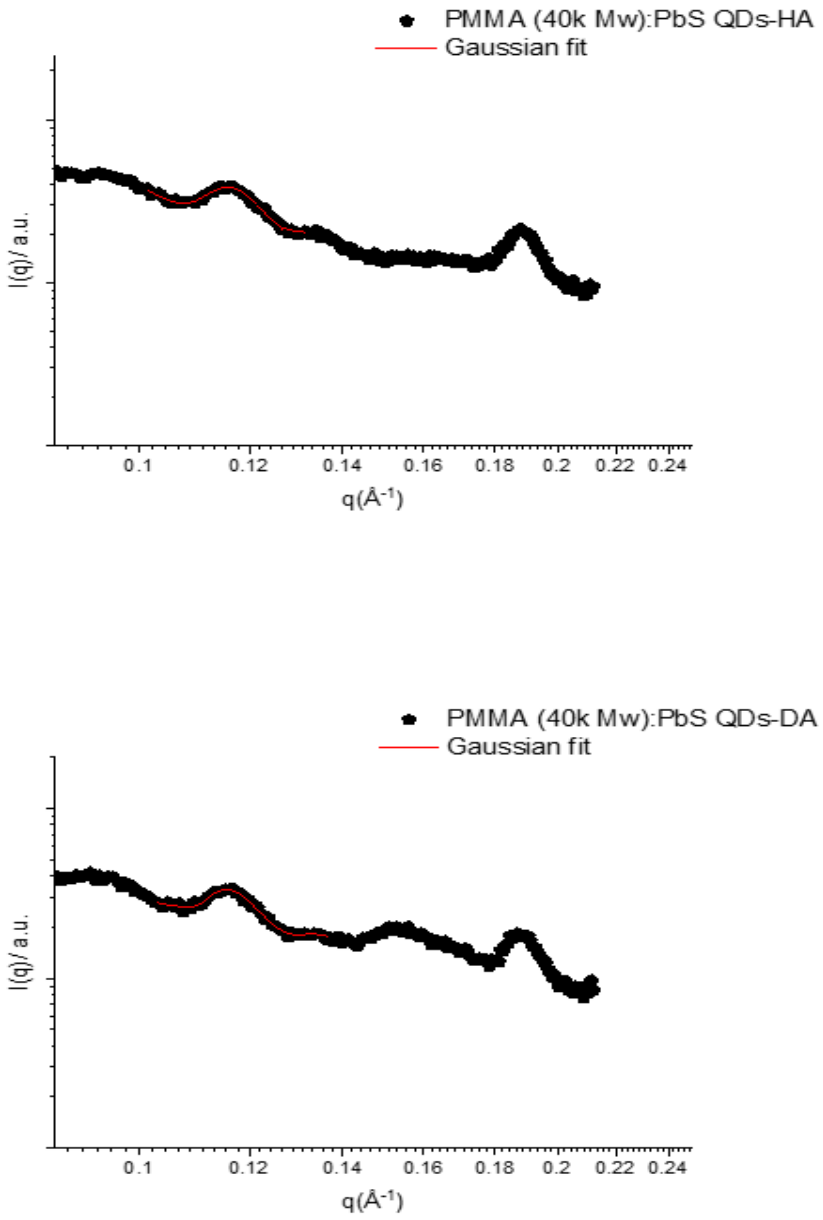

Figure 5.16/ radially integrated GISAXS data of PMMA (40k M_w): PbS QDs-HA and PMMA (40k M_w): PbS QDs-DA. This is an example of 1D integrated data and Gaussian fitting.

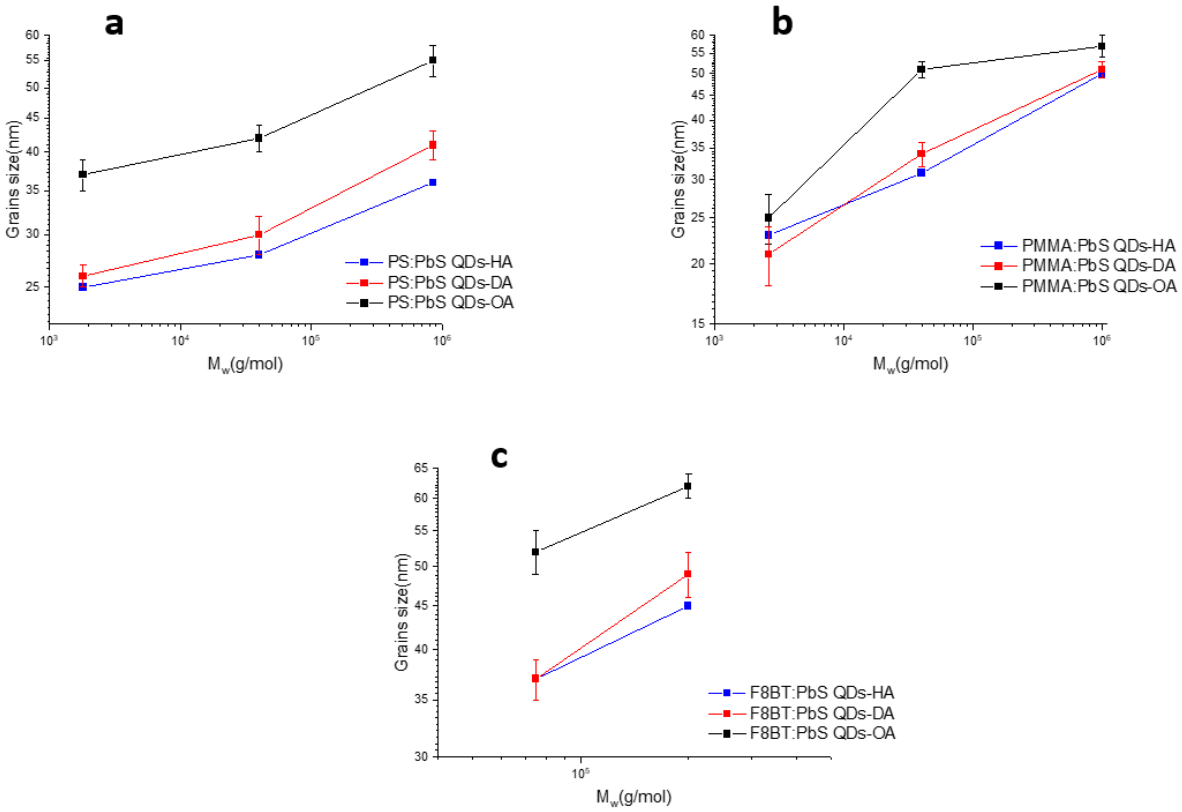

Figure 5.17/The effect of different ligands and polymer M_w on the grain size, (a) PS system; (b) PMMA system; (c) F8BT system. The data on the OA ligands is from the last chapter.

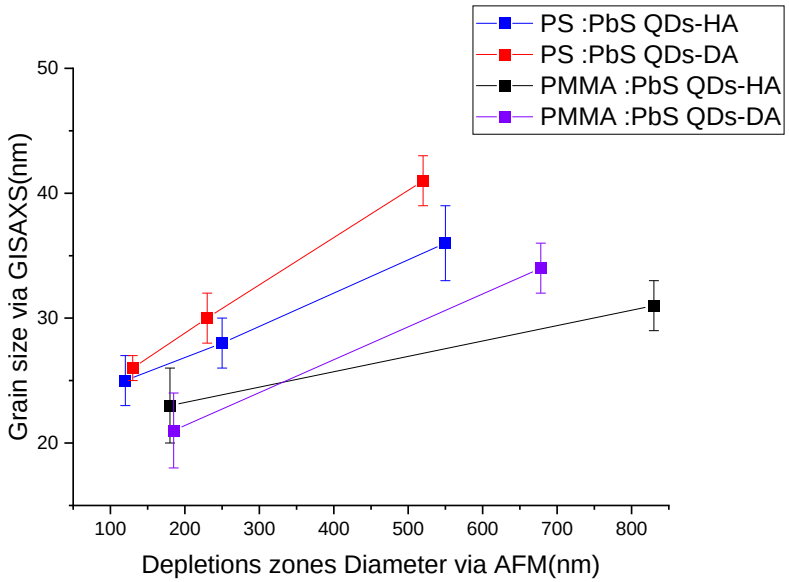

Figure 5.18/ Grains size via GISAXS vs depletion zone via AFM for PS and PMMA systems (the F8BT systems were not included because the F8BT 200k: PbS QDs-HA and DA samples were not shown QD-poor doman). For the same reason, the PMMA(1M M_w): PbS QDs-HA and DA samples were not included.

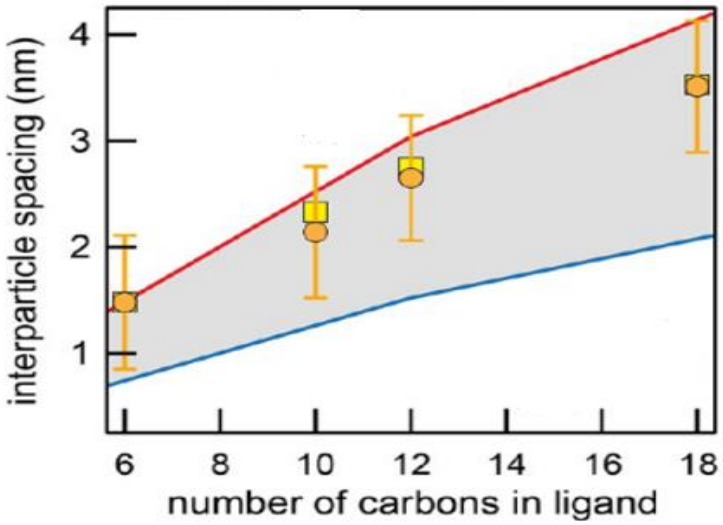

Figure 5.19/ An estimation of the interparticle separation for some ligands plotted against the number of carbons in each ligand (HA contains 6)and (DA has 10), the blue lines one ligand length and the red lines two ligands length[163].

5.4. Conclusions

To summarise the work in this chapter, the effect of the exchange ligands approach, where the ligands changed from the native ligands (OA) to carboxylic acid ligands (HA and DA), was investigated. Three different polymers were used in this experiment, with different polymer M_w (low-medium-high) for each, except the F8BT polymer, where only two M_w are available.

Results show an enhancement of the PbS QDs towards the dispersibility into the polymer matrices compared to the samples with the native ligands (OA). This indicates a change in the relative interaction between the PbS QDs and the polymer chains when the nature of the QDs switched from the aliphatic (native ligands) to carboxylic acid by exchanging ligands from OA to HA and DA. First, the films thickness decreased slightly with the carboxylic acid ligands (HA and DA), as seen from the ellipsometry section. Also, the effect of the (HA and DA) ligands could be seen in the AFM results when the QD-rich domains became smaller for the samples with HA and DA ligands. Also, the GISAXS results show similar behaviours when the grains size is reduced compared to the samples with the native ligands.

The unfavourable nature of the oleate ligands for interaction with the polymer chains and the shorter chain length of the HA and DA ligands could be the main reasons for this enhancement and determine the increase in miscibility between the QDs and the polymer

chains. The Interparticle separation decreased in the films with HA and DA ligands compared to the films with the native ligands (OA); this can be understood based on their shorter chain length and different interaction parameters. Still, the interparticle separation is less than the extended length of the ligands, which indicates that the ligands either fold back or interdigitate between the surrounding QDs.

Despite the structural improvements noticed in this chapter, the QDs aggregations, which is the main issue, still exist, meaning that there is still work that needs to be done on this issue, which takes us to the next chapter.

Chapter 6

The effect of changing the volume fraction on the dispersibility of the quantum dots into the polymer matrix.

6.1. Introduction

This project aims to develop or discover processing routes that could help disperse lead sulphide quantum dots (PbS QDs) into the polymer matrices to form Nanocomposite films that can be used in technological applications such as optoelectronic devices. The effect of volume fractions of the PbS QDs and polymers on the structure of PbS QDs: Polymer blend films have been studied in this chapter. The volume fraction is defined as the ratio of the volume of one component of a composite to the total volume of the composite. It is a dimensionless and unitless quantity, with a minimum value > 0 and a maximum possible value of one and taking symbol of $\boldsymbol{\phi}$. I calculated the volume fraction mathematically and the 0 represents the absence of the constituent, while one represents the entire volume being occupied by the constituent.

The volume fraction is a key parameter in optimising the nanocomposite film structure; for example, changing the QDs volume fraction could affect the arrangement and distribution of the QDs within the polymer matrix and, thus, significantly affect the structure and properties of the nanocomposite films. It has been seen previously in this thesis the effect of polymer M_w and changing ligands on the dispersion state of QDs. Adjusting the volume fractions of both QDs and the polymer could play an essential role in further enhancing the QD dispersibility and add to the understanding of the work done in the previous chapters.

The experiments in this chapter have been varying the PbS QDs and polymer volume fraction in solution status up and down (the range studied will be detailed in the sample preparations section) to see how this affects the surface and the internal morphology of the nanocomposite films.

6.2. Experimental methods

This experiment used three different M_w of PS and PMMA (low-medium-high) and the two M_w of the F8BT that were available, as shown in Table 6.1. The chemicals were used as they arrived without further purification.

Polymer	Supplier	M_w (g/mol)	M_n (g/mol)	PDI (M_w/ M_n)
PS	Polymer source	1,800	1600	1.13
PS	Sigma-Aldrich	40,000	39,000	1.02
PS	Polymer source	850,000	790,000	1.08
PMMA	Polymer source	2,600	2,500	1.09
PMMA	Polymer source	40,000	36,363	1.10
PMMA	Polymer source	1,000,000	666,666	1.5
F8BT	Sigma-Aldrich	75,000	72,815	1.03
F8BT	Sigma-Aldrich	200,000	192,307	1.04

Table 6.1/ The polymers used in these experiments.

substance	**Empirical formula**	**Density (g/cm^3)**	**Melting temperature (^oC)**	**Boiling temperature (^oC)**
Oleic Acid (OA)	$C_{18}H_{34}O_2$	0.87	14	360
Hexanoic Acid (HA)	$C_6H_{12}O_2$	0.93	-3.4	205
Decanoic Acid (DA)	$C_{10}H_{20}O_2$	0.89	31.6	269

Table 6.2/ The PbS QDs ligands that were used in this chapter.

6.2.1. Samples preparations

Two different concentrations of PbS QDs were used for each specimen in this experiment, volume fraction of PbS QDs ~ 0.024 and PbS QDs ~ 0.00024. Firstly, the polymer solutions were made, as explained in Chapter 1. Still, instead of taking 200µL from the QDs and polymer solution, the volume fraction is changed here to take 200µL from the polymer solution and 20µL from the QDs solution to make (PbS QDs volume fraction ~ 0.00024) and (polymer volume fraction ~ 0.0420. 0.037 and 0.043 for PS, PMMA and F8BT, respectively). To make the concentration (PbS QDs volume fraction ~ 0.024) and (polymer volume fraction ~ 0.0042, 0.0037 and 0.0043 for PS, PMMA and F8BT, respectively), 200µL from the QDs solution was mixed with 20µL from the polymer solutions, as seen in Table 6.3.

Then, the nanocomposite solutions were left at room temperature for 48-72 hours before the drying process to ensure the nanocomposite solution mixed well without any precipitates. Then, for each sample, 30 µL from the nanocomposite solutions were deposited on clean silicon substrates and spun using a spin coater for the 30s at 2000 rpm.

substance	Volume fraction	Volume percentage (%)
PbS -(OA or HA or DA) (200 µl)	0.024	2.4
PS (20 µl)	0.0042	0.42
PMMA (20 µl)	0.0037	0.37
F8BT (20 µl)	0.0043	0.43
PbS -(OA or HA or DA) (20 µl)	0.00024	0.024
PS (200 µl)	0.0420	4.2
PMMA (200 µl)	0.037	3.7
F8BT (200 µl)	0.043	4.3

Table 6.3/ The volume percentage and volume fraction of the nanocomposites. The initial weight fraction of polymer: PbS QD nanocomposite in case of 200µl (QD) and 20µl (polymer) is: (2.4% QDs, 0.42% PS and 97.18% toluene), (2.4% QDs, 0.37% PMMA and 97.23% toluene) and (2.4% QDs, 0.43% F8BT and 97.17% toluene). In the case of 200µl (polymer) and 20µl (QD), the initial weight fraction of the composite is (0.024% QDs, 4.2% PS and 95.77% toluene), (0.024% QDs, 3.7% PMMA and 96.28% toluene) and (0.024% QDs, 4.3% F8BT and 95.68% toluene).

6.3. Results and Discussion

6.3.1. Ellipsometry

The nanocomposite film thicknesses of the PS, PMMA and F8BT systems were measured by Ellipsometry and the values are presented in Table 6.4, Table 6.5 and Table 6.6. There is a difference in thicknesses between the samples with (PbS QDs volume fraction ~ 0.024) and (PbS QDs volume fraction ~ 0.00024). The specimens with higher PbS QDs volume fraction (~ 0.024) show a significant decrease in thicknesses compared to those with lower PbS QDs volume fraction ~ 0.00024), as shown in Figure 6.1. The nanocomposite film thickness of the samples with a concentration of (PbS QDs volume fraction ~ 0.024) in the PS system ranged between 10-34 nm, while it was between 90-294nm in the samples with a concentration of (PbS QDs volume fraction ~ 0.00024). Similar behaviour is shown in the PMMA and F8BT

systems, where the thickness of the nanocomposite films ranged between 19-29 nm and 9-23 nm in the concentration of (PbS QDs volume fraction ~ 0.024) and in the concentration of (PbS QDs volume fraction ~ 0.00024) it ranged between 110-217nm and 146-275 nm, respectively.

The reason for the decrease in the thickness of the blend films with increasing the PbS QDs volume fraction could be the viscosity and the evaporation rate. The nanocomposite solutions with higher PbS QDs volume fraction (~ 0.024) are less viscous than those with lower PbS QDs volume fraction (~ 0.00024) and higher polymer volume fraction. As a result, the thickness of the films in this experiment is determined by the initial solution viscosity and the amount of radial flow of the solution. Increasing the initial QDs volume fraction and reducing the volume fraction of the polymers makes the solution less viscous and increase the amount of the radial flow of the solution, which increases the evaporation rate during the same spinning speed and time, resulting in a lower thickness of the blend films.

Not only does the QD concentration affect the thickness of the nanocomposite films, but also the polymer M_w has an effect, where the thickness of the film increases with an increase in M_w, which is noticed in both concentrations, as illustrated in Figure 6.1. Rising M_w means increasing the initial viscosity of the solutions, causing the thickness of the blended films to increase due to hydrodynamics.

Films	Thickness (nm)	Error bar (nm)
PS(1800 Mw): PbS QDs-OA (0.00024)	93	± 2
PS(1800 Mw): PbS QDs-OA (0.024)	10	± 2
PS(1800 Mw): PbS QDs-HA (0.00024)	90	± 1
PS(1800 Mw): PbS QDs-HA (0.024)	17	± 3
PS(1800 Mw): PbS QDs-DA (0.00024)	90	± 1
PS(1800 Mw): PbS QDs-DA (0.024)	16	± 1
PS(40k Mw): PbS QDs-OA	226	±2

(0.00024)		
PS(40k Mw): PbS QDs-OA (0.024)	28	±1
PS(40k Mw): PbS QDs-HA (0.00024)	214	±3
PS(40k Mw): PbS QDs-HA (0.024)	29	±1
PS(40k Mw): PbS QDs-DA (0.00024)	233	±2
PS(40k Mw): PbS QDs-DA (0.024)	30	±1
PS(850k Mw): PbS QDs-,OA (0.00024)	261	±3
PS(850k Mw): PbS QDs-OA (0.024)	33	±1
PS(850k Mw): PbS QDs-HA (0.00024)	294	±3
PS(850k Mw): PbS QDs-HA (0.024)	31	±1
PS(850k Mw): PbS QDs-DA (0.00024)	292	±2
PS(850k Mw): PbS QDs-DA (0.024)	34	±1

Table 6.4/ Thickness of the PS system samples.

Films	Thickness (nm)	Error bar (nm)
PMMA(2600 Mw): PbS QDs-OA (0.00024)	110	±2
PMMA(2600 Mw): PbS QDs-OA (0.024)	19	±1
PMMA(2600 Mw): PbS QDs-HA (0.00024)	141	±3
PMMA(2600 Mw): PbS QDs-HA (0.024)	23	±1
PMMA(2600 Mw): PbS QDs-DA (0.00024)	115	±2
PMMA(2600 Mw): PbS QDs-DA (0.024)	22	±3

PMMA(40k Mw): PbS QDs-OA(0.00024)	156	±1
PMMA(40k Mw): PbS QDs-OA(0.024)	26	±3
PMMA(40k Mw): PbS QDs-HA (0.00024)	163	±2
PMMA(40k Mw): PbS QDs-HA (0.024)	26	±1
PMMA(40k Mw): PbS QDs-DA (0.00024)	145	±1
PMMA(40k Mw): PbS QDs-DA (0.024)	26	±2
PMMA(1m Mw): PbS QDs-OA (0.00024)	173	±3
PMMA(1m Mw): PbS QDs-OA (0.024)	29	±1
PMMA(1m Mw): PbS QDs-HA (0.00024)	196	±2
PMMA(1m Mw): PbS QDs-HA (0.024)	29	±1
PMMA(1m Mw): PbS QDs-DA (0.00024)	217	±3
PMMA(1m Mw): PbS QDs-DA (0.024)	28	±2

Table 6.5/ Thickness of the PMMA system samples.

Films	Thickness (nm)	Error bar (nm)
F8BT(75k Mw): PbS QDs-OA (0.00024)	162	±1
F8BT(75k Mw): PbS QDs-OA (0.024)	20	±4
F8BT(75k Mw): PbS QDs-HA (0.00024)	146	±3
F8BT(75k Mw): PbS QDs-HA (0.024)	9	±1
F8BT(75k Mw): PbS QDs-DA (0.00024)	160	±4
F8BT(75k Mw): PbS QDs-DA (0.024)	15	±3

F8BT(200k Mw): PbS QDs-OA (0.00024)	275	±2
F8BT(200k Mw): PbS QDs-OA (0.024)	26	±1
F8BT(200k Mw): PbS QDs-HA (0.00024)	252	±2
F8BT(200k Mw): PbS QDs-HA (0.024)	23	±1
F8BT(200k Mw): PbS QDs-DA (0.00024)	248	±1
F8BT(200k Mw): PbS QDs-DA (0.024)	24	±3

Table 6.6/ Thickness of the F8BT system samples.

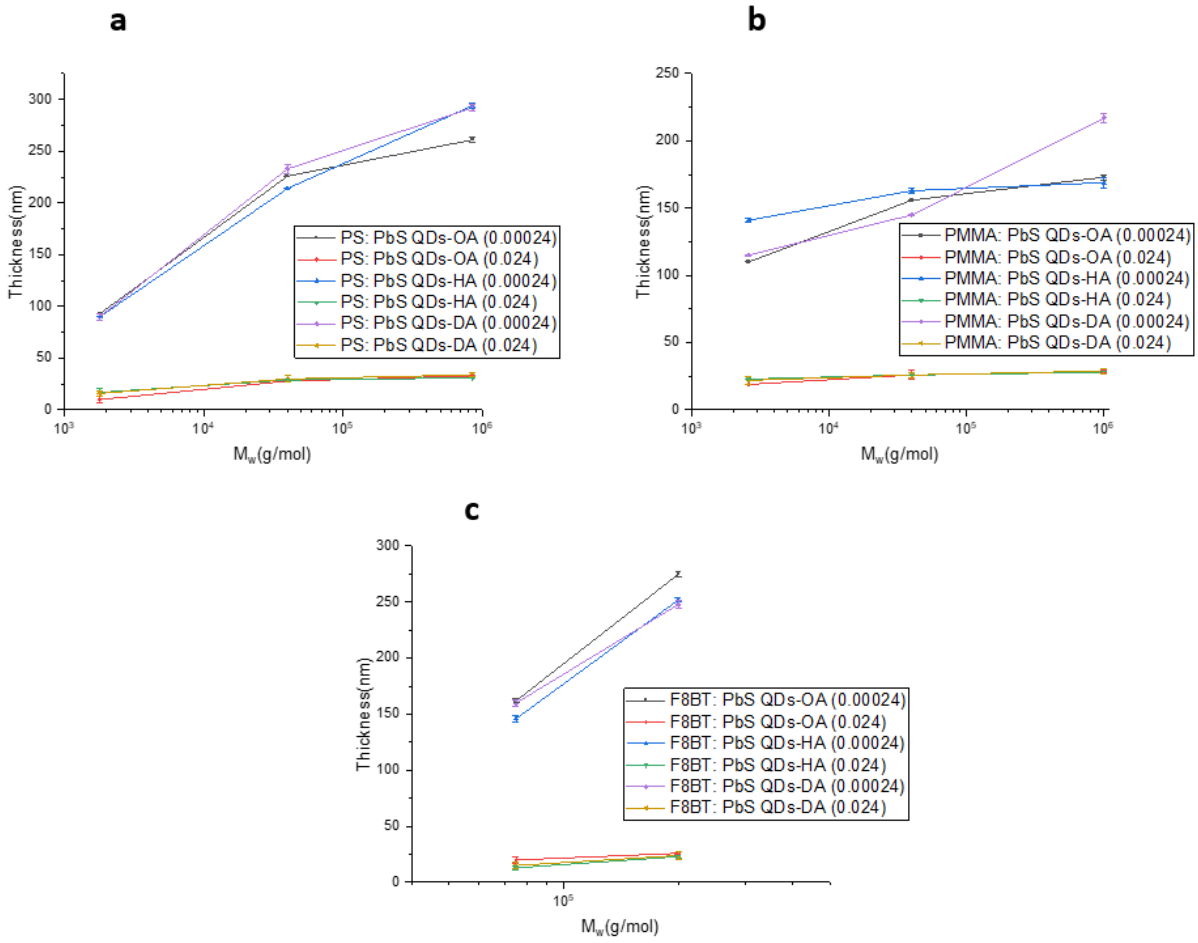

Figure 6.1/ Blends films thicknesses vs polymers M_w for (a) PS system, (b) PMMA system and (c) F8BT system. This shows the effect of the QD and polymer concentration on the thickness, where increasing the PbS QDs volume friction decreased the thicknesses of the films.

6.3.2. AFM

The images of the nanocomposite films surface morphology of the PS: PbS QDs, PMMA: PbS QDs and F8BT: PbS QDs are presented in Figure 6.2, Figure 6.3, Figure 6.4, Figure 6.5, Figure 6.6, Figure 6.7, Figure 6.8 and Figure 6.9, respectively. Substantial surface morphology differences were noted between the nanocomposite films, such as having some spherical domains or holes with different diameters. In contrast, some films look uniform and relatively smooth and show no domains or holes in their surface morphology. The diameter of the domains and the holes are measured as in the previous chapters, and the values are presented in Table 6.7, Table 6.8, Table 6.9, Table 6.10, Table 6.11, Table 6.12, Table 6.13 and Table 6.14.

In contrast to what we have seen in the last two chapters, the changes in the surface morphology of the nanocomposite films in this experiment do not follow any specific order. In the PS: PbS QDs system, substantial surface morphologies are shown in the surface morphology of the nanocomposite films, such as QD-rich domains, holes, stripy patterns and smooth surfaces.

The QD-rich domains range between 30-25 nm, and the holes range between 40-160nm. For instance, the sample of PS(1800 M_w): PbS QDs-OA (QDs volume fraction ~ 0.00024) (Figure 6.2 a) has QD-rich domains with an average diameter of ~ 70nm, while the same sample with a different QD volume fraction (volume fraction ~ 0.024) show a stripy patterns surface which indicates two distinct phases (Figure 6.2 b). Also, the samples of PS (1800 M_w): PbS QDs-DA (volume fraction ~ 0.00024) have QD-rich domains with an average diameter of ~ 30nm, while the PS (1800 M_w): PbS QDs-DA (volume fraction ~ 0.024) show no QD-rich domains in the surface (Figure 6.2 c and d).

However, some samples showed holes in the surface morphology with different diameters, such as PS(1800 M_w): PbS QDs-HA (volume fraction ~ 0.00024), PS(1800 M_w): PbS QDs-HA (volume fraction ~ 0.024) (Figure 6.2 e and f), PS(40k M_w): PbS QDs-HA (volume fraction ~ 0.00024) (Figure 6.3e), PS(850k M_w): PbS QDs-OA (volume fraction ~ 0.024), PS(850k M_w): PbS QDs-DA (volume fraction ~ 0.00024), PS(850k M_w): PbS QDs-DA

(volume fraction ~ 0.024), PS(850k M_w): PbS QDs-HA (volume fraction ~ 0.00024) and PS(850k M_w): PbS QDs-HA (volume fraction ~ 0.024) (Figure 6.4 b, c, d, e and f, respectively). The specimens of PS (1800 M_w): PbS QDs-DA (volume fraction ~ 0.024) (Figure 6.2 d) do not show domains or holes except for a few impurities or polymer domains.

The PMMA: PbS QDs system is similar to the PS: PbS QDs system, where the films show domains, holes, and stripy patterns, and some samples show relatively smooth surfaces without any special features.

The average diameters of the QD-rich domains ranged between 120-650nm, while in the holes, they were between 70-245nm. The films of PMMA (2600 M_w): PbS QDs-OA (volume fraction ~ 0.024), PMMA (2600 M_w): PbS QDs-DA (volume fraction ~ 0.00024) (Figure 6.5 b and c), PMMA(40k M_w): PbS QDs-OA (volume fraction ~ 0.00024), PMMA(40k M_w): PbS QDs-OA (volume fraction ~ 0.024) (Figure 6.6 a and b) and PMMA(1m M_w): PbS QDs-HA (volume fraction ~ 0.00024) (Figure 6.7 e) show QD-rich domains with an average diameter of 120-189-650-200-120 nm, respectively.

The holes average diameters are 70-245-95-45-110-110 nm in the films of PMMA (2600 M_w): PbS QDs-HA (volume fraction ~ 0.00024) (Figure 6.5 e), PMMA (40k M_w): PbS QDs-DA (volume fraction ~ 0.00024)(Figure 6.6 c), PMMA (40k M_w): PbS QDs-DA (volume fraction ~ 0.024) (Figure 6.6 d), PMMA (40k M_w): PbS QDs-HA (volume fraction ~ 0.00024) (Figure 6.6 e), PMMA(1m M_w): PbS QDs-OA (volume fraction ~ 0.024) (Figure 6.7 b) and PMMA(1m M_w): PbS QDs-DA (volume fraction ~ 0.00024), (Figure 6.7 c), respectively. Some films show uniform and relatively smooth surface morphology, such as PMMA (2600 M_w): PbS QDs-DA (volume fraction ~ 0.024) (Figure 6.5 d), PMMA (2600 M_w): PbS QDs-HA (volume fraction ~ 0.024) (Figure 6.5 f), PMMA (40k M_w): PbS QDs-HA (volume fraction ~ 0.024) (Figure 6.6 f).

The surface morphology of the nanocomposite films in the F8BT: PbS QDs system is uniform and smooth except for three films (F8BT 75k M_w: PbS QDs-HA (volume fraction ~ 0.024) (Figure 6.8 f), F8BT 200k M_w: PbS QDs-OA (volume fraction ~ 0.00024) (Figure 6.9 a) and F8BT 200k M_w: PbS QDs-DA (volume fraction ~ 0.00024) (Figure 6.9 c) which show holes with average diameter 40-70-100 nm, consecutively.

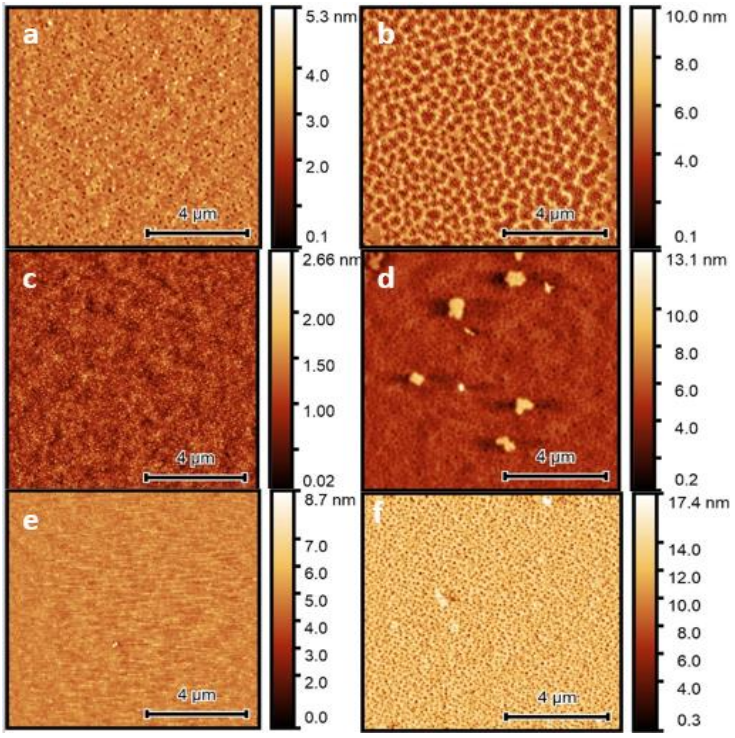

Figure 6.2/ Blend film AFM images of PS: PbS QDs with PS M_w is 1800, a) PS: PbS QDs-OA (volume fraction ~ 0.00024), b) PS: PbS QDs-OA (volume fraction ~ 0.024), c) PS: PbS QDs-DA (volume fraction ~ 0.00024), d) PS: PbS QDs-DA (volume fraction ~ 0.024), e) PS: PbS QDs-HA (volume fraction ~ 0.00024), f) PS: PbS QDs-HA (volume fraction ~ 0.024).

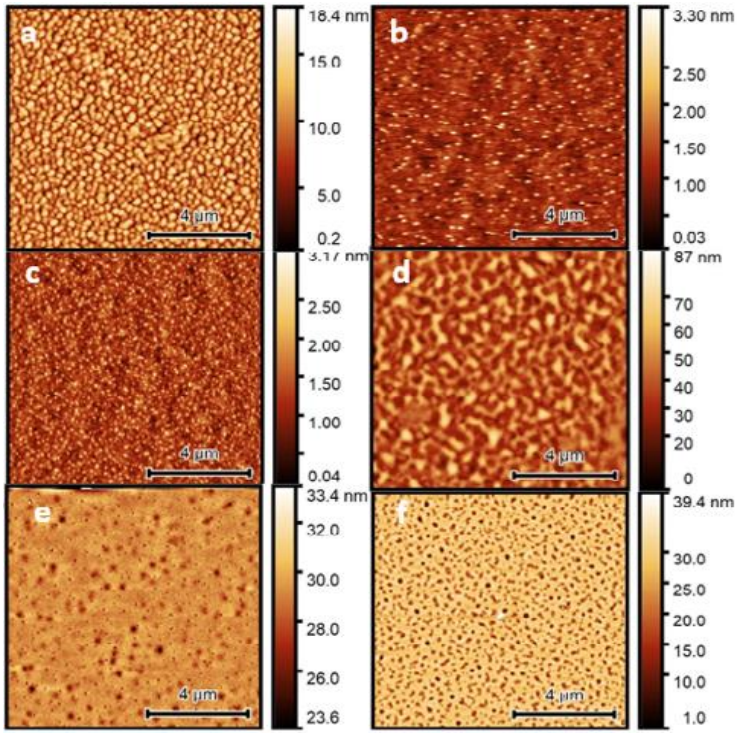

Figure 6.3/ Blend film AFM images of PS: PbS QDs with PS M_w is 40k, PS M_w is 40k; a) PS: PbS QDs-OA (volume fraction ~ 0.00024), b) PS: PbS QDs-OA (volume fraction ~ 0.024), c) PS: PbS

QDs-DA (volume fraction ~ 0.00024), d) PS: PbS QDs-DA (volume fraction ~ 0.024), e) PS: PbS QDs-HA (volume fraction ~ 0.00024), f) PS: PbS QDs-HA (volume fraction ~ 0.024).

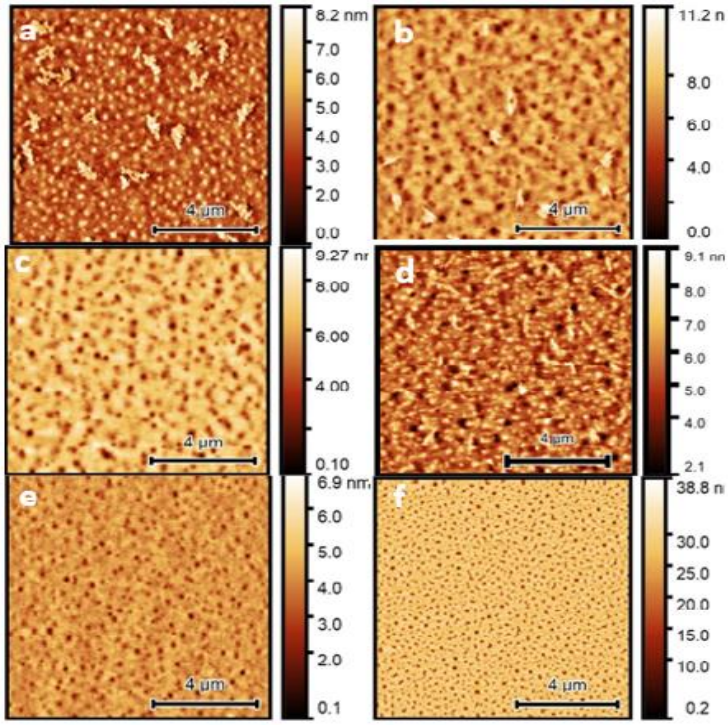

Figure 6.4/ Blend film AFM images of PS: PbS QDs with PS M_w is 850k, a) PS: PbS QDs-OA (volume fraction ~ 0.00024), b) PS: PbS QDs-OA (volume fraction ~ 0.024), c) PS: PbS QDs-DA (volume fraction ~ 0.00024), d) PS: PbS QDs-DA (volume fraction ~ 0.024), e) PS: PbS QDs-HA (volume fraction ~ 0.00024), f) PS: PbS QDs-HA (volume fraction ~ 0.024).

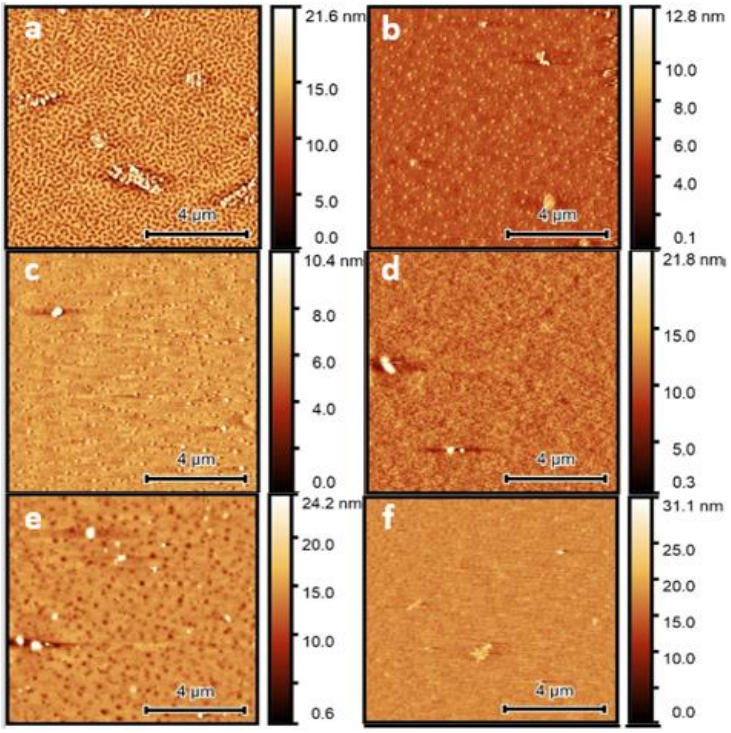

Figure 6.5/ Blend film AFM images of PMMA: PbS QDs with PMMA M_w is 2600, a) PMMA: PbS QDs-OA (volume fraction ~ 0.00024), b) PMMA: PbS QDs-OA (volume fraction ~ 0.024), c) PMMA: PbS QDs-DA (volume fraction ~ 0.00024), d) PMMA: PbS QDs-DA (volume fraction ~ 0.024), e) PMMA: PbS QDs-HA (volume fraction ~ 0.00024), f) PMMA: PbS QDs-HA (volume fraction ~ 0.024).

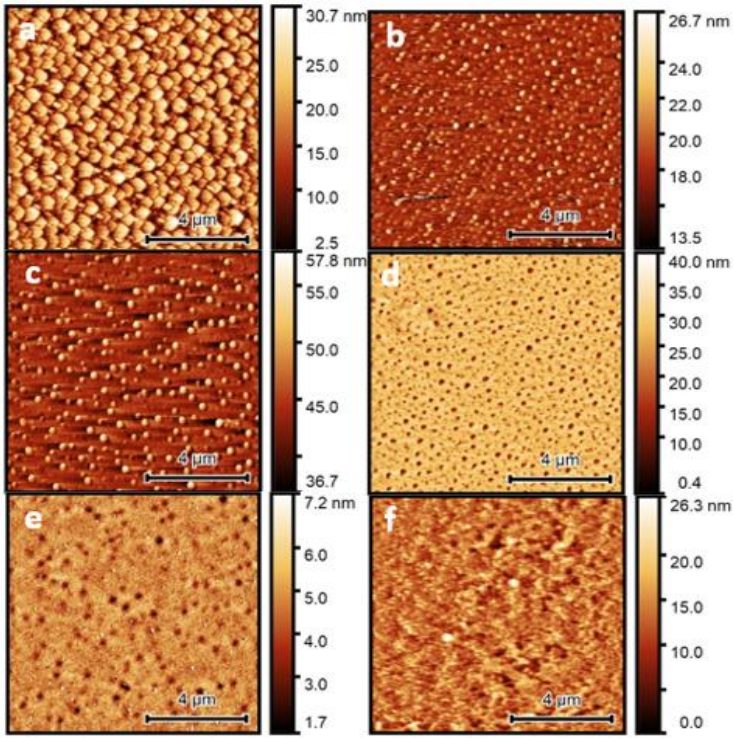

Figure 6.6/ Blend film AFM images of PMMA: PbS QDs with PMMA M_w is 40k, a) PMMA: PbS QDs-OA (volume fraction ~ 0.00024), b) PMMA: PbS QDs-OA (volume fraction ~ 0.024), c) PMMA: PbS QDs-DA (volume fraction ~ 0.00024), d) PMMA: PbS QDs-DA (volume fraction ~

0.024), e) PMMA: PbS QDs-HA (volume fraction ~ 0.00024), f) PMMA: PbS QDs-HA (volume fraction ~ 0.024).

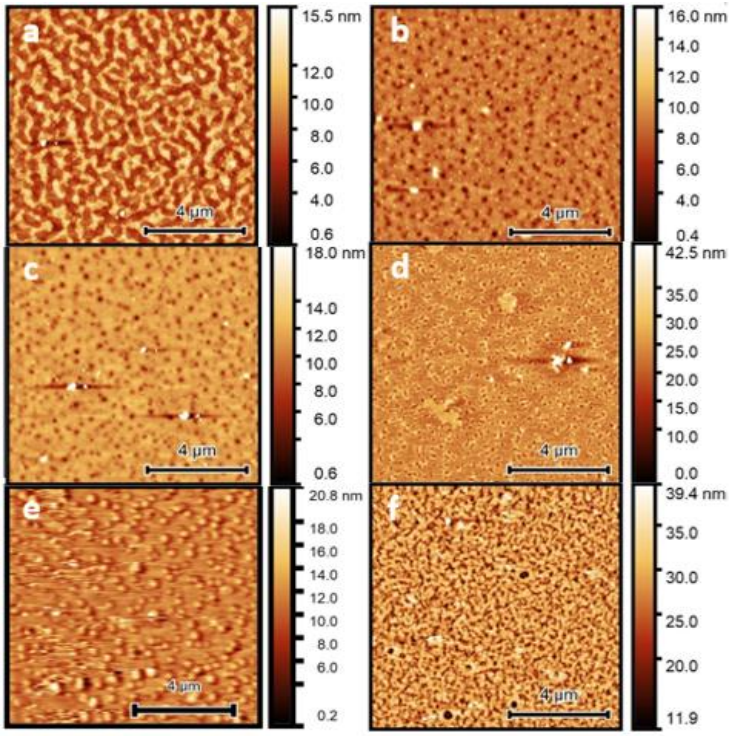

Figure 6.7/ Blend film AFM images of PMMA: PbS QDs with PMMA M_w is 1m, a) PMMA: PbS QDs-OA (volume fraction ~ 0.00024), b) PMMA: PbS QDs-OA (volume fraction ~ 0.024), c) PMMA: PbS QDs-DA (volume fraction ~ 0.00024), d) PMMA: PbS QDs-DA (volume fraction ~ 0.024), e) PMMA: PbS QDs-HA (volume fraction ~ 0.00024), f) PMMA: PbS QDs-HA (volume fraction ~ 0.024).

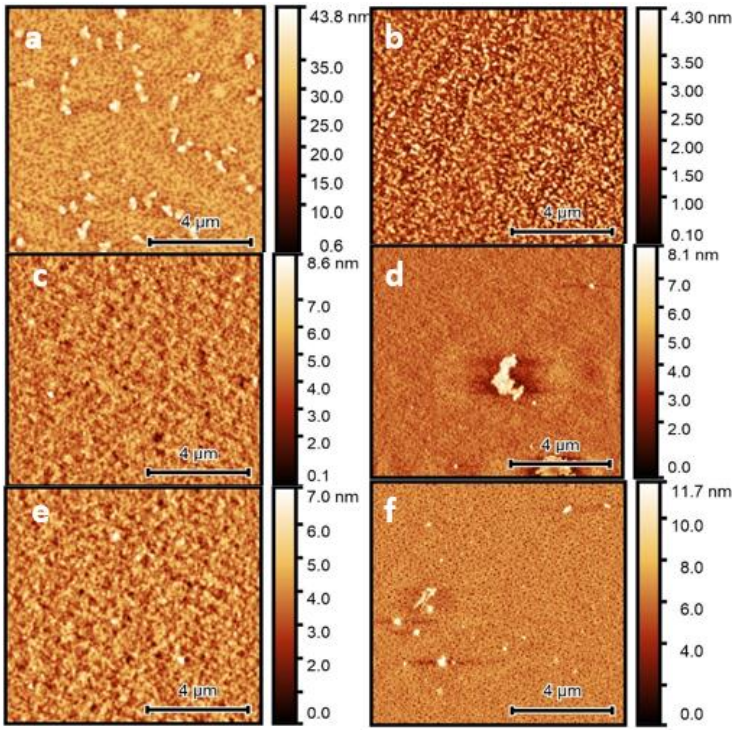

Figure 6.8/ / Blend film AFM images of F8BT: PbS QDs with F8BT Mw is 75k, a) F8BT: PbS QDs-OA (volume fraction ~ 0.00024), b) F8BT: PbS QDs-OA (volume fraction ~ 0.024), c) F8BT: PbS QDs-DA (volume fraction ~ 0.00024), d) F8BT: PbS QDs-DA (volume fraction ~ 0.024), e) F8BT: PbS QDs-HA (volume fraction ~ 0.00024), f) F8BT: PbS QDs-HA (volume fraction ~ 0.024).

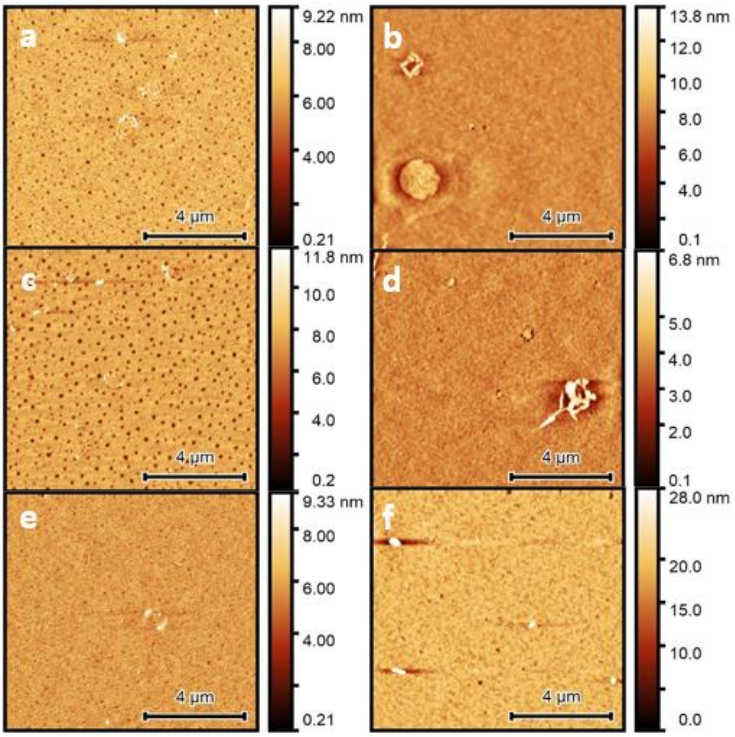

Figure 6.9/ Blend film AFM images of F8BT: PbS QDs with F8BT Mw is 200k, a) F8BT: PbS QDs-OA (volume fraction ~ 0.00024), b) F8BT: PbS QDs-OA (volume fraction ~ 0.024), c) F8BT: PbS

QDs-DA (volume fraction ~ 0.00024), d) F8BT: PbS QDs-DA (volume fraction ~ 0.024), e) F8BT: PbS QDs-HA (volume fraction ~ 0.00024), f) F8BT: PbS QDs-HA (volume fraction ~ 0.024).

sample	Average QD-rich domains (nm)	Average holes diameter (nm)
PS(1800 Mw): PbS QDs-OA (0.00024)	70	
PS(1800 Mw): PbS QDs-OA (0.024)	--------	--------
PS(1800 Mw): PbS QDs-DA (0.00024)	30	
PS(1800 Mw): PbS QDs-DA (0.024)	--------	--------
PS(1800 Mw): PbS QDs-HA (0.00024)		40
PS(1800 Mw): PbS QDs-HA (0.024)		50

Table 6.7/ Diameter of the holes and QD-rich domains in the surface morphology of the PS (1800 M_w): PbS QDs nanocomposite films.

sample	Average QD-rich domains (nm)	Average holes diameter (nm)
PS(40k Mw): PbS QDs-OA (0.00024)	250	
PS(40k Mw): PbS QDs-OA (0.024)	70	
PS(40k Mw): PbS QDs-DA (0.00024)	50	
PS(40k Mw): PbS QDs-DA (0.024)	--------	--------
PS(40k Mw): PbS QDs-HA (0.00024)		80
PS(40k Mw): PbS QDs-HA (0.024)		125

Table 6.8/ Diameter of the holes and QD-rich domains in the surface morphology of the PS (40k M_w): PbS QDs nanocomposite films.

sample	Average QD-rich domains (nm)	Average holes diameter (nm)
PS(850k Mw): PbS QDs-OA (0.00024)	200	
PS(850k Mw): PbS QDs-OA (0.024)		160
PS(850k Mw): PbS QDs-DA (0.00024)		150
PS(850k Mw): PbS QDs-DA (0.024)		75
PS(850k Mw): PbS QDs-HA (0.00024)		110
PS(850k Mw): PbS QDs-HA (0.024)		100

Table 6.9/ Diameter of the holes and QD-rich domains in the surface morphology of the PS (850k M_w): PbS QDs nanocomposite films.

sample	Average QD-rich domains (nm)	Average holes diameter (nm)
PMMA (2600 Mw): PbS QDs-OA (0.00024)	--------	--------
PMMA (2600 Mw): PbS QDs-OA (0.024)	120	
PMMA (2600 Mw): PbS QDs-DA (0.00024)	180	
PMMA (2600 Mw): PbS QDs-DA (0.024)	--------	--------
PMMA (2600 Mw): PbS QDs-HA (0.00024)		70
PMMA (2600 Mw): PbS QDs-HA (0.024)	--------	--------

Table 6.10/ Diameter of the holes and QD-rich domains in the surface morphology of the PMMA (2600Mw): PbS QDs nanocomposite films.

sample	Average QD-rich domains (nm)	Average holes diameter (nm)
PMMA(40k Mw): PbS QDs-OA (0.00024)	650	
PMMA(40k Mw): PbS QDs-OA (0.024)	200	
PMMA(40k Mw): PbS QDs-DA (0.00024)		245
PMMA(40k Mw): PbS QDs-DA (0.024)		95
PMMA(40k Mw): PbS QDs-HA (0.00024)		45
PMMA(40k Mw): PbS QDs-HA (0.024)	--------	--------

Table 6.11/ Diameter of the holes and QD-rich domains in the surface morphology of the PMMA (40k Mw): PbS QDs nanocomposite films.

sample	Average QD-rich domains (nm)	Average holes diameter (nm)
PMMA(1m Mw): PbS QDs-OA (0.00024)	--------	--------
PMMA(1m Mw): PbS QDs-OA (0.024)		110
PMMA(1m Mw): PbS QDs-DA (0.00024)		110
PMMA(1m Mw): PbS QDs-DA (0.024)	--------	--------
PMMA(1m Mw): PbS QDs-HA (0.00024)	120	
PMMA(1m Mw): PbS QDs-HA (0.024)	--------	--------

Table 6.12/ Diameter of the holes and QD-rich domains in the surface morphology of the PMMA (1m Mw): PbS QDs nanocomposite films.

sample	Average QD-rich domains (nm)	Average holes diameter (nm)
F8BT (75k Mw): PbS QDs-OA (0.00024)	--------	--------

F8BT (75k Mw): PbS QDs-OA (0.024)	--------	--------
F8BT (75k Mw): PbS QDs-DA (0.00024)	-------	--------
F8BT (75k Mw): PbS QDs-DA (0.024)	--------	--------
F8BT (75k Mw): PbS QDs-HA (0.00024)	--------	
F8BT (75k Mw): PbS QDs-HA (0.024)		40

Table 6.13/ Diameter of the holes and QD-rich domains in the surface morphology of the F8BT (75k Mw): PbS QDs nanocomposite films.

sample	**Average QD-rich domains (nm)**	**Average holes diameter (nm)**
F8BT (200k Mw): PbS QDs-OA (0.00024)		70
F8BT (200k Mw): PbS QDs-OA (0.024)	--------	--------
F8BT (200k Mw): PbS QDs-DA (0.00024)		100
F8BT (200k Mw): PbS QDs-DA (0.024)	--------	--------
F8BT (200k Mw): PbS QDs-HA (0.00024)	--------	--------
F8BT (200k Mw): PbS QDs-HA (0.024)	--------	--------

Table 6.14/ Diameter of the holes and QD-rich domains in the surface morphology of the F8BT (75k Mw): PbS QD nanocomposite films.

Changing the volume fraction of PbS QDs affects the surface morphology of the nanocomposite films in the three systems. The changes in the surface of the blend films could be due to many reasons, such as the difference in the thickness of the films, the size of crystal QD aggregation, the film surface tension and the miscibility between the polymer and the QD. The most important factor that affects the phase segregation in the surface morphology of the blend films is the miscibility between the PbS QDs and the polymers [152]. So, the nanocomposite films that show smooth and relatively uniform surface morphology may indicate a higher level of miscibility between the components of the films.

Another effect of the miscibility increase in this experiment is a decrease in the average diameter of the QD-rich domains or the holes compared to the same samples with different PbS QDs volume fractions (~ 0.0024) seen in the last two chapters. For instance, the average QD-rich domains of the domains in PS (1800 M_w): PbS QDs-OA and PS (1800 M_w): PbS QDs-DA (volume fraction ~ 0.0024) is 240 and 130nm; this decreased to ~70 and 30 nm when the PbS QDs volume fraction changed to 0.00024. Moreover, the average diameter is ~ 120 and 200 in the samples of PMMA (2600 M_w): PbS QDs-OA and PMMA(40k M_w): PbS QDs-OA volume fraction ~ 0.024, while it is ~ 280 and 1560 nm when the volume fraction of the QD ~ 0.0024.

Interestingly, many specimens in the three systems showed substantial changes in the surface morphology from making QD-poor domains with (PbS QDs volume fraction ~ 0.0024) to making holes with (PbS QDs volume fraction ~ 0.024) and (PbS QDs volume fraction ~ 0.00024). An example of this is the sample of PS(1800 M_w): PbS QDs-HA (PbS QDs volume fraction ~ 0.0024), where the average diameter of the QD-rich domains is ~ 120 nm; this turns into a hole or void with an average diameter of ~ 40 and 50 nm when changed the PbS QDs volume fraction to 0.00024 and 0.024, respectively. This behaviour includes other samples, such as PS(40k M_w): PbS QDs-HA, PS(850k M_w): PbS QDs-OA, PS(850k M_w): PbS QDs-DA, PS(850k M_w): PbS QDs-HA, PMMA (2600 M_w): PbS QDs-HA, PMMA(40k M_w): PbS QDs-DA, PMMA(40k M_w): PbS QDs-HA, PMMA(1m M_w): PbS QDs-OA and F8BT (75k M_w): PbS QDs-HA.

The voids or holes in the surface morphology of the blend films could be a cluster or aggregation of the PbS QDs on the surface of the blend films, leaving voids in the surrounding polymer matrices. The formation of holes happened due to either different solubilities or because there is a difference in the film surface tension, especially with changes in the thickness of the films. Both reasons could occur when the concentration changed from the same amount of QDs and polymers (PbS QDs volume fraction ~ 0.0024) to (PbS QDs volume fraction ~ 0.00024 and 0.024).

So, changing the PbS QDs and polymer volume fraction affects the nanocomposite films surface morphology. Substantial surface morphology differences, including QD-rich domains, QD-poor holes, stripy patterns, and relatively smooth surfaces, have been noted in this experiment. The surface morphologies of QD-poor domains, QD-poor holes and stripy patterns probably indicate relative immiscibility between the QDs and the host polymers, which leads to QDs aggregations or phase segregation in the surface morphology of the blend films. However, some films provided flat planar, relatively smooth surface structures such as PS (1800 M_w): PbS QDs-DA (PbS QDs volume fraction ~ 0.024), PMMA (2600 M_w): PbS QDs-DA (PbS QDs volume fraction ~ 0.024) and most films for the F8BT: PbS QDs system. The smooth surface structures could indicate increased miscibility between the QDs and the polymer host.

6.3.3. GISAXS

The internal morphology of the three systems (PS: PbS QDs, PMMA: PbS QDs and F8BT: PbS QDs) nanocomposite films are studied via GISAXS in this section, and the 2D reshaped images of the three systems are shown in Figure 6.10, Figure 6.11, Figure 6.12, Figure 6.13, Figure 6.14, Figure 6.15, Figure 6.16 and Figure 6.17, respectively. Most films in this experiment have exhibited aggregated QDs structures, except for a few; this could be demonstrated by the aggregation rings or peaks, which have different positions depending on the type of aggregation structures and grain size. Initially between 0.10 $Å^{-1}$ and 0.15 $Å^{-1}$. Mostly, the aggregation structure in the blend films forms HCP where the position of the reflections shows ratios $q_i/q_1 = 1, \sqrt{3}, \sqrt{4}, \sqrt{7}$, which is consistent with HCP structure. Some films, such as PS (1800 M_w): PbS QDs-HA (PbS QDs volume fraction ~ 0.00024) and PS (1800 M_w): PbS QDs-HA (PbS QDs volume fraction ~ 0.024) (Figure 6.10 e and f) form FCC-CP aggregations structure, where the positions of the reflections display ratios $q_i/q_1 = 1, \sqrt{4/3}, \sqrt{8/3}, \sqrt{11/3}$ [166, 167]; this has been explained previously to be due to paracrystalline distortion [179].

In addition, some films do not show any aggregation structure in the surface morphology, such as PS (1800 M_w): PbS QDs-DA (PbS QDs volume fraction ~ 0.024) (Figure 6.10 d), PMMA (2600 M_w): PbS QDs-DA (PbS QDs volume fraction ~ 0.024) (Figure 6.13 d) and F8BT (75K M_w): PbS QDs-DA (PbS QDs volume fraction ~ 0.024) (Figure 6.16 d). These samples showed one peak for each of them with positions in q around 0.14 $Å^{-1}$, 0.13$Å^{-1}$ and 0.15 $Å^{-1}$ for PS (1800 M_w): PbS QDs-DA (PbS QDs volume fraction ~ 0.024), PMMA (2600 M_w): PbS QDs-DA (PbS QDs volume fraction ~ 0.024) and F8BT (75K M_w): PbS QDs-DA (PbS QDs volume fraction volume fraction ~ 0.024).

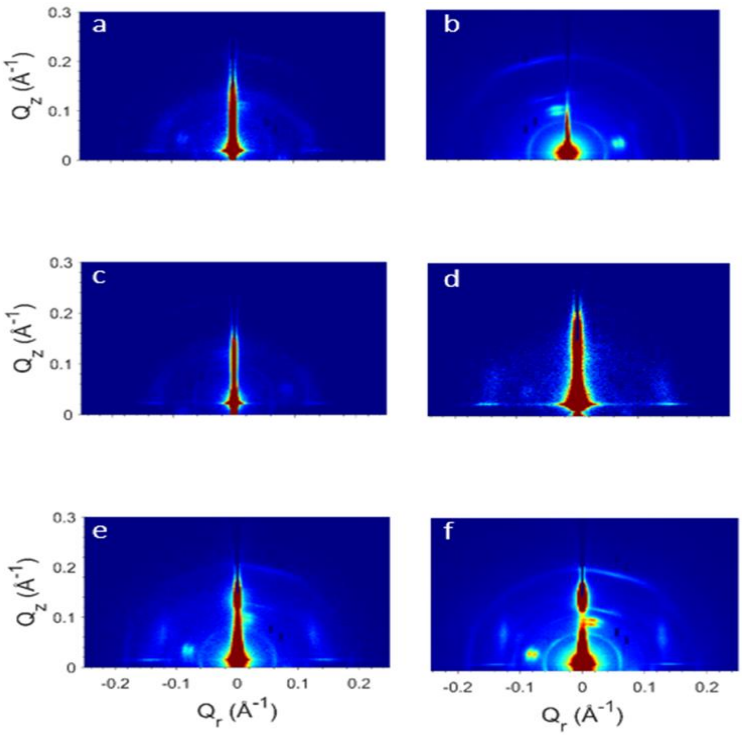

Figure 6.10/ 2D reshaped GISAXS images of the PS system samples with PS M_w is 1800, a) PS: PbS QDs-OA (volume fraction ~ 0.00024), b) PS: PbS QDs-OA (volume fraction ~ 0.024), c) PS: PbS QDs-DA (volume fraction ~ 0.00024), d) PS: PbS QDs-DA (volume fraction ~ 0.024), e) PS: PbS QDs-HA (volume fraction ~ 0.00024), f) PS: PbS QDs-HA (volume fraction ~ 0.024).

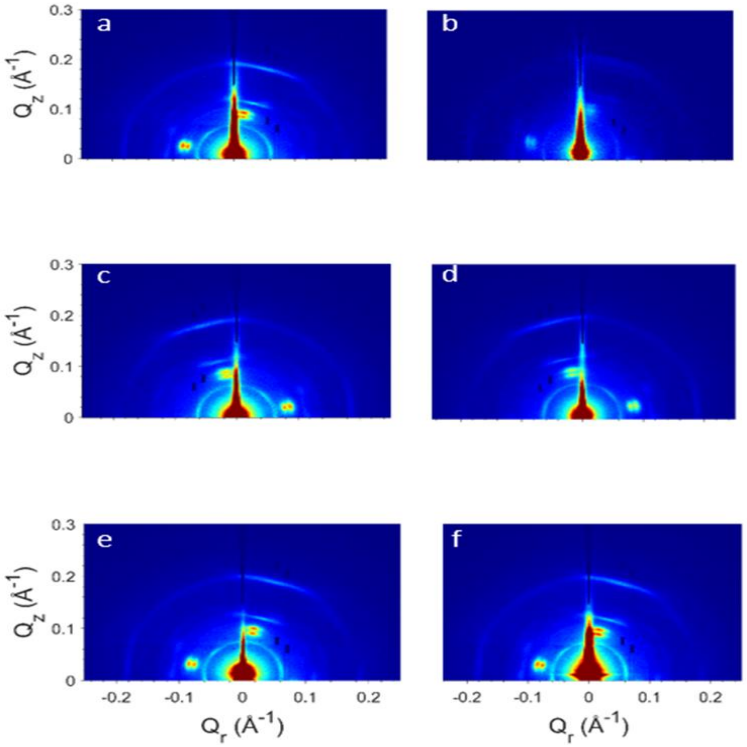

Figure 6.11/2D reshaped GISAXS images of the PS system samples with PS M_w is 40k, a) PS: PbS QDs-OA (volume fraction ~ 0.00024), b) PS: PbS QDs-OA (volume fraction ~ 0.024), c) PS: PbS

QDs-DA (volume fraction ~ 0.00024), d) PS: PbS QDs-DA (volume fraction ~ 0.024), e) PS: PbS QDs-HA (volume fraction ~ 0.00024), f) PS: PbS QDs-HA (volume fraction ~ 0.024).

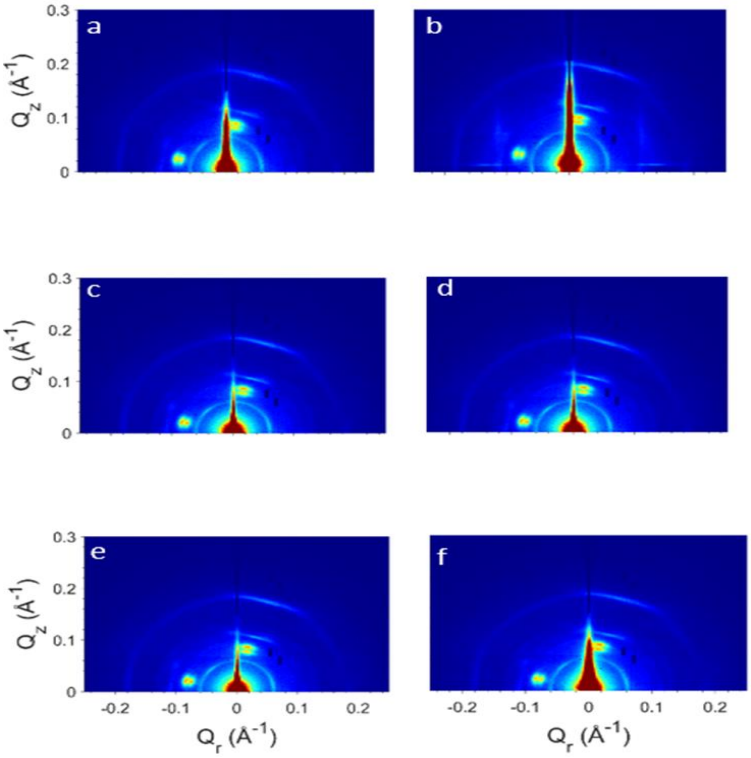

Figure 6.12/2D reshaped GISAXS images of the PS system samples with PS M_w is 850k, a) PS: PbS QDs-OA (volume fraction ~ 0.00024), b) PS: PbS QDs-OA (volume fraction ~ 0.024), c) PS: PbS QDs-DA (volume fraction ~ 0.00024), d) PS: PbS QDs-DA (volume fraction ~ 0.024), e) PS: PbS QDs-HA (volume fraction ~ 0.00024), f) PS: PbS QDs-HA (volume fraction ~ 0.024).

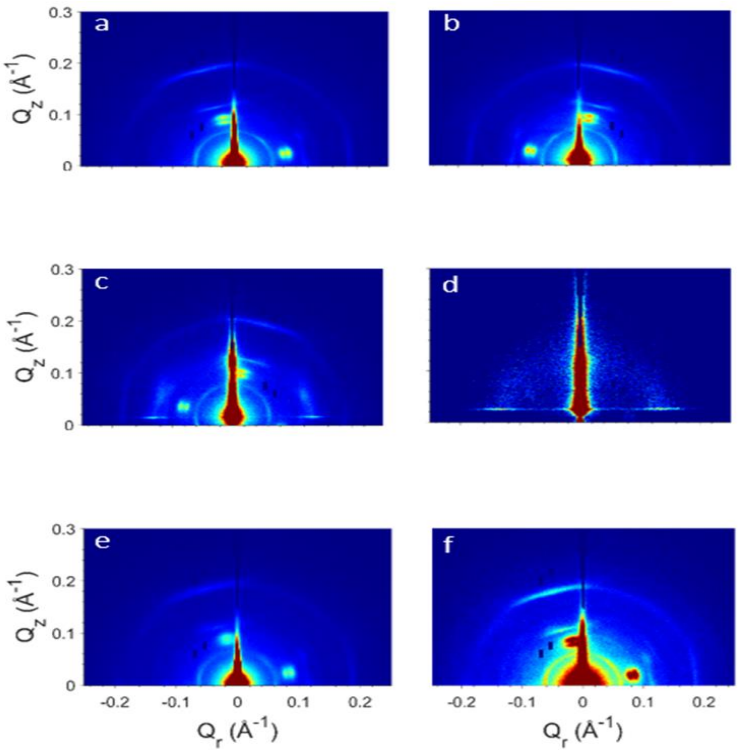

Figure 6.13/2D reshaped GISAXS images of the PMMA system with PMMA M_w is 2600, a) PMMA: PbS QDs-OA (volume fraction ~ 0.00024), b) PMMA: PbS QDs-OA (volume fraction ~ 0.024), c) PMMA: PbS QDs-DA (volume fraction ~ 0.00024), d) PMMA: PbS QDs-DA (volume fraction ~ 0.024), e) PMMA: PbS QDs-HA (volume fraction ~ 0.00024), f) PMMA: PbS QDs-HA (volume fraction ~ 0.024).

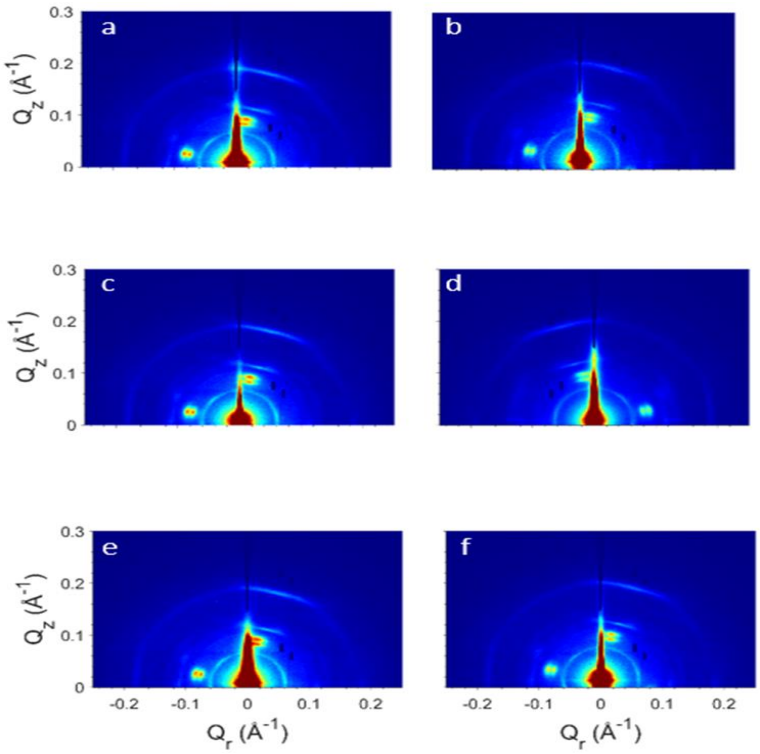

Figure 6.14/2D reshaped GISAXS images of the PMMA system with PMMA M_w is 40k, a) PMMA: PbS QDs-OA (volume fraction ~ 0.00024), b) PMMA: PbS QDs-OA (volume fraction ~ 0.024), c) PMMA: PbS QDs-DA (volume fraction ~ 0.00024), d) PMMA: PbS QDs-DA (volume fraction ~ 0.024), e) PMMA: PbS QDs-HA (volume fraction ~ 0.00024), f) PMMA: PbS QDs-HA (volume fraction ~ 0.024).

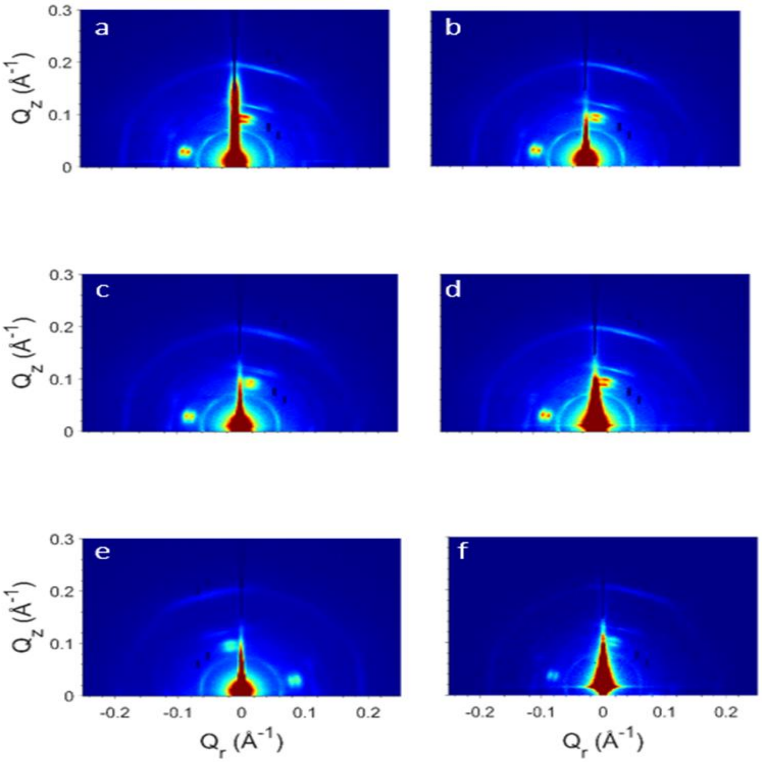

Figure 6.15/ 2D reshaped GISAXS images of the PMMA system with PMMA M_w is 1m; a) PMMA: PbS QDs-OA (volume fraction ~ 0.00024), b) PMMA: PbS QDs-OA (volume fraction ~ 0.024), c)

PMMA: PbS QDs-DA (volume fraction ~ 0.00024), d) PMMA: PbS QDs-DA (volume fraction ~ 0.024), e) PMMA: PbS QDs-HA (volume fraction ~ 0.00024), f) PMMA: PbS QDs-HA (volume fraction ~ 0.024).

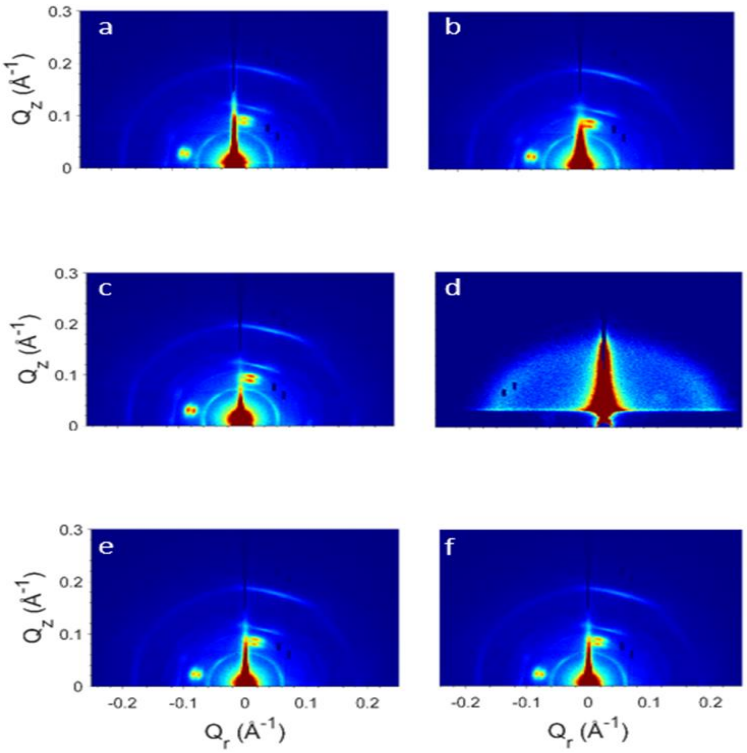

Figure 6.16/ 2D reshaped GISAXS images of the F8BT system with F8BT M_w is 75k, a) F8BT: PbS QDs-OA (volume fraction ~ 0.00024), b) F8BT: PbS QDs-OA (volume fraction ~ 0.024), c) F8BT: PbS QDs-DA (volume fraction ~ 0.00024), d) F8BT: PbS QDs-DA (volume fraction ~0.024), e) F8BT: PbS QDs-HA (volume fraction ~ 0.00024), f) F8BT: PbS QDs-HA (volume fraction ~ 0.024).

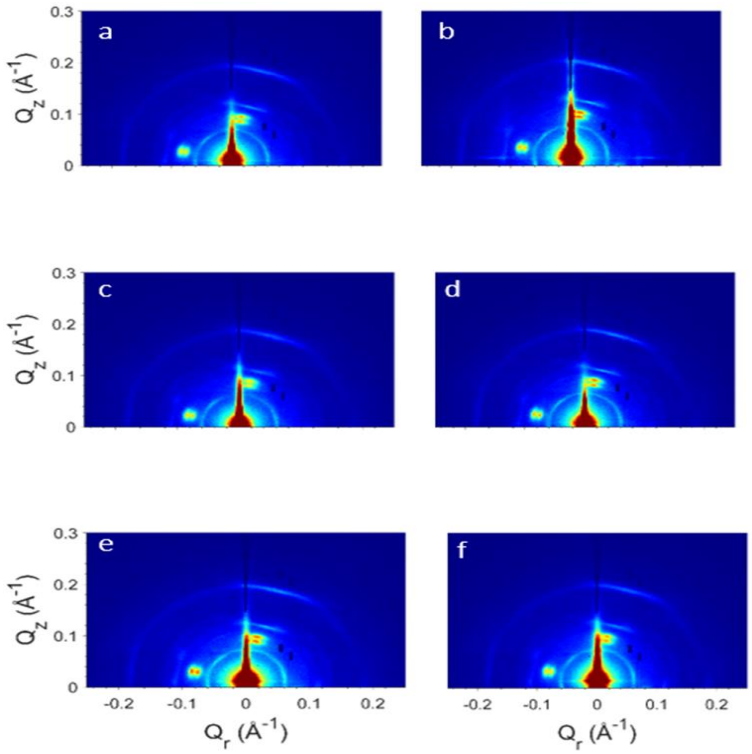

Figure 6.17/ 2D reshaped GISAXS images of the F8BT system with F8BT M_w is 200k, F8BT M_w is 200k; a) F8BT: PbS QDs-OA (volume fraction ~ 0.00024), b) F8BT: PbS QDs-OA (volume fraction ~0.024), c) F8BT: PbS QDs-DA (volume fraction ~0.00024), d) F8BT: PbS QDs-DA (volume fraction ~ 0.024), e) F8BT: PbS QDs-HA (volume fraction ~ 0.00024), f) F8BT: PbS QDs-HA (volume fraction ~ 0.024).

Similar to what has been seen in the last two chapters, the aggregation peaks were fitted to estimate the crystal grain size from the full width of the half maximum (FWHM) of the diffraction peaks using the Scherrer equation [168, 172, 176], to give insight into the aggregations structure (Figure 6.18). The data are provided in Table 8.7, Table 8.8, Table 8.9, Table 8.10, Table 8.11, Table 8.12, Table 8.13 and Table 8.14 in the Appendix.

This showed that the nanocomposite films of PS: PbS QDs, PMMA: PbS QDs and F8BT: PbS QDs form crystal grains that vary in size, measuring between 5-46 nm, 5-47nm and 9-45 nm, consecutively. The range between the biggest and smallest grains has increased in this experiment compared to the two previous experiments, where it can be seen that in some samples, such as PS (1800 M_w): PbS QDs-DA (PbS QDs volume fraction ~ 0.024) and PMMA (2600 M_w): PbS QDs-DA (PbS QDs volume fraction ~ 0.024) have grains size ≃5 nm, the grain sizes in these films almost reach the core diameter of the QDs, which is (≃

4.8nm). These two films have shown high miscibility in their surface morphology already mentioned in the AFM section, where their surface is flat planar and relatively smooth.

This could indicate that the QDs are well dispersed within the polymer matrices in these films, which is the aim of this project. It is worth noting that these two films have identical ligands (DA) and PbS QDs volume fraction 0.024. Through this research, the smaller grain sizes always come with the lower M_w of the host polymer, as seen in Chapter 4. The grain size decreased with the shorter length ligands (HA and DA), as seen in Chapter 5; in this experiment, the core diameter was almost reached by the samples that have the lowest host polymer M_w, both have DA ligands which contain (10 carbons) and have higher volume fraction of PbS QDs 0.024. This means that it possible to have the better structure in these systems (QD dispersed in polymer matrix) via decreasing the host polymer molecular weight, make the QD volume fraction more that polymer volume fraction and very thin films.

Apart from these two samples, the crystal grains size refers to an aggregation of the QDs in polymer matrices in the blend films, where it is 3-10 times bigger than the core diameter of the PbS QDs (~ 4.8nm). However, the crystal grains exhibited a decrease in size when the PbS QDs volume fraction changed to be 0.024, compared to the grains size in the last two chapters, where the grains size was ~ 5-13 and ~ 7-14 times bigger than the core diameter of the PbS QDs when varying the host polymers M_w and ligand exchange experiments.

Moreover, looking into the aggregation, the inter-particle separation was found in the same way as in the previous chapters, and the data are produced in Table 8.7, Table 8.8, Table 8.9, Table 8.10, Table 8.11, Table 8.12, Table 8.13 and Table 8.14 in the Appendix. The inter-particle separation is slightly bigger in the samples with the native ligands (OA) compared to those with HA or DA ligands. For instance, it is 9 and 8 Å in PS (40k M_w): PbS QDs-OA (volume fraction ~ 0.00024) and PS (40k M_w): PbS QDs-OA (volume fraction ~ 0.024) films; this decreased to 6 Å in films of PS (40k M_w): PbS QDs-HA (volume fraction ~ 0.00024), PS (40k M_w): PbS QDs-HA (volume fraction ~ 0.024), and 7Å PS (40k M_w): PbS QDs-DA (volume fraction ~ 0.00024) and PS (40k M_w): PbS QDs-DA (volume fraction ~ 0.024). This behaviour was noticed in all systems (PS, PMMA and F8BT). However, films such as PS (1800 M_w): PbS QDs-DA (PbS QDs volume fraction ~ 0.024) and PMMA (2600 M_w): PbS

QDs-DA (PbS QDs volume fraction ~ 0.024) are not included in this behaviour, where the QDs dispersed into the polymer matrix in these films and do not form any specific aggregate structure of the QDs.

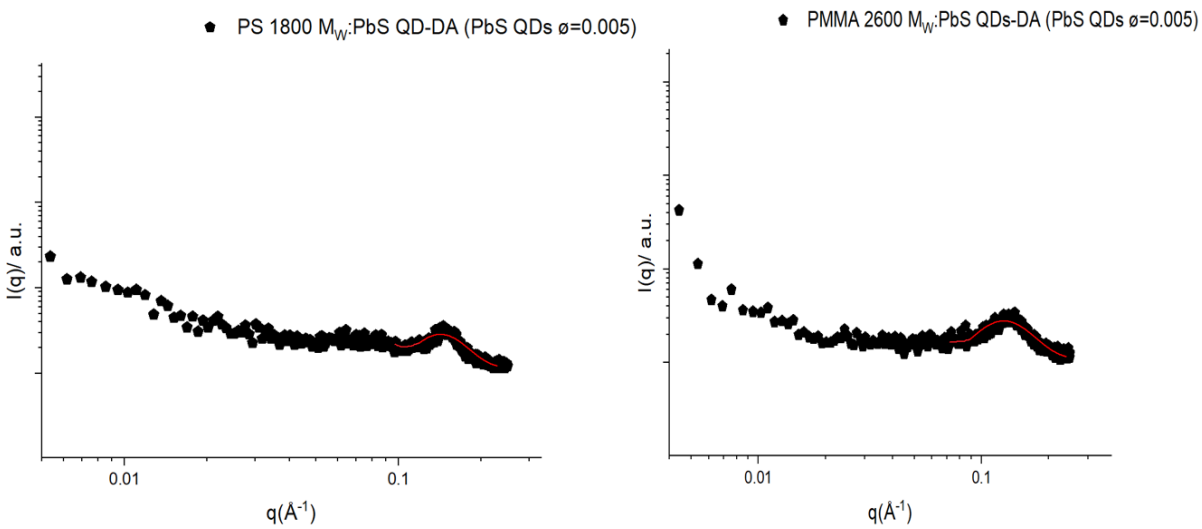

Figure 6.18/ GISAXS radially integrated data of PS (1800 M_w): PbS QDs-DA (PbS QDs volume fraction ~ 0.024) and PMMA (2600 M_w): PbS QDs-DA (PbS QDs volume fraction ~ 0.024) nanocomposite films; examples of the 1D integrated (the red lines is the Gaussian fitting).

The grain size is influenced by several factors in this experiment, such as the M_w of the host polymer, the type of Ligand used and the volume fractions of the PbS QDs. Figure 6.19 (a), Figure 6.20 (a) and Figure 6.21 (a) illustrate the effect of the polymer M_w and the ligands on the grain size in PS, PMMA and F8BT systems. It was found that the grain size increased with increasing the polymer M_w, and the crystal grain size was bigger in the samples with the native ligands (OA) compared to the same samples with the same concentrations (PbS QDs volume fraction). The effect of the host polymers M_w on the grain size has been explained previously in this thesis, particularly in the first result chapter. Raising the polymer M_w means bigger polymer R_g, which results in a lack of space for the QDs to fit in and, eventually, stronger depletion interactions between the QDs.

Also, the effect of modifying the surface chemistry of the QDs (exchange ligands) in reducing the grain size has been explained in the second result chapter of this thesis. The

miscibility between the QDs and the polymers increased more with (HA and DA) ligands than with the oleate ligands (OA). This could be due to the shorter length chains of the (HA and DA) ligands compared to the native ligands. Another possible reason for decreasing the crystal grain size with shorter carboxylic acid ligands is because they are more favourable (similar) for the polymer chains than the native ligands, which increases the interaction between the QDs and the polymer chains, resulting in more miscibility between the QDs and the polymers [180].

Figure 6.19 (b), Figure 6.20 (b) and Figure 6.21 (b) illustrate the effect of the PbS QDs volume fractions in grain size; it is clear that the crystal grains size is bigger when the PbS QDs ø decreases (volume fraction ~ 0.00024) and smaller when it increases(volume fraction ~ 0.024). This can be seen even with different variables, such as different host polymers (PS, PMMA and F8BT), varying M_w of the host polymers and different ligands. So, increasing the PbS QDs volume fraction 0.024 effectively decreases the crystal grains size in the nanocomposite films, indicating a better dispersion of the QDs with the polymer matrices. For instance, the samples of PS (1800 M_w): PbS QDs-DA (PbS QDs volume fraction ~ 0.024) and PMMA (2600 M_w): PbS QDs-DA (PbS QDs volume fraction ~ 0.024) (Figure 6.10 d and Figure 6.13 d, respectively); the 1D integrations presented in Figure 6.18) have the size of the grain ~ 5 nm, which close to the core diameter of the QDs (~ 4.8 nm). This could indicate dispersion of the QDs within the polymer matrices, not only a decrease in the grain size in these two films. These two films share identical ligands (DA) and concentrations (PbS QDs volume fraction ~ 0.024), and both have the lowest host polymer M_w compared to other films in the same system.

The potential cause for the crystal grains size to be smaller with increasing the PbS QDs volume fraction is the thickness of the blend films. As the PbS QDs volume fraction rose, the composite solution became less viscous; this made the films thinner (as seen in Figure 6.1), affecting the evaporation rate of the solvent by making it faster during the drying process. As a result, the films reach the solid state sooner, and the QDs do not have sufficient time to make large clusters or aggregations or make them at all at the same time and spin speed (it is known from the previous chapters that the QDs are well dispersed in polymer matrices in the solution state).

In addition, the higher concentration of the QDs is supposed to increase the homogeneous distribution of the QDs within the polymer matrix, which can further decrease the size of the QDs aggregations. Additionally, the homogeneous distribution of the QDs may increase the interaction between the QDs and reduce the distance over which they can diffuse and aggregate into the larger cluster, especially with the appropriate ligands. So, by increasing the PbS QDs volume fraction and decreasing the volume fraction of the polymers, the grains size reduces in the nanocomposite films.

Also, reducing the polymer volume fraction could affect the cohesive forces that cause the aggregation of the QDs, such as the depletion force by reducing it. As explained, the depletion force increases with increasing the M_w of the host polymers and decreases with lowering it. Increasing the polymer M_w and volume fraction increases the polymer R_g size, leaving less space for the QDs to fit in and increasing the depletion force effect. Similar behaviour has been seen in this experiment. Still, the grains size is smaller when increasing the PbS QDs volume fraction (0.024) and reducing the volume of the polymer, which could indicate a decrease in the effect of the depletion force that causes the aggregation of the QD, resulting in better dispersion of the QDs into the polymer matrixes (Figure 6.22).

The behaviour of the interparticle separation is not affected by changing the QDs volume fraction; it is still less than the extended length of all ligands (OA-DA-HA). It has been seen in the last chapters that the extended length of the ligands is represented by the number of carbon atoms in the ligands, which is 18 carbon atoms in the OA ligand, 10 in the DA ligands and 6 in the HA ligands[163]. According to Weidman et al., to have a full interparticle separation between the neighbouring QDs around 36 Å, 22Å and 14Å in films with OA, DA and HA ligands, respectively. This is not the situation in this experiment, where the interparticle separation is shorter than these lengths, which indicates the ligands either interdigitating between neighbouring QDs or folding back on the QDs.

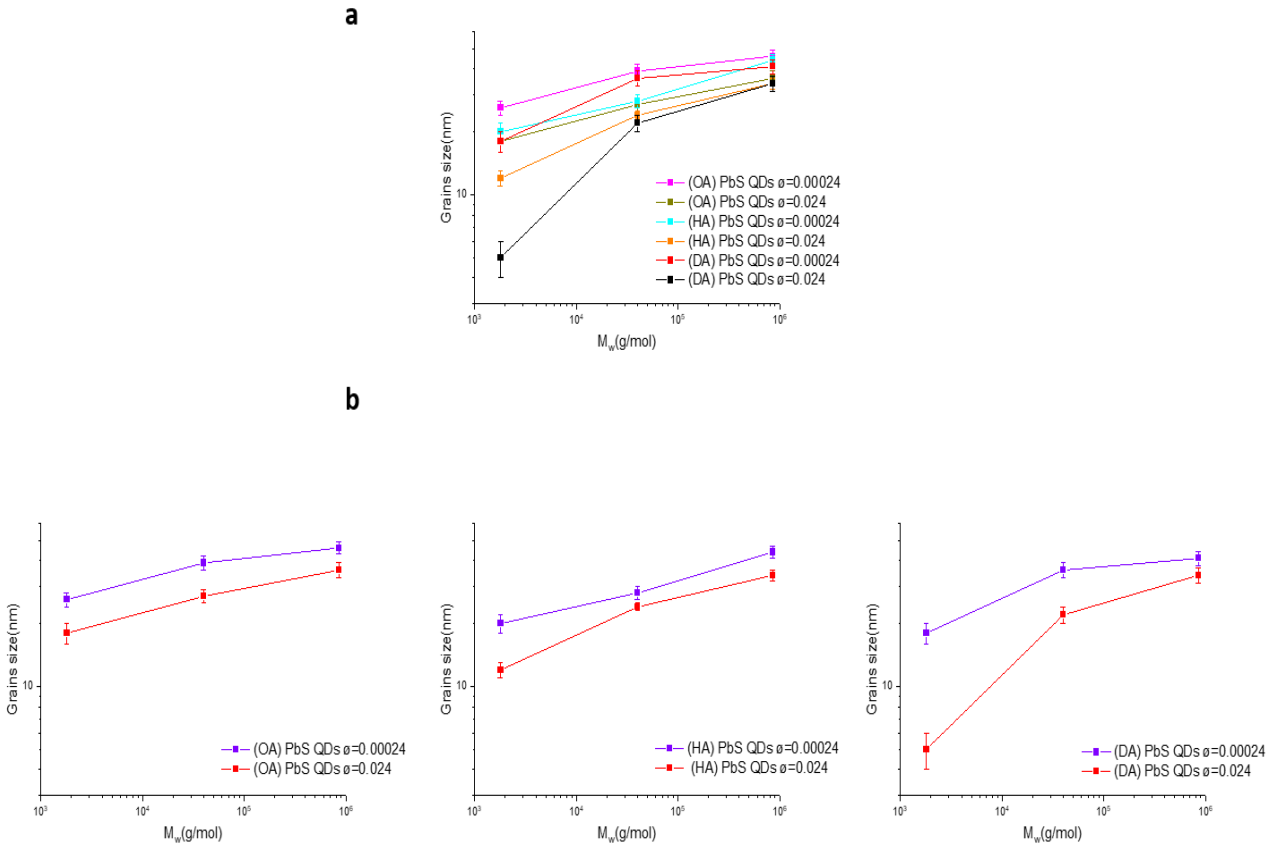

Figure 6.19/ (a) This graph illustrates the effect of Polymer M_w and different ligands on the grain size in the PS system and (b)the influence of changing volume fraction of PbS QDs on the grain size in the PS system.

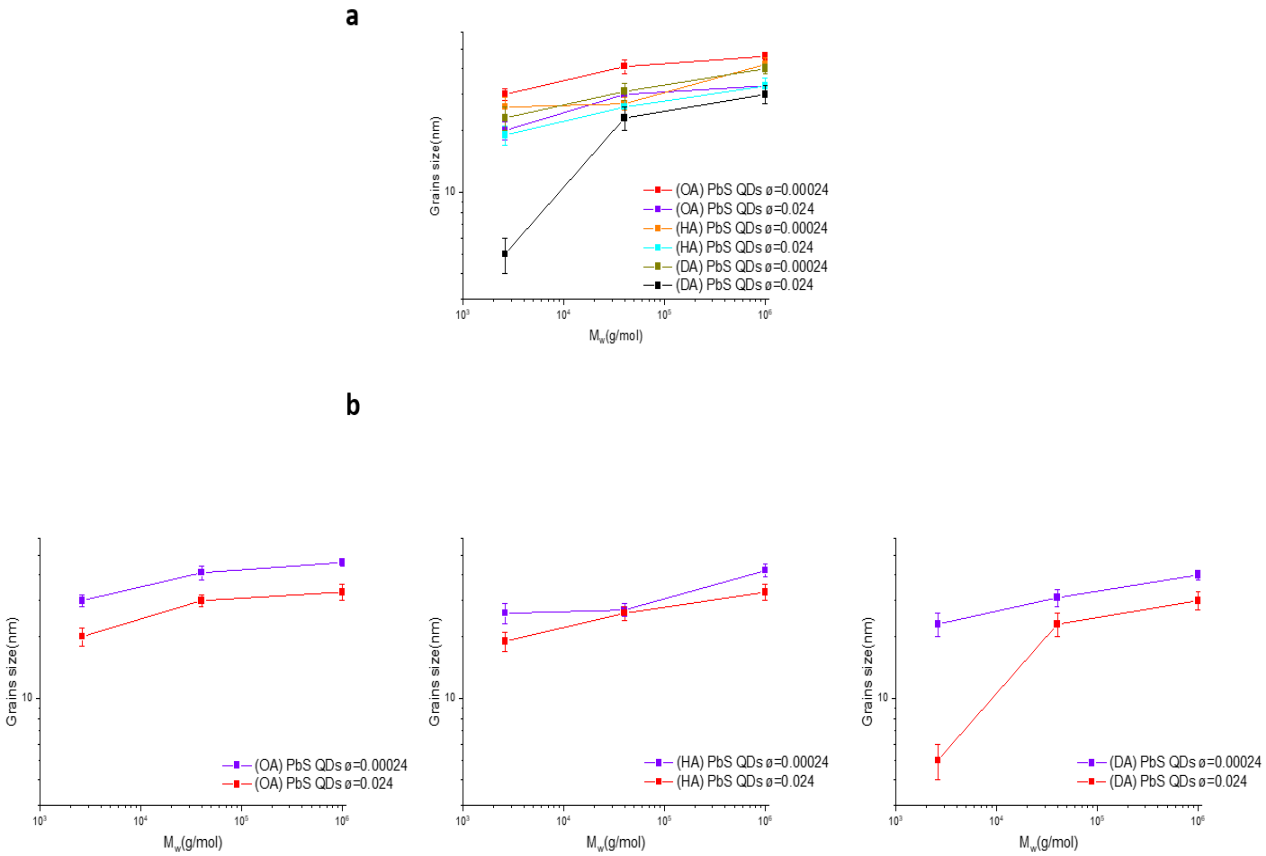

Figure 6.20/ (a) This graph illustrates the effect of Polymer M_w and different ligands on the grains size in the PMMA system, (b) The influence of changing PbS QDs volume fraction on the grain size in the PMMA system.

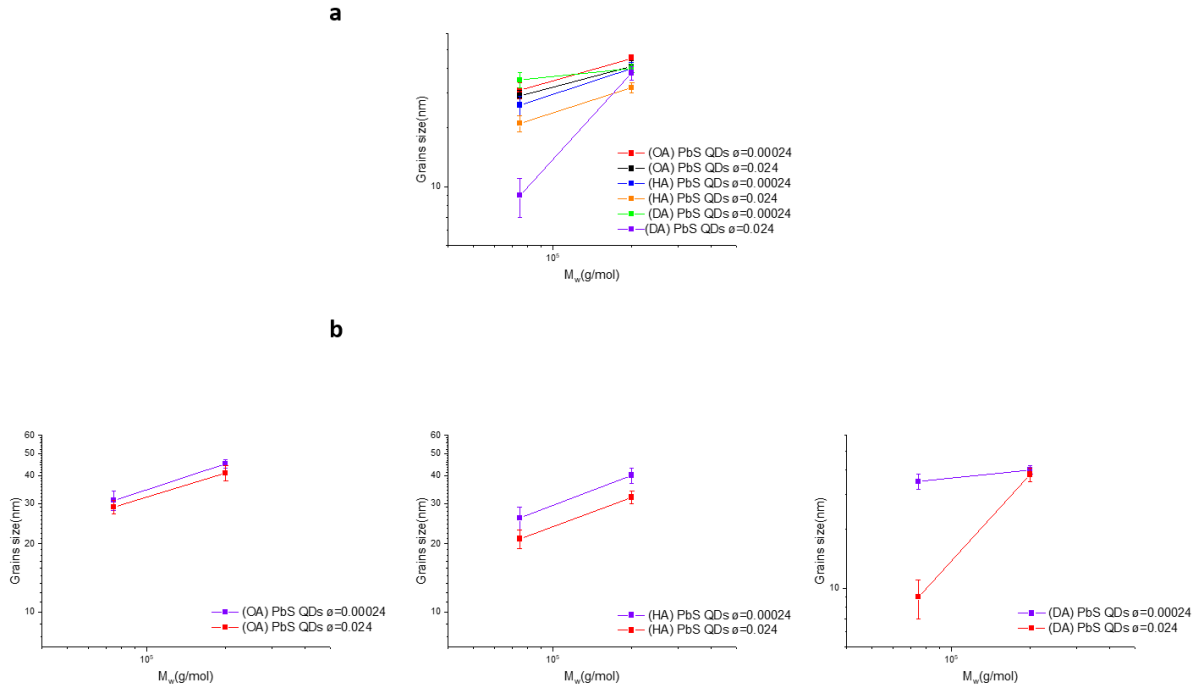

Figure 6.21/ (a) This graph illustrates the effect of Polymer M_w and different ligands on the grains size in the F8BT system, (b) the influence of the changing PbS QDs volume fraction on the grain size in the F8BT system.

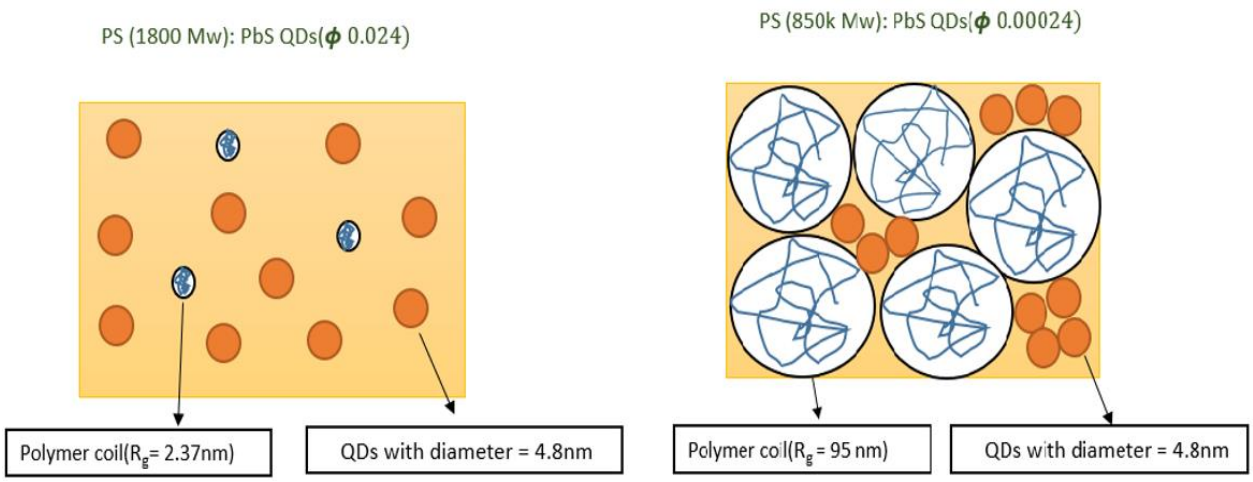

Figure 6.22/ Sketch showing the effect of polymer M_w and volume fraction of the polymer and QD blend films morphology. Increasing the polymer M_w volume fraction means increasing the polymer R_g, leaving less space for QD to fit in and a higher depletion force.

6.4. Conclusion

The effect of the PbS QDs volume fraction on the morphology of nanocomposite films was examined in this experiment. This experiment used two different volume fractions ~ 0.024 and ~ 0.00024 of the PbS QDs. The blend films vary in thickness, where the films with lower volume fraction of QDs ~ 0.00024 are much thicker than those with higher volume fractions ~ 0.024. This could be ascribed to the viscosity; decreasing the volume fraction of the PbS QDs and increasing the volume of the polymer make the nanocomposite solution more viscous, which lowers the film thinning and films reach the glassy state sooner, and this results in thicker films.

Substantial surface morphology changes were noted between the nanocomposite films, such as QD-rich domains and holes, and some films show neither of them, and they are relatively smooth on their surface. In contrast to what we have seen in the last two chapters, the surface morphological changes do not follow any specific order, and the domains and the holes vary in size. Some reasons may determine these changes in the surface morphology of the blend films, such as the miscibility between the QDs and polymers, surface tension and the thickness of the films. The domains and the holes could be QD-rich domains and become smaller in diameter compared to the samples in the last two chapters. Besides, some films do not show domains or holes in their surface and are smooth, indicating an increase in the miscibility between the components when the PbS QDs volume fraction is altered.

Most nanocomposite films form crystal aggregations with QDs in the internal structure, as either HCP or FCC-CP structure. However, the films of PS (1800 M_w): PbS QD-DA (PbS QD volume fraction 0.024) and PMMA (2600 M_w): PbS QDs-DA (PbS QDs volume fraction 0.024) are not included in this, these show a crystal grain size around 5nm which nearly reach the QD core diameter (4.8nm), and this is an indication for good dispersion of the PbS QD in these films especially with the absence of the aggregation peaks in these films. The films with PbS QD volume fraction ~ 0.024 show smaller grains than volume fraction of 0.00024 and 0.0024, especially with shorter ligand lengths (HA and DA) and lower polymer M_w. This is attributed to the effect of thickness; increasing the volume fractions of the PbS QD results in a decrease in the viscosity of the nanocomposite solution, which results in thinner films and eventually, a faster evaporation rate. This made the blend films reach the glassy state faster,

which did not give sufficient time for the system to make bigger aggregations of QDs at the same spin speed and time. Also, this could be attributed to a decrease in the effect of the depletion force that causes the QDs to aggregate when the polymer volume fraction is reduced, especially in samples with lower polymer M_w. In addition, increasing the QD volume fraction and reducing the polymer's volume could increase the homogenous distribution of the QD within the polymer, improving the interaction between the QDs.

Changing the QD volume fraction has no impact on interparticle separation. It behaves similarly to the previous two experiments in this thesis, where it is larger in films with OA ligands than in films with HA or DA ligands; in all cases, it is less than the length of the extended ligand, indicating that the ligands are either interdigitating between neighbouring QD or folding back on the QD.

Chapter 7 Conclusions and Future Work

7.1. Conclusions

This thesis presents structural studies of nanocomposite films of PbS QD embedded into three different polymer matrices (PS-PMMA-F8BT). This study includes in depth analysis of nanocomposite film thickness, surface morphology and inner morphology. These nanocomposite films often face structural issues, such as aggregation of the QD when incorporated into polymer matrix; this affects the final optical properties of these films. So, this thesis aims to have well-dispersed QD in a polymer matrix to form nanocomposite films that can be used in several different applications. To achieve the main objective of the thesis, there are some processing aspects that the thesis has examined and studied in detail, such as the effect of the host polymer M_w on the morphology of the nanocomposite films, the impact of exchanging ligands from the native oleic acid (OA) ligand to shorter ligand like Hexanoic acid (HA) and Decanoic acid (DA), and the effect of altering QD volume fraction.

The host polymer M_w affects the blend film thickness, surface morphology and inner morphology, as seen in Chapter 4. The thickness was measured via ellipsometry. The thickness increased with increasing host polymer M_w in all three systems (PS –PMMA-F8BT), and this is attributed to the increase in the viscosity of the solution as the host polymer M_w increased; increasing the M_w of the host polymer means increasing the initial viscosity of the solutions, which causes the thickness of the blended films to increase due to the change in the rheology of the films altering when spin coated. In simple terms, the ability to thin a polymer solution by shear forces becomes harder as the viscosity of the solution increases.

The surface morphology of the nanocomposite films was characterised using the highly sensitive technique of AFM; the blend films showed QD-rich domains on the surface morphology that varied in size and shape. From the AFM images, the average QD-rich domains diameter was extracted, and it was found that it increased with increasing M_w of the host polymer; for example, it was 240nm in the film of PS 1800 M_w: PbS QDs-OA; this

increased to 1280nm in the film of PS 350k M_w: PbS QD-OA. This is due to the effective change in the depletion force that causes the QD to aggregate, which can be partially controlled by the choice of host polymer M_w. However, some films with higher polymer M_w, such as PMMA (1.5M M_w): PbS QDs-OA, PS (850k M_w): PbS QDs, PS (1.5m M_w): PbS QDs-OA, and F8BT (200k M_w): PbS-OA, their surface morphology shows no QD-rich domains. This could be because of the high viscosity of these solutions, which causes a reduction in the QD aggregation kinetics, preventing QD-poor domains from forming on the surface morphology at the short timescales encountered in the spin coating.

The inner morphology of the blend films and precursor solutions was characterised via GISAXS; firstly, the SAXS solution scattering showed well-dispersed QD in the polymer matrix precursor solution, and the QD core diameter was measured as ($\simeq$ 4.8nm). However, the film GISAXS scattering showed different crystal grain sizes and interparticle separation. The grain sizes ranged between 37-56nm, 25-59nm and 52-62 nm in PS, PMMA and F8BT systems, respectively; this is 5 to 13 times bigger than the PbS QD-OA core diameter (4.8nm), which indicates aggregation of the QD due the depletion force, the QD aggregates in all nanocomposite films formed HCP structure in all specimens studied. The grain size increased with increasing host polymer M_w; this is attributed to the change in the depletion force that was affected by the difference in the host polymer M_w. The interparticle separation varied between the films in PS and F8BT systems, ranging between 6-9 Å and 7-8 Å, respectively, while it was 8 Å in the PMMA system; this is probably due to the ligands either being tilted or partially interdigitated in neighbouring QD in all systems because it is lower than the extended length of the ligands.

Chapter 5 examined the effect of exchanging ligands on the nanocomposite film morphology. The native ligand Oleic Acid (OA) was replaced with Hexanoic Acid (HA) and Decanoic Acid DA; these are shorter-length carbon chain ligands than the native ligand. This experiment applied three different M_w of PS and PMMA (low-medium-high) and the two accessible M_w of F8BT. The thickness of the blend films increased with increasing polymer M_w. At the same time, it decreased compared to the films with OA ligands, ascribed to the shorter length of the HA and DA ligands; this results in a reduction in the size of the QD

(core + shell), which changes the volume fractions of the QD, resulting in decreased viscosity of the solution with HA and DA ligands compared to the solution with OA ligands.

The AFM probed the surface morphology of the blend films, which showed QD-rich domains that vary in size from one sample to another. The average diameter shows a reduction in these QD-rich domains compared to the samples with native ligands (OA). This is due to the HA and DA ligands' shorter chain lengths modifying the interaction parameters between the polymer chains and QD, such that there is a much more favourable interaction with the polymer chains than with the native ligands. This results in better miscibility and compatibility between the polymer components of the nanocomposite films. The polymer M_w still has an effect, where the QD-rich domain average diameter increased with increasing molecular weight.

GISAXS was used to analyse the internal morphology; first, solution scattering shows the dispersion of PbS QD into the polymer matrix, and the diameter of the core QD is ≃4.8nm. Second, thin film scattering demonstrates that after the solvent evaporated, the PbS QD aggregated due to the depletion interaction. The QD aggregates form two distinct structural phases, HCP and FCC-CP, and the crystal grain sizes in PS: PbS QDs-HA and DA, PMMA: PbS QD-HA and DA, and F8BT: PbS QD-HA and DA systems ranged between 25-41nm, 23-51nm, and 37-49nm, respectively. The grain size increased with host polymer M_w, and compared to films that have OA ligands, the grain size was somewhat reduced; for instance, the crystal grain size was 37nm in the film of PS: PbS QD-OA; this decreased to 25nm in PS: PbS QD-HA and to 26nm in PS: PbS QDs-DA. This is ascribed to the shorter length ligands of HA and DA compared to native ligands (OA), which increases the interactions between QD-QD and QD-polymer, reducing the driving force for QD aggregation and increasing the miscibility between the QD and polymers.

The interparticle separation was reduced in HA and DA ligand specimens compared to OA ligand samples; this was expected due to the longer chain length of the OA (18 carbons) compared to DA (10 carbons) and HA (6 carbons). Nonetheless, it is shorter than the ligands' extended length, indicating that the ligands are tilted or partially interdigitated in surrounding QD.

Chapter 6 investigated the influence of changing the volume fraction of PbS QD and polymer on the morphology of the nanocomposite films. This experiment utilised two distinct volume fractions of PbS QD (volume fraction ~ 0.024 and ~ 0.00024). The thickness of the blend films differs, with lower volume fractions of QD ~ 0.00024 being significantly thicker than higher volume fractions ~0.024. This could be attributed to viscosity; decreasing the volume fraction of PbS QD and increasing the volume of the polymer make the nanocomposite solution more viscous, reducing component movements and enabling films to reach the solid state quicker, which results in thicker films.

Notable surface morphological changes, such as QD-rich domains and holes, were observed between the nanocomposite films, with some films exhibiting neither and being very smooth on their surface. In contrast to the previous two chapters, the surface morphological changes are not in a specific sequence, and the domains and holes vary in size. Some factors influence these changes in the surface morphology of the blend films, such as the miscibility of the QD and the host polymer, surface tension, and film thickness. The domains and holes could be QD-rich domains with smaller diameters than the samples in the previous two chapters. Furthermore, some films have smooth surfaces with no domains or holes, indicating increased compatibility between the components as the PbS QD volume fraction is altered.

In the internal structure investigated via GISAXS, the aggregation of the QDs forms a crystal grain in the nanocomposite films. However, this is not include some specimens, such as PMMA (2600 M_w): PbS QDs-DA (PbS QDs volume fraction ~ 0.024) and PS (1800 M_w): PbS QD-DA (PbS QD volume fraction ~ 0.024), where the crystal grain size is around 5nm and nearly reaches the QD core diameter (4.8nm), and this could be an indicator of good PbS QD dispersion in these films. Generally, the films with higher PbS QD volume fraction ~ 0.024 show smaller crystal grains than the samples with lower PbS QD volume fraction ~ 0.00024, also smaller grains than samples with PbS QDs volume fraction ~ 0.00024 that are seen in the previous chapters. This is due to the thickness of the blend films. As the PbS QD volume fraction rose, the composite solution became less viscous; this made the film thinner, affecting the evaporation rate of the solvent by making it faster during the drying process, which does not provide enough time for the system to create larger aggregations of QD at the

same spin speed and time. This could also be related to an increase in the homogeneous distribution of QDs within the polymer, which increases QD interaction.

The interparticle separation is largely unaffected by changing the volume fraction of the QDs. It behaves similarly to the last two experiments in this thesis, where it is greater in films packed with OA ligands than in films packed with HA or DA ligands; in all cases, it is less than the length of the extended ligand, indicating that the ligands are either interdigitating between surrounding QDs or folding back on the QDs.

The aim of this thesis is to find conditions that lead to a well-dispersed QD in a polymer matrix to have a functional nanocomposite film that can be used in applications. This is not fully achieved except in films of (1800 M_w): PbS QD-DA (PbS QD volume fraction ~ 0.024) and PMMA (2600 M_w): PbS QDs-DA (PbS QDs volume fraction ~ 0.024). This means that, to have a well-dispersed QD in the polymer matrix you need to make films with low host polymer M_w, high QD loading and very thin films.

7.2. Future work

Firstly, following the completion of the PhD study, one essential goal for the future is to publish the work from Chapters 4 to Chapters 6 in a relevant journal.

Polymer nanocomposites are employed in various applications, from high-tech and high-performance materials to daily household goods. Nanocomposites are a rapidly developing field with many opportunities for future exploration. Several additional experimental parameters and ideas were identified during this thesis to improve the initial objectives. To stay within the project scope, and due to time constraints and instrument limitations, not all ideas could be addressed through to completion. However, from a technological perspective, many challenges and obstacles must be overcome before these materials can reach their full potential in real-world applications. So, I will discuss a few strategies and ideas that could improve the current research in the following sections.

On the materials side, this project used relatively simple amorphous homopolymers (PS, PMMA and the more complicated semicrystalline polymer F8BT). The amorphous polymers were chosen, as we can gain more from understanding lower complexity situations and can also easily source highly monodisperse polymers in a wide range of molecular weights, which this thesis has focused on. However, the next step may include using more complex architectures like block copolymers such as polyethylene-vinyl acetate (PEVA) to control the interactions between the QD and polymer matrix more precisely. Future work may also include using other lead chalcogenides QD such as CdS, PbSe and CdSe to examine if we can generalise the processing routes on PbS QD on whole lead chalcogenides QD. Also, future work could expand to include more efficient QD like lanthanide QD.

It may be that we can use general trends in our choice of ligand to enable us to switch between different QDs. The ligands are essential for the QD: polymer system, where they play an important role in the QD overall stability, and solubility and assist in nanocrystal growth in a wide range of organic solvents. The OA ligands are considered ideal for controlling the size and shape of QD in organic solutions. However, when introducing QD into other matrices, such as polymers, the insolating nature of OA ligand for interactions leads to structural issues such as aggregation or phase separation of the components. So, for specific applications, such as optoelectronics, it is helpful to add some more complex ligands. In this thesis, the short-length carboxylate ligands (HA and DA) were used to exchange with the long chains native ligands (OA); this resulted in some changes in the surface and internal morphology of the nanocomposite films, such as smaller QD-poor domains and grain size. However, future work may involve using even more complicated functional ligands with specified optoelectronic properties, for instance, Benzoic acid (BA), Hydrocinnamic acid (HCA) and Naphthoic acid (NA); these ligands are expected to tune the QD surface chemistry and interfacial properties, which may result in more control of the relative interaction between the nanoparticle and the polymer, and then achieve better QD dispersion in the host polymer and so ultimately improve both the electronic and optical properties of the nanocomposite films.

Future work may also include other materials, such as Organic-inorganic nanocomposite films made from a combination of colloidal quantum dots and small-molecule organic

semiconductors, which are promising prospects for high-efficiency, low-cost solar energy harvesting systems.

On the processing routes side, one processing route (spin coating) was used in this thesis because I have been focusing on different aspects; the samples were deposited on clean silicon substrates and spun at 2000 rpm for 30s. Different processing routes may be considered in the future, such as the effect of viscosity during the kinetics of the drying process. As the solvent leaves, the film becomes very viscous and finally glassy, which locks in the nanostructure. So, it might be expected that higher molecular weight materials with a high glass transition temperature in a more volatile solvent (more volatile than toluene) would lead to a reduction in aggregation because the mobility of the QD would decrease more rapidly due to faster vitrification.

Moreover, having insight into the formation of nanocomposite films during the coating process is of consequence and important and will be considered in future work. This would be achieved via high-speed stroboscopic fluorescence microscopy or in situ grazing incidence X-ray scattering (GIXS). These reveal how polymers and colloidal quantum dots self-assemble during blade coating, providing insight into the factors affecting the final blend films in such systems. These methods allow the intensity to be directly mapped to composition, accurately evaluating compositional changes during the spin coating process. It is difficult as the high spin speed reduces the spatial resolution of data obtained from experiments. However, some studies have been done using similar approaches before. Moreover, future work should include the photophysics of the nanocomposite films, such as photoluminescence (PL) spectra and relate the results to their morphology and the processing routes.

On the characterisation side, many tools and instruments are employed to characterise the nanocomposite, including spectroscopy and microscopy. Small-angle X-ray scattering (SAXS), ellipsometry, and Atomic Force Microscopy (AFM) are the principal characterisation techniques that have been used in the current study. However, future work may include additional instruments, such as Small-angle neutron scattering (SANS). This is highly penetrating uses natural (or isotopically labelled) nuclear contrast, and exhibits

exceptional ability in determining QD ligand structure when combined with rigorous chemical-physical analyses (e.g., concentration and mass measurements) and provides additional information to complement SAXS or the microscopy measurements (AFM, TEM or SEM).

Finally, the field of polymer physics is a rich field that is full of research opportunities and is widely used in applications in our daily lives. I did some work on this thesis, but I think the future will be bright ahead of me. Hopefully, the PhD phase will be the first step of many steps, and I contribute to the progress in this field.

Chapter 8 Appendix

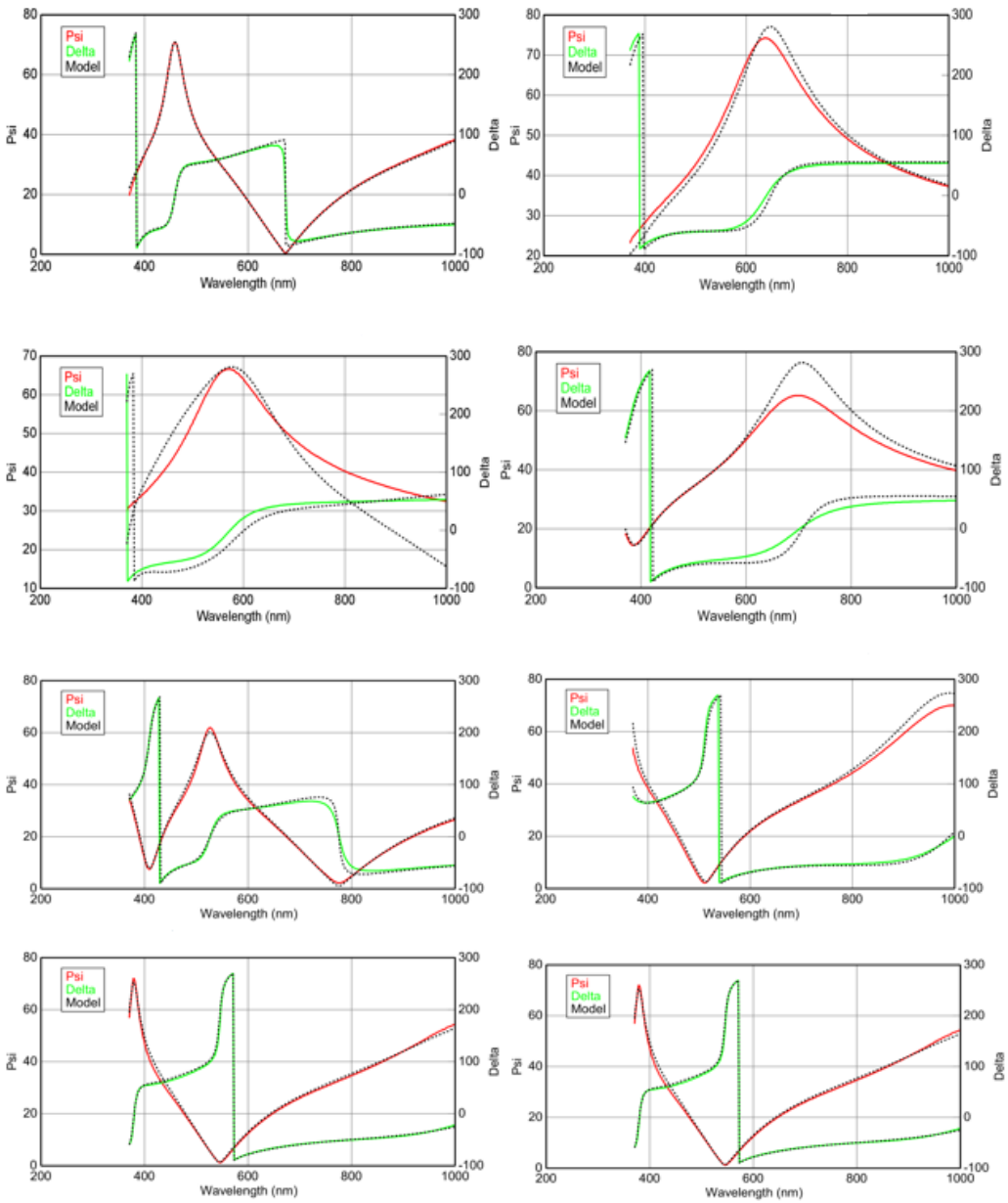

Figure 8.1/ Ellipsometry data for PS: PbS QDs-OA blends films.

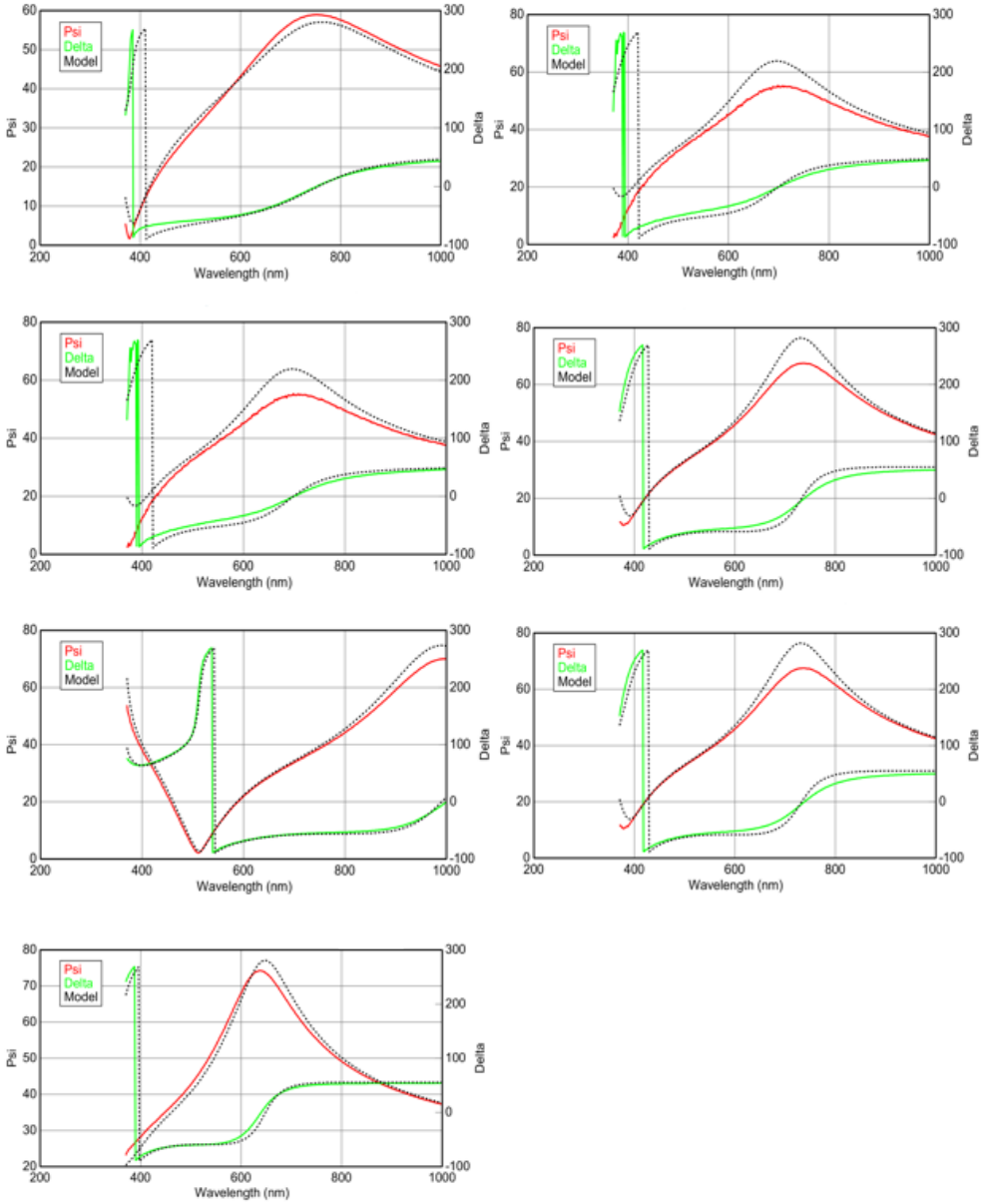

Figure 8.2/ Ellipsometry data for PMMA: PbS QDs-OA blends films.

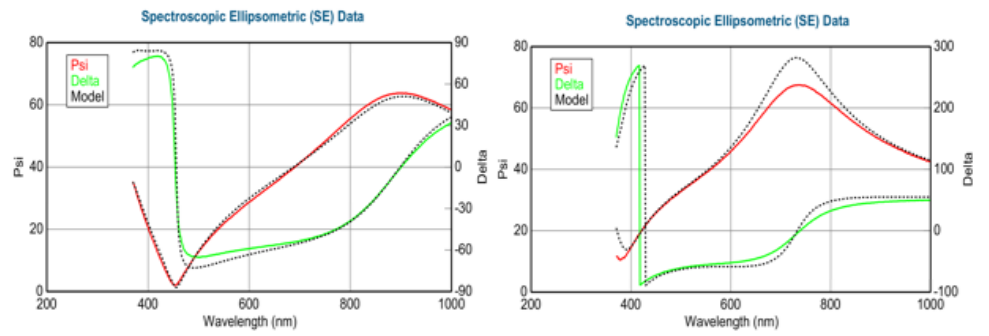

Figure 8.3/ Ellipsometry data for F8BT: PbS QDs-OA blends films.

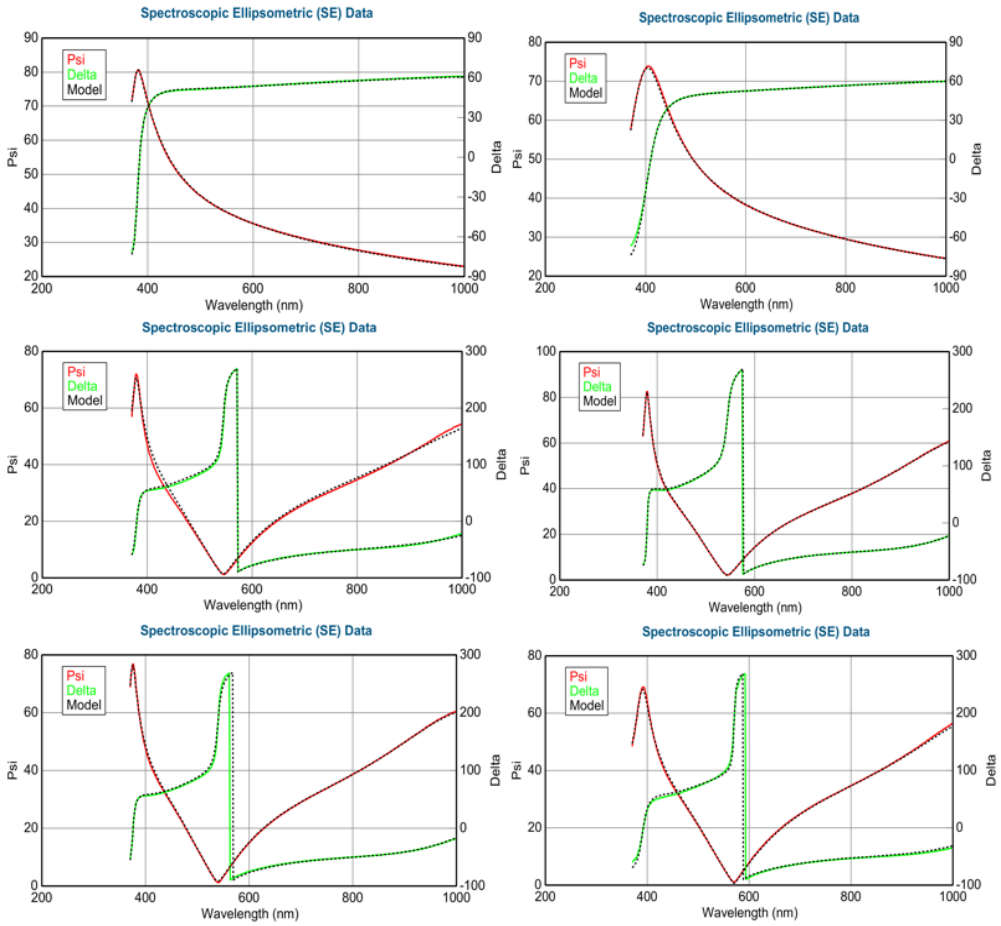

Figure 8.4/ Ellipsometry data for PS: PbS QDs-HA and DA blend films.

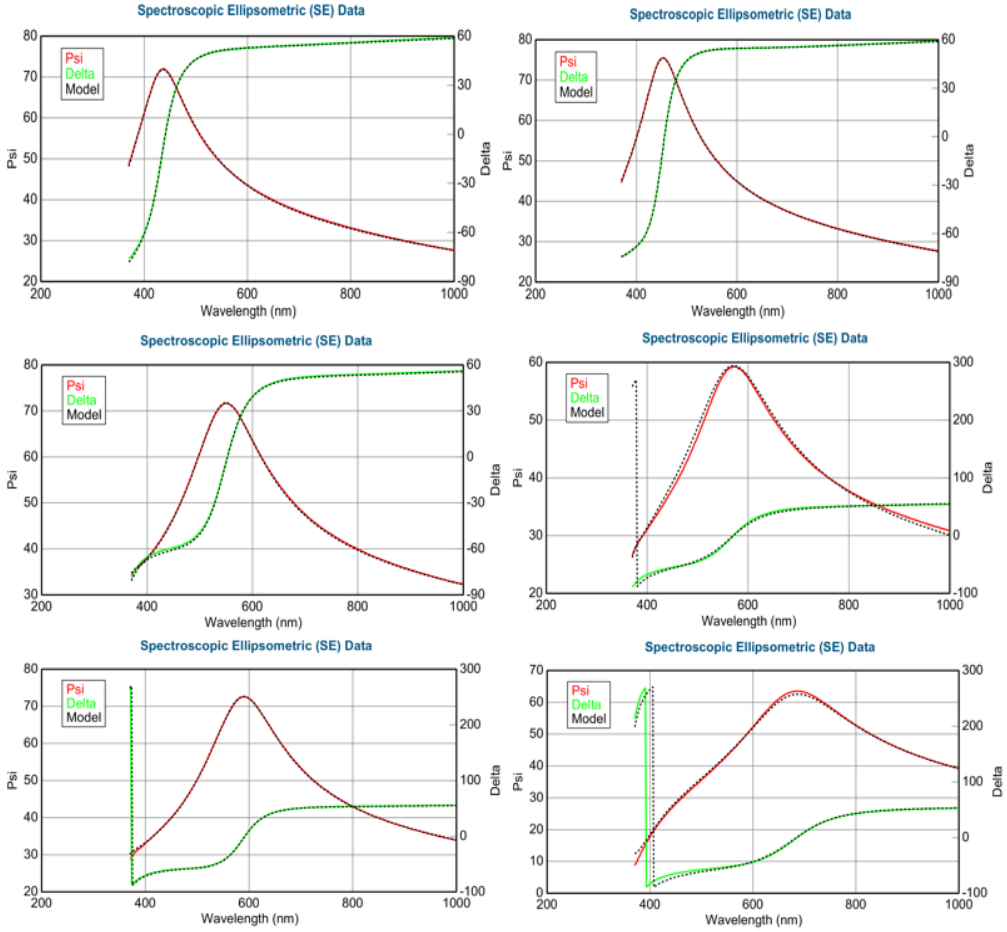

Figure 8.5/ Ellipsometry data for PMMA: PbS QDs-HA and DA blend films.

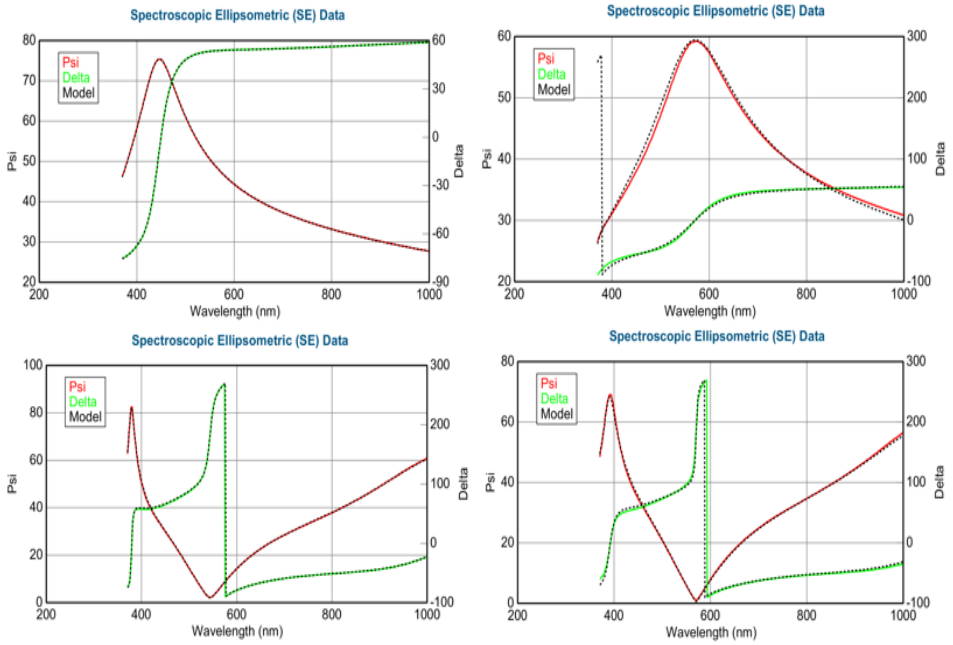

Figure 8.6/ Ellipsometry data for F8BT: PbS QDs-HA and DA blend films.

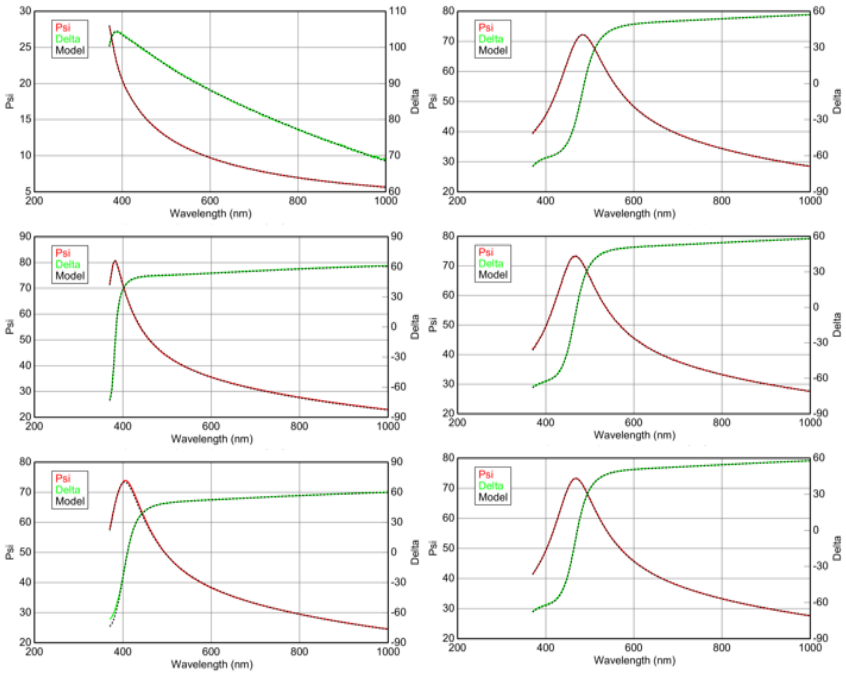

Figure 8.7/ Ellipsometry data graph of PS (1800): PbS QDs blend films with different ligands and concentrations.

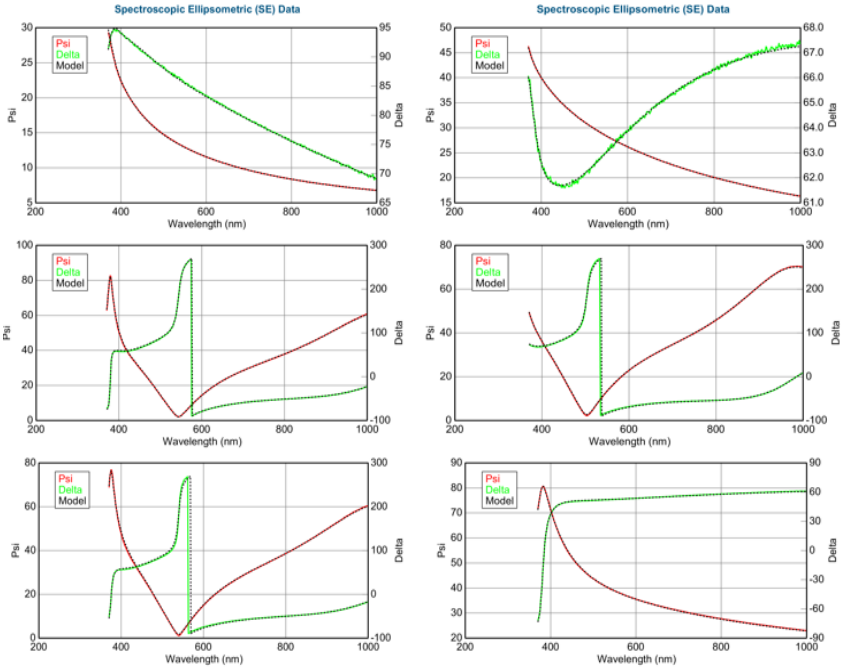

Figure 8.8/ Ellipsometry data graph of PS (40k): PbS QDs blend films with different ligands and concentrations.

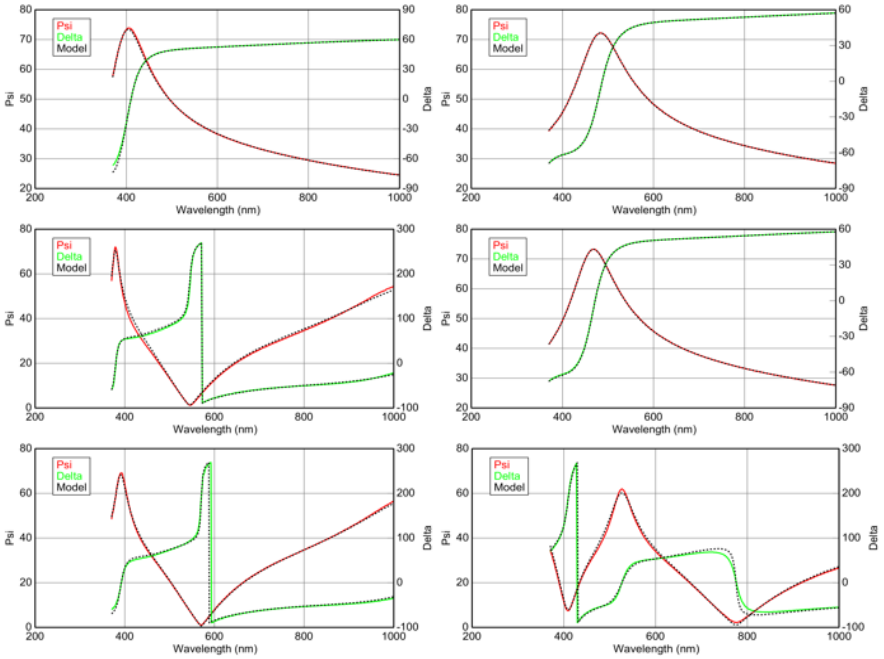

Figure 8.9/ Ellipsometry data graph of PS (850k): PbS QDs blend films with different ligands and concentrations.

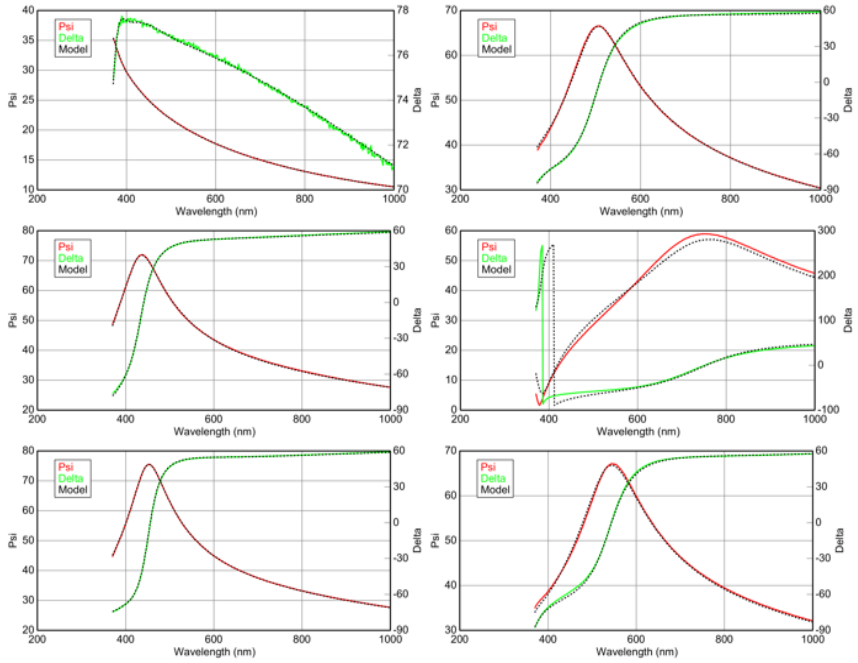

Figure 8.10/ Ellipsometry data graph of PMMA (2600): PbS QDs blend films with different ligands and concentrations.

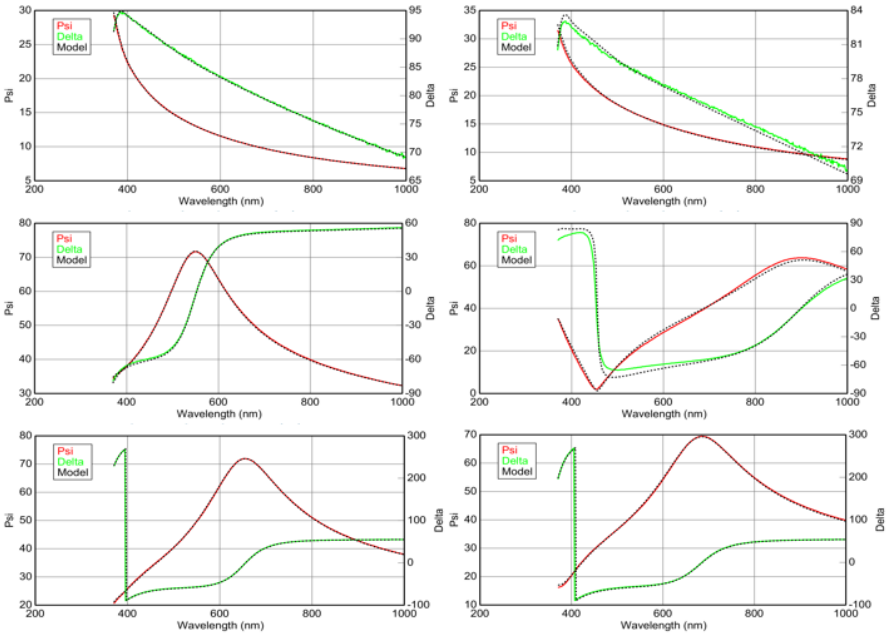

Figure 8.11/ Ellipsometry data graph of PMMA (40k): PbS QDs blend films with different ligands and concentrations.

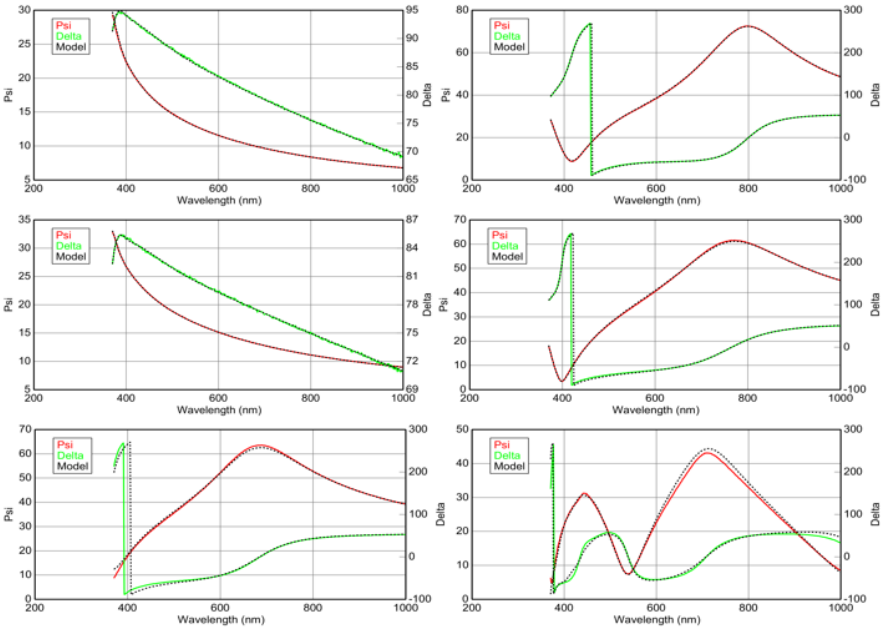

Figure 8.12/ Ellipsometry data graph of PMMA (1M): PbS QDs blend films with different ligands and concentrations.

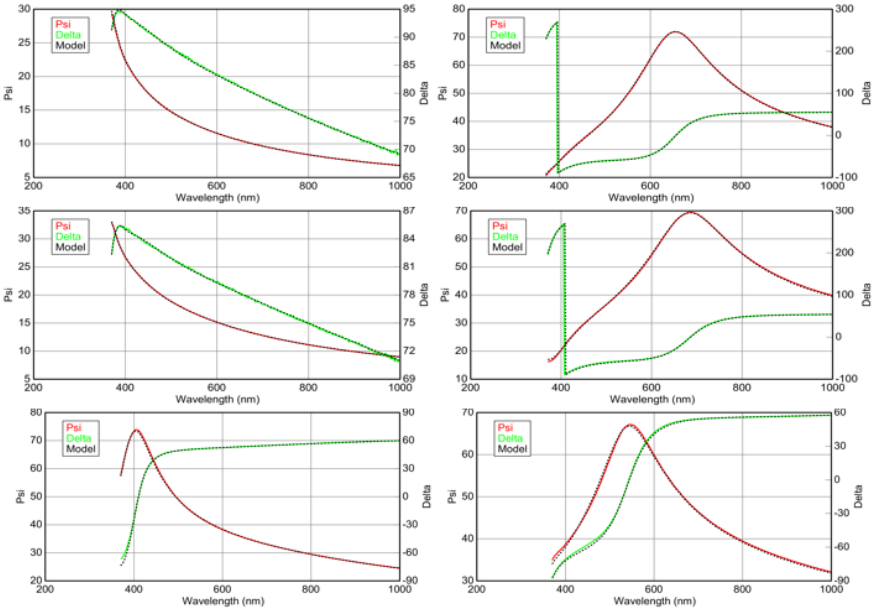

Figure 8.13/ Ellipsometry data graph of F8BT (75k): PbS QDs blend films with different ligands and concentrations.

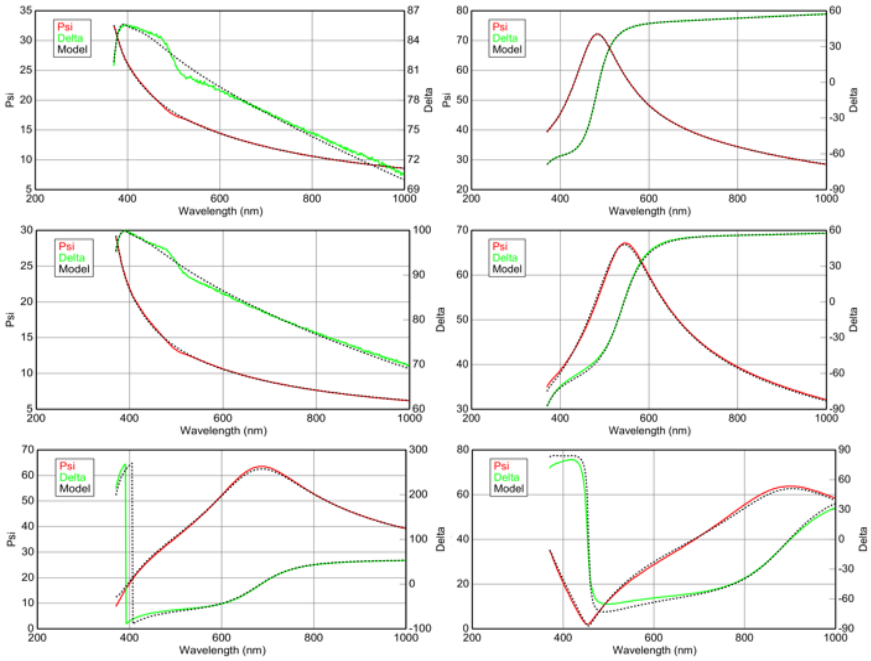

Figure 8.14/ Ellipsometry data graph of F8BT (200k): PbS QDs blend films with different ligands and concentrations.

Samples Index	Peak position ($q/Å^{-1}$)	FWHM ($q/Å^{-1}$)	Centre-to-centre distance (Å)	Inter-particle separation (Å)	Grain size (nm)	Morphology
PS(1800 Mw):PbS QDs	0.1101	0.01600±0.0014	57	9	37 ±1	HCP
PS(7.5k Mw):PbS QDs	0.1125	0.01459±0.0023	56	8	40 ±2	HCP
Ps(40K Mw):PbS QDs	0.1095	0.01405±0.0022	57	9	42 ±2	HCP
Ps(50K Mw):PbS QDs	0.1118	0.01199±0.0025	56	8	47 ±2	HCP
Ps(89k Mw):PbS QDs	0.1110	0.01168±0.0023	57	9	51 ±2	HCP
Ps(350k Mw):PbS QDs	0.1116	0.01098±0.0021	56	8	54 ±2	HCP
Ps(850k Mw):PbS QDs	0.1113	0.01069±0.0024	56	8	55 ±2	HCP
Ps(1.6M Mw):PbS QDs	0.1106	0.01049±0.0023	57	9	56 ±2	HCP

Table 8.1/ Data of the PS: PbS QDs-OA nanocomposite films, the data comes from fitting the distinctive peaks around 0.1 $Å^{-1}$ found using GISAXS.

Samples Index	Peak position ($q/Å^{-1}$)	FWHM ($q/Å^{-1}$)	Centre-to-centre distance (Å)	Inter-particle separation (Å)	Grain size (nm)	Morphology
PMMA(2600 Mw)_PbS QDs	0.1124	0.01669±0.0021	56	8	35±2	HCP
PMMA(8.4k Mw)_PbS QDs	0.1114	0.01306±0.0023	56	8	45±2	HCP
PMMA(40k Mw)_PbS QDs	0.1110	0.01157±0.0021	56	8	51±2	HCP
PMMA(50k Mw)_PbS QDs	0.1121	0.01138±0.0025	56	8	52±2	HCP

PMMA(350k Mw)_PbS QDs	0.1118	0.01092±0.002	56	8	54±2	HCP
PMMA(1M Mw)_PbS QDs	0.1116	0.01030±0.0022	56	8	57±2	HCP
PMMA(1.5M Mw)_PbS QDs	0.1118	0.00995±0.0023	56	8	59±2	HCP

Table 8.2/ Data of the PMMA: PbS QDs-OA nanocomposite films, the data come from fitting the distinctive peaks around 0.1 $Å^{-1}$ measured by GISAXS.

Samples Index	**Peak position ($q/Å^{-1}$)**	**FWHM ($q/Å^{-1}$)**	**Centre-to-centre distance (Å)**	**Inter-particle separation (Å)**	**Grain size** (nm)	**Morphology**
F8BT(75K Mw):PbS QDs	0.1125	0.0114±0.0022	56	8	52±2	HCP
F8BT(200K Mw):PbS QDs	0.1095	0.0094±0.0034	57	9	62±3	HCP

Table 8.3/ Data of the F8BT: PbS QDs-OA nanocomposite films, the data come from fitting the distinctive peaks around 0.1 $Å^{-1}$ found by GISAXS.

Samples Index	Peak position ($q/Å^{-1}$)	FWHM ($q/Å^{-1}$)	Centre-to-centre distance (Å)	Inter-particle separation (Å)	Grain size (nm)	Morphology
PS(1800 Mw):PbS QDs-HA	0.1176	0.0235±0.0034	53	5	25±2	HCP
PS(1800 Mw):PbS QDs-DA	0.1173	0.02267±0.0013	54	6	26±1	HCP
Ps(40K Mw):PbS QDs-HA	0.1197	0.02136±0.0021	52	4	28±2	FCC-CP
Ps(40K Mw):PbS QDs-DA	0.1176	0.01950±0.0024	53	5	30±2	FCC-CP
Ps(850k Mw):PbS QDs-HA	0.1198	0.01638±0.0032	52	4	36±3	HCP
Ps(850k Mw):PbS QDs-DA	0.1176	0.01450±0.002	53	5	41±2	HCP

Table 8.4 / Data of PS: PbS QDs blend films with HA and DA ligands and different PS M_w (1800-40k-850k).

Samples Index	Peaks position ($q/Å^{-1}$)	FWHM ($q/Å^{-1}$)	Centre-to-centre distance (Å)	Inter-particle separation (Å)	Grain size (nm)	Morphology
PMMA(2600 Mw):PbS QDs-HA	0.1201	0.02546±0.0034	52	4	23±3	HCP
PMMA(2600 Mw):PbS QDs-DA	0.1188	0.02805±0.0032	53	5	21±3	FCC-CP
PMMA(40K Mw):PbS QDs-HA	0.1198	0.01918±0.0024	52	4	31±2	HCP

PMMA(40K Mw):PbS QDs-DA	0.1160	0.01727±0.0022	54	6	34±2	FCC-CP
PMMA(1M Mw):PbS QDs-HA	0.1188	0.01169±0.003	53	4	50±3	HCP
PMMA(1M Mw):PbS QDs-DA	0.1181	0.01158±0.0023	52	5	51±2	HCP

Table 8.5 / Data of PMMA: PbS QDs blend films with HA and DA ligands and different PS M_w (2600-40k-1m).

Samples Index	**Peaks position ($q/Å^{-1}$)**	**FWHM ($q/Å^{-1}$)**	**Centre-to-centre distance (Å)**	**Inter-particle separation (Å)**	**Grain size (nm)**	**Morphology**
F8BT(75k):PbS QDs-HA	0.1176	0.01589±0.0031	53	5	37±3	HCP
F8BT(75k):PbS QDs-DA	0.1169	0.01577±0.0024	54	6	37±2	HCP
F8BT(200k):PbS QDs-HA	0.1182	0.01311±0.0023	53	5	45±2	HCP
F8BT(200K Mw):PbS QDs-DA	0.1168	0.01215±0.003	54	6	49±3	HCP

Table 8.6/ Data of F8BT: PbS QDs blend films with HA and DA ligands and different F8BT M_w (75k-200k).

Samples Index	Peak position ($q/Å^{-1}$)	FWHM ($q/Å^{-1}$)	Centre-to-centre distance (Å)	Inter-particle separation (Å)	Grain size (nm)	Morphology
PS(1800 Mw):PbS QDs-OA 0.00024	0.1122	0.02236±0.0024	56	8	26±2	HCP
PS(1800 Mw):PbS QDs-OA 0.024	0.1115	0.02929±0.0022	56	8	20±2	HCP
PS(1800 Mw):PbS QDs-HA 0.00024	0.1157	0.03198±0.0022	54	6	18±2	FCC -CP
PS(1800 Mw):PbS QDs-HA 0.024	0.1159	0.03680±0.0012	54	6	16±1	FCC-CP
PS(1800 Mw):PbS QDs-DA 0.00024	0.1152	0.0333±0.002	55	7	18±2	HCP
PS(1800 Mw):PbS QDs-DA 0.024	0.1417	0.11279±0.0013	45	---	5±1	---

Table 8.7/ fitted data of PS (1800 M_w): PbS QDs films with different ligands and concentrations.

Samples Index	Peak position ($q/Å^{-1}$)	FWHM ($q/Å^{-1}$)	Centre-to-centre distance (Å)	Inter-particle separation (Å)	Grain size (nm)	Morphology
PS(40k Mw):PbS QDs-OA 0.00024	0.1099	0.01478±0.0031	57	9	39±3	HCP
PS(40k Mw):PbS QDs-OA 0.024	0.1115	0.02212±0.0024	56	8	27±2	HCP
PS(40k Mw):PbS QDs-HA 0.00024	0.1154	0.02095±0.002	54	6	28±2	HCP
PS(40k Mw):PbS QDs-HA 0.024	0.1155	0.02483±0.0011	54	6	24±1	HCP
PS(40k Mw):PbS QDs-DA 0.00024	0.1132	0.01647±0.0033	55	7	36±3	HCP

PS(40k Mw):PbS QDs-DA 0.024	0.1139	0.02636±0.0024	55	7	22±2	HCP

Table 8.8/ fitting data of PS (40k M_w): PbS QDs films with different ligands and concentrations.

Samples Index	**Peak position ($q/Å^{-1}$)**	**FWHM ($q/Å^{-1}$)**	**Centre-to-centre distance (Å)**	**Inter-particle separation (Å)**	**Grain size (nm)**	**Morphology**
PS(850k Mw):PbS QDs-OA 0.00024	0.1082	0.012750.0033	58	10	46±3	HCP
PS(850k Mw):PbS QDs-OA 0.024	0.1107	0.01650±0.0035	57	9	36±3	HCP
PS(850k Mw):PbS QDs-HA 0.00024	0.1140	0.01325±0.0032	55	7	44±3	HCP
PS(850k Mw):PbS QDs-HA 0.024	0.1149	0.01721±0.0025	54	6	34±2	HCP
PS(850k Mw):PbS QDs-DA 0.00024	0.1123	0.01449±0.0034	56	8	41±3	HCP
PS(850k Mw):PbS QDs-DA 0.024	0.1129	0.01712±0.0031	56	8	34±3	HCP

Table 8.9/ fitted data of PS (40k M_w): PbS QDs films with different ligands and concentrations.

Samples Index	**Peak position ($q/Å^{-1}$)**	**FWHM ($q/Å^{-1}$)**	**Centre-to-centre distance (Å)**	**Inter-particle separation (Å)**	**Grain size (nm)**	**Morphology**
PMMA(2600 Mw):PbS QDs-OA 0.00024	0.1091	0.01955±0.0024	58	10	30±2	HCP
PMMA(2600 Mw):PbS QDs-OA 0.024	0.10946	0.02885±0.002	57	9	20±2	HCP
PMMA(2600 Mw):PbS QDs-HA 0.00024	0.1148	0.02248±0.0031	55	7	26±3	HCP
PMMA(2600 Mw):PbS QDs-HA 0.024	0.1139	0.02998±0.0022	55	7	19±2	HCP
PMMA(2600 Mw):PbS QDs-DA 0.00024	0.1130	0.02529±0.0033	56	8	23±3	FCC-CP
PMMA(2600 Mw):PbS QDs-DA 0.024	0.1306	0.11938±0.0013	48	0	5±1	---

Table 8.10 / fitted data of PMMA (2600 M_w): PbS QDs films with different ligands and concentrations.

Samples Index	Peak position ($q/Å^{-1}$)	FWHM ($q/Å^{-1}$)	Centre-to-centre distance (Å)	Inter-particle separation (Å)	Grain size (nm)	Morphology
PMMA(40k Mw):PbS QDs-OA 0.00024	0.1091	0.01423±0.003	58	10	41±3	HCP
PMMA(40k Mw):PbS QDs-OA 0.024	0.1107	0.01946±0.0023	57	9	30±2	HCP
PMMA(40k Mw):PbS QDs-HA 0.00024	0.1155	0.02207±0.0024	54	6	27±2	HCP
PMMA(40k Mw):PbS QDs-HA 0.024	0.1175	0.02233±0.0023	53	5	26±2	HCP
PMMA(40k Mw):PbS QDs-DA 0.00024	0.1142	0.01895±0.0032	55	7	31±3	HCP
PMMA(40k Mw):PbS QDs-DA 0.024	0.1152	0.02572±0.0035	55	7	23±3	HCP

Table 8.11/ fitted data of PMMA (40k M_w): PbS QDs films with different ligands and concentrations.

Samples Index	Peak position ($q/Å^{-1}$)	FWHM ($q/Å^{-1}$)	Centre-to-centre distance (Å)	Inter-particle separation (Å)	Grain size (nm)	Morphology
PMMA(1m Mw):PbS QDs-OA 0.00024	0.1091	0.01266±0.0021	58	10	47±2	HCP
PMMA(1m Mw):PbS QDs-OA 0.024	0.1110	0.01799±0.0033	57	9	33±3	HCP
PMMA(1m Mw):PbS QDs-HA 0.00024	0.1176	0.01413±0.0031	53	5	42±3	HCP
PMMA(1m Mw):PbS QDs-HA 0.024	0.1160	0.01771±0.003	54	6	33±3	HCP
PMMA(1m Mw):PbS QDs-DA 0.00024	0.1115	0.01461±0.0024	56	8	40±2	HCP

PMMA(1m Mw):PbS QDs-DA 0.024	0.1141	0.01934±0.0033	55	7	30±3	HCP

Table 8.12/ fitted data of PMMA (1m M_w): PbS QDs films with different ligands and concentrations.

Samples Index	**Peak position ($q/Å^{-1}$)**	**FWHM ($q/Å^{-1}$)**	**Centre-to-centre distance (Å)**	**Inter-particle separation (Å)**	**Grain size** (nm)	**Morphology**
F8BT (75K Mw): PbS QDs-OA 0.00024	0.1097	0.01914	57	9	31	HCP
F8BT (75K Mw): PbS QDs-OA 0.024	0.1119	0.02030	56	8	29	HCP
F8BT (75K Mw): PbS QDs-HA 0.00024	0.1177	0.02241	53	5	26	HCP
F8BT (75K Mw): PbS QDs-HA 0.024	0.1156	0.02774	54	6	21	HCP
F8BT (75K Mw): PbS QDs-DA 0.00024	0.1150	0.01687	55	7	35	HCP
F8BT (75K Mw): PbS QDs-DA 0.024	0.1620	0.06271	38	---	9	---

Table 8.13/ fitted data of F8BT (75k M_w): PbS QDs films with different ligands and concentrations.

Samples Index	**Peak position ($q/Å^{-1}$)**	**FWHM ($q/Å^{-1}$)**	**Centre-to-centre distance (Å)**	**Inter-particle separation (Å)**	**Grain size** (nm)	**Morphology**
F8BT (200K Mw): PbS QDs-OA 0.00024	0.1099	0.01308	57	9	45	HCP
F8BT (200K Mw): PbS QDs-OA 0.024	0.11307	0.01424	56	8	41	HCP
F8BT (200K Mw): PbS QDs-HA 0.00024	0.1177	0.0147	53	5	40	HCP
F8BT (200K Mw): PbS QDs-HA 0.024	0.1174	0.01859	53	5	32	HCP

F8BT (200K Mw): PbS QDs-DA 0.00024	0.1149	0.01482	55	7	40	HCP
F8BT (200K Mw): PbS QDs-DA 0.024	0.1157	0.01553	54	6	38	HCP

Table 8.14/ fitted data of F8BT (200k M_w): PbS QDs films with different ligands and concentrations

References

1. Matvienko, O.O., Y.N. Savin, A.S. Kryzhanovska, O.M. Vovk, M.V. Dobrotvorska, N.V. Pogorelova, and V.V. Vashchenko, *Dispersion and aggregation of quantum dots in polymer–inorganic hybrid films.* Thin Solid Films, 2013. **537**: p. 226-230.
2. Helgesen, M., R. Søndergaard, and F.C. Krebs, *Advanced materials and processes for polymer solar cell devices.* Journal of Materials Chemistry, 2010. **20**(1): p. 36-60.
3. Zhao, N., T.P. Osedach, L.-Y. Chang, S.M. Geyer, D. Wanger, M.T. Binda, A.C. Arango, M.G. Bawendi, and V. Bulovic, *Colloidal PbS quantum dot solar cells with high fill factor.* ACS nano, 2010. **4**(7): p. 3743-3752.
4. Moulé, A.J., L. Chang, C. Thambidurai, R. Vidu, and P. Stroeve, *Hybrid solar cells: basic principles and the role of ligands.* Journal of Materials Chemistry, 2012. **22**(6): p. 2351-2368.
5. Coe, S., W.-K. Woo, M. Bawendi, and V. Bulović, *Electroluminescence from single monolayers of nanocrystals in molecular organic devices.* Nature, 2002. **420**(6917): p. 800-803.
6. Zorn, M., W.K. Bae, J. Kwak, H. Lee, C. Lee, R. Zentel, and K. Char, *Quantum dot− block copolymer hybrids with improved properties and their application to quantum dot light-emitting devices.* Acs Nano, 2009. **3**(5): p. 1063-1068.
7. Gray, V., K. Moth-Poulsen, B. Albinsson, and M. Abrahamsson, *Towards efficient solid-state triplet–triplet annihilation based photon upconversion: Supramolecular, macromolecular and self-assembled systems.* Coordination Chemistry Reviews, 2018. **362**: p. 54-71.
8. Gray, V., J.R. Allardice, Z. Zhang, and A. Rao, *Organic-quantum dot hybrid interfaces and their role in photon fission/fusion applications.* Chemical Physics Reviews, 2021. **2**(3): p. 031305.
9. Shang, M., S. Zhang, N. Li, X. Gu, L. Li, and Z. Wang, *Di-functional nanocomposite films for efficient conversion and storage of solar energy.* Solar Energy Materials and Solar Cells, 2017. **164**: p. 188-192.

10. Ashraf, M.A., W. Peng, Y. Zare, and K.Y. Rhee, *Effects of size and aggregation/agglomeration of nanoparticles on the interfacial/interphase properties and tensile strength of polymer nanocomposites.* Nanoscale research letters, 2018. **13**(1): p. 1-7.
11. Fu, S., Z. Sun, P. Huang, Y. Li, and N. Hu, *Some basic aspects of polymer nanocomposites: A critical review.* Nano Materials Science, 2019. **1**(1): p. 2-30.
12. McCumiskey, E.J., N. Chandrasekhar, and C.R. Taylor, *Nanomechanics of CdSe quantum dot–polymer nanocomposite films.* Nanotechnology, 2010. **21**(22): p. 225703.
13. van Rijssel, J., B.H. Erne, J.D. Meeldijk, M. Casavola, D. Vanmaekelbergh, A. Meijerink, and A.P. Philipse, *Enthalpy and entropy of nanoparticle association from temperature-dependent cryo-TEM.* Physical Chemistry Chemical Physics, 2011. **13**(28): p. 12770-12774.
14. Greenham, N., X. Peng, and A. Alivisatos, *Charge separation and transport in conjugated polymer/cadmium selenide nanocrystal composites studied by photoluminescence quenching and photoconductivity.* Synthetic metals, 1997. **84**(1-3): p. 545-546.
15. Martinez-Ferrero, E., J. Albero, and E. Palomares, *Materials, nanomorphology, and interfacial charge transfer reactions in quantum dot/polymer solar cell devices.* The Journal of Physical Chemistry Letters, 2010. **1**(20): p. 3039-3045.
16. Chen, J., Y. Yu, J. Chen, H. Li, J. Ji, and D. Liu, *Chemical modification of palygorskite with maleic anhydride modified polypropylene: mechanical properties, morphology, and crystal structure of palygorskite/polypropylene nanocomposites.* Applied Clay Science, 2015. **115**: p. 230-237.
17. Khan, A., M.H. Shamsi, and T.-S. Choi, *Correlating dynamical mechanical properties with temperature and clay composition of polymer-clay nanocomposites.* Computational Materials Science, 2009. **45**(2): p. 257-265.
18. Yang, H., Q. Zhang, M. Guo, C. Wang, R. Du, and Q. Fu, *Study on the phase structures and toughening mechanism in PP/EPDM/SiO2 ternary composites.* Polymer, 2006. **47**(6): p. 2106-2115.
19. Torriss, B., A. Haché, and S. Gauvin, *White light-emitting organic device with electroluminescent quantum dots and organic molecules.* Organic Electronics, 2009. **10**(8): p. 1454-1458.
20. Teng, F., A. Tang, B. Feng, and Z. Lou, *The optical properties of the blends of CdSe nanocrystals and poly (N-vinylcarbazole).* Applied surface science, 2008. **254**(20): p. 6341-6345.

21. Díez-Pascual, A.M., *Nanoparticle reinforced polymers*. 2019, MDPI. p. 625.
22. Akpan, E., X. Shen, B. Wetzel, and K. Friedrich, *Design and synthesis of polymer nanocomposites*, in *Polymer composites with functionalized nanoparticles*. 2019, Elsevier. p. 47-83.
23. Gil, H.M., T.W. Price, K. Chelani, J.-S.G. Bouillard, S.D. Calaminus, and G.J. Stasiuk, *NIR-quantum dots in biomedical imaging and their future.* Iscience, 2021. **24**(3): p. 102189.
24. Singh, S., S.K. Paswan, P. Kumar, R.K. Singh, and L. Kumar, *Nanomaterials based sensors for detecting key pathogens in food and water: developments from recent decades*, in *Environmental Applications of Microbial Nanotechnology*. 2023, Elsevier. p. 65-80.
25. Piao, Z., D. Yang, Z. Cui, H. He, S. Mei, H. Lu, Z. Fu, L. Wang, W. Zhang, and R. Guo, *Recent Advances in Metal Chalcogenide Quantum Dots: From Material Design to Biomedical Applications.* Advanced Functional Materials, 2022. **32**(44): p. 2207662.
26. Okada, A. and A. Usuki, *Twenty years of polymer‐clay nanocomposites.* Macromolecular materials and Engineering, 2006. **291**(12): p. 1449-1476.
27. Mal, J., Y. Nancharaiah, E. Van Hullebusch, and P. Lens, *Metal chalcogenide quantum dots: biotechnological synthesis and applications.* RSC advances, 2016. **6**(47): p. 41477-41495.
28. Lei, L., D. Huang, S. Chen, C. Zhang, Y. Chen, and R. Deng, *Metal chalcogenide/oxide-based quantum dots decorated functional materials for energy-related applications: Synthesis and preservation.* Coordination Chemistry Reviews, 2021. **429**: p. 213715.
29. Park, J., T. Kim, and D. Kim, *Charge Injection and Energy Transfer of Surface-Engineered InP/ZnSe/ZnS Quantum Dots.* Nanomaterials, 2023. **13**(7): p. 1159.
30. Ma, X., M. Sheikholeslami, M. Jafaryar, A. Shafee, T. Nguyen-Thoi, and Z. Li, *Solidification inside a clean energy storage unit utilizing phase change material with copper oxide nanoparticles.* Journal of Cleaner Production, 2020. **245**: p. 118888.
31. Rao, A. and R.H. Friend, *Harnessing singlet exciton fission to break the Shockley–Queisser limit.* Nature reviews materials, 2017. **2**(11): p. 1-12.
32. Algar, W.R., K. Susumu, J.B. Delehanty, and I.L. Medintz, *Semiconductor quantum dots in bioanalysis: crossing the valley of death*. 2011, ACS Publications.
33. Terlan, B., A.A. Levin, F. Börrnert, J. Zeisner, V. Kataev, M. Schmidt, and A. Eychmüller, *A Size‐Dependent Analysis of the Structural, Surface, Colloidal, and Thermal Properties of Ti1–xB2 (x= 0.03–0.08)*

Nanoparticles. European Journal of Inorganic Chemistry, 2016. **2016**(21): p. 3460-3468.
34. Nozik, A.J., M.C. Beard, J.M. Luther, M. Law, R.J. Ellingson, and J.C. Johnson, *Semiconductor quantum dots and quantum dot arrays and applications of multiple exciton generation to third-generation photovoltaic solar cells.* Chemical reviews, 2010. **110**(11): p. 6873-6890.
35. Kershaw, S.V., A.S. Susha, and A.L. Rogach, *Narrow bandgap colloidal metal chalcogenide quantum dots: synthetic methods, heterostructures, assemblies, electronic and infrared optical properties.* Chemical Society Reviews, 2013. **42**(7): p. 3033-3087.
36. De Nolf, K., S.M. Cosseddu, J.J. Jasieniak, E. Drijvers, J.C. Martins, I. Infante, and Z. Hens, *Binding and packing in two-component colloidal quantum dot ligand shells: linear versus branched carboxylates.* Journal of the American Chemical Society, 2017. **139**(9): p. 3456-3464.
37. Pang, Z., J. Zhang, W. Cao, X. Kong, and X. Peng, *Partitioning surface ligands on nanocrystals for maximal solubility.* Nature communications, 2019. **10**(1): p. 2454.
38. Ondry, J.C., J.P. Philbin, M. Lostica, E. Rabani, and A.P. Alivisatos, *Colloidal synthesis path to 2D crystalline quantum dot superlattices.* ACS nano, 2020. **15**(2): p. 2251-2262.
39. Anderson, N.C., M.P. Hendricks, J.J. Choi, and J.S. Owen, *Ligand exchange and the stoichiometry of metal chalcogenide nanocrystals: spectroscopic observation of facile metal-carboxylate displacement and binding.* Journal of the American Chemical Society, 2013. **135**(49): p. 18536-18548.
40. Kirkwood, N., J.O. Monchen, R.W. Crisp, G. Grimaldi, H.A. Bergstein, I. Du Fossé, W. Van Der Stam, I. Infante, and A.J. Houtepen, *Finding and fixing traps in II*−*VI and III–V colloidal quantum dots: the importance of Z-type ligand passivation.* Journal of the American Chemical Society, 2018. **140**(46): p. 15712-15723.
41. Fan, Z. and M. Grünwald, *Orientational order in self-assembled nanocrystal superlattices.* Journal of the American Chemical Society, 2019. **141**(5): p. 1980-1988.
42. Nagaoka, Y., R. Tan, R. Li, H. Zhu, D. Eggert, Y.A. Wu, Y. Liu, Z. Wang, and O. Chen, *Superstructures generated from truncated tetrahedral quantum dots.* Nature, 2018. **561**(7723): p. 378-382.
43. Lee, H., D.-E. Yoon, S. Koh, M.S. Kang, J. Lim, and D.C. Lee, *Ligands as a universal molecular toolkit in synthesis and assembly of semiconductor nanocrystals.* Chemical Science, 2020. **11**(9): p. 2318-2329.

44. Calvin, J.J., J.K. Swabeck, A.B. Sedlak, Y. Kim, E. Jang, and A.P. Alivisatos, *Thermodynamic investigation of increased luminescence in indium phosphide quantum dots by treatment with metal halide salts.* Journal of the American Chemical Society, 2020. **142**(44): p. 18897-18906.
45. Kim, T.-G., D. Zherebetskyy, Y. Bekenstein, M.H. Oh, L.-W. Wang, E. Jang, and A.P. Alivisatos, *Trap passivation in indium-based quantum dots through surface fluorination: mechanism and applications.* ACS nano, 2018. **12**(11): p. 11529-11540.
46. Reed, M., R. Bate, K. Bradshaw, W. Duncan, W. Frensley, J. Lee, and H. Shih, *Spatial quantization in GaAs–AlGaAs multiple quantum dots.* Journal of Vacuum Science & Technology B: Microelectronics Processing and Phenomena, 1986. **4**(1): p. 358-360.
47. Bawendi, M.G., M.L. Steigerwald, and L.E. Brus, *The quantum mechanics of larger semiconductor clusters (" quantum dots").* Annual Review of Physical Chemistry, 1990. **41**(1): p. 477-496.
48. Garshasbi, S., S. Huang, J. Valenta, and M. Santamouris, *On the combination of quantum dots with near-infrared reflective base coats to maximize their urban overheating mitigation potential.* Solar Energy, 2020. **211**: p. 111-116.
49. Elyasi, P. and A. SalmanOgli, *Investigation of potential profile effects in quantum dot and onion-like quantum dot-quantum well on optical properties.* Optics Communications, 2014. **318**: p. 26-30.
50. Brus, L.E., *Electron–electron and electron-hole interactions in small semiconductor crystallites: The size dependence of the lowest excited electronic state.* The Journal of chemical physics, 1984. **80**(9): p. 4403-4409.
51. Mansur, H.S., *Quantum dots and nanocomposites.* Wiley Interdisciplinary Reviews: Nanomedicine and Nanobiotechnology, 2010. **2**(2): p. 113-129.
52. Nozik, A.J., *Multiple exciton generation in semiconductor quantum dots.* Chemical Physics Letters, 2008. **457**(1-3): p. 3-11.
53. Sarikov, A. and I. Lisovskyy, *Spinodal decomposition versus nucleation and growth mechanism of phase separation in nonstoichiometric silicon oxide films during high temperature annealing.* Solid State Communications, 2019. **287**: p. 19-22.
54. Beard, M.C., *Multiple exciton generation in semiconductor quantum dots.* The Journal of Physical Chemistry Letters, 2011. **2**(11): p. 1282-1288.
55. Nozik, A.J., *Quantum dot solar cells.* Physica E: Low-dimensional Systems and Nanostructures, 2002. **14**(1-2): p. 115-120.

56. Alivisatos, A.P., *Semiconductor clusters, nanocrystals, and quantum dots.* science, 1996. **271**(5251): p. 933-937.
57. Zhao, Y., J. Zou, and W. Shi, *In situ synthesis and characterization of lead sulfide nanocrystallites in the modified hyperbranched polyester by gamma-ray irradiation.* Materials Science and Engineering: B, 2005. **121**(1-2): p. 20-24.
58. Kim, J.-H., H.-R. Kim, B.-R. Lee, E.-S. Choi, S.-I. In, and E. Kim, *Carcinogenic activity of PbS quantum dots screened using exosomal biomarkers secreted from HEK293 cells.* International Journal of Nanomedicine, 2015: p. 5513-5528.
59. Ayoubi, M., P. Naserzadeh, M.T. Hashemi, M. Reza Rostami, E. Tamjid, M.M. Tavakoli, and A. Simchi, *Biochemical mechanisms of dose-dependent cytotoxicity and ROS-mediated apoptosis induced by lead sulfide/graphene oxide quantum dots for potential bioimaging applications.* Scientific reports, 2017. **7**(1): p. 12896.
60. Hines, M.A. and G.D. Scholes, *Colloidal PbS nanocrystals with size‐tunable near‐infrared emission: observation of post‐synthesis self‐narrowing of the particle size distribution.* Advanced Materials, 2003. **15**(21): p. 1844-1849.
61. Lu, K., Y. Wang, Z. Liu, L. Han, G. Shi, H. Fang, J. Chen, X. Ye, S. Chen, and F. Yang, *High‐Efficiency PbS Quantum‐Dot Solar Cells with Greatly Simplified Fabrication Processing via "Solvent‐Curing"*. Advanced Materials, 2018. **30**(25): p. 1707572.
62. Zhao, H. and F. Rosei, *Colloidal quantum dots for solar technologies.* Chem, 2017. **3**(2): p. 229-258.
63. Harris, R.D., S. Bettis Homan, M. Kodaimati, C. He, A.B. Nepomnyashchii, N.K. Swenson, S. Lian, R. Calzada, and E.A. Weiss, *Electronic processes within quantum dot-molecule complexes.* Chemical reviews, 2016. **116**(21): p. 12865-12919.
64. Zhang, Z., K. Edme, S. Lian, and E.A. Weiss, *Enhancing the rate of quantum-dot-photocatalyzed carbon–carbon coupling by tuning the composition of the dot's ligand shell.* Journal of the American Chemical Society, 2017. **139**(12): p. 4246-4249.
65. Huang, Z., X. Li, M. Mahboub, K.M. Hanson, V.M. Nichols, H. Le, M.L. Tang, and C.J. Bardeen, *Hybrid molecule–nanocrystal photon upconversion across the visible and near-infrared.* Nano letters, 2015. **15**(8): p. 5552-5557.
66. Davis, N.J., J.R. Allardice, J. Xiao, A.J. Petty, N.C. Greenham, J.E. Anthony, and A. Rao, *Singlet fission and triplet transfer to PbS quantum dots in TIPS-tetracene carboxylic acid ligands.* The Journal of Physical Chemistry Letters, 2018. **9**(6): p. 1454-1460.

67. Mongin, C., P. Moroz, M. Zamkov, and F.N. Castellano, *Thermally activated delayed photoluminescence from pyrenyl-functionalized CdSe quantum dots.* Nature Chemistry, 2018. **10**(2): p. 225-230.
68. Choi, J.-H., H. Wang, S.J. Oh, T. Paik, P. Sung, J. Sung, X. Ye, T. Zhao, B.T. Diroll, and C.B. Murray, *Exploiting the colloidal nanocrystal library to construct electronic devices.* Science, 2016. **352**(6282): p. 205-208.
69. Cowie, J.M.G. and V. Arrighi, *Polymers: chemistry and physics of modern materials*. 2007: CRC press.
70. Jones, R.A., *Soft condensed matter*. Vol. 6. 2002: Oxford University Press.
71. Rubinstein, M. and R.H. Colby, *Polymer physics*. Vol. 23. 2003: Oxford university press New York.
72. Yoon, J., J. Kwag, T.J. Shin, J. Park, Y.M. Lee, Y. Lee, J. Park, J. Heo, C. Joo, and T.J. Park, *Nanoparticles of Conjugated Polymers Prepared from Phase‐Separated Films of Phospholipids and Polymers for Biomedical Applications.* Advanced Materials, 2014. **26**(26): p. 4559-4564.
73. Hall, L.M., A. Jayaraman, and K.S. Schweizer, *Molecular theories of polymer nanocomposites.* Current Opinion in Solid State and Materials Science, 2010. **14**(2): p. 38-48.
74. Chevallier, C., F. Becquart, and M. Taha, *Polystyrene/polycarbonate blends compatibilization: Morphology, rheological and mechanical properties.* Materials Chemistry and Physics, 2013. **139**(2-3): p. 616-622.
75. Ullah, A., T. Vasanthan, D. Bressler, A.L. Elias, and J. Wu, *Bioplastics from feather quill.* Biomacromolecules, 2011. **12**(10): p. 3826-3832.
76. Derjaguin, B.V., *Theory of the stability of strongly charged lyophobic sol and of the adhesion of strongly charged particles in solutions of electrolytes.* Acta phys. chim. URSS, 1941. **14**: p. 633.
77. Verwey, E.J.W., *Theory of the stability of lyophobic colloids.* The Journal of Physical Chemistry, 1947. **51**(3): p. 631-636.
78. Asakura, S. and F. Oosawa, *Interaction between particles suspended in solutions of macromolecules.* Journal of polymer science, 1958. **33**(126): p. 183-192.
79. Vrij, A., *Polymers at interfaces and the interactions in colloidal dispersions.* Pure and Applied Chemistry, 1976. **48**(4): p. 471-483.
80. Hunter, R.J., *Foundations of Colloid Science, Vol. II.* Clarendon, Oxford, 1989: p. 992-1052.
81. Mutch, K.J., J.S. van Duijneveldt, and J. Eastoe, *Colloid–polymer mixtures in the protein limit.* Soft Matter, 2007. **3**(2): p. 155-167.

82. Joanny, J., L. Leibler, and P. De Gennes, *Effects of polymer solutions on colloid stability.* Journal of Polymer Science: Polymer Physics Edition, 1979. **17**(6): p. 1073-1084.
83. De Gennes, P.-G., *Scaling concepts in polymer physics*. 1979: Cornell university press.
84. Odijk, T., *Protein− Macromolecule Interactions.* Macromolecules, 1996. **29**(5): p. 1842-1843.
85. Strobl, G.R. and G.R. Strobl, *The physics of polymers*. Vol. 2. 1997: Springer.
86. De Gennes, P.-G. and P.-G. Gennes, *Scaling concepts in polymer physics*. 1979: Cornell university press.
87. Agasty, A., A. Wisniewska, T. Kalwarczyk, K. Koynov, and R. Holyst, *Scaling equation for viscosity of polydimethylsiloxane in ethyl acetate: From dilute to concentrated solutions.* Polymer, 2020. **203**: p. 122779.
88. Shakeri, P., M. Jung, and R. Seemann, *Characterizing purely elastic turbulent flow of a semi-dilute entangled polymer solution in a serpentine channel.* Physics of Fluids, 2022. **34**(7).
89. Dunstan, D.E., *The viscosity-radius relationship for concentrated polymer solutions.* Scientific reports, 2019. **9**(1): p. 543.
90. Agasty, A., A. Wisniewska, T. Kalwarczyk, K. Koynov, and R. Holyst, *Macroscopic viscosity of polymer solutions from the nanoscale analysis.* ACS Applied Polymer Materials, 2021. **3**(5): p. 2813-2822.
91. Pusey, P., *Nature (London) https://doi. org/10.1038/320340a0 320, 340 (1986); Google Scholar Crossref PN Pusey, W. van Megen, P. Bartlett, BJ Ackerson, JG Rarity, and SM Underwood.* Phys. Rev. Lett. https://doi. org/10.1103/PhysRevLett, 1989. **63**(63): p. 2753.
92. Bian, K., R. Li, and H. Fan, *Controlled self-assembly and tuning of large PbS nanoparticle supercrystals.* Chemistry of Materials, 2018. **30**(19): p. 6788-6793.
93. Choi, J.J., C.R. Bealing, K. Bian, K.J. Hughes, W. Zhang, D.-M. Smilgies, R.G. Hennig, J.R. Engstrom, and T. Hanrath, *Controlling nanocrystal superlattice symmetry and shape-anisotropic interactions through variable ligand surface coverage.* Journal of the American Chemical Society, 2011. **133**(9): p. 3131-3138.
94. Li, R., K. Bian, T. Hanrath, W.A. Bassett, and Z. Wang, *Decoding the superlattice and interface structure of truncate PbS nanocrystal-assembled supercrystal and associated interaction forces.* Journal of the American Chemical Society, 2014. **136**(34): p. 12047-12055.
95. Mahynski, N.A., S.K. Kumar, and A.Z. Panagiotopoulos, *Relative stability of the FCC and HCP polymorphs with interacting polymers.* Soft Matter, 2015. **11**(2): p. 280-289.

96. Mahynski, N.A., A.Z. Panagiotopoulos, D. Meng, and S.K. Kumar, *Stabilizing colloidal crystals by leveraging void distributions.* Nature communications, 2014. **5**(1): p. 4472.
97. Kittel, C., *Introduction to solid state physics Eighth edition.* 2021.
98. Napper, D.H., *Polymeric stabilization of colloidal dispersions*. Vol. 3. 1983: Academic Press.
99. Poon, W.C., *The physics of a model colloid–polymer mixture.* Journal of Physics: Condensed Matter, 2002. **14**(33): p. R859.
100. Yang, S., D. Yan, H. Tan, and A.-C. Shi, *Depletion interaction between two colloidal particles in a nonadsorbing polymer solution.* Physical Review E, 2006. **74**(4): p. 041808.
101. Mousavi, S.S., B. Sajad, and M.H. Majlesara, *Fast response ZnO/PVA nanocomposite-based photodiodes modified by graphene quantum dots.* Materials & Design, 2019. **162**: p. 249-255.
102. Kausar, A., *Polymer/carbon-based quantum dot nanocomposite: forthcoming materials for technical application.* Journal of Macromolecular Science, Part A, 2019. **56**(4): p. 341-356.
103. Dirheimer, L., T. Pons, F. Marchal, and L. Bezdetnaya, *Quantum Dots Mediated Imaging and Phototherapy in Cancer Spheroid Models: State of the Art and Perspectives.* Pharmaceutics, 2022. **14**(10): p. 2136.
104. Albaladejo-Siguan, M., D. Becker-Koch, A.D. Taylor, Q. Sun, V. Lami, P.G. Oppenheimer, F. Paulus, and Y. Vaynzof, *Efficient and stable PbS quantum dot solar cells by triple-cation perovskite passivation.* ACS nano, 2019. **14**(1): p. 384-393.
105. Gordillo, H., I. Suárez, R. Abargues, P. Rodríguez-Cantó, S. Albert, and J. Martínez-Pastor, *Polymer/QDs nanocomposites for waveguiding applications.* Journal of Nanomaterials, 2012. **2012**: p. 33-33.
106. Matea, C.T., T. Mocan, F. Tabaran, T. Pop, O. Mosteanu, C. Puia, C. Iancu, and L. Mocan, *Quantum dots in imaging, drug delivery and sensor applications.* International journal of nanomedicine, 2017. **12**: p. 5421.
107. Rhee, J.H., C.-C. Chung, and E.W.-G. Diau, *A perspective of mesoscopic solar cells based on metal chalcogenide quantum dots and organometal-halide perovskites.* NPG Asia Materials, 2013. **5**(10): p. e68-e68.
108. Sarma, S. and P. Datta, *Characteristics of poly (vinyl alcohol)/lead sulphide quantum dot device.* Nanoscience and Nanotechnology Letters, 2010. **2**(3): p. 261-265.
109. Wang, Y., A. Suna, W. Mahler, and R. Kasowski, *PbS in polymers. From molecules to bulk solids.* The Journal of chemical physics, 1987. **87**(12): p. 7315-7322.

110. Grisorio, R., D. Debellis, G.P. Suranna, G. Gigli, and C. Giansante, *The dynamic organic/inorganic interface of colloidal PbS quantum dots.* Angewandte Chemie, 2016. **128**(23): p. 6740-6745.
111. Blachowicz, T. and A. Ehrmann, *Recent developments of solar cells from PbS colloidal quantum dots.* Applied Sciences, 2020. **10**(5): p. 1743.
112. Ewan, T., *The estimation of sulphide in alkali cyanide.* Journal of the Society of Chemical Industry, 1909. **28**(1): p. 10-13.
113. Patel, M.H., T.K. Chaudhuri, V.K. Patel, T. Shripathi, U. Deshpande, and N. Lalla, *Dip-coated PbS/PVP nanocomposite films with tunable band gap.* RSC advances, 2017. **7**(8): p. 4422-4429.
114. Shen, K., S. Baig, G. Jiang, Y.-h. Paik, S.J. Kim, and M.R. Wang, *Improved light emitting UV curable PbS quantum dots-polymer composite optical waveguides.* Optics Communications, 2017. **402**: p. 606-611.
115. Wang, R., F. Wang, W. Zhou, J.Z. Fan, F.P.G. de Arquer, K. Xu, E.H. Sargent, and Z. Ning, *Colloidal-quantum-dot-in-perovskite nanowires.* Infrared Physics & Technology, 2019. **98**: p. 16-22.
116. Mastria, R., A. Rizzo, C. Giansante, D. Ballarini, L. Dominici, O. Inganäs, and G. Gigli, *Role of polymer in hybrid polymer/PbS quantum dot solar cells.* The Journal of Physical Chemistry C, 2015. **119**(27): p. 14972-14979.
117. Rath, A.K., M. Bernechea, L. Martinez, F.P.G. De Arquer, J. Osmond, and G. Konstantatos, *Solution-processed inorganic bulk nano-heterojunctions and their application to solar cells.* Nature Photonics, 2012. **6**(8): p. 529-534.
118. Tavakoli Dastjerdi, H., P. Qi, Z. Fan, and M.M. Tavakoli, *Cost-effective and semi-transparent PbS quantum dot solar cells using copper electrodes.* ACS applied materials & interfaces, 2019. **12**(1): p. 818-825.
119. Haverinen, H., *Inkjet-printed quantum dot hybrid light-emitting devices—towards display applications.* 2010.
120. Li, C., A. Hassan, M. Palmai, P.T. Snee, P.C. Baveye, and C.J. Darnault, *Colloidal stability and aggregation kinetics of nanocrystal CdSe/ZnS quantum dots in aqueous systems: effects of pH and organic ligands.* Journal of Nanoparticle Research, 2020. **22**: p. 1-29.
121. Jia, X., J. Listak, V. Witherspoon, E.E. Kalu, X. Yang, and M.R. Bockstaller, *Effect of matrix molecular weight on the coarsening mechanism of polymer-grafted gold nanocrystals.* Langmuir, 2010. **26**(14): p. 12190-12197.
122. Kasaliwal, G.R., A. Göldel, P. Pötschke, and G. Heinrich, *Influences of polymer matrix melt viscosity and molecular weight on MWCNT agglomerate dispersion.* Polymer, 2011. **52**(4): p. 1027-1036.

123. Warner, T., N. Kirkwood, H. Yang, N. Wu, P. Mulvaney, and G. Rosengarten. *Reducing Quantum Dot Aggregation in Luminescent Solar Concentrators*. in *Asia-Pacific Solar Research Conference, Australian PV Institute (APVI)*. 2019.
124. Ramkumar, V. and S. Ju, *Quantum-dot and polychalcone mixed nanocomposites for polymer light-emitting diodes.* Journal of Nanomaterials, 2017. **2017**.
125. Li, M., X. Yuan, H. Ruan, X. Wang, Y. Liu, Z. Lu, and J. Hai, *Synthesis of PbS-CH3NH3PbI3 core-shell nanoparticles with enhanced photoelectric properties.* Journal of Alloys and Compounds, 2017. **706**: p. 395-400.
126. Balan, A.D., J.H. Olshansky, Y. Horowitz, H.-L. Han, E.A. O'Brien, L. Tang, G.A. Somorjai, and A.P. Alivisatos, *Unsaturated ligands seed an order to disorder transition in mixed ligand shells of CdSe/CdS quantum dots.* ACS nano, 2019. **13**(12): p. 13784-13796.
127. Wuister, S.F., A. Van Houselt, C. de Mello Donegá, D. Vanmaekelbergh, and A. Meijerink, *Temperature antiquenching of the luminescence from capped CdSe quantum dots.* Angewandte Chemie International Edition, 2004. **43**(23): p. 3029-3033.
128. Antanovich, A., A. Achtstein, A. Matsukovich, A. Prudnikau, P. Bhaskar, V. Gurin, M. Molinari, and M. Artemyev, *A strain-induced exciton transition energy shift in CdSe nanoplatelets: the impact of an organic ligand shell.* Nanoscale, 2017. **9**(45): p. 18042-18053.
129. Kagan, C.R. and C.B. Murray, *Charge transport in strongly coupled quantum dot solids.* Nature nanotechnology, 2015. **10**(12): p. 1013-1026.
130. Hughes, K.E., J.L. Stein, M.R. Friedfeld, B.M. Cossairt, and D.R. Gamelin, *Effects of surface chemistry on the photophysics of colloidal InP nanocrystals.* ACS nano, 2019. **13**(12): p. 14198-14207.
131. Fukuda, T., A. Takahashi, K. Takahira, H. Wang, T. Kubo, and H. Segawa, *Limiting factor of performance for solution-phase ligand-exchanged PbS quantum dot solar cell.* Solar Energy Materials and Solar Cells, 2019. **195**: p. 220-227.
132. Kim, B.-S., J. Hong, B. Hou, Y. Cho, J.I. Sohn, S. Cha, and J.M. Kim, *Inorganic-ligand exchanging time effect in PbS quantum dot solar cell.* Applied Physics Letters, 2016. **109**(6): p. 063901.
133. Owen, M.J., *Coupling agents: chemical bonding at interfaces*, in *Adhesion science and engineering*. 2002, Elsevier. p. 403-431.
134. Plueddemann, E.P., *Adhesion through silane coupling agents.* The Journal of Adhesion, 1970. **2**(3): p. 184-201.
135. Ramdani, N., *Polymer and ceramic composite materials: Emergent properties and applications*. 2019: CRC Press.

136. Rong, M.Z., M.Q. Zhang, Y.X. Zheng, H.M. Zeng, R. Walter, and K. Friedrich, *Structure–property relationships of irradiation grafted nano-inorganic particle filled polypropylene composites.* Polymer, 2001. **42**(1): p. 167-183.
137. Sato, K., S. Kondo, M. Tsukada, T. Ishigaki, and H. Kamiya, *Influence of solid fraction on the optimum molecular weight of polymer dispersants in aqueous TiO2 nanoparticle suspensions.* Journal of the American Ceramic Society, 2007. **90**(11): p. 3401-3406.
138. Palmqvist, L. and K. Holmberg, *Dispersant adsorption and viscoelasticity of alumina suspensions measured by quartz crystal microbalance with dissipation monitoring and in situ dynamic rheology.* Langmuir, 2008. **24**(18): p. 9989-9996.
139. Pileni, M.-P., *The role of soft colloidal templates in controlling the size and shape of inorganic nanocrystals.* Nature materials, 2003. **2**(3): p. 145-150.
140. Gioria, S., F. Caputo, P. Urbán, C.M. Maguire, S. Bremer-Hoffmann, A. Prina-Mello, L. Calzolai, and D. Mehn, *Are existing standard methods suitable for the evaluation of nanomedicines: some case studies.* Nanomedicine, 2018. **13**(5): p. 539-554.
141. Aublant, J.M., *Standardization of Nanomaterials: Methods and Protocols.* Metrology and Standardization of Nanotechnology: Protocols and Industrial Innovations, 2017: p. 289-298.
142. Korolkov, D., P. Busch, L. Willner, E. Kentzinger, U. Rücker, A. Paul, H. Frielinghaus, and T. Brueckel, *Analysis of randomly oriented structures by grazing-incidence small-angle neutron scattering.* Journal of applied crystallography, 2012. **45**(2): p. 245-254.
143. Castellanos, M.M., A. McAuley, and J.E. Curtis, *Investigating structure and dynamics of proteins in amorphous phases using neutron scattering.* Computational and structural biotechnology journal, 2017. **15**: p. 117-130.
144. Maes, J., N. Castro, K. De Nolf, W. Walravens, B. Abécassis, and Z. Hens, *Size and concentration determination of colloidal nanocrystals by small-angle X-ray scattering.* Chemistry of Materials, 2018. **30**(12): p. 3952-3962.
145. Weir, M.P., D.T. Toolan, R.C. Kilbride, N.J. Penfold, A.L. Washington, S.M. King, J. Xiao, Z. Zhang, V. Gray, and S. Dowland, *Ligand shell structure in lead sulfide–oleic acid colloidal quantum dots revealed by small-angle scattering.* The Journal of Physical Chemistry Letters, 2019. **10**(16): p. 4713-4719.
146. Fan, L., M. Degen, S. Bendle, N. Grupido, and J. Ilavsky. *The absolute calibration of a small-angle scattering instrument with a laboratory X-*

ray source. in *Journal of Physics: Conference Series*. 2010. IOP Publishing.
147. Jiang, Z., *GIXSGUI: a MATLAB toolbox for grazing-incidence X-ray scattering data visualization and reduction, and indexing of buried three-dimensional periodic nanostructured films.* Journal of Applied Crystallography, 2015. **48**(3): p. 917-926.
148. May, R.A. and K.J. Stevenson, *Software review of Origin 8*. 2009, ACS Publications.
149. Moberly, J.G., M.T. Bernards, and K.V. Waynant, *Key features and updates for origin 2018.* Journal of Cheminformatics, 2018. **10**: p. 1-2.
150. Pletikapić, G. and N. Ivošević DeNardis, *Application of surface analytical methods for hazardous situation in the Adriatic Sea: monitoring of organic matter dynamics and oil pollution.* Natural Hazards and Earth System Sciences, 2017. **17**(1): p. 31-44.
151. Litvin, A.P., A.A. Babaev, P.S. Parfenov, A. Dubavik, S.A. Cherevkov, M.A. Baranov, K.V. Bogdanov, I.A. Reznik, P.O. Ilin, and X. Zhang, *Ligand-assisted formation of graphene/quantum dot monolayers with improved morphological and electrical properties.* Nanomaterials, 2020. **10**(4): p. 723.
152. Yuan, J., A. Gallagher, Z. Liu, Y. Sun, and W. Ma, *High-efficiency polymer–PbS hybrid solar cells via molecular engineering.* Journal of Materials Chemistry A, 2015. **3**(6): p. 2572-2579.
153. Nečas, D. and P. Klapetek, *Gwyddion: an open-source software for SPM data analysis.* Open Physics, 2012. **10**(1): p. 181-188.
154. Neshat, M. and N. Armitage, *Developments in THz range ellipsometry.* Journal of Infrared, Millimeter, and Terahertz Waves, 2013. **34**: p. 682-708.
155. Hechster, E. and G. Sarusi, *Modeling the PbS quantum dots complex dielectric function by adjusting the Ek diagram critical points of bulk PbS.* Journal of Applied Physics, 2017. **122**(2): p. 024302.
156. Gordon, G.V., R.G. Schmidt, M. Quintero, N.J. Benton, T. Cosgrove, V.J. Krukonis, K. Williams, and P.M. Wetmore, *Impact of polymer molecular weight on the dynamics of poly (dimethylsiloxane)− polysilicate nanocomposites.* Macromolecules, 2010. **43**(23): p. 10132-10142.
157. Yimsiri, P. and M.R. Mackley, *Spin and dip coating of light-emitting polymer solutions: Matching experiment with modelling.* Chemical engineering science, 2006. **61**(11): p. 3496-3505.
158. Jones, R.A.L., R.A. Jones, and R. Jones, *Soft condensed matter*. Vol. 6. 2002: Oxford University Press.

159. Smith, J.S., D. Bedrov, and G.D. Smith, *A molecular dynamics simulation study of nanoparticle interactions in a model polymer-nanoparticle composite.* Composites science and technology, 2003. **63**(11): p. 1599-1605.
160. Fetters, L., N. Hadjichristidis, J. Lindner, and J. Mays, *Molecular Weight Dependence of Hydrodynamic and Thermodynamic Properties for Well - Defined Linear Polymers in Solution.* Journal of physical and chemical reference data, 1994. **23**(4): p. 619-640.
161. Milchev, A. and A. Bhattacharya, *Polymer depletion interaction between a colloid particle and a wall: A Monte Carlo study.* The Journal of chemical physics, 2002. **117**(11): p. 5415-5420.
162. Winslow, S.W., J.W. Swan, and W.A. Tisdale, *The importance of unbound ligand in nanocrystal superlattice formation.* Journal of the American Chemical Society, 2020. **142**(21): p. 9675-9685.
163. Weidman, M.C., Q. Nguyen, D.-M. Smilgies, and W.A. Tisdale, *Impact of size dispersity, ligand coverage, and ligand length on the structure of PbS nanocrystal superlattices.* Chemistry of Materials, 2018. **30**(3): p. 807-816.
164. Shaqfeh, E.S. and G.H. Fredrickson, *The hydrodynamic stress in a suspension of rods.* Physics of Fluids A: Fluid Dynamics, 1990. **2**(1): p. 7-24.
165. Helfand, E. and Z.R. Wasserman, *Block copolymer theory. 4. Narrow interphase approximation.* Macromolecules, 1976. **9**(6): p. 879-888.
166. Ryan, A.J., S.-M. Mai, J.P.A. Fairclough, and I.W. Hamley, *Structures of amphiphilic block copolymers in their liquid and solid states.* Amphiphilic Block Copolymers; Alexandridis, P., Lindman, B., Eds, 2000: p. 151-167.
167. Marino, E., T.E. Kodger, G.H. Wegdam, and P. Schall, *Revealing driving forces in quantum dot supercrystal assembly.* Advanced materials, 2018. **30**(43): p. 1803433.
168. Kwon, S.G., G. Krylova, P.J. Phillips, R.F. Klie, S. Chattopadhyay, T. Shibata, E.E. Bunel, Y. Liu, V.B. Prakapenka, and B. Lee, *Heterogeneous nucleation and shape transformation of multicomponent metallic nanostructures.* Nature materials, 2015. **14**(2): p. 215-223.
169. Roe, R.-J., *Methods of X-ray and neutron scattering in polymer science*. 2000: Oxford University Press on Demand.
170. Rivnay, J., R. Noriega, R.J. Kline, A. Salleo, and M.F. Toney, *Quantitative analysis of lattice disorder and crystallite size in organic semiconductor thin films.* Physical Review B, 2011. **84**(4): p. 045203.

171. Park, S.Y., A.K. Lytton-Jean, B. Lee, S. Weigand, G.C. Schatz, and C.A. Mirkin, *DNA-programmable nanoparticle crystallization.* Nature, 2008. **451**(7178): p. 553-556.
172. Senesi, A.J., D.J. Eichelsdoerfer, K.A. Brown, B. Lee, E. Auyeung, C.H.J. Choi, R.J. Macfarlane, K.L. Young, and C.A. Mirkin, *Oligonucleotide flexibility dictates crystal quality in DNA‐programmable nanoparticle superlattices.* Advanced Materials, 2014. **26**(42): p. 7235-7240.
173. Langford, J.I. and A. Wilson, *Scherrer after sixty years: a survey and some new results in the determination of crystallite size.* Journal of applied crystallography, 1978. **11**(2): p. 102-113.
174. Li, T., A.J. Senesi, and B. Lee, *Small angle X-ray scattering for nanoparticle research.* Chemical reviews, 2016. **116**(18): p. 11128-11180.
175. Toolan, D.T., M.P. Weir, S. Dowland, J.F. Winkel, J.R. Willmott, Z. Zhang, V. Gray, J. Xiao, A.J. Petty, and J.E. Anthony, *Linking microscale morphologies to localised performance in singlet fission quantum dot photon multiplier thin films.* Journal of Materials Chemistry C, 2022. **10**(31): p. 11192-11198.
176. Toolan, D.T., M.P. Weir, R.C. Kilbride, J.R. Willmott, S.M. King, J. Xiao, N.C. Greenham, R.H. Friend, A. Rao, and R.A. Jones, *Controlling the structures of organic semiconductor–quantum dot nanocomposites through ligand shell chemistry.* Soft matter, 2020. **16**(34): p. 7970-7981.
177. Kwak, J., W.K. Bae, M. Zorn, H. Woo, H. Yoon, J. Lim, S.W. Kang, S. Weber, H.J. Butt, and R. Zentel, *Characterization of quantum dot/conducting polymer hybrid films and their application to light‐emitting diodes.* Advanced materials, 2009. **21**(48): p. 5022-5026.
178. Gao, L., L.N. Quan, F.P. García de Arquer, Y. Zhao, R. Munir, A. Proppe, R. Quintero-Bermudez, C. Zou, Z. Yang, and M.I. Saidaminov, *Efficient near-infrared light-emitting diodes based on quantum dots in layered perovskite.* Nature Photonics, 2020. **14**(4): p. 227-233.
179. Toolan, D.T., M.P. Weir, R.C. Kilbride, J.E. Anthony, N.C. Greenham, R.H. Friend, A. Rao, O.O. Mykhaylyk, R.A. Jones, and A.J. Ryan, *Mixed Small-Molecule Matrices Improve Nanoparticle Dispersibility in Organic Semiconductor-Nanoparticle Films.* Langmuir, 2023.
180. Toolan, D.T., M.P. Weir, J. Allardice, J.A. Smith, S.A. Dowland, J. Winkel, J. Xiao, Z. Zhang, V. Gray, and A.L. Washington, *Insights into the Structure and Self‐Assembly of Organic‐Semiconductor/Quantum‐Dot Blends.* Advanced Functional Materials, 2022. **32**(13): p. 2109252.